Europium based valence fluctuating systems with $ThCr_2Si_2$ structure type

Dissertation
zur Erlangung des Doktorgrades
der Naturwissenschaften
vorgelegt beim Fachbereich 13 (Physik)
der Johann Wolfgang Goethe-Universität
in Frankfurt am Main

Marius Peters
aus Frankfurt am Main

Frankfurt am Main, 2022

Vom Fachbereich 13 (Physik) der Johann-Wolfgang-Goethe-Universität Frankfurt als Dissertation angenommen.

Dekan: Prof. Dr. Harald Appelshäuser

1. Gutachter: Prof. Dr. Cornelius Krellner

2. Gutachter: Prof. Dr. Michael Lang

Termin der Verteidigung: 08. Juni 2022

Abstract

This work ties in with the investigation of the intermediate valent states and valence fluctuations in certain Europium based intermetallic systems. Valence fluctuations are a property of the electronic system of a compound that is possibly accompanied by structural effects – which, in some cases, are quite noticable. By assuming how the changes in the electronic system and in the crystal lattice are connected, valence fluctuations of europium are believed to be a possible probe for the theory of quantum critical elasticity, which is investigated on by the SFB TRR 288 (Frankfurt, Mainz, Karlsruhe, Bochum, Dresden).
Here, the proceedings in growing single crystals of different compounds related to this field of research are reported. This includes the $ThCr_2Si_2$ (122) type compounds $EuPd_2Si_2$ as well as the doping series $EuPd_2(Si_{1-x}Ge_x)_2$, the Europium based ternary Phosphides $EuFe_2P_2$, $EuCo_2P_2$, $EuNi_2P_2$ and $EuRu_2P_2$, and attempts to grow compounds of a derived 1144 structure by ordered substitution of half the Europium, $EuKRu_4P_4$.
The largest part of this work focusses on the $EuPd_2Si_2$ system, which exhibits intermediate valent europium and a temperature dependent transition between two different intermediate valent states of europium. Crystals of this system were grown using the Czochralski method with a levitating melt and an europium excess flux after a two step prereaction process. Also, explorations of a PdSi-rich flux and external flux methods are reported. Ten Czochralski grown experiments, in six generations iteratevely seeded by the previous generation, were prepared. Thermodynamical and structural analyses of the crystals located the transition between the different intermediate valent states of europium between 140 K and 165 K, transitioning from a high temperature $Eu^{2.3+}$ state to a low temperature $Eu^{2.7+}$ state, and classified it as a second order transition. To this transition a lattice anomaly of the a-parameter collapsing about 2% is connected, while the c-parameter remains largely unaffected. Large differences between individual samples can be explained by combining thermodynamical and structural analyses with compositional analysis, revealing the valence transition temperature as strongly dependent on the sample composition and Pd-Si site interchanges.
Searching to change the character of the valence transition to first order, silicon was substituted by germanium to introduce negative pressure. Germanium doped samples of $EuPd_2(Si_{1-x}Ge_x)_2$ were grown using the Czochralski method with the optimized parameters from the growth experiments for the undoped compound. Samples were prepared with a nominal substitution of $x = 0.05$, $x = 0.10$, $x = 0.15$, $x = 0.20$ (twice) and $x = 0.30$. The incorporation rate was found to be about 60% of the nominal substitution level. Transition temperatures are suppressed strongly by introducing germanium to the unit cell, but remain of second order. With a real doping of $x = 0.105$, valence transition is suppressed and taken over by a long range antiferromagnetic order of europium spins. In this particular system, no first order valence transition could be found, promoting the conclusion that germanium substitution, despite isoelectronic, is not equivalent to exerting pressure. Instead, disorder seems to play a role in veiling the first order valence transition, that is proposed to occur in the generalized phase diagram of europium based compounds.
In ternary europium phosphides EuT2P2, the position of the compounds in the

generalized phase diagram and the question of long range magnetic order or valence transition appear connected to an isostructural transition of the tetragonal crystal structure, drastically decreasing the length of the c-parameter while establishing covalent bonds between phosphorus atoms of different interlayers of the structure, the so called "collapse". While $EuFe_2P_2$ (ferromagnetic at 29 K), EuT_2P_2 (ferromagnetic at 29 K) and $EuCo_2P_2$ (helimagnetic at 67 K) display both long range magnetic order and a non-collapsed crystal structure, $EuNi_2P_2$ shows both a valence transition between two intermediate valent states at a characteristic temperature of 36 K – accompanied by a small lattice anomaly of the a-parameter shrinking about 0.2% – and a collapsed crystal structure. Samples of $EuFe_2P_2$, $EuCo_2P_2$ and $EuNi_2P_2$ were grown in tin flux yielding platelike samples with an edge length of at least 2 mm and average masses ranging from 4 mg ($EuFe_2P_2$) to 13 mg ($EuCo_2P_2$). EuFe2P2 and EuRu2P2 were also grown using solid-solid sintering approaches to gain powderous samples of the compounds.
Single crystals of $EuFe_2P_2$, $EuCo_2P_2$ and $EuRu_2P_2$ were investigated at ESRF in Grenoble with single crystal X-ray diffractometry on a pressure range up to 15 GPa and at temperatures down to 15 K to investigate the nature of the structural transitions in the compounds. While in $EuCo_2P_2$ the structural transition occurs as a transition of first order at all temperatures (e.g. at 2 GPa for 15 K), in $EuFe_2P_2$ and $EuRu_2P_2$ the structural collapse evolves over a broad pressure range up to 8 GPa and as a transition of second order troughout the temperature ranges, albeit seeming to sharpen at lower temperatures. From the crystallographic data, elastic constants of the compounds could be derived, revealing $EuFe_2P_2$ and $EuRu_2P_2$ as unexpectedly elastic materials with bulk moduli of (34 ± 1) GPa at 300 K and (28 ± 3) GPa at 15 K ($EuRu_2P_2$) and (31 ± 4) GPa at 300 K and (28 ± 4) GPa at 15 K ($EuFe_2P_2$).
In order to probe the structural collapse at more accessible pressures, crystals with a sturcture derived from the 122 structure, but with ordered 50% substitution of europium and hence altering the symmetry from I4/mmm to P4/mmm in a 1144 structure, were exploratively pursued. Different experiments to obtain $EuAT_4P_4$ (with A = K, Rb, Cs and T = Fe, Ru) from binary or ternary prereactants or directly from the elements remained largely unsuccessful.

Preface

This work is a literary inscription concluding the time of my training as a PhD candidate in the lab group of Prof. Dr. Cornelius Krellner at the Goethe University in Frankfurt. While in the following round about 200 pages, everything will be dedicated to Europium based valence fluctuators and what I learned about them, there are also some words to be said about how I want to communicate my report. In this short preface, I want to take position regarding two issues: the first is, that this work is foremost a scientific report, but not entirely so because of the specific context - the scientific training - it originated in. This is why I will comment on how I structured this work to make it also accessible to non expert readers. Secondly, this work developed over the course of some years, and hence the style it is written in is layered. Instead of cleansing this in a last revision, I opted for using the different text layers for reflecting on things I learned over the last years not *in*, but *about* science.

On the structure of this monography

Firstly, and most importantly, this monography is not only serving the purpose of being a thesis for achieving the Doctoral degree. This is its cause and main purpose. But additionally, this work also is a contribution to working history and state of the art within the SFB TRR 288. This means, that in order to conserve at least some form of knowledge about the history of the coming about, processes of working get a fair share of attention besides results, and also, especially in chapter 11, I report on failures and problems in detail.
Additionally, I do not only try to close of my own work, and not only to communicate the state of the project into the assemblage of the SFB TRR 288, but I also intent to open up this work as a window to the field of solid state physics to younger students. With a basic understanding of the matter in a usual introductory lecture to solid state physics, I hope to be able to at least give some idea of what this work is about also to the non specialist reader. This motivates me to adopt two main measures: first, to try and formulate quite extensively. And second, it motivates me to include some chapters in the front of the monography, that might serve as a detailed glossary, introducing just a little bit more of basic terms and concepts (with some hints to basic literature). Hopefully, this motivation excuses for the extension of this work.
The chapters 2-4 include basic information on the nature of phase transitions, magnetic phases and the reading of phase diagrams, that hopefully help to bridge the gap between introductory lectures and this work, and at least give the inclined reader a vague idea of how the matter of this work is organized. In chapter

5, not only the theory of Quantum Critical Elasticity is reviewed, but also the basic terms are introduced, which the theory relies on. Although many of those do not explicitly play a role later on, it is useful to know about their constitution in order to see the targets of this work properly. Only after that, the scientific part in chapters 8-11 is prepared by bridging from the Quantum Critical Elasticity theory to the europium valence in chapter 6 and a discussion of the methods applied in chapter 7.

On the style of this monography

This monography came into being over the course of several years of every now and then writing up some crumbs of literature or laboratory work. Hence, the whole work is layered in terms of style. This might be most obvious for dealing with the role of the researcher as a subject in science.
Do we use “I“, “we“ or passive constructions reporting about the coming about of laboratory work? This is not only an abstract question of a correct scientific style, but also reflects on the role of the scientist as an individual and the scientific collective of e.g. a lab group in the process of doing science. Whether individual researchers or collective show up in the report of a scientific work ties directly to the image of nature and truth transported in our scientific communities [1]. Do we accept a transcendent nature, in which facts merely exist, or do we acknowledge the artificiality of the laboratorial situation, and hence also acknowledge, that our laboratorial situation confines our perspective on our research topics and likewise enables us to construct and test theories and hypotheses, that appear in a certain form?
With the latter, the constructional work of single scientists or small scientific collectives is not neglegible anymore. And this is also consistent with the everyday laboratory experience - everyone working in a laboratory is a specialist for a highly confined set of topics and methods, where in this exact composition of topics and methods, there are but few people who can discuss the processes and results of the work in their full scope. Hence, the “I“ raises to be important, because it is the specialist who mobilizes a certain set of methods to claim a field, and so does the “we“, for the specialist, who works in the lab, works together and discusses the results of the work with a scientific collective, that is likewise specialized, and it is primarily in those groups and scientific networks, and not in the scientific “plenum“, that ambiguities in interpreting the experiments are discussed.
Dismissing the individual researcher as the scientific subject, and dissolving them in a diffuse, but by construction intersubjective and seemingly trustworthy scientific “plenum“ is one of the great narratives of modern science from its beginning on [2]. If something is true, so the narrative, everyone should be able to approve - and the whole community of science is conceptualized to witness the finding of truth in the scientific process. This narrative is powerful in how scientists reflect the working of science over all; but it fails immediately when being confronted with the highly specialized everyday struggle in the laboratory. Here, the individual researcher and their small group of peers is still in charge.
This role of the researcher - myself - and their peers - the lab group of Prof. Krellner mostly, but also cooperating scientists of other groups - I reflected in

various different ways over the course of the three years, that I spent on carrying together all the pieces, that form this work in the end. First, I did not think about it at all and conformed to the erasure of the subject unaware of this conflict, that needs to be reflected. Later, I started using the "I" to highlight the role of the researcher doing the work, which then I conveyed to rather highlighting the "we", as the network is condition and productive participant in every step of a scientific construction. In the end, I started to follow the main path of erasing the subject again, since all of the work of a scientific network is to produce for the rest of the world, all the other networks, what *is the case*, the construction of a fact, that conventionally is presented standing for itself. The constructional work behind it is unreflectedly known when the word is handed over to the things under scrutiny.
This reflection process shows in the different layers of the work at hand, which I refrained from clearing out to one style (not only referring to who is the subject in the reports, but also more subtle reflections on scientific constructional work), instead preserving the respective styles the parts were originally written in, so that the whole process of reflecting the role of the lab worker can be seen in various facets in the text here and there.

After this preface, I hope the ground is well prepared for both the reporting of scientific results and the description of scientific processes; for highly specialized peers to follow through the work in detail and utilize the science presented here, and for "strangers" to the field to be able to get some slim insight into a broad field; and for both comprehending the scientific processes, that lead to this work, its position in ongoing scientific research, and also the directions, in which subsequent works may be lead from here on.

Contents

List of Figures

List of Tables

1 Introduction

In most of the textbook theories of solid state physics, there is a strong focus on describing the dynamics of the electronic system of a solid with a certain degree of approximation dependent on the model, whilst assuming the lattice of the (here assumed to be crystalline) solid to be a static environment in which the properties of the electronic system can unfold. May it be, that a description of lattice degrees of freedom is also used to describe thermodynamical properties of a solid - those descriptions of phonons and quasi particles is widely decoupled from the description of the electronic system in the textbook theories. Theories, that couple electronic and lattice degrees of freedom to describe the properties of a crystal as the properties of an integrated system of electrons and a lattice, are very rarely seen. One example, that is being discussed very frequently and extensively is the coupling of electrons and phonons in the description of superconductivity, but apart from this, such theories are not very prominent.
About 2020, a DFG funded SFB assembled in Frankfurt, Mainz, Karlsruhe, Dresden and Bochum in order to anew stake the field of coupled electron-lattice-phenomena and the description of systems with both lattice and electronic degrees of freedom, around the idea of conjoining the classical description of criticality in elastical phenomena with the quantum nature and statistics of contemporary solid state physics, with a given expertise in dealing with Quantum Criticality in purely electronic systems. Hence the whole assemblage sort of evolved around a newly emerging theory of Quantum Critical Elasticity, as proposed by Mario Zacharias, Idranil Paul and Markus Garst [3], and builds on experimental findings as e.g. of the breakdown of Hooke's law in organic charge transfer salts by Elena Gati et al [4]. The assemblage was then brought forward and awarded a transregional SFB grant by the DFG in 2020.
Within this SFB, this work is located in the A03 subproject (lead by Cornelius Krellner and Kristin Kliemt as joint Principal Investigators). Beginning in October 2018, it was the second work - after Eunhyung Chos bachelor's thesis [5], which was a first scouting towards the $EuPd_2Si_2$ system and produced a seeding crystal and a rough working point for the start of this work - targeting the compounds, that should later form the base of one of the branches of the SFB, centering around europium based intermetallic systems, $EuPd_2Si_2$ exhibiting valence fluctuations conjoined with a large lattice anomaly. About one and a half years of this work were done in preparation of the application for the transregional SFB grant, while later it was then transferred to the successfully granted SFB's roster.
This work focusses on europium based intermetallic systems in (and related to) the tetragonal $ThCr_2Si_2$ structure. In 2017, Onuki et al [6] proposed a generalized phase diagram for europium based compounds (described in section 6.3),

that seemed to allow a general agreement with the theory of Quantum Critical Elasticity [3] for a variety of systems.
Together with this, they also reported the first single crystals of the $EuPd_2Si_2$ system; a system, that was extensively studied in the 1980s until the 2000s using polycrystalline samples (e.g. [7, 8, 9, 10, 11]), and is known to exhibit both valence fluctuations and a transition between two different intermediate valent states and a strong lattice anomaly connected to the change of the valence. Different dopings were also applied to the polycrystalline system: Ge [12], Sn [13], Au and Pt [10].
With all these prospects, the system was chosen to be one of the prime targets for project A03 to provide large scale single crystalline samples for the SFB's investigation on elastic and critical behaviour, promising accessible, strong effects with quite a good tunability. Hence, the two main chapters of this work center around the undoped $EuPd_2Si_2$ compound (chapter 8) and applied doping, specifically germanium (chapter 9).
Furthermore, another lattice anomaly in europium based $ThCr_2Si_2$ structural type systems is also target for investigation of its connection to the valence transition of the europium in the compound, this is: the collapse of the c-axis in the 122 phodphides (i.e. with phosphorus on the silicon place), driven by the formation of a covalent bonding of the phosphorus atoms between different interlayers. Not only is there, using common transition metals on the chromium place, only one collapsed structure (with T = Ni), while the others (T = Fe, Co, Ru) are non-collapsed, also, the divide between systems that magnetically order (T = Fe [14], Co [15], Ru [16]) and intermediate valent systems (T = Ni [17]) is the same. Also, studies from the 1990s indicate, that one might be able to exert pressure on the noncollapsed, ordering compounds into a structural collapse and a state of intermediate valence [18]. This motivates raising the question of whether and how the structural collapse and the transition to intermediate valence are connected. For this, the ternary phodphides in discussion were grown and investigated under pressure (chapter 10), and also, some effort was taken to try and obtain a 1144 structural type compound, where 50% of the europium spaces are replaced with a dopant in an ordered fashion, to see whether this sort of structure exists as a stable and obtainable compound, and a (partial) collapse of the structure can be arranged at near ambient conditions (chapter 11).

2 Thermodynamic and quantum phase transitions

A state of matter is a macroscopic property of an ensemble of atoms, whose observables are governed by statistically determined behaviour. When an ensemble in a consistent state of matter is called "a phase", every interaction with matter and every process within a material - as long as they fulfil certain demands - can be described in terms of transitions between differend phases, i.e. states of matter with different properties. This is why this chapter will focus on defining the concept of a phase more clearly and then will continue to describe and classify transitions between phases in a classical/thermodynamical regime at finite temperatures as well as in a quantum regime at potentially zero temperature.

2.1 Phases and phase transitions

For a basic understanding of the concept of phases and phase transitions we will follow the standard textbooks, e.g. [19].
A *phase* is a state of matter, where the matter is observable to display certain macroscopic properties homogeneously, such as the density, the aggregate state, the spatial symmetries, mechanical responses, electric and magnetic behaviour.
The specific phase a system will be in, is determined by the specific state of the system's degrees of freedom. So, if all degrees of freedom (whose number is determined by the number of distinguishable actors, e.g. atoms) are settled to a specific state, there is only one phase to exist, since phases are homogeneous. If degrees of freedom remain unsettled, they enable phases to coexist. This is expressed in the *Gibb's phase rule*:

$$f = 2 + N - P \tag{2.1}$$

where we determine the phase space dimensionality of a phase region f by counting the degrees of freedom $2 + N$ (Temperature, pressure and others due to composition; e.g. for aggregate phases we use the number of different elements) and weigh it against the number of coexisting phases P.
A subspace containing two or more phases could hence be described as a phase interface. Tuning a degree of freedom over such an interface and beyond forces a system to change its phase at the interface, where both adjacent phases can coexist. This process is then called a *phase transition*. At those interfaces, the describing energy functions for the system change, and hence are discontinuous to a certain level.

2.1.1 Ehrenfest's classification of phase transitions

Due to a change in the describing energy functions of a system upon a phase transition, some derived functions of the free enthalpy function $G = G(T,p)$ are discontinuous while the phase transition is taking place. The derivation order on which discontinuities occur, characterises the phase transition. This classification of phase transitions follows a model developed by Paul Ehrenfest.

First order phase transitions

For a first order phase transition, the Gibb's enthalpy G is continuous with respect to both natural variables the temperature T and the pressure p, but the first derivatives of the Gibb's enthalpy with respect to the natural variables are discontinuous (fig. 2.1a), i.e. the *volume* ($\partial G/\partial p = V$) and the entropy ($\partial G/\partial T = \Delta S$).

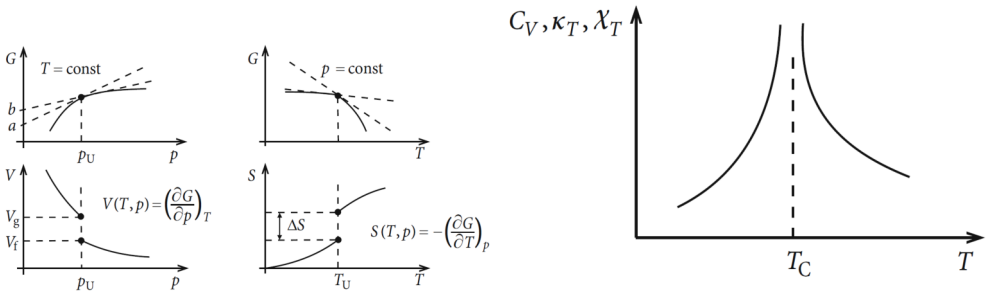

(a) (b)

Figure 2.1: Behaviour of first and second order phase transitions in physical properties [19]. (a) Schematic behaviour of a systems Gibb's enthalpy and first derivations with respect to T and p at a phase transition of first order. (b) Schematic behaviour of a systems second order derivatives with respect to T, p and H at a phase transition of second order.

The discontinuities in the entropy function of the system necessitates a finite amount of energy to be expended in order to conduct the phase transition. This is called the latent heat of a phase transition.

Second order phase transitions

For a second order phase transition, the Gibb's enthalpy G is continuous as well as its first derivatives with respect to the natural variables, the volume V and the entropy S, but the second derivatives, i.e. the heat capacity ($c_p = \partial^2 G/(\partial T)^2$) and the compressibility ($\kappa_T = \partial^2 G/(\partial p)^2$), are discontinuous at the phase tranisition. In addition, the phase separation curve needs to fullfil the Ehrenfest equation:

$$\frac{dp}{dT} = \frac{\alpha^{(1)} - \alpha^{(2)}}{\kappa_T^{(1)} - \kappa_T^{(2)}}$$

where $\alpha = (1/V)((\partial V/\partial T)_p)$ is the thermal expansion coefficient, and (1) and (2) refer to the two equilibrated phases.

The Ehrenfest classification is criticised in that way, that it is too narrow, since second order phase transitions may also diverge in the second order of derivation, where the leap in the first order derivation connected to that divergence is thought to be infinitely small - still, they may behave as in figure 2.1b.

2.2 Landau theory of phase transitions

Lew Landau developed another phenomenological mean field theory on how to describe phase transitions [20] and part them into different classes, complementing Ehrenfests classification. The theory starts one layer below the Ehrenfest description, not describing the energy functions of the system, but the enthalpy of the phase transition itself. The central aspect of the classification of a phase transition is here whether the change in symmetry takes place in a continuous or a discontinuous way.
Landau describes "ordinary" phase transitions (of a first kind) as such phase transitions altering a system from one symmetry to another within a discontinuous process, that also needs to turn over a finite amount of enthalpy.
On the other hand, a phase transition "of the second kind" is a phase transition altering the system's symmetry in a continuous way. This means, that, on the transition point, the system will at the same time behave compatible to the description of both phases, and thus there will also be no enthalpy turned over during the process. For a description of a phase transition of the second kind, an order parameter is to be identified, which can be used to Taylor-expand the (vanishing) enthalpy of the process around zero to use it as a potential for a general description of the phase diagram.

2.2.1 Order parameters

When a system undergoes a phase transition, there might be macroscopic variables, that are non-zero only for one of the phases connected in the pase transition, e.g. the spontaneous magnetisation for a paramagnetic-to-ferromagnetic phase transition or the electron-phonon coupling for a transition into a superconducting phase. This macroscopic variable is referred to as the *order parameter* η of a phase transition.
Landau exemplifies the order parameter for phase transitions of first and second kind with the example of an alloy of copper and zinc. He proposes the order parameter:

$$\eta = \frac{w_{Cu} - w_{Zn}}{w_{Cu} + w_{Zn}}$$

with w_i the probability to find an atom of the kind i on a neighboured space, where $\eta \neq 0$ corresponds to a crystalline order and $\eta = 0$ corresponds to a state of continuous spatial symmetry.
He explains, that we obersve a phase transition of first kind, if the order parameter drops from non-zero to zero discontinuously, and a phase transition of second kind, if it drops to zero continuously.

2.2.2 Potential of a phase transition

To describe the properties of phase transitions of the second kind (e.g. the specific heat jump), the enthalpy $G = \int dV \Phi(p,T,\eta)$ is expanded with a Taylor expansion in terms of η. The actual value of η is to be determined out of the condition of thermal equilibrium (i.e. the condition for Φ to actually have a minimum for any given p and T).
Since for a phase transition of the second kind, the order parameter η will be arbitrarily small around the phase transition, we can expand the enthalpy in terms of η around the transition point:

$$T_0^4 \left[\Phi(\eta)\right] = \Phi_0 + \alpha \cdot \eta + A \cdot \eta^2 + B \cdot \eta^3 + C \cdot \eta^4. \tag{2.2}$$

The coefficients may depend on temperature and pressure. The so called conjugated variable $\alpha \to 0$ needs to approach zero for phases $\eta = 0$ and $\eta \neq 0$ distinguishing in symmetry (which is the assumption). Later we see in chapter 5, that this property needs to be created.
$A(p,T)$ also needs to vanish in the transition point itself, since it needs to be positive in one and negative in the other phase. This means we can linearly expand the parameter $A(T)$ for a fixed pressure around the transition point:

$$A(T) = a(T - T_c).$$

For the transition point to be a stable state, i.e. $\Phi(p_c, T_c, \eta)$ to be a minimum, also the coefficient of the third order needs to be $B = 0$. $C > 0$ is to be positive for the same reason.
The temperature dependence of the order parameter in the ordered phase can be easily determined by the condition for $\Phi(\eta)$ to have a minimum, i.e.

$$\frac{\partial \Phi}{\partial \eta} = 0.$$

With this condition, we gain

$$\eta(A + 2C\eta^2) = 0$$

thus as a solution for the order parameter in the unsymmetric phase ($\eta = 0$ corresponds to the symmetric phase)

$$\eta^2 = \frac{A}{2C}$$

and using condition 2.2.2

$$\eta^2 = \frac{a}{2C}(T_c - T)$$

for the closest proximity to the transition.
Important is to notice the form necessary for enthalpy (which we will call the Landau potential) required to apply the Landau theory of phase transitions to describe it as a phase transition of second order, $A \to 0$, $C > 0$:

$$\Phi(\eta) \approx \Phi_0 + A \cdot \eta^2 + C \cdot \eta^4. \tag{2.3}$$

2.2.3 Critical exponents

Based on the potential approach for the enthalpy G:

$$G = \int dV \left[K \left(\nabla \eta \right)^2 + r\eta^2 + u\eta^4 - h\eta \right] \tag{2.4}$$

(Wosnitza [21] introduces a slightly different nomenclature we will use from now on, with $\alpha \to h$ the conjugated variable, $A \to r$ and $C \to u$, because it is also later used in the publications on quantum elasticity theory, see chapter 5.2; this review paper is leading literature for this section.)
a set of critical exponents can be derived for a phase transition to describe the diverging behaviour of different physical properties (specific heat, order parameter, susceptibility, correlation length) in close proximity to the transition point. The specific heat, for example, behaves as $C \propto |t|^{-\alpha}$, where $t = \dfrac{T - T_c}{T_c}$ is the reduced temperature. A mean field like theory as the Landau theory would predict $\alpha = 0$ to vanish for a constant jump. Real phase transitions often deviate from this prediction and show a λ-shape. This deviations grow important if the (in the Landau theory neglected) fluctuations of the order parameter grow large. This is the case for a small range of $|t|$, that depends on the system observed.
α can be extracted from specific heat data by using the fit function

$$C^{\pm} = \frac{A^{\pm}}{\alpha} |t|^{-\alpha} + B + E \cdot t \tag{2.5}$$

where α is the critical exponent, A, B and E parameters, and $\pm$ refers to different parameter values for $t < 0$ and $t > 0$. $B + E \cdot t$ is meant to locally approximate the noncritical part of the specific heat in a low order Taylor expansion. The last term describes the divergent behaviour.
The determination of α and other critical exponents is used to gain insight into the universality class of the phase transition, i.e. the dimensionality, pattern and model of ordering (e.g. [22], or even as a characterization in a phase diagram [4]).

2.3 Quantum criticality

For classical phase transitions, thermal fluctuations destroy the coherence of quantum phenomena in a system [21]. When the temperature of the system is approaching zero, a phase transition can not be driven by thermal fluctuations anymore, but needs another driving parameter (e.g. the magnetic field, [21] again).
If there is a phase transition at zero temperature, that is driven by another parameter, the quantum critical point influences its vicinity and causes a parameter region (i.e. an interval of the relevant parameter r, that is broadening with rising finite temperature, and originates from the quantum critical point), where the behaviour of the system is dominated by thermal excitations of the quantum critical ground state and leads to non-Fermi liquid behaviour and unconventional power laws in the physical properties of a system [23, 24, 25].

3 | Magnetic properties of solids

Up to now, we were able to describe all the emerging effects and properties within an approximation of noninteracting single electrons. When it comes to magnetism now, we get hand on a collective phenomenon. Single electrons do not display any magnetism unless interacting with external fields or other electrons.
At least, we need to collect and summarize all the electrons of one ion. With this, we can already understand the interaction of ions with external fields, i.e. para- and diamagnetism, as well as the coming about of an ion's magnetic moment.
Placing more than only one ion, each with a magnetic moment, on a grid and have them interacting will add a layer of interaction to the system and display long range ordering phenomena, e.g. Ferro, Ferri- and Antiferromagnetism or more exotic kinds of collective magnetism.
For the expositions in this chapter, J. Coey's book on "magnetism and magnetic materials" [26] serves as a source, if not mentioned otherwise.

3.1 Magnetic moment of an atom

A magnetic moment arises from the motion of charge, for which the angular momentum of a charge carrier is an identifier. In an atom, this is, within the approximation to neglect the core motion and spin, a matter of describing the electrons and their orbital states. This leads, since the most exact description of atomic electron levels is quantised, to a quantum theory of magnetism.
In order to determine the magnetic moment of a given ion, it is to evaluate the contributing electrons, their spins, that lead to an effective total spin, and their orbital momentum distribution. Furthermore we need to learn about the mechanisms to couple this two kinds of magnetic moments to finally evaluate the ion's moment.

3.1.1 Orbital moment

The term "orbital" remains from the by now manifoldly revised Bohr model of atoms, in which the idea is for the electrons to cycle around the core on closed orbits, which correspond to a certain level of energy as well as a certain angular momentum.
The Bohr model with all its flaws and problems was tuned to already find the correct expression for the orbital magnetic moment $\mathbf{m}$ of electrons, that is

$$\mathbf{m} = -\frac{e\hbar}{2m_e}\mathbf{l} \tag{3.1}$$

where $\mathbf{l}$ is the vector (with an absolute of l) displaying direction and amount of quantised portions of angular momentum with a value of $\hbar$ each. For a particular direction (conventionally called z), the magnetic moment is given as

$$m_z = -\frac{e\hbar}{2m_e} m_l \tag{3.2}$$

where $m_l < l \in \mathbb{Z}$ is the orbital magnetic quantum number, quantising the angular momentum with respect to that particular axis to multiples of $\hbar$ and thus the magnetic moment to multiples of the Bohr magneton μ_B

$$\mu_B = \frac{e\hbar}{2m_e}$$

In the conventional naming of orbitals, the angular momentum of the orbital (in analogy to the corresponding orbit) is denoted by a letter, that encodes the quantum number: s (sharp) means $l = 0$, p (principal) is for $l = 1$, d (diffuse) for $l = 2$, f (fundamental) for $l = 3$ and from there on it is alphabetically following the f.
In an ion, an orbital may contain a certain amount of different electronic states (not respecting spin doubling for now), that equals $2l+1$. Each state corresponds to a different value of the orientation quantum number m_l. The totality of electronic angular momenta $L = \sum_{|m_l|<l} m_l$ is called the total angular momentum of the orbit.

3.1.2 Spin

Additionally to their angular momentum due to their affiliation to a certain orbital, electrons also carry an intrinsic magnetic moment due to their spin. This moment displays the value of

$$\mathbf{m} = -\frac{e\hbar}{m_e}\mathbf{s} \tag{3.3}$$

where the absolute value of the spin vector is 1/2. This is displayable by an orientation quantum number of $m_s = \pm 1/2$. The mechanisms of spin moment creation seem to be twice as efficient as the orbital moment mechanisms. Still, there is no intermediate third spin state that would equalise this misrelation.
Generally you can add up all the spins of an orbital of interest to its resulting total spin $S = \sum_{electrons} m_s$.

3.1.3 Spin-orbit coupling

A virtual atom, that possesses both a resulting spin S and a resulting angular momentum of the orbitals L, will generally couple them, so that they can be handled as a total magnetic moment J. This is valid, if the spin-orbit interaction

$$\hat{H}_{so} = \lambda \hat{L} \cdot \hat{S}$$

(where λ is the coupling energy, $\hat{L}$ and $\hat{S}$ the quantum number operators) is the second leading order of magnitude (after the dominating coulomb force, which is isotropic and thus does not contribute to a magnetic moment) for the electronic interactions. This is especially true for heavy elements, since the spin-orbit coupling energy scales with the proton number to a recognisably large power $\propto Z^4$.

3.1.4 Hund's rules

The Hund's rules give the willing user advice how to distribute the electrons of the orbital of interest over the available states, if the anisotropic intraatomic exchange is dominated by spin orbit coupling.
Since all fully occupied orbitals contribute a magnetic moment of zero, it is only necessary to have a closer treatment of the not fully occupied orbital of any given atom. The magnetic moment J of such an orbital constructs, following Hund's rules, as follows:

1. Maximize S for the given electronic configuration. (There are $2l+1$ spin-up and $2l+1$ spin-down states available in the orbital.)

2. Maximize L. This step needs to be consistent with step number one.

3. The coupling is $J = |L-S|$ for a less then half filled orbital and $J = L+S$ otherwise. (Note: if the orbital is exactly half full, $L = 0$ and thus $J = S$ ist consistent with both rules.)

3.1.5 Crystal electric fields

One of the main competitors of the spin-orbit coupling when it comes to exchange interactions of electrons in solids is the crystal electric field (CEF). They are tools of a mean field theory to describe not only the environment of electrons inside an ion, but in a greater context of a set of ions, where an electron exchanges with all the electrons in its surrounding and observes their local distribution.
While spin-orbit coupling weakens slightly with growing distance to the ionic core, the crystal electric field effects enhance strongly for a broader electronic distribution. Thus, CEF effects are of greatest importance for the diffusely distributed 3d-electrons in the transition metals, and even compete to the Coulomb force, and a magnetic moment is not accessible via the Hund's rules.
Opposed to this, for the localised 4f-electrons of the Lanthanoids, the spin-orbit coupling is a whole order of magnitude stronger than the CEF effects; hence, a construction of the magnetic moment by the Hund's rules works out just nice. (Compare table 3.1 for orders of magnitude of different energy contributions.)
A magnetic moment, that is mainly influenced by the crystal electric field, cannot be determined analytically, but needs to be simulated (by simulating the electronic surrounding) or interpolated (from actual measurement data).

Orbital	Coulomb ($\hat{H}_0$)	Spin-Orbit ($\hat{H}_{SO}$)	CEF ($\hat{H}_{CEF}$)	Zeeman ($\hat{H}_Z$)
3d	$1-5\cdot10^4$	10^2-10^3	10^4-10^5	1
4f	$1-6\cdot10^5$	$1-5\cdot10^3$	$\approx 3\cdot10^2$	1

Table 3.1: Orders of magnitude of the contributions to the Hamiltonian of an ion in a solid state environment, energy scales in Kelvin, following [26].

3.1.6 Itinerant and local magnetism

One refers to the different behaviours of the d- and f-orbitals with the concept of locality of the magnetism. The magnetism is said to be more local, the closer the electronic distribution of the magnetic orbital is located to the ion core. The further the electronic distribution expands away from the ion core, the more itinerant (i.e. "wandering around") is a magnetic moment held to be.
Referring to the project's main elements, the magnetism of Europium moments are formed by the 4f orbital and are hence very close to the core. Thus, magnetism displayed by Europium ions is a local magnetism with a distinct magnetic moment that is determinable by applying the Hund's rules.
For transition metals on the other hand, the constituents of the magnetic moment sit in the d-orbitals, which are widely distributed around the ion core. The magnetism is itinerant and dominated by crystal electric field effects. The magnetic moment of transition metals can be simulated, but not analytically calculated, since the Hund's rules do not apply here.

3.2 Magnetic phases

Now, having constructed a magnetic moment of an ion, this raises the question for the vast multiplicity of possibilities of magnetic moments interacting with external magnetic fields (responsive magnetism), or different magnetic moments interacting with each other (collective ordering). Various possibilities for both interactions will be treated in the following subchapter, as far as they might be relevant for Europium based systems.

3.2.1 Para- and diamagnetism

Para- and diamagnetism are the two main classes of interaction between ionic magnetic moments and an external magnetic field. While paramagnetism describes a scenario, where the magnetic moment couples to the external field via a positive susceptibility and orientates along the fields main direction, diamagnetism describes the counterscenario, where the magnetic moment couples to the external field via a negative susceptibility and will orientate against the external field.

Pauli-Paramagnetism

The Pauli-paramagnetism (description following [27]) is a sort of paramagnetic behaviour that even exists within the concept of a free electron gas, since it only describes the orientation of free spins along an external magnetic field $\mathbf{B}_0$.
Spins parallel to B_0 will experience an energy ease of $-\frac{1}{2}g_0\mu_B B_0$, spins antiparallel to the field will experience an energy lift of $\frac{1}{2}g_0\mu_B B_0$. Thus, the energy levels of this two states are separate by a total energy of $g_0\mu_B B_0$. At low temperatures $T \ll E_F$, this leads to a total of electrons which will have an uncompensated spin moment of $\frac{1}{2}D(E_F)g_0\mu_B B_0$.
The magnetisation then is

$$\mathbf{M} = \frac{1}{2} D(E_F) g_0 \mu_B \mathbf{B}_0 \frac{1}{2} g_0 \mu_B$$

and thus the Pauli susceptibility

$$\chi_P = \frac{\partial M}{\partial B} = \frac{\mu_0 g_0^2 \mu_B^2}{4} D(E_F) \tag{3.4}$$

Curie-Paramagnetism

If carried one step further, we still observe the field splitting of the localised spin states, but at finite temperatures we do not any longer observe the direct influence of the density of states at the Fermi edge, but of a temperature region around the Fermi edge, that is thermally activated and populates both spin states (up and down, well defined through the localisation) according to a Boltzmann factor $\exp(\pm \mu B / k_B T)$.
This yields a magnetisation of

$$M \propto \mu_B \left[\exp(\mu B / k_B T) - \exp(-\mu B / k_B T)\right]$$

With a definition of $x = \mu B / k_B T$ we can express the average magnetic moment in a specific direction in terms of comparation of the external field and the temperature:

$$\langle m_z \rangle = \mu \frac{\exp(x) - \exp(-x)}{\exp(x) + \exp(-x)} = \mu \tanh(x)$$

which yields a magnetisation of

$$M = n \cdot \langle m_z \rangle = n\mu \tanh(x).$$

For room temperature ($\mu B \ll k_B T$) with $\tanh(x) \approx x$ for small values of x we find then for the Curie-susceptibility

$$\chi_C = \mu_0 \frac{\partial M}{\partial B} = \frac{n \mu_0 \mu^2}{3 k_B T} = \frac{C}{T} \tag{3.5}$$

where $C = n\mu_0\mu^2/3k_B$ is the Curie constant. Approaching zero, the susceptibility will diverge.

Van Vleck-Paramagnetism

Alternatively to a split state Boltzmann population of spin states and according interaction with external fields, another possibility of basic interaction between a ground state and a low lying excited state due to an external field is the mixing of states. It is possible, that some of the excited state's character contributes to the ground state under influence of an external field. This yields a temperature independent kind of paramagnetism of notably smaller order of magnitude than the Curie paramagnetism linked to a finite magnetic moment.
For Europium systems, this Van Vleck paramagnetism is especially interesting, because Eu^{3+} ions have a $J = 0$ ground state and a low lying $J = 1$ excited state

at 330 K, which yields a contribution to the ions paramagnetism.
The energy terms and thus the susceptibility arise from perturbation theory:

$$\chi_V = 2n\mu_0 \left[\frac{\mu_B}{\hbar}\right]^2 \frac{\left|\left\langle g \left| \hat{\mathbf{L}}_Z + 2\hat{\mathbf{S}}_Z \right| e \right\rangle\right|^2}{\Delta\epsilon} \tag{3.6}$$

with g the ground state, e the excited state and $\Delta\epsilon$ the energy gap.
As we can see, the Van Vleck paramagnetism depends on offdiagonal matrix elements of the magnetic moment and thus is related to a mixing or interchange of ground state and excited state. This is especially important for ions with a zero magnetic moment in the ground state, for example Eu^{3+} (see chapter 6.2).

Orbital diamagnetism

An electron with an orbital momentum will preceed under the influence of an external magnetic field. This precession is known as the Larmor precession. It itself induces a magnetic moment that adds to the moment of the resting electron. With Lenz's rule, we can easily see this moment to be orientated antiparallel to its cause, which is the external field.
As a susceptibility for this orbital diamagnetism it is found

$$\chi_{orb} = \frac{-n\mu_0 e^2 \left\langle r^2 \right\rangle}{6m_e} \tag{3.7}$$

where $\langle r^2 \rangle$ is the average squared distance of an electron in the orbital in demand to the ionic core.

Landau-Diamagnetism

Lew Landau then used the free-electron model to calculate a temperature dependent behaviour of orbitally diamagnetic ions as in equation 3.7. He found

$$\chi_L = -\frac{n\mu_0\mu_B^2}{2k_BT} = -\frac{\chi_P}{3}$$

For free electrons, diamagnetism thus is always weaker than paramagnetism and would only correct paramagnetic terms. This only renders incorrect, if we introduce band structure effects via the effective mass m^*. For small effective masses, the diamagnetic term can then dominate the paramagnetic term:

$$\chi_L = -\frac{m_e}{m^*}\frac{\chi_P}{3} \tag{3.8}$$

3.2.2 Ferro- and Antiferromagnetism

While para- and diamagnetism describe the response of magnetic moments to an external field, where the magnetic moments themselves do not interact, the coupling of a magnetic moment's behaviour with the behaviour of magnetic moments in its vicinity gives rise to actual collective ordering phenomena of magnetic moments, that not only accidentially order with respect to the same external field, but are able to order even in absence of an external field.

The different basic varieties of collective magnetic ordering phenomena are a positive coupling between two moments (ferromagnetism) and a negative coupling between two moments (antiferromagnetism). Both are described in a common law, the Curie-Weiss-law.
For a basic overview we will only have a look at direct neighbour coupling. All sorts of superexchange and others will not be covered, since we only need the classifiers of ferromagnetism for Europium-compounds which are not valence fluctuating, and are not too deeply interested in those.

Exchange energy modelling

There is a manifold of different models for the exchange energy of interaction between different magnetic moments, with different levels of exactness, different strenghts and applicabilities. To get hand on the very basic concepts of ferroic magnetism, we will utilise one of the oldest and simplest models for magnetic exchange, the Heisenberg model.
Within the Heisenberg model, the coupling between two magnetic moments $\vec{\mu}_k$ is linear with a coupling constant J:

$$E_{mag} = -J \sum_{i,j} \vec{\mu}_i \vec{\mu}_j \tag{3.9}$$

Ferromagnetism and the Curie law

If the coupling constant in equation (3.9) is positive, $J > 0$, all magnetic moments couple positively to their neighbours, i.e. tend to show the same orientation. This means, below a certain critical temperature T_C, that is the Curie temperature, all the magnetic moments will orient themselves and add up to a finite macroscopic magnetisation. This process happens on a very short scale; both magnetisation and susceptibility saturate quickly. The behaviour of ferromagnets with respect to their Curie temperature and their saturation magnetisation is a general behaviour.
A ferromagnet in its ordered phase stabilises itself against reorientation by external magnetic fields to a certain extent. A ferromagnet that is magnetised by an external field, which is then reduced to zero, will thus not reduce its magnetisation to zero, but to a finite value, te so called remanence. To reduce the remanence to zero, it needs a finite external field in the opposing direction to the ferromagnet's moments' orientation, the coercitive field. This effect of memory is called hysteresis.

Antiferromagnetism

If the coupling constant in equation (3.9) is negative on the other hand, $J < 0$, the resulting magnetic order depends on the exact lattice geometry and site-to-site interactions between the magnetic moments located at a site. This is a broad class of different ordering types, e.g. antiferromagnetism, ferrimagnetism and frustrated magnetism.
The simplest type of this negative coupling ordering is the antiferromagnetism. Here, each moment couples to an even number of moments and is directly opposed

to them in terms of ordering direction of the magnetic moment. Below the critical temperature T_N, that is the Néel temperature, a magnetic landscape emerges, in which every moment is surrounded by opposing moments, and the average magnetisation of the system approaches zero. Simultaneously, the susceptibility of the system also approaches zero for the ordering direction and remains constant for other directions.

The Curie-Weiss-law

If a system orders magnetically below a certain temperature, this ordering process already foreshadows in the paramagnetic phase above that temperature.
This is instructively understandable for ferromagnets, which approach magnetic saturation in the ordered phase. Hence, the magnetic susceptibility needs to diverge at the Curie temperature. This happens following an inverse linear powerlaw:

$$\chi_{pm} = \frac{C}{T - \theta_C} \text{ with } \theta_C \approx T_C$$

For the antiferromagnetically ordered systems, an alike powerlaw is found with the Néel temperature, which however does not lead to a divergence of the magnetic susceptibility at the magnetic phase transition:

$$\chi_{pm} = \frac{C}{T + \theta_N} \text{ with } \theta_N \approx T_N$$

Both equations can be summarized within a single linear powerlaw, the Curie-Weiss-law:

$$\chi_{pm} = \frac{C}{T - \theta} \tag{3.10}$$

where $C = \mu_0 n \mu_{eff}^2 / 3k_B$ is the Curie constant (with the effective magnetic moment μ_{eff}) and θ is the Weiss temperature.
While the absolute value of the Weiss temperature gives a rough estimate for the systems ordering temperatures under certain circumstances, the sign of the Weiss temperature yields information about the dominating ordering mechanism. $\theta > 0$ indicates ferromagnetic ordering mechanisms or a $J > 0$, while on the other hand $\theta < 0$ indicates antiferromagnetic ordering or a $J < 0$.
The Weiss temperature is found by a linear fit to the high temperature regime of the inverse susceptibility.

3.2.3 Kondo screening

The Kondo effect, named after the japanese physicist Jun Kondo, in its original form describes how to deal with magnetic impurities in a nonmagnetic metal, when the magnetic moment of the impurity couples negatively to the electronic surrounding. The ion and the surrounding electrons then may form a singlet state with a significantly smaller magnetic moment than the ion previously had. The magnetic moment of the ion is "screened" by the spin moments of the surrounding electrons. Below a certain temperature T_K, the so called Kondo temperature, this singlet emerges and functions as an additional scattering center. Hence, Kondo screening leads to increasing electrical resistivity at temperatures below the Kondo temperature T_K. Kondo temperatures usually are located in a broad range between 1 K and 1000 K.

4 Phase diagrams

In chapter 2 we defined what a phase is and what the conditions are for several phases to coexist, i.e. to transition one into another. Since each of the phases is parametrized using the parameters of the described system (i.e. temperature T, pressure p, molar ratios x_i, magnetic field B), we can map all the phases into a diagram, displaying the system's phase depending on its parameters.
Dimensionality of the system's phase space is determined by the number of independent parameters available to describe the system (for a zero field system of n distinguishable components, this is given by $2 + (n - 1) = 1 + n$ dimensions). Inside the phase space (and thus its representation in a phase diagram), the phases will obey Gibb's phase rule (see chapter 2.1), describing the dimensionality of the subspace a set of phases can exist or coexist in.
For the sake of interpretability and presentability, the representation of phase space in phase diagrams is in the most cases restricted to a twodimensional cut through the phase space. For all systems with $n > 1$ this means a loss of dimensionality. The terms of projection can differ. In each case where a cut is displayed, the Gibb's rule yields not a fixed dimensionality for phase areas anymore, but only an upper bound for their dimensionality. E.g. two-dimensional phase areas in a three-dimensional phase space might be reduced to one-dimensional lines, but may also stay two-dimensional areas upon making a representative cut.

Phase diagrams are a widely used concept in different disciplines that profit from a parametrized displaying of a system's states, that transition by the rules of phase transitions, and hence can be called phases and obey the Gibb's rule. In this work, we will see and use different kinds of phase diagrams, created by different disciplines of science. We will make use of the chemistry's phase diagrams displaying the states of aggregation of a system defined by a set of chemical elements, as well as of the solid state physics' phase diagrams displaying properties and features of an electronic system.

4.1 Diagrams of chemical phases and alloys

Phase diagrams, as they are explored by chemists, mapping the states of aggregation of a composed system of several elements are of crucial importance for (successfully) attempting to grow crystals of a certain compound (i.e. structure and composition). With rising complexity of a system, of course, the share of investigated system drops significantly - while there are many unary (i.e. of systems consistent of only one distinguishable constituent, e.g. an element) and binary (i.e. of systems consistent of two distinguishable constituents) phase diagrams

available, systems of three constituents are rarely explored (and it is even rarer that they are fully explored), and systems of four or more constituents are in almost every case totally unknown, except, of course, for the cuts that are equivalent to a known lower dimensional phase diagram.
There are possibilities to represent phase diagrams for one, two or three constituents of a system. All of them have a certain use when thinking about how to grow a specific compound as a single crystal. In the following, these three main kinds of phase diagrams of the states of aggregation will be explained how to read them. The explanation will mostly follow [28].

4.1.1 Unary diagrams

Unary phase diagrams are the only chemical phase diagrams that display a phase space in its full dimensionality, since with $n = 1$ we only need two dimensions. The information we can utilize from unary diagrams are limited (we can find

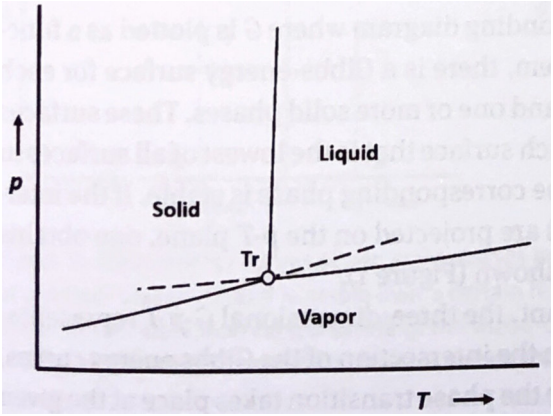

Figure 4.1: Schematic unary phase diagram [28].

melting and vaporisation temperatures and get an idea of the behaviour of our used elements at higher pressures occuring inside a fused crucible upon heating), but still they are very useful to understanding basic features of phase diagrams. A schematic unary phase diagram is shown in fig. 4.1. Since $n = 1$, we only have two independent parameters at hand to describe the system. Hence, in a two-dimensional plot we can represent both temperature and pressure, and have covered the whole possibilities of the system. Since this is the case, Gibb's phase rule applies as a rigid rule: single phase areas are displayed as two-dimensional areas, two phase interfaces are displayed as (one-dimensional) lines, and there is only a (zero-dimensional) point of three phase coexistence. The lines and the triple point correspond to first order phase transitions between states of aggregation. In this scheme, the phases are solid, liquid and vaporous, but for many elements there exist more than only one solid realisation, discriminated by different crystal structures, as for example to see in the unary phase diagram of Cesium (fig. 4.2a), where different solid phases (the ambient pressure bcc phase, two different fcc phases and another phase) are stabilized for a certain range of pressure. Also, we can gain information about the melting behaviour of Cesium upon pressure.

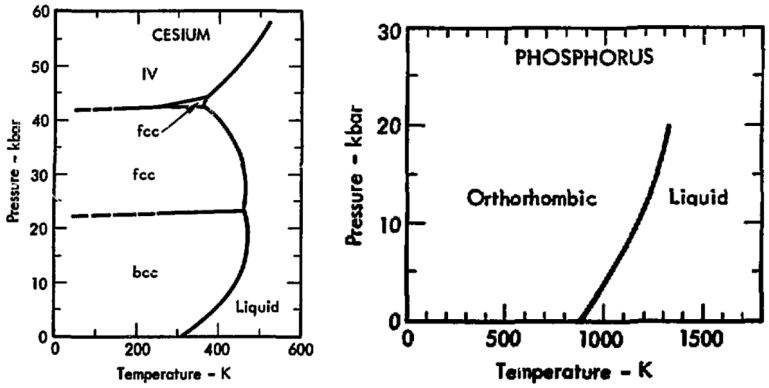

(a) Cesium (Cs) (b) Phosphorus (P)

Figure 4.2: Unary phase diagrams of Cesium (Cs) and Phosphorus (P) [29].

On the other hand, there are also elements, for which the unary phase diagrams are rather pointless for an everyday use. For example, we can gain information about the pressure dependence of the melting point of phosphorus out of the unary phosphorus phase diagram (fig. 4.2b), but won't be able to apply this knowledge, since the vapor pressure curve of phosphorus is so steep, it starts heavily evaporating at low temperatures and reaches its boiling point at 431 °C [30], so only negligibly small ratios of the Phosphorus involved in growth experiments will reach the melting point in solid form.
For our purposes, unary phase diagrams are not from greatest interest in the end, because they serve some basic information about a system, that are interesting, but can easily be determined otherwise (ambient pressure transition temperatures) and need to be backed up (see the Phosphorus example), and other information which are simply not applicable in a black box that is a crystal growth crucible.

4.1.2 Binary diagrams

Binary phase diagrams, i.e. phase diagrams for a system with two constituents such as elements, are a case much more interesting for our applications. With $n = 2$ we have now three parameters (temperature T, pressure p and ratio between the two elements x) to describe our system. Thus we have to cut out one of the parameters for a proper representation in a (two-dimensional) phase diagram. For this we choose the least controllable and also for our purposes least interesting parameter - the pressure p, which will be assumed to be ambient pressure. Binary phase diagrams usually display phases and phase transition lines dependent on the temperature of the system and its composition ratio between the elements. The temperature T will be displayed in an apropriate range, while the composition ratio x will usually be expressed normalized to 1 or in percent, where 0 means "only component A" and 1 - or 100 respectively - means "only component B", with the values in between corresponding to a certain ratio, that expresses the amount ratio of B in the total system.
In the following, we will clarify some of the most important terms and concepts, that are key to reading and understanding both binary and partly ternary phase

diagrams. These will be explained using fig. 4.3.
First, we can, as in every other phase diagram, identify phases: The large area denoted "liquid (L)" represents the area of homogeneous melt, where both components A and B form a joint melt, which can usually exist in a continuous interval $x \in [0;1]$ for sufficiently large temperatures, but also in many cases already for temperatures lower than at least one, possibly both of the sole elements' melting temperatures in more restricted intervals. The line, that functions as border for the liquid phase area, is called the "liquidus line" i.e. the line, above which you will only find the liquid phase.
The interpretation of the liquidus line of two elements is one of the main approaches to get an idea, whether a material is convenient to be used as an external flux, i.e. whether it is able to form a melt with all of the ingredient elements and significantly lower the joint melting temperature for high melting solvents, if needed.
The solid phases of the binary system on the other hand have a certain composi-

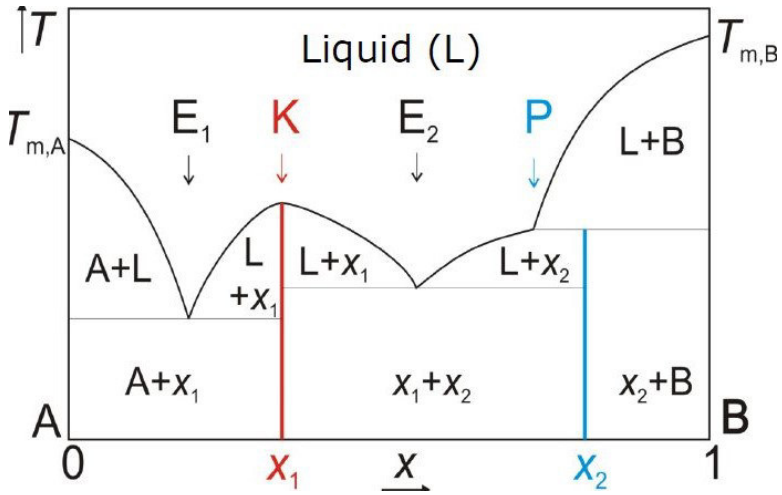

Figure 4.3: Schematic binary phase diagram. Picture by Cornelius Krellner.

tion and thus are displayed as lines in the phase diagram. (Here, the x-parameter is ideally not accessible for the solid phases; since we had to erase one dimension to draw the phase diagram, Gibb's rule is only an upper bound.) We find the elements A and B at the values for x of 0 and 1 respectively. In our example, we have two additional solid phases of the compositions x_1 and x_2. The knowledge of the existing binary compounds is, of course, also important when growing ternary compounds, since in every real growth experiment one expects side phases to grow in addition to the aimed results, and those can very well be binary phases. Also, the existence of binary phases can be utilized, for example when we want to grow crystals composed of very high melting components on their own - maybe there is a lower melting binary compound we can prereact our components into.
The areas in between two phases, labelled with the names of two phases, are areas of phase separation, in which the system decomposes into parts of both phases following the lever rule (see [28]).
Three more terms should be discussed, that are applicable for both binary and ternary diagrams:

- *Congruently melting phase*: x_1 is a congruently melting phase, i.e. at the composition x_1 the solidus line (i.e. the line below which temperature there are only solid phases to be found) and the liquidus line meet, and the solid phase x_1 can be translated directly into a melt with the exact same composition. Congruently melting compounds, given a sufficiently low melting temperature, are rather simple to grow.

- *Incongruently melting phase/peritectic phase*: x_2 is an incongruently melting or peritectic phase, i.e. if we have some amount of x_2 and heat it, upon melting it will not translate into a melt with the same composition, but decompose into a melt with another composition and some other phase. The other way around, a peritectic phase can not be grown by simply weighing the compositional amount of elements together, composing a melt and then cooling down until x_2 forms, because the phase x_2 is hidden from the melt, which would have to cross a phase separation area in order to reach the solid phase x_2.

- *Eutectic points*: An eutectic point (E in the schematic phase diagram) is a point in the phase diagram, where the liquidus line falls to a local minimum, i.e. the locally most stable composition of a melt, to which, upon lowering the temperature and deposition of forming phases, the composition of a melt will converge, before solidifying at once.

The consultation of the binary phase diagrams of the combinations of the participating elements is a central aspect of planning and preparing a growth experiment. For these consultations, both a compendium by Massalski [31] and an online database by *ASM international* (citation by paper) are available.

Quasi-binary diagrams

A way of dealing with more than 2 elements, especially when using salts, is to draw a quasi-binary phase diagram, that does not choose elements as A and B, but salts or other compounds. x then is a parameter shifting linarly and gradually from one composition to the other.

4.1.3 Ternary diagrams

Most crystals grown in the Frankfurt crystals and materials lab consist of at least three elements. Setting up ternary phase diagrams are a standard step in the process of planning crystal growth experiments. (Any additional dimensions for e.g. fluxes will only be tested locally.)
Since we have $n = 3$ and thus 4 parameters to describe the system, we need to leave out two of them. There are two ways of solving this: only looking at a certain shift in composition, e.g. between two compounds. This was previously described as a quasi binary phase diagram, because it looks the same as a binary phase diagram and is interpreted in the same way.
The other way is a "proper" ternary phase diagram, displaying the whole range of element ratios, but leaving out the information about temperature the binary diagrams still carried. A ternary phase diagram merely displays ratios of elements. For this, a possible choice would be to refer elements A and B to element C and

use: $x_1 = n_A/n_C$ and $x_2 = n_B/n_C$. But then, the diagram would be distorted in the sense that equal distances in the diagram would not refer to equal composition shifts. Hence, we need another display option for intuitive interpretability. The solution, that is usually applied, is to actually use three element ratios, and reduce the dimensionality by normalization:

$$x_A = \frac{n_A}{n_{total}},\ x_B = \frac{n_B}{n_{total}},\ x_C = \frac{n_C}{n_{total}} \text{ with } n_{total} = n_A + n_B + n_C$$

x_A, x_B and x_C can now be displayed in a triangular graph, since they are normalized to the interval $x_i \in [0;1]$ and by $\sum_i x_i = 1$. This also guarantees equal distances in the diagram to correspond to equal shifts in composition.

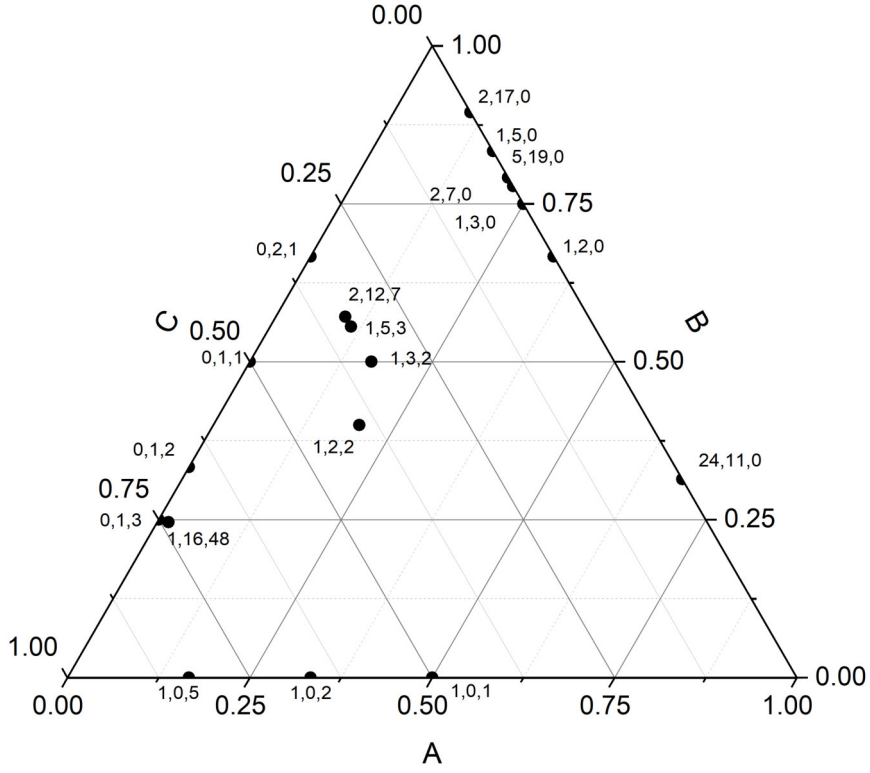

Figure 4.4: Schematic ternary phase diagram.

This figure (4.4) shows schematic ternary phase diagram. On the edges of the diagram, one of the components is always zero. Only two of the elements come together on the edges and their ratio behaves according to the position on the edge line. As we easily see, the edge lines thus correspond to the respective binary phase diagrams, deprived of their temperature dimension. The crystalline phases, which are said to have a certain composition, hence are shrinked to mere points (i.e. dimensionless) on the edges, but also in the rest of the diagram. Each crystalline phase's composition can be identified by reading the scales of each of the elements, where the same ratio of the said element is contained for points on a line parallel to the edge corresponding to the binary phase diagram not containing the element.
In a ternary phase diagram, we usually try to identify areas of phase separation,

or to put it the experimentally realized way: for a given experimental starting composition, we try to identify, into which area of phase separation we enter, i.e. which phases are formed during an experiment, how they relate to each other, and how we can optimize the growth towards growing more of the desired target compound and less other phases. The diagrams are used both for tracking of the phases formed in experiments and for trying to educatedly guess sensible starting compositions for successful growth experiments.
Since most of the time there is no information available about the liquidus plane of a ternary system, the eutectic points described in section 4.1.2 are often used quite prominently, especially for self flux experimental designs. As a self flux, either one low melting element or a binary eutectic point can be selected.

4.1.4 Homogenity regions

In both the sections on binary phase diagrams (4.1.2) and on ternary phase diagrams (4.1.3) we referred to crystalline phases to be accurately composed, i.e. not only owning a certain crystal structure, but also being strictly confined to a certain composition (e.g. 20%-40%-40% for the 122-compounds).
This assumption is useful for general considerations and the rather coarse process of planning a growth experiment, but in reality, there is no compound which actually displays a sharp composition. Crystalline defects always make possible, that a compound deviates from its "ideal" composition to some extent. This extent is variable - ranging from below 0.1 at-% of deviation from the ideal up to several at-% of deviation - but never zero. Ipser [28] calls this property of solid phases "non-stochiometry" (i.e. some systematic deviations from "stochiometry", a term rather inaccurately used here to describe a compounds composition ratio; stochiometry actually refers to the calculation of initial material ratios), but the term "homogenity region" expresses the nature of this property even better: Crystalline phases mostly don't have a single, sharp composition ratio. Rather their structure is compatible with a range of compositions around a "nominal" composition. E.g., a 122 compound is named after the composition XY_2Z_2, but can easily deviate from this nominal composition to $X_{1+\alpha}Y_{2+\beta}Z_{2+\gamma}$ with α,β,γ in the range of up to several percent with respect to the percentage-normalized representation 20-40-40. In this range, the compound can exist "homogeniously" with different or even shifting compositions. This range is usually also dependent on the system's temperature.

Fig 4.5 shows an example of a binary phase diagram where the solid phases α (i.e. nominally element A), β (a composed phase) and γ (nominally element B) each exist with their specific crystal structure in a region of homogenity, allowing the elemental composition to deviate from the nominal composition within a temperature dependent range. This effect also exists for ternary phase diagrams. In both cases (the binary and the ternary cases) the crystalline phases appear as areas of finite size of their allowed composition corresponding to a certain crystal structure instead of lines or points respectively. A homogenity region is usually made possible by the occurrence of crystal defects, such as interchanges between atomic sites, or partial occupancies.
Upon growing crystals of a certain compound, the composition of the samples may thus shift due to e.g. the starting composition of the experiment, or even

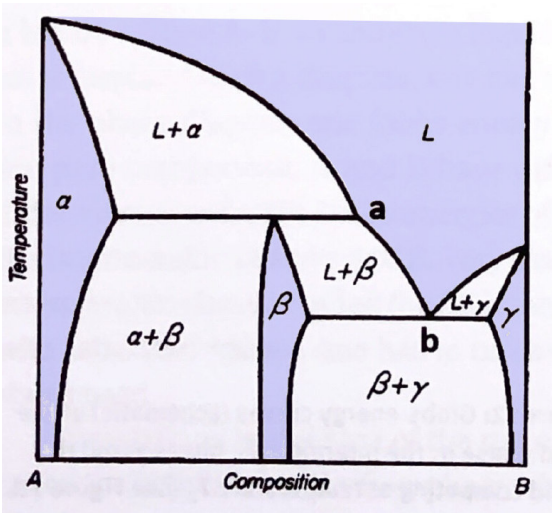

Figure 4.5: Schematic binary phase diagram, modified after [28]. The phases α, β and γ each exist on a composition interval with a temperature dependent size. Light blue areas designate allowed phases, white areas designate areas of phase separation.

due to local expletions or accumulations of one of the elements in the melt, altering the direction from where and the temperature at which the homogenity region is entered, and thus the final composition of a sample. Composition shifts may occur between different samples or even within a larger sample. The latter case is especially interesting when growing larger crystals using the Czochralski method.
In many cases, these shifts in composition don't have a significant impact on the physical properties of the samples. In my master's thesis, I described the growth and properties of the ternary rare earth cobalt phosphide $CeCo_2P_2$ and the antiferromagnetic ordering of the compound seemed to stay the same for crystals of the composition 20%-40%-40% and of the composition 18%-38%-44% [32]. But it is not revealed to much information in advance to say, that the homogenity region of the Eu-based compound $EuPd_2Si_2$ is one of the cases where this is not true and the actual composition of a sample, i.e. the actual position in the homogenity region, has a major impact on the physical properties of the sample.

4.2 Diagrams of physical phases

States of aggregation are not the only phases we can display in diagrams. In fact, every set of states satisfying the definition of phases (i.e. to always be in a sole identifiable state, to undergo phase transitions upon change, to fulfil Gibb's phase rule) can be drawn into a phase diagram. And so, it is very common to draw phase diagrams of various physical phases, i.e. electronic and magnetic states, to map the electronics of a system dependent on its describing parameters.
Within these, the conventions are less strict than within the states of aggregation phase diagrams. Not only phase transitions of first order are displayed, but all phase transitions, that are necessary to show the properties of the underlying

theory. Also, the choice of parameters is less restricted. Mostly, but not always, temperature is selected as one of the parameters, because it is easily accessible and object to many predictions, but the other parameter depends on what the phase diagramm is meant to express, and can display all the other parameters (pressure p, different molar ratios x_i, magnetic field B, etc).
In chapter 6.3, an electronic phase diagram relevant for this work is read out and thus can be used as an example.

5 Quantum critical elasticity theory

Elasticity theory is the theory dealing with linear responses of rigid solid bodies to external forces and deformations. Advanced from this per se classical theory and the contained scenario of critical wave propagation, a quantum theory of directionally restricted phase transitions can be developed. This chapter is dedicated to explaining this idea.

5.1 Classical elasticity

The theory of classical elasticity explains the (linear) response of rigid bodies to external strain. It evolves around the fundamental quantities of a body's deformation, distortions and stress. As a central statement, the elasticity theory brought about the law of Hooke, which relates stress and distortions in a solid. From this relation, the more popular form of the law can be determined, expressing the impact of shear forces on a solid.
The main areas of focus for the theory of classical elasticity are isotropic solids (realiter polycrystals), their mechanical properties and equilibrium conditions at finite temperatures, and furthermore behaviour under boundary conditions as well as surface effects. But the theory also yields concepts to deal with anisotropic solids (single crystals) and dynamic (non-equilibrium) behaviour, e.g. thermal conductivity or distortion waves as well as their critical behaviour.
In this Subchapter, the basic quantities of the classical elasticity theory will be explained, and also account willbe given for the main points of interest for the later understanding of the quantum critical elasticity, i.e. dealing with anisotropy and with dynamic properties, wave propagation and critical breakdown of wave modes ("mode softening"). This exposition will follow Lev Landau and Evgeny Lifshitz with their course book's seventh volume on "Theory of elasticity" [33].

5.1.1 Deformation

Consider an arbitrary solid body, that consists of infinitesimally closely located grid points on a lattice. The infinitesimal distance between two directly neighboured grid points in three spatial dimensions dl is then given as

$$dl = \sqrt{dx_1^2 + dx_2^2 + dx_3^2},$$

where dx_i is the infinitesimal distance between the two points in the spatial direction i.

Upon deformation every grid point changes from its former position $\mathbf{x}$ to its new position $\mathbf{x}+\mathbf{u}$, where $\mathbf{u}$ is the local shift. For the two neighboured grid points this means that their difference has changed to

$$dl' = \sqrt{(dx_1')^2 + (dx_2')^2 + (dx_3')^2},$$

after the deformation, where $dx_i' = dx_i + du_i$ is the distance between the two grid points in the spatial direction i shifted by the deformation.
To ease furher formulations, we state, using the Einstein convention for sums:

$$dl^2 = dx_i^2 \text{ and}$$

$$dl'^2 = (dx_i')^2 = (dx_i + du_i)^2. \tag{5.1}$$

5.1.2 Distortion

We know the total differential of the shift $\mathbf{u}$ is given as

$$du_i = \frac{\partial u_i}{\partial x_k} dx_k. \tag{5.2}$$

Substituting equation (5.1) with equation (5.2) yields

$$dl'^2 = dl^2 + 2u_{ik} dx_i dx_k,$$

where

$$u_{ik} = \frac{1}{2}\left(\frac{\partial u_i}{\partial x_k} + \frac{\partial u_k}{\partial x_i} + \frac{\partial u_l}{\partial x_i}\frac{\partial u_l}{\partial x_k}\right) \tag{5.3}$$

is called the distortion tensor.
The distortion tensor is a symmetric tensor of second order and hence diagonalisable in every spatial position with eigenvalues $u^{(1)}$, $u^{(2)}$ and $u^{(3)}$. The main values $u^{(i)}$ roughly correspond to the relative deformability of the solid in the corresponding direction. Note, that diagonalised at a certain spatial position, the tensor is generally not diagonalised at other spatial positions.

5.1.3 Stress

To change the distortion tensor from equation (5.3), there is a certain amount of work to be done, that is (within the framework of a linear approximation, that is necessary for the system to be elastic in a sense that it is not dissipative) linearly dependent of the distortion induced. This is expressed as

$$\delta W = -\sigma_{ik}\, \delta u_{ik}.$$

The proportionality factor σ_{ik} is called the stress tensor of the given system. It emerges from a reflection on the balance of forces within the system:

$$\int p_i \, dV = \int \frac{\partial \sigma_{ik}}{\partial x_k} \, dV = \oint \sigma_{ik} \, df_k.$$

Here, a generalised form of the Gauss theorem for tensors of order higher than one was used to find the defining form for the stress tensor.

5.1.4 Hooke's law

A distortion in a solid is, by adding a zero, accountable as

$$u_{ik} = \left(u_{ik} - \frac{1}{3}\delta_{ik}u_{ll}\right) + \frac{1}{3}\delta_{ik}u_{ll}. \tag{5.4}$$

The bracketed term in equation (5.4) features a trace of zero and couples only distinct directions. Thus, it can be identified as a torsion term (5.4a). The non bracketed term on the other hand is diagonalised with a finite trace and can thus be interpreted as a compression term (5.4b).
This two terms appear in the elastic contribution to the free energy of the solid:

$$F = \mu\left(u_{ik} - \frac{1}{3}\delta_{ik}u_{ll}\right)^2 + \frac{K}{2}u_{ll} \text{ with } \mu,K > 0,$$

where K is the compression module and μ is the torsion module.

From the total differential of the free energy of the solid is derived a relation between the stress tensor and the distortion tensor:

$$\sigma_{ik} = K\delta_{ik}u_{ll} + 2\mu\left(u_{ik} - \frac{1}{3}\delta_{ik}u_{ll}\right),$$

vice versa:

$$u_{ik} = \frac{1}{9K}\delta_{ik}\sigma_{ll} + \frac{1}{2\mu}\left(\sigma_{ik} - \frac{1}{3}\delta_{ik}\sigma_{ll}\right),$$

where the relation is, via their influence on the free energy, shaped as a sum of a torsion term arising from (5.4a) and a compression term arising from (5.4b). This relation is known as Hooke's law.

5.1.5 Anisotropy and the Elastic Constant's Tensor

When we consider single crystals, the isotropic form for the free energy is not valid anymore. The contribution of the distortions in the crystal to the free energy need to reflect the anisotropic nature of a singe crystalline solid. The quadradic contribution of the distortions desintegrates into a possible coupling of different distortive directions:

$$F = \frac{1}{2}\lambda_{iklm}u_{ik}u_{lm}$$

λ_{iklm} is called the elastic constant's tensor. It is a tensor of fourth order and symmetric upon exchange of i and k, of l and m and the tuples (i,k) and (l,m) - so, it conserves the symmetries of the distortion tensors it couples and is also symmetric under exchange of the coupled distortions. These symmetry operations leave us with a maximum of 21 different elastic constants (i.e. a maximum of 21 different entries for the elastic constant's tensor). The maximum of 21 elastic constants is reached by triclinic systems.
This formulation of the free energy also grants us an elegant way of formulating the stress tensor:

$$\sigma_{ik} = \frac{\partial F}{\partial u_{ik}} = \lambda_{iklm}u_{lm} \tag{5.5}$$

Anisotropic systems of higher symmetry

As mentioned, the maximum of elastic constants, 21, is reached for triclinic systems. In other crystal systems, symmetry operations cause a degeneration of the elastic constants of different directions.
For example, considering a tetragonal system of the family $(C4_V, D2_d, D4, D4_h)$, i.e. tetragonal systems, that maintain a true fourfold rotational symmetry (rather than a fourfold winding symmetry), operations (x), (y), $(-x)$ and $(-y)$ are equivalent with respect to the z axis. Thus, the number of possibly different elastic constants is restriced to six of the types:
$(xxxx)$, $(zzzz)$, $(xxzz)$, $(xyyy)$, $(xyxy)$ and $(xzxz)$.
Other elastic constants vanish by choosing "convenient" coordinate systems, i.e. the irreducible representation of the crystals symmetry class in group theory. This system inherent coordinate system, defined by the systems symmetry, also later on defines the possible elastic modes in the solid.

5.1.6 Elastic waves

Putting a system under stress σ_{ik} induces a deformation u_i via

$$\rho \ddot{u}_i = \frac{\partial \sigma_{ik}}{\partial x_k}. \tag{5.6}$$

Introducing the definition of the stress tensor by derivation of the anisotropic free energy from (5.5) to the wavelike equation of motion (5.6), as well as the deformative definition of the distortion from (5.3), yields another equation of motion:

$$\rho \ddot{u}_i = \lambda_{iklm} \frac{\partial^2 u_m}{\partial x_k \partial x_l},$$

which solves under the condition that

$$|\rho \omega^2 \delta_{im} - \lambda_{iklm} k_k k_l| = 0 \tag{5.7}$$

This yields three solutions $\omega(k_i)$ for each value of λ_{iklm}, the so called elastic modes of the solid. In an isotropic solid, the solutions for (5.7) were degenerate. The anisotropy of the system lifts the degeneracy of the solutions.

The critical scenario

Every solution to equation (5.7) is a distinct wave mode. Together with the corresponding solutions, an entry of the elastic constant's tensor may collapse. This is, the elastic constant approaches zero, the directions are elastically isolated from each other, and the wave modes connected to this elastic constant vanish. The other eigenvalues of the elastic constant's tensor remain unaffected.
This classical critical scenario of statics and dynamics of elastic phase transitions of second order was thoroughly described e.g. by Folk, Iro and Schwabl [34, 35]. This second order description may be applicable to the studied case beyond the critical endpoint of the phase transition of first order (see chapter 6.3).

5.2 Quantum critical elasticity

This subchapter's task is to scetch the development of a quantum theory of elasticity out of the classical theory. This is a sort of special way, compared to the development of other quantum theories, since the upcoming of the latter was in the main part either a development analogous to a classical theory or a methodised quantisation of a classical theory on a formal level. (E.g. quantum mechanics as an analogy to classical optics, as well as a formulation of classical mechanics with quantum operators.) The quantum theory of elasticity on the other hand arises from the generalisation of a classical concept over the quantum scale, i.e. a direct derivation of quantum properties of a system from the classical elastic properties.
This exposition of the coming about and the classification of a quantum theory of elasticity will follow [3].

5.2.1 The dynamical matrix

Within a critical scenario, selected eigenvalues of the elastic constant's tensor λ_{iklm} vanish, and thus, the response of the system to distortion along the corresponding directions suffers a breakdown.
But the elastic constant's tensor does not only apply to macroscopic distortions. It is also defining for the dynamical matrix of the system, which manages the description of microscopic distortions, i.e. phonons. The dynamical matrix derives from the elastic constant's tensor as

$$M_{ik}(\mathbf{k}) = \lambda_{iklm} k_l k_m \tag{5.8}$$

whereof the eigenvalues equal the acoustic phonon velocities of the crystal.
Since the eigenvalues of the dynamical matrix are determined both by the momentum $\mathbf{k}$ and the eigenvalues of the elastic constant's tensor λ_{iklm}, the phonon velocities - and thus the transport of acoustic phonons - vanish along the same certain crystal axes whenever an elastic constant approaches zero. This is referred to as "mode softening".

5.2.2 Critical subspace

An elastic phase transition that is propagated by acoustic phonons hence is restricted to a subspace of dimension $m \leq d$, where d is the dimension of the system. (For a conventional phase transition this subspace is, of course, d-dimensional.)
We would think of a quantum critical scenario, if the roll of acoustic phonons would be non-neglegible for the physical properties of our system. If a phase transition occurs, but the acoustic phonons can't serve as order parameter for the transition, the question arises, what other order parameters are possible on the critical subspace.

5.2.3 Classification of elastic quantum critical scenarios

Hence, a scenario that is elastically quantum critical is not quantum critical in a "static" sense, since the proposed order parameters couple to the strain of the

system and hence are related to long range forces. In an elastic quantum scenario, a phase transition would hence naturally be of first order, but there are certain scenarios to find them to be of second order.
There are two main types of elastic quantum phase transitions of second order, for which the coupling of the order parameter to macroscopic strain differs in the linear coupling in the corresponding Landau potential. (This is important, since for a phase transition to occur, you want to suppress the lower polynomial orders of the order parameter dependence.)

Symmetry breaking phase transitions of second order

The first class of elastic quantum critical scenarios involves phase transitions which break the spatial symmetry of the crystal in a distinct way. From a tetragonal phase, e.g., it would only be possible to enter an orthorombic phase via two different ways, that correspond to two different external strains and two different elastic constants that will vanish during the transition.
The Landau potential of this kind of phase transition is

$$V(\epsilon) = \sigma\epsilon + \frac{r}{2}\epsilon^2 + \frac{u}{16}\epsilon^4 \tag{5.9}$$

where ϵ is the order parameter. For a phase transition of second order it is to be $u > 0$, as well as r needs to be approaching zero to eleminate the second polynomial order. (This is managed by hydrostatic pressure, since $r = r(p)$.) The parameter r also defines the wave propagation frequency of elastic waves in the crystal in leading order:

$$\omega^2 \propto r\mathbf{p}^2$$

where $\mathbf{p}$ is the critical component of the momentum vector $\mathbf{k}$. Hence, a vanishing r leads to the critical scenario.
Since the linear term couples directly to the stress on the system, this sort of phase transition only occurs in unstressed systems, $\sigma = 0$.

Isostructural phase transitions of second order

The other kind of second order phase transition scenarios are such, in which the phase transition is accompanied by a structural transition that is not symmetry breaking. Hence, this phase transitions are called “isostructural“ transitions.
For the Landau potential of those transitions, the cubic term does not naturally vanish, so it is extinguished by a constant order parameter shift $\epsilon \to \epsilon + \epsilon_0$. This yields a Landau potential as for the symmetry breaking case, but the linear term does not couple directly to the stress of the system anymore, but to a new emergent tuning parameter h:

$$V(\epsilon) = h(\sigma,p)\epsilon + \frac{r}{2}\epsilon^2 + \frac{u}{16}\epsilon^4 \tag{5.10}$$

A phase transition of first order is located on the line $r < 0$, $h = 0$. ($h = 0$ generally may correspond to a finite value of σ. The system is not necessarily unstressed.) For r approaching zero, we find the phase transition of first order

ending in a critical endpoint of second order. Again, vanishing r leads simultaneously to an elastic critical scenario.
It is unclear, whether this elastic quantum critical endpoints behave just as conventional quantum critical endpoints.

6 | Valence fluctuations in solids

In the previous chapter we had a closer look at the quantum critical elasticity theory and the observable features intsances of this theory would display. To find possible instantiations of the theory, we need to look out for cases displaying all the features that are accounted to an instantiation as derived by theory.
In europium based systems, we might find such an instantiation of the quantum critical elasticity theory. As Onuki described in his 2017 publication [6], europium ions in compounds display different temperature dependent behaviour according to the pressure they are experiencing, i.e. the combination of physical pressure and those interactions with the environment which can be expressed as a certain equivalent of pressure (so called "chemical pressure").
The exact behaviour will be discussed later, but the form of the valence fluctuations of europium and the transition between different valence fluctuating states might meet the requirements for an instantiation that may be described by the quantum critical elasticity theory.
So, in this chapter we will clearify how europium's electronics behave in compounds, what valence fluctuations are and how europium valence fluctuations connect to the quantum critical elasticity theory.

6.1 Valence fluctuations

First of all, we have to state, that the electronic valence state of an atom inside a solid of course depends on the environment the atom is experiencing, i.e. the surrounding atoms, established bonds and crystal electric field contributions on the electronic background, hence the experienced chemical pressure of the atom at its spatial position in the solid's unit cell.
So, the electronics of an atom in a solid are generally determined by the solid's electronic structure. But there are scenarios in which the electronics of the atoms, hence the solid's electronic structure, also couples strongly to the spatial structure of the solid itself, in form of an elastic coupling to the lattice.
A case, in which this coupling of electronic and spatial structure occurs, is the case of *valence fluctuations*. This is of course the case due to the difference of ionic radii for different ions, i.e. valences, of the same element. So, if two valence states of an atom are, in the specific surrounding of a solid, energetically close enough to interchange (mediated through external parameters as temperature or physical pressure), with a change of the electronic structure (the valence of the atoms) a strong spatial effect may occur - this is, when the atoms change from the valence state (1) with the radius r_1 to the valence state (2) with the radius r_2 and the crystal lattice adapts to those changes.

In case of elastic coupling of the electronic structure to the lattice structure, we need to describe the effects in terms of elasticity theory (chapter 5). In case of the europium valence fluctuation more closely described later in this chapter we describe an elastic coupling between the electronic valence state transition of europium and an isostructural lattice parameter transition (i.e. an extraordinary large and non-linear shift) in the a-b-plane of a tetragonal lattice.

6.1.1 Interconfiguration fluctuations model

The interconfiguration fluctuations model is a classical statistical model, that is used to describe the free energy and the entropic contributions of valence fluctuations in solids, for example valence fluctuations of rare earth atoms [36, 37]. In this model, the free energy F is assumed to be

$$F = -k_B T^* \cdot ln(Z) + \frac{1}{2}\alpha E_0 p_2^2 \tag{6.1}$$

where $T^* = (T^2 + T_f^2)^{1/2}$ is (with the broadening of states T_f) an effective temperature accounting for state broadening, the partition function $Z = Z(T^*, E_0, \alpha, p_2)$, $p_2 = 1 - p_3$ the occupation number of the divalent state and E_0 and α the model parameters. The entropy S_V is then derived from the free energy:

$$S_V = -\frac{\partial F}{\partial T}.$$

Since

$$C_V = -\frac{\partial^2 F}{\partial T^2}$$

we can, under assumption of $S_V(T = 0) = 0$ (a distinct ground state), gain information about the entropy contribution of the valence fluctuations up to a certain temperature T_0 by integrating the specific heat:

$$S_V = \int_{T=0}^{T=T_0} C_V \, dT.$$

6.2 Energy states of Eu-atoms in crystal lattices

In this work, valence transitions of europium ions in metallic compounds are to be described. Hence, we need to state some basic properties of europium's ionic states[1], as done in table 6.1. The total angular momentum J is calculated after the Hund's rules (chapter 3.1.4), and the magnetic moment then according to J by $\mu = g\sqrt{J(J+1)}\mu_B$, where the Landé factor for Eu^{2+} is $g = 2$.
As we see, not only is the Eu^{2+}-ion carrying a finite magnetic moment (hence being Curie paramagnetic) where the Eu^{3+}-ion is carrying zero magnetic moment (only displaying Van Vleck paramagnetism, see section 3.2.1), so that we will be able to see a transition from an Eu^{2+}-state to an Eu^{3+}-state in the magnetic susceptibility of the compound. Also, the Eu^{2+}-ion is much larger than the Eu^{3+}-ion, which will heavily affect the unit cell (i.e. the lattice parameters) and hence a valence transition of the electronic structure will manifest in an isostructural spatial lattice phase transition.

[1] From looking at the ionic states, of course, only qualitative arguments can be drawn for discussing metallic states. This is done nonetheless, since the easier accessible and understandable ionic setting is documented quite extensively.

Ion	radius (Å) [38]	el. configuration	J	magn. moment (μ_B)
Eu^{2+}	1.17	Xe 4f7 6s2	3.5	7.94
Eu^{3+}	0.95	Xe 4f6 6s2 5d1	0	0

Table 6.1: Properties of the europium 2+ and 3+ ionic states. (6s and 5d electrons contribute to the conduction bands, electron configuration in metallic convention)

6.2.1 Separation of energy levels

A proposition, that is often read, is that the difference in the energy level of the binding of Eu^{2+} and Eu^{3+} is comparably small, giving rise to the valence fluctuations in the first place. This is for example proposed by Onuki *et al* [6]. The idea behind this proposition is, that both europium states Eu^{2+} and Eu^{3+} have a stabilizing factor working for them. Eu^{2+} is stabilized by the strong spin alignment and the maximum possible total spin for an f shell, Eu^{3+} is stabilized by the total spin-orbit-coupled angular momentum $J = 0$ vanishing. Both effects compete and thus lead to a small difference in energy levels between the different europium ions.
Since this is a rather handwaving argument, the actual behaviour of europium ions in solids, concerning their binding, remains unclear. To get a first idea of how the valence of the europium comes about, determining to a first order for the valence of the europium in a solid is the binding energy of the Eu^{2+}- and Eu^{3+}-ions in the solid respectively, measured as the so called enthalpy of formation ΔH_F, as well as their difference.
A first glance on how europium might behave in solids can be gained by simply comparing the enthalpy of formation of Eu^{2+}- and Eu^{3+}-ions in an environment as neutral as possible, with clearly identifiable europium valence at the same time. For this considerations, we choose the europium oxides EuO (clearly Eu^{2+}) and Eu_2O_3 (clearly Eu^{3+}). In table 6.2, the enthalpy of formation of the said oxides is displayed. Assuming an uniform distribution of the enhalpy over the ions, we can also give an estimate for an enthalpy per ion.

Ion	Oxide	ΔH_F (kJ/mol) [39]	ΔH_F per ion (kJ/mol)
Eu^{2+}	EuO	$-(593 \pm 5)$	-296.5
Eu^{3+}	Eu_2O_3	$-(1650 \pm 4)$	-275

Table 6.2: Enthalpy of formation of Eu-Oxides

In this strongly simplifying consideration, we would find a difference in binding energy between the two kinds of europium ions of $\Delta = 21.5\,\mathrm{kJ/mol}$, which is equivalent to 0.223 eV or 2587.8 K on a temperature scale. Since the ground state (with the higher binding energy) of europium is identified to be Eu^{2+}, we can estimate the valence of a "solid" of free europium ions at ambient pressure (which should reproduce the left edge of the phase diagram in fig. 6.1) using simple Boltzmann factors

$$\text{valence(T)} = 2 \cdot \exp\left(\frac{\text{T}}{\Delta E}\right) + 3 \cdot \left(1 - \exp\left(\frac{\text{T}}{\Delta E}\right)\right)$$

to be

$$\text{valence}(0\,\text{K}) = 2 \cdot \exp\left(\frac{0\,\text{K}}{2587.8\,\text{K}}\right) + 3 \cdot \left(1 - \exp\left(\frac{0\,\text{K}}{2587.8\,\text{K}}\right)\right) = 2$$

and

$$\text{valence}(300\,\text{K}) = 2 \cdot \exp\left(\frac{300\,\text{K}}{2587.8\,\text{K}}\right) + 3 \cdot \left(1 - \exp\left(\frac{300\,\text{K}}{2587.8\,\text{K}}\right)\right) = 2.11$$

which is an acceptable result. So, we can assume the difference in the enthalpy of formation between the two kinds of europium ions to probably be in the range of several 1000 K under ambient conditions.

6.3 Generalized phase diagram for Eu valence states

In 2017, Onuki *et al* published an overview article over multiple europium based intermetallic compounds [6]. Within, they described the magnetic behaviour of compounds including Eu^{2+}-states, and also valence fluctuating behaviour of compounds with an effective valence of the europium of larger than 2.
They also proposed a p-T-phase diagram of the europium valence. Since the environment of an atom site inside the crystal structure corresponds to a certain pressure (so called "chemical pressure"), every realisation of an europium based compund, due to its structure and chemistry, is located at a certain pressure in the phase diagram (fig. 6.1), defining its properties at ambient pressure.
At low pressures the more stable Eu^{2+}-state can be maintained over the whole range of temperatures. Below a certain ordering temperature, the compound then will undergo a phase transition (red line in fig. 6.1) from a paramagnetic (light blue colored area) to a magnetically ordered state (dark blue colored area), obeying all the rules for simple magnetic states (see chapter 3.2). At higher pressures, the magnetic order is enhanced to higher temperatures at first, while in the paramagnetic phase the valence of the europium atoms starts to shift slightly into a state with a fluctuating valence $Eu^{2+\delta}$ (yellowish colored area).

Upon a certain pressure, the magnetic phase breaks down and a valence state more close to the Eu^{3+}-state, which would be more unstable than Eu^{2+} under ambient conditions. From the high temperature valence fluctuating state $Eu^{2+\delta}$ (yellowish colored area) to the low temperature valence fluctuating state $Eu^{3-\delta}$ (orange colored area) leads a first order phase transition now (white line), which at even higher pressures is proposed to end in a critical endpoint of second order and transition into a crossover area of finite size.
Since we can observe an electronic phase transition, the change between two valence fluctuating states, in a certain area of this phase diagram, and since we know this transition to be accompanied by a structural phase transition (a shift of lattice parameters) due to the size of the europium ions, the critical endpoint of this phase transition is of interest to test the Quantum Elasticity Theory (chapter 5), which makes predictions about the elastic properties of systems around endpoints of this design.

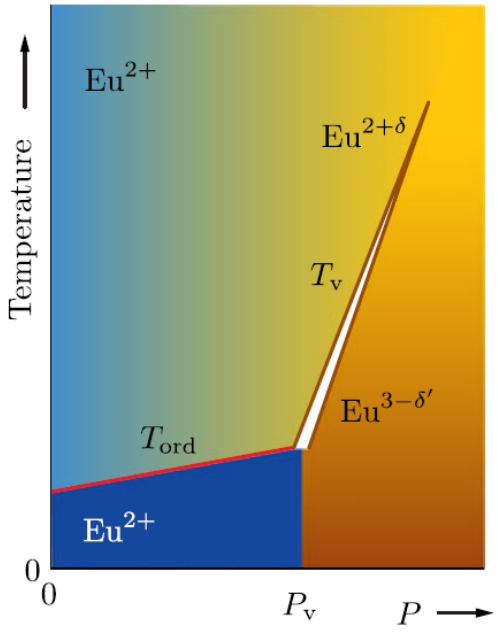

Figure 6.1: Generalized p/T phase diagram of europium based compounds [6].

The main compound of this work, $EuPd_2Si_2$, is said to be located somewhere close around this critical endpoint, and thus the hope is that, if properly controlled, this system will only need a small amount of tuning (e.g. by doping) to be suitable to actually investigate this endpoint's behaviour.

7 Processes and methods

This chapter gives an introduction into the methods applied in order to grow the samples of interest, identify and refine their structure and composition and investigate various of their physical properties. Thereby this chapter claims to mediate between the theories and the experiments.

7.1 Crystal growth methods

This first section will deal with the different options used to process the growth of crystalline samples. The EuT_2P_2 and $EuAFe_4P_4$ samples were grown in external flux, as many compounds of the RT_2X_2-family (R: rare earth, T: transition metal, X: 4th or 5th main group element) are. For $EuPd_2Si_2$ this method was unsuccessfully used, but the growth succeeded performing both a self flux method and Czochralski growth out of a self flux.

7.1.1 Differential thermal analysis

Differential Thermal Analysis (DTA), i.e. the measurement of a crucible's temperature during a sample's growth process and comparison to a reference not containing any sample, can be utilized to locate phase transitions during the crystal growth process on a temperature scale. Within a DTA setup, a conventional flux growth is performed.
Especially easily done is this for solid-liquid phase transitions, which are of first order. The latent heat of a first order phase transition causes the temperatures of heating reference and stagnating sample to diverge, producing a clearly visible, peak-like signal.
For example, in fig. 8.4 the solidification and melting temperatures of $EuPd_2Si_2$ and the remnant of the self flux are obtained from a Differential Thermal Analysis.
DTA experiments are performed with a Netzsch STA 409 measurement device. Thermal measurements are conducted with type S thermocouples, heating can be performed using two different furnaces; a platinum furnace, yielding up to 1500 °C under a static argon atmosphere, and a silicon carbide furnace, yielding up to 1700 °C under a static argon atmosphere or argon flow.

7.1.2 Flux methods

If you want to grow a system that is either incongruently melting, or consists of components with a high melting temperature, flux growth is the method of

choice. Also, you choose flux growth, if you want to grow a system consisting of three or more components and don't have an existing working point enabling any other growth method, to gain knowledge about your system.
What you want a flux to do is to act on the components of the melt like a solvent. The solubility of the components in a melt of this metallic flux is then utilized to undergo the higher original melting temperatures of the components. This may be necessary, since generating high enough temperatures to melt e.g. iron ($T_{Fe} \approx 1500\,^{\circ}\mathrm{C}$) or palladium ($T_{Pd} \approx 1550\,^{\circ}\mathrm{C}$) is technically challenging - and also might surpass the optimal temperature for the target compound to grow.
Usually, by solving the temperature problem, we cause a solubility problem. We need the solvent to interact with the reactants by dissolving them, but we also need the solvent to not react with the crucible or be incorporated into the resulting crystals. To the raising question of how to reach the sweet spot of solving the reactants, but not incorporating the solvent into the results, two answers can be given and are valid under different circumstances: We can add a dimension to the phase diagram by chosing an additional element as *external flux*, or we can try to use a set of elements (e.g. an excess of a single element or an eutectic point of a binary phase diagram) that also takes part in the target reaction and is counted with to be gradually incorporated, to perform the growth in a *self flux*.
Flux method experiments can be conducted in a variety of different box or tube furnaces, for different temperature ranges, with or without protective atmposphere, depending on the experimental design. Mostly used furnaces in this work are the Linn box furnace (up to 1100 °C with protective atmosphere), the Therm-Concept box furnace (up to 1300 °C without protective atmosphere) and the Gero high temperature tube furnace (up to 1500 °C with protective atmosphere).

External flux methods

An external flux is an additional element, that is not to be contained in the target phase. For intermetallic growth experiments, mostly a metal with a low melting point and a high boiling point is chosen (e.g. tin, indium, lead, germanium, bismuth etc.; [40] shows a nice overview on how to choose metallic fluxes and yields some additional suggestions). The low melting point is self explanatory with respect to one of the main goals being to achieve a homogeneous melt at lower temperatures than without the solvent. The boiling point needs to assure there will be no evaporation of the main constituent out of the melt at even the highest temperatures achieved in the experimental process. The solvent ideally is liquid over the whole temperature range of the experiment.
The solubility of the components with the solvent metal usually can be estimated by consulting the binary phase diagrams of every element to solve with the solvent metal. The binary phase diagrams also tell which phases a candidate to be a solvent could form with the reactants. Ideally, we want a metal, whose binary phase diagrams with every reactant have a low lying liquidus line over a range as broad as possible, and don't contain many binary phases.
The removal of external fluxes is relatively easy, given the case that they are not incorporated into the resulting crystals. If the target phase is known to be stable against etching, the flux can be etched away using a suitable acid. In most cases, Hydrochloric Acid is sufficient. In case it is unstable against etching or the knowledge about all phases developing during the growth process is needed,

the property of the flux to melt (and solidify) at low temperatures allows to use a centrifugue to separate the flux from the already solidified phases, while still liquid. For this procedure, a pair of crucibles, separated by a sieve, is used. The experiment is performed in one of the crucibles and afterwards brought into the centrifugue upside down to move the flux through the sieve into the other crucible. In chapter 8.4.1 considerations of several external fluxes are made to exemplify the sorts of argumentation made. In general, Tin (Sn) and Indium (In) are the most common external metallic fluxes, and are also the fluxes used during this work. Especially Tin proved itself to be a suitable candidate when working with Phosphorus, as it is done in chapters 11 and 10.

Self flux methods

A self flux on the other hand is a flux based on the materials already involved into an experiment. For example, a singe element (ideally with a low melting point) could start with an excess of material compared to what should be incorporated in the target compound; or, to ensure low melting points in a system with high melting constituents, an eutectic point of one of the binary phase diagrams of the elements involved could be used as a flux composition.
Using a self flux changes the question of how inert flux and reactants need to be. An incorporation of flux material into the target compound is counted on to a certain degree. Still, flux incorporations in form of other compounds is to avoid, especially when possible phases show a strong magnetic response. Especially fluxes containing e.g. iron or cobalt can be dangerous from this perspective. The general downside of a flux not inert to, but part of the reaction, is, that the removal of the flux can be more of a problem. Some fluxes, especially those containing rare earth elements, decompose with time upon air contact, but otherwise a removal of flux remnants is mostly done mechanically, since it is improbable to find any acids that decompose the flux, but not the samples, and since the temperature window between solidification of the target phase and solidification of the flux is mostly insufficient for centrifugation. For example, $EuPd_2Si_2$ solidifies at about 1200 °C, but a flux we might have chosen does so at about 825 °C (Eu excess) or about 900 °C (PdSi flux).
And these for fluxes relatively high melting temperatures already are to be achieved by preliminary work. When an eutectic point is chosen as a flux, but both of the elements have themselves high melting points (e.g. Pd with a melting point of about 1550 °C and Si with a melting point of about 1400 °C), they need to be prereacted in order to actually form a melt with them at lower temperatures.
But if all those obstacles can be dealt with, self flux methods yield a way of flux growth that secures a better understanding of the ongoing growth, since the dimensionality of the phase diagram is not artificially increased by adding new materials. It also allows optimizing the material throughput in e.g. via crucibles spacially restricted experiments.
In chapters 8 and 9, it is described how $EuPd_2Si_2$ is grown from a self flux (Eu excess) via Czochralski technique.

7.1.3 Czochralski method

While a flux growth (with or without a temperature gradient) can be optimized to gain crystals of several millimeter scale and several milligram of weight, the solution/flux growths are first restricted by the amount of material that is used, second by multiple seeding (and competing crystals growing), and of course third by the natural habitus of the samples. If the targeted system e.g. tends to form thin platelets or needles, there is no way to force them into a bulky shape. For some measurements and applications, samples might be needed that surpass a certain size or weight, or that come in a certain form. Sound measurements for example need the sample to be extended in measurement direction. A system with the natural habit of platelets thus could not be measured out of plane with sound on samples from a flux growth.

With the Czochralski growth technique, it is possible to try and extend the limits

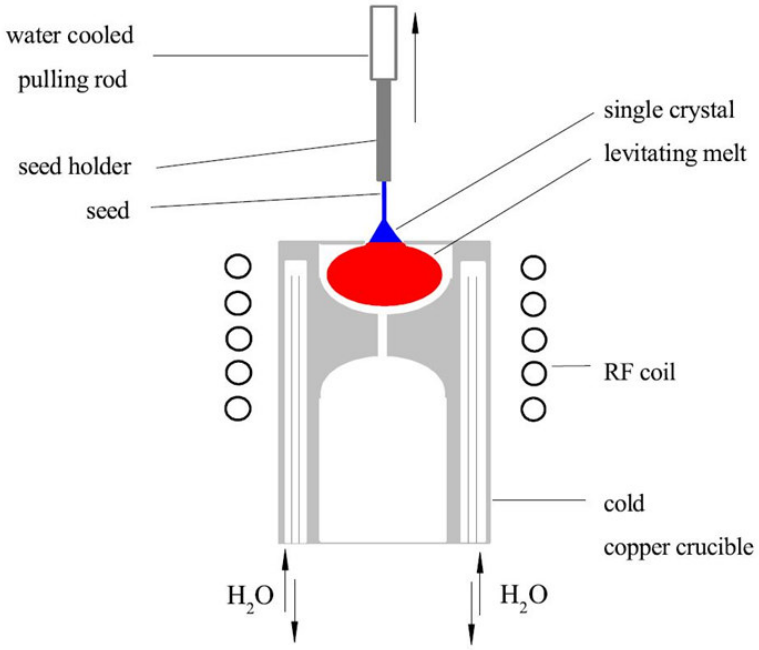

Figure 7.1: Schematic design of a Czochralski experimental site [41]

of size and weight to larger scales - centimeter and gram for the lab applications on ternary systems. Also, growth of crystals in not preferred directions is possible. A Czochralski growth is usually performed on a melt that is, in the ideal case, stochiometrically identical to the target compound, which needs to be congruently melting in this case, or else a melt with the least possible amount of (self) flux to minimize flux inclusions.

For the general setup, the starting materials are put into a crucible, where they are melted and the melt is homogenized. Into the melt a seed is introduced, i.e. a piece of sample, from where on a crystal can continue to grow, placed on a cooled pulling rod. The seed is then, as it is the coolest spot of the melt, the spot, where also the actual growth starts, pulled out at a certain velocity. At a certain height of the melt, the cooling of the seed then is stronger than the continued heating of the melt, and a crystal forms. With this technique, ideally the whole melt could

be translated into a resulting bulky single crystal.
In our group's setup for Czochralski growth, before the experiment the materials are placed in an open cold copper crucible (see sketch in fig. 7.1). Around the crucible an induction coil is wound, which is used to heat the metals forming the melt. Also, the materials are placed slightly out of range of the homogeneous field. The inhomogeneity of the field and thus the Lorentz force causes the melt to levitate. This enables the setup to deal with materials which form aggressive melts, since the melt is no longer in contact with the crucible and can't attack it. The whole setup (crucible, cooling, heating coil, pulling rod) is placed inside a cavern, in which an argon atmosphere of up to 20 bar can be applied. This way, in this setup we can also deal with moderate vapor pressures, which is important for experiments with Europium.
The experimental setup used in the laboratory is a cavern by Arthur D. Little, hence called the ADL apparatus, and features all the necessities for a Czochralski growth after the scheme described above.

7.1.4 Sintering

Sintering, as Uphadyaya describes it, is "the process by which an assembly of particles, compacted under pressure or simply confined in a container, chemically bond themselves into a coherent body under the influence of an elevated temperature" ([42], p. 68), which usually is below the melting temperature of the main constituent. Sintering hence mostly is realized within a solid-solid setting.
Upon sintering, solid particles bond together and form a porous system. If there are more than one constituent, also a chemical reformation may occur. Driving parameter for sintering reactions is the surface free energy of the particles.
A sintering process from a powder consistent of unbound particles to a porous solid can be conceptualized as a sequence of certain steps (after [42]):

1. Initial bonding among particles: the particles experience physical contact and stick together, conceptually only in single points.

2. Neck growth: Larger contact areas between the individual grains are forming.

3. Pore channel closure: The necks are closing the free space between the grains, so that only isolated "caves" remain between the grains compounded.

4. Pore rounding: By minimizing the surface free energy, the pores tend to take a round shape with the course of the experiment.

5. Densification: Upon further heating, the pores tend to shrink, the material condenses.

6. Pore coarsening: The surface of the grains converge towards being self similar.

While sintering a powderous sample, also the individual grains can react to and with each other and form new crystalline phases. Solid-solid approaches for growing polycrystalline samples utilize the sintering technique. The powders of the ingredients are thoroughly grinded, mixed together and pressed into a pellet, in

which the individual powder grains are compacted in a way that sintering may occur.
Solid-solid reactions and sintering is usually performed in the same furnaces as the flux experiments are, depending on the design of the protective layers (crucibles etc), but mostly in the Linn furnace, since the experiments take place at lower temperatures, and the protective atmosphere makes an experimental design exceptionally easy.

7.2 Structural characterization methods

When a crystal is grown, its structure and composition are still to be determined. For the determination of structure, composition and orientation of a given crystal, a range of analysis methods was used, based on optics, X-ray diffraction and electron microscopy. These methods will be explained in the following section. A short overview on many of the methods can be found in [43].

7.2.1 Optical microscopy

For flux grown samples, optical analysis of the results is a necessary first step of investigating the outcomes. Spacial scope, habitus, colour and metallic shininess can be used to preselect crystals for structural and physical analyses.
For Czochralski grown samples, the role of optical microscopy changes to getting a thorough overview over the surface macrostructure of the sample and identifying surface areas possibly corresponding to certain crystallographic planes. Also, by looking at the colour of a polished sample, a coarse pre-estimation of clean and flux including areas can be made, if the colour scheme of the sample allows for it. For optical investigations and imaging, a Keyence VHX-600 digital microscope is at hand.

7.2.2 Polarization microscopy

A polarization microscope is used for grain analyses of larger crystalline compounds. The sample under investigation is polished and then lighted by a polarized light source. If the sample under investigation is birefractive, which is the case for non cubic systems, the refraction of the light will depend on the specific orientation of the two main axes refractive index ellipsoid, which differs between differently orientated grains of a crystal. Grains sufficiently diverging in orientation (and hence in the orientation of their refractive index ellipsoid) will appear in different brightness or colours in the resulting image. A polarization microscope by Carl Zeiss is available in the laboratory.

7.2.3 Powder X-ray diffractometry

X-ray diffractometry (XRD) is the best choice if we want to determine, confirm or refine a crystals structure. By confirmation of the structure, i.e. of the symmetry group and the lattice parameters, we make a strong argument for the identification of the phase or phases contained in a sample. The following description of the technique took information from [44], where a more detailed view can be

found.
XRD experiments can be performed on single crystals (and thus a sample with a single orientation) or on powderous samples (i.e. a sample consistent of many single crystallites with a distribution of different orientations). In either case, X-rays are refracted by the crystal lattice, the reflexes are counted angular dependent, and every reflex contributes a degree of freedom to the solution space, i.e. one information we can extract from the diffractogram. For single crystal refraction, this is in the order of magnitude of several 100s of reflexes, which is why they are used to determine unit cells. For powderous samples this is in the order of magnitude of several 10s of reflexes. This makes a description of a unit cell nearly impossible, but is perfectly suited to determine the symmetry group and lattice parameters of the crystal lattice.
For a diffraction experiment, in general the wavelength of the used light needs to be in the order of magnitude of the characteristic lengthscales of the sample, i.e. the distances of the atomic planes of the crystal lattice that is under investigation, which are the centers of diffraction. Typical unit cell sizes are in the order of magnitude of several Ångström for anorganic crystals, hence also are typical atomic plane distances. This scale corresponds to the X-ray spectrum. Usually, the characteristic radiation of a specific element (e.g. Cu Kα radiation, Mo Kα radiation) is used for sharp reflexes.
Atomic planes function as centers of diffraction. A reflex is seen when full cycles of the wavelength λ fit the distance between two planes of an atomic plane set with the Miller indices (h,k,l) which is d_{hkl} under a certain angle 2θ. This is called the Bragg refraction condition:

$$2 \cdot d_{hkl} \cdot \sin(\theta) = \lambda. \tag{7.1}$$

This condition is equivalent to the Laue condition, which says the refraction wave vector $\mathbf{k} - \mathbf{k'}$ to be equal to a crystal momentum vector $\mathbf{k} - \mathbf{k'} = \mathbf{G}_{hkl}$. A crystal momentum vector denomenates a point in the reciprocal space with the Miller indices hkl, that corresponds to the crystal planes with the same index triple. The symmetry of the lattice yields the position of the reflexes of the different hkl-planes. It can cause reflexes corresponding to different atomic planes to fall together, e.g. the (100), ($\bar{1}$00), (010) and (0$\bar{1}$0) in tetragonal lattices, since the directions are symmetrically equivalent, and also the symmetry of the lattice might suppress reflexes following a specific indexation rule. Furthermore the hight of the reflexes is determined by interferences between the different atoms' contributions to the atomic form factor. In principle, a diffractogram to a given structure and unit cell can be determinded analytically. Usually they are determined numerically.
The shape of the reflexes are dominated by the crystalinity of the sample, the scope of the crystallites and their thermic factor, counting mostly thermal excitations of the lattice.
Powder X-ray diffraction measurements were carried out using two Bragg-Brentano diffractometers with copper X-ray tubes and a double monochromator setup, a Bruker D-8 type for room temperature measurements and a Siemens D-500 type with helium-pump cold head (reaching temperatures of down to 10 K) for low temperature measurenments.
Qualitative phase analysis was done using powderCell 2.3 [45]. Refinements and

quantitative phase analysis were performed using the refinement software GSAS II [46].
X-ray fluorescence, which under copper radiation is a major problem especially for samples containing the classical transition metals iron, cobalt, nickel and manganese, is come by, since both use a doubled set of monochromator crystals. This works at the expense of some of the intensity of the measured diffraction patterns.
In most cases, this is not a great problem; but if it is, one can fall back on a third diffractometer, using a transmissive Guinier geometry and a Molybdenum radiation source instead of copper. Also, the brilliancy of the Mo-Guinier diffractometer is significantly higher than the brilliancy of the copper diffractometers.

7.2.4 Laue diffractometry

X-ray Laue diffractometry is a primitive realisation of the idea of single crystal X-ray diffractometry. A X-ray beam (diameter in the range of half a millimeter) consistent of a continuous spectrum of braking radiation (generated with a Tungsten tube) is directed towards a static spot on the sample under investigation, and the refraction pattern is collected on a detector plate (e.g. a photosensitive image plate).
The refraction pattern is a set of points, each of which is related to one set of atomic planes. The points are arranged along lines that resemble the rotational symmetry of the crystal system's direction investigated. Hence, X-ray Laue diffractometry is used to gain information about the orientation of a crystal. This information can be used to confirm the growth direction of flux grown samples, or to set up for oriented cuts through larger pieces of e.g. Czochralski grown crystals.
Also, the confinement of the spots is an indicator for the amount of disorder in the crystal, since small defects will already lead to a broadening of the spots. A doubled and slightly shifted image indicates multiple grains and grain boundaries.

7.2.5 Scanning electron microscopy

Inside a Scanning Electron Microscope (SEM), a sample is penetrated by a high energy electron beam (accelerated with a high voltage of 30 kV), falling on the sample normal to the surface. The electron beam dissolves in various (elastic and inelastic, reflecting, transmitting and absorbing) effects. Two of this effects are used for imaging purposes:

- The secondary electrons (SE) are electrons secondarily produced by the inflecting beam inside the sample, and are collected on the transmission side. They are sensitive for edges and surface structures of the sample.

- The backscattered electrons (BSE) are electrons directly scattered back by slingshotting around the sample's nuclei. Since the nuclei backscatter the electrons with a crosssection proportional to a polynome of their atomic charge number, the brightness contrast detected by the detector will yield a map, on which areas containing heavier elements will be brighter than areas containing lighter elements.

In the group, an electron microscope DSM940A by Zeiss is available, supplemented with an EDAX detector for EDX measurements.

7.2.6 Electron backscatter diffraction

One additional analysis option inside a Scanning Electron Microscope is to perform diffraction experiments with the backscattered electrons (BSE). This method is then called electron backscatter diffraction (EBSD). Diffraction experiments are carried out by tilting the sample to a certain degree, so that the beam does not impact normal to the surface anymore. The detector is placed in a way to be able to collect the diffraction pattern that resembles the symmetry of the crystal investigated with respect to the crystal's surface. The symmetry is displayed via a line pattern, that shows the same pattern as a Laue image, but with continuous lines instead of reflex spots. With an EBSD mapping, one can investigate absolute and relative orientation of large samples. EBSD measurements on our samples were conducted at the geology institute of the Goethe university in Frankfurt, by Jolien Linckens.

7.2.7 Energy/Wavelength dispersive X-ray analysis

A third effect of electrons interacting with matter inside the Scanning Electron Microscope, that can be made use of for sample analysis, is X-ray fluorescence of the elements. The X-ray fluorescence effect is used for investigation in the energy dispersive X-ray analysis (EDX) method. The high energy electron beam can ionize the elements of a sample by depopulizing the low lying states of the atoms. The ions then repopulize the low lying states with electrons from the outer orbitals. The energy difference is emitted as a photon in the X-ray spectrum. These differences are characteristic for each element, and different spectral lines (K names the lines related to the innermost shell, L the second innermost, M the third innermost shell) of an element can be used to estimate the amount share of said element inside the sample. The X-ray quanta are collected with an energy sensitive detector. Relations between the countrates at different characteristic energies indicate the weight and atomic ratio between different elements in the sample. This can be used for a quantitative elemental analysis of a sample. For wavelength dispersive X-ray analysis, the detector setup includes a refraction tool (e.g. a single crystal) to utilize Bragg refraction and enhance resolution between elements which are close in their characteristic energies.
EDX measurements were conducted in the crystals and materials laboratory. WDX measurements were conducted at the geology institute of the Goethe university in Frankfurt, by Heidi Höfer and Dominik Hezel.

7.3 Physical characterization methods

The physical properties of the grown and structurally characterized samples, and especially the properties related to the valence fluctuations, are investigated utilizing a variety of measurement techniques which will be shortly described in the following section. For the measurement of magnetization via VSM, specific heat and resistivity via AC-transport, a Physical Properties Measurement System

(PPMS) by QuantumDesign was used. Other measurements have been conducted with the devices of the collaborating groups.

7.3.1 Magnetization via VSM

Magnetization and magnetic susceptibility of a sample can be measured using the vibrating sample magnetometer (VSM) option of a QD-PPMS. A sample on a sample holder (either made of quartz, or a plastics or alumina capsule held by a metal sheet holder) is put into and magnetized in a homogeneous external magnetic field. The sample is periodically moved through the external field. A pick-up coil functions as a detector of the magnetization by detecting the magnetic flux through the coil, that varies with the sample position [43]. This magnetic flux Φ induces a voltage:

$$U_{ind} = \frac{\partial \Phi}{\partial t} = \frac{\partial \Phi}{\partial z} \cdot \frac{\partial z}{\partial t}$$

where z is the axis of motion. The flux gradient along this axis, and hence the induced voltage, is directly proportional to the magnetic moment investigated, that leads to the flux alteration, $U_{ind} \propto m$ [47].

7.3.2 Measuring specific heat

Heat capacity is also measured inside a QD-PPMS, using the relaxation time method. Here, the sample, placed on a drop of low temperature grease to have a good, homogeneous coupling between the heater and the sample, is locally heated (and the temperature measured) on a platform, that forms a thermally isolated system as a whole, only connected to the thermal bath (the sample carrier puck) by a set of connecting wires, which form a "gate" for thermal transport between the sample system and the bath with a known thermal conductivity. For the time relaxation method, we assume that the time scales, on which two physical systems of different temperature with heat capacities C_1 and C_2 are connected via a thermal conductivity λ find their thermal equilibrium, are only dependent on the heat capacities of the systems and the thermal conductivity. The thermal conductivity of the wires λ and the heat capacity of the bath C_2 are acquired via calibration of the puck. For the estimations of equilibrated temperature, since $C_2 \gg C_1$ and the puck is constantly cooled, the equilibrium temperature is technically the bath temperature controlled by the sample chamber thermometer. Hence, a given thermal pulse, exalting the sample temperature to above the bath temperature, leads to a relaxation of the sample back to the bath temperature on a time scale, whose only unknown determining parameter is the heat capacity of the sample system C_1 (where the sample can be separated from the grease by an addenda measurement of only the grease conducted in advance). The power applied through the heating pulse P translates into a temperature change of the sample (with T_B being the bath temperature) by

$$P\left[T(t)\right] = c\frac{d\,T(t)}{dt} + \lambda\left[T(t) - T_B\right] \tag{7.2}$$

When we choose a time t_0 to be the time where the heating pulse starts, we can integrate equation 7.2, and get

$$T(t) - T(t_0) = \frac{1}{c} \int_{t_0}^{t} \left[P\left[T(t)\right] - P(t_0)\right] \, dt - \frac{\lambda}{c} \int_{t_0}^{t} \left[T(t) - T(t_0)\right] \, dt \qquad (7.3)$$

where the first term describes the heating pulse, and the second term describes the equilibration process, which will be exponential with a time scale $\tau = (\lambda/c)$, when the heating pulse stops [48]. For a better fit, a two time-scales approach is selected, where the relaxation curve is fitted with two separate exponential time scales.

7.3.3 Resistivity via AC-transport methods

Resistivity is measured applying the four point method with amplified current. This method, since the current through the sample is controlled externally and not determined by the sample resistivity itself, is especially well designed for measuring samples with a small resistivity. The sample is connected to the measurement puck via four wires (platinum, 25 μm in diameter). The outer two wires are connected to the source of the circuit and establish the current through the sample. The inner wires connect a voltage-meter parallel to the sample in order to measure the voltage corresponding to the current determined by the outer wires. All of the contacts are loaded with a load resistance much larger than the sample resistance, so that all parameters, especially the current through the sample, are determined solely by the experimental setup (and the sample resistance's contribution to the total resistance is neglegible). Resistance is then determined by Ohm's law.

8 | $EuPd_2Si_2$

The 122-$ThCr_2Si_2$-type europium based compound $EuPd_2Si_2$ is the first compound that was chosen to investigate in order to probe the valence transition, as it was proposed to be first order and to end in a critical endpoint of second order by Onuki [6] (compare chapter 6.3), whether it is a model transition for the theory of quantum critical elasticity by Markus Garst [3] (compare chapter 5.2). This compound is held to be located quite close to the critical endpoint of the valence transition in terms of chemical pressure and thus a system, that might be easily tunable around and over this critical endpoint, maybe even by hydrostatic pressure. Later in this chapter, to not scatter information too much, used chemicals are only named. Chemicals used for the experiments are more thoroughly described in appendix A.

8.1 Structural type

The compound $EuPd_2Si_2$ is part of the rich $ThCr_2Si_2$ structure type family (colloquially called the "122 family"), which refers to a tetragonal bodycentered structural type that was first confirmed for $ThCr_2Si_2$ in 1965 [49]. The structural type is allocated to the structural type number 139 (Symmetry group I4/mmm) in the International Tables For X-Ray Crystallography [50] with the wyckoff positions a, d and e (table 8.1). The unit cell shows as in fig. 8.1. A symmetry scheme of

Wyckoff position	relative position	$ThCr_2Si_2$	$EuPd_2Si_2$
a	(0,0,0)	Th	Eu
d	$\left(\frac{1}{2},0,\frac{1}{4}\right), \left(0,\frac{1}{2},\frac{1}{4}\right)$	Cr	Pd
e	(0,0,z), (0,0,$\bar{z}$)	Si	Si

Table 8.1: Wyckoff positions of the 122 compounds [49, 50, 51]. Body centering yields the positions of the second formula unit with the given positions + (0,5; 0,5; 0,5).

this symmetry class is shown in figure 8.2.
In the late 80s and the early 90s, the structure type of the recently discovered compound $EuPd_2Si_2$ was determinded by numerous groups and confirmed to match the $ThCr_2Si_2$ structural type with lattice parameters of $4.231\text{Å} < a < 4.242\text{Å}$ and $9.851\text{Å} < c < 9.864\text{Å}$ [51, 52, 53].

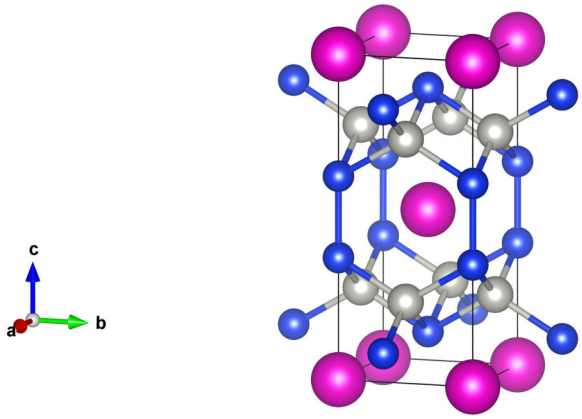

Figure 8.1: $EuPd_2Si_2$ unit cell after [52], pink: europium, blue: silicon, grey: palladium.

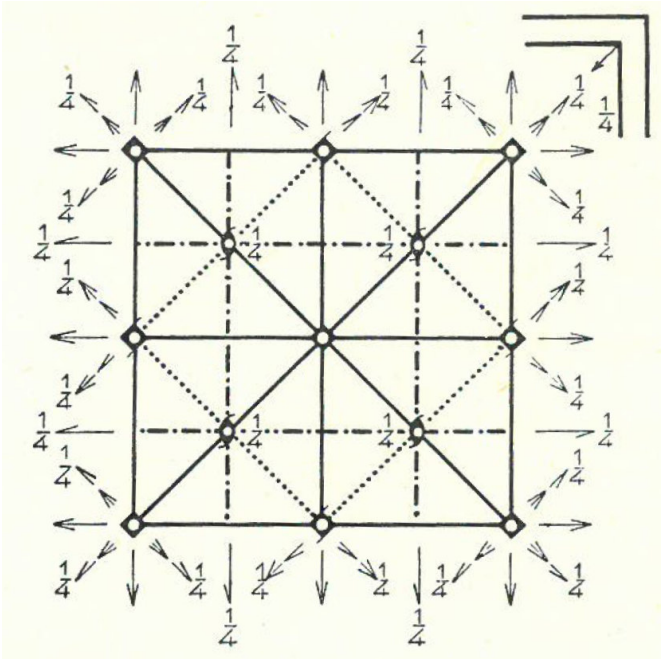

Figure 8.2: Symmetry scheme of a No. 139 (I4/mmm) ITXC classified structure [50].

8.2 Previous works

$EuPd_2Si_2$ is a compound known for about 40 years now. The lattice structure [51, 52, 53], valence states [7] and temperature dependent lattice effects as the shifting of the (200) reflex in powder X-ray data between 295 K and 80 K [9] have been discussed and investigated since the 1980's and 1990's. All of the expected effects already have been registered a long time ago. So, why is this compound interesting for a todays crystal growers research? There are some reasons to this:

- Despite the compound being known since the 1980's, it was only 2018, when Onuki [6] published to have grown the first single crystals of $EuPd_2Si_2$. Every previous work we can refer to (as [7, 9, 10, 11]) did their research on powderous samples of $EuPd_2Si_2$.
  The system seems to be quite resilient on being grown as a single crystal, and thus it is not only a challenge to the crystal grower to gain access to single crystals of $EuPd_2Si_2$ with a reasonably large size, but also a demand of the solid state low temperature community, which needs to confirm the previous findings on single crystals and enhance data quality. A supply with sufficient crystals for different thermodynamic investigations is needed.

- The valence transition in europium based systems is said to possibly be an instance of the effects described in the theory of quantum critical elasticity (compare chapter 5.2), published 2015 by Markus Garst and others [3], for the case of transitions accompanied by an isostructural lattice transition. The said system $EuPd_2Si_2$ now is of larger interest to an investigation of this theory, because it is said to be closely located to the second order critical endpoint of the valence transition line in terms of (chemical) pressure. To find a system, that is tunable beyond the critical endpoint possibly only by hydrostatic pressure, and to have sufficiently many sufficiently large and pure samples of that system at hand is, of course, of great interest for the thorough investigation on the validity of the theory. With a suitable system, we can try to describe the behaviour around the critical endpoint and compare it to the predictions of the quantum critical elasticity theory.

- Over the course of time of investigation on $EuPd_2Si_2$, different proposals were made on how the valence transition and the related lattice parameter shift (i.e. isostructural lattice transition) carry out and where the transitions are located temperaturewise. This conflicting proposals roughly agree on the overall development of europium valence and the lattice parameters, but they majorly differ in at which temperature the transition is located, in such a major way actually, that this conflict may not arise simply from differences between measurement methods. The transition is located at 140 K in some works, in others the transition temperature rises up to 170 K. The single works will be explained within a little more detail in the following. The pursue of a solution for this conflict whatsoever also can motivate the work on this system.

The system $EuPd_2Si_2$ was investigated physically first in 1981, after it was found and reported to show a lattice volume anomaly [54]. This pointed towards a valence anomaly of the europium Sampathkumaran planned to investigate on.

They prepared their samples by arcmelting the ingredients and afterwards homogenising it at temperatures of 800 °C [7]. This way, they did they research on polycrystalline samples and with this set the standard for the next 36 years. Sampathkumaran determined the magnetic susceptibility of $EuPd_2Si_2$ and non-valence-fluctuating $EuPd_2Ge_2$ and $EuRu_2Si_2$ as a reference. From the difference of the $EuPd_2Si_2$ susceptibility and the $EuPd_2Ge_2$ susceptibility they calculated the fraction of magnetic (Eu^{2+}) and nonmagnetic (Eu^{3+}) europium ions, utilising the expected magnetic moment of Eu^{2+} (see chapter 6.2).
Also determining the temperature dependent valence trend using Mössbauer spectroscopy, Sampathkumaran could clearly determine two different states of mean valence of the europium ions, between which is changed over a range of temperature, but inflects at between 150 K and 160 K for both investigations and displays very similar behaviour in the lower temperature realm. There they found a mean valence of the europium ions of about 2.85, where in the higher temperature realm the susceptibility investigation saturates at a valence of about 2.2, whereas the Mössbauer investigation stays back at a valence of about 2.3. In 1987 then, Jhans reproduced the isomer shift of Mössbauer measurements on polycrystalline $EuPd_2Si_2$ samples (including the qualitative form of the shift as well as the inflection temperature range between 140 K and 160 K) and associated this measurements with the findings of X-ray diffractometry and thermal expansion investigations [9]. Within the latter, Jhans detected that, while the lattice parameter c remained unaffected by the valence transition and simply evolved linearly in temperature, the evolution of the lattice parameter a displays the same general form as the valence evolution does, as well as the thermal expansion coefficient a_T, of course. By looking at $a_T^{-1} \cdot (\partial a_T / \partial T)$, the inflection temperature could be identiefied at roughly 145 K. Furthermore, a broadening of x-ray-diffraction reflexes associated with the a-direction is found around the inflection temperature of the lattice parameter evolution of 145 K. In the early 2000s then, Wada [10] determined the specific heat of $EuPd_2Si_2$ to find a broad and large anomaly peaking at 142 K indicating the valence transition and, by comparing it to $LaPd_2Si_2$ as a nonmagnetic reference material, estimated the entropy associated with the valence transition. In order to do so, they assumed the specific heat to be composed of an electronic (linear) term C_e, a phononic (cubic) term C_l and an anomaly term C_V to $C = C_l + C_e + C_V$. The anomaly contribution C_V could be separated from the other parts and the resulting C_V/T was integrated with respect to T to gain information about S_V, the entropy associated to the valence transition. They found S_V to contribute even at low temperatures to a small extent, but sharply increase at the transition temperature T_V and saturating against $22 - 23\,\mathrm{J/K}$ at room temperature. They also modelled the entropy contribution utilising the interconfiguration-fluctuations-model (ICF-model, chapter 6.1.1). The model can explain the steep rise in the entropy contribution at the transition temperature and the high temperature behaviour, but fails to explain the low temperature behaviour of the entropy.
In 2011 then, Mimura conducted PES measurements on $EuPd_2Si_2$ [11] and found the valence of the europium in the compound shifting with temperature between a high temperature state $Eu^{2.25+}$ and a low temperature state $Eu^{2.75+}$ in a broad transition centered around 140 K by comparing the Eu^{2+}- and Eu^{3+}-spectra temperature dependently. They also found the spectral form of the Eu^{3+}-contribution

to change in the course of temperature, and accounted this, using the Anderson model, to hybridisation with the contuction electrons. But it was first in 2017 when Onuki published his paper dealing with a large number of Eu-based compounds [6], which also contained some parts to the growth and characterisation of $EuPd_2Si_2$. In this paper, 2017 was the first year after about 40 years of research on this compound to see over mm-sized single crystalline samples of $EuPd_2Si_2$ reported. Also, heat capacity measurements and measurements of the magnetic susceptibility of $EuPd_2Si_2$ and the related antiferromagnet $EuPd_2Ge_2$ were reported in this paper. They will later be used as reference in our own charts.
Notable to see is again the size of the specific heat peak related to the valence transition, indicating a large increase in entropy due to the valence shift (from momentless Eu^{3+} to Eu^{2+} carrying a magnetic moment), and also, that in the high temperature regime the magnetic susceptibility data of $EuPd_2Ge_2$ (purely Eu^{2+}) and $EuPd_2Si_2$ (mixed valence state) the Eu^{2+}/Eu^{3+}-ratio could be estimated in comparison to the Ge-compound.
Also very notable is that the reported transition temperature of $T_V = 170\,\mathrm{K}$ differs from the previously reported temperatures by about 30 K - a mismatch, that was not explained and still is open to investigation.

8.3 Ternary phase diagram of the Eu-Pd-Si system

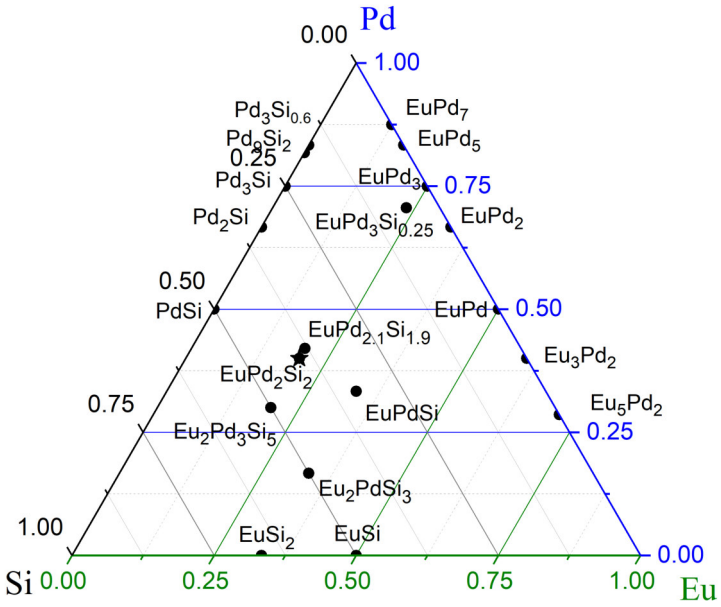

Figure 8.3: Eu-Pd-Si ternary phase diagram. Phase information: [31, 51, 52, 53, 55, 56, 57, 58]

In order to approach the $EuPd_2Si_2$ system via growth experiments, it is required to have some basic information about the Eu-Pd-Si systemic complex. This

starts with setting up a ternary phase diagram in fig. 8.3 (on how to read them, see section 4.1.3). The information on the binary phases were gained from the Massalski collection of binary phase diagrams [31]. The information on the existing ternary phases stems from publications on single phases [51, 52, 53, 55, 56, 57]. The information on the phase $Eu_2Pd_3Si_5$ seen in EDX was given to me via a private communication [58]. Later in our own growth experiments, it showed that this might as well still belong to the outer rim of the homogenity region of $EuPd_2Si_2$ (see section 8.6.1, discussion there).

8.4 Growth experiments

So now, with the first single crystalline samples of $EuPd_2Si_2$ there are lots of opportunities to more thoroughly probe the valence transition. With the valence transition as a possible probe system for the quantum critical elasticity theory (chapter 5), both elastic transport (sound transport measurements) and the hybridisation of the bands accounted to valence fluctuating states with the conduction bands (ARPES measurements) will be of great interest. For both methods, very pure singlecrystalline samples are required to conduct measurements on, as well as a certain size of samples. This in mind, we tried both flux growth experiments (where the plateletts we hoped to successfully grow would be optimal to conduct ARPES measurements on) and Czochralski growth (where one may hope for a bulky single crystal, appropriate for sound measurements and many other methods). While the attempts to grow $EuPd_2Si_2$ from an external flux failed, from internal flux growth a seed could be gained to establish an iterative process of Czochralski growths of the requested system.

8.4.1 Flux method experiments

A growth of $EuPd_2Si_2$ was attempted using different flux methods. Both different external fluxes and self fluxes were tried to be utilised. With the self flux method, mainly later Czochralski experiments were to be prepared, and this was achieved by Eunhyung Cho's bachelor's thesis within our lab group [5], so this part counts as "previous work". The external flux method was tested when the Czochralski growth of $EuPd_2Si_2$ was already established and tried to achieve some plate-like crystals.

The external flux method experiments

As an external flux, six metals were considered: bismuth (Bi), germanium (Ge), indium (In), lead (Pb), tin (Sn) and zinc (Zn). The considerations (using mainly [31] to consider binary phase diagrams) lead to the following conclusions:

bismuth: While with palladium a low melting liquid mixed phase exists and there is not much information about the behaviour with europium, the solution curve with silicon rises quite steeply to high temperatures, with the melting temperatures exceeding 1400 °C quite fast. Hence, bismuth is not an appropriate flux to deal with silicon.
Germanium: A handling of palladium and europium would probably work with

Germanium quite well, since the binary phase diagrams indicate liquid mixed phases from temperatures in the range of $700 - 800\,^{\circ}C$ on. Again, Silicium is ruining the deal, because Germanium is isoelectronic to silicon and can form a homogenious binary phase over the whole composition range.
Indium: For the Indium system, more data is available. Okamoto documented the binary europium-Indium solvabilities [59]. With additional consideration of binary phase diagrams, Indium presented itself as the probably most promising candidate as an external flux for a growth of $EuPd_2Si_2$. In a private communication, Silvia Seiro from Dresden even warned, that the palladium solubility in Indium might be too high and a palladium excess might be necessary in the growth preparation, since a 235-compound would form, if palladium would not exit the melt in a sufficient amount [58].
Lead: Lead behaves well with europium and palladium, but shows the same problems with silicon as bismuth does. Hence, it is not an appropriate flux.
Tin: tin behaves similarly to Indium with silicon, and is also compatible with palladium. Not much is known about the behaviour of tin towards europium. So, tin is another candidate for attempting to grow $EuPd_2Si_2$, but a way more uncertain candidate than Indium is.
Zinc: Zinc behaves very well with silicon, but forms a system with a tendency to evaporation with europium. Hence, it is not an appropriate choice to attempt a growth of $EuPd_2Si_2$.

Having evaluated this 6 usual metallic fluxes, both Indium and tin seem qualified to be tried out in a first experiment. Thus, the experiments MP403 and MP404 were prepared, with 8 gram of 1:2:2:30 (Eu:Pd:Si:In) and 6,5 gram of 1:2:2:30 (Eu:Pd:Si:Sn) respectively, inside a Canfield centrifugation alumina crucible, sealed inside a quartz ampoule.

For the tin-experiment MP404, only the formation of silicon single crystals and some tin-silicon binaries could be confirmed by EDX. Since there were very limited possibilities to gain information from this experiment on how to proceed, this remained the only experiment in tin flux.

For the Indium-experiment MP403, also the main result were single element silicon crystals. But also, in a powder diffractogram a not identifiable phase. Since powder data for the 235-phase mentioned by Sylvia Seiro were unavailable, we could not test whether this was the mentioned phase. Also, in EDX a ternary In-Si-Pd phase could be identified, which also could be responsible for the unknown PXRD reflexes.

Nevertheless the results of both this experiments indicated it to be more promising to continue attempts of growing $EuPd_2Si_2$ with Indium flux. A series of three experiments was made under the same conditions, adjusting firstly the palladium content of the melt to 2.2 (MP405), 2.35 (MP407) and 2.5 (MP406) within the above ratio.
PXRD patterns of all three experiments only confirmed only Silicium crystallised out of the melt. Seemingly, the rest of the elements still was dissolved in the tin flux during centrifugation.

Since only offering more palladium did not change any of the results, another experiment MP408 was made to offer more of europium to the melt, adjusting two parameters: enhancing the europium content from 1 to 1.5 in the ratio above (with a palladium share of 2.2), and also changing the material of the inner crucible from alumina (which was known from the self-flux experiments to react with europium containing melts according to the europium share) to graphite (to which europium containing melts only tend to stick a little to the crucible walls). The results of MP408 were some shiny single crystals with a size of up to four millimeters for the longest edge, and were identified to also be silicon single crystals. The powderous rest of the sample also did not seem to contain any other crystalline phases to a noticable amount.

While the efforts taken to actually grow $EuPd_2Si_2$ out of an external flux were not the largest, still the experiments resulting each only in silicon single crystals as a result after centrifuguing consistently were very resistant to being read towards whether the growth process was possible with a certain and not too large amount of tweaking of the experiment, or which parameters were to be tweaked.

Self-flux growth experiments with Eu self flux

The self flux growth experiments performed for $EuPd_2Si_2$ were predating the course of this work. Yet they should be shortly noticed here, since from Eunhyung Cho's bachelors thesis [5] there were different pieces of information to be learned and also a seed for the Czochralski growths of $EuPd_2Si_2$ to be gained.
In the course of her thesis, Eunhyung Cho developed a self-flux growth receipe for $EuPd_2Si_2$ after the descriptions in [6]. This receipe is based on an initial weight ratio of the elements Eu:Pd:Si of 1.4:2:2 to 1.5:2:2, so the experiments start with an excess of europium.
Cho performed differential thermal analysis (DTA) experiments (chapter 7.1.1) to determine the melting temperature of the target compound $EuPd_2Si_2$. Two melting temperatures were found, placed somewhere around 910 °C and somewhere between 1165 °C and 1186 °C respectively (see fig. 8.4), one of which belongs to the target compound, the other to anonther compound, which is remnant. It is firstly proposed, the higher temperature at about 1180 °C belongs to the target compound, the lower temperature to the remnant flux. This will later be confirmed when conducting Czochralski experiments on the target compound in 8.4.2.
Of course, there were basic information gained on the appearance of the compound. The target compound itself (confirmed by EDX and PXRD in various situations) appears metal-like with a golden colour, while compositionwise flux-like compounds contrast this in a distinguishable metal-gray. Remarks on the composition of the self-flux experiments will be made in chapter 8.6.1.
Furthermore, the behaviour of the melt towards different crucible materials (alumina, tantalum, graphite) was investigated. The melt seems to interact aggressively with alumina, to dissolve aluminum to quite a large amount (with a dissolution depth for the crucible walls of up to half almost a millimeter, see fig. 8.5a) and possibly incorporate it into compounds (grey boundary phase between the golden target phase and the crucible wall).

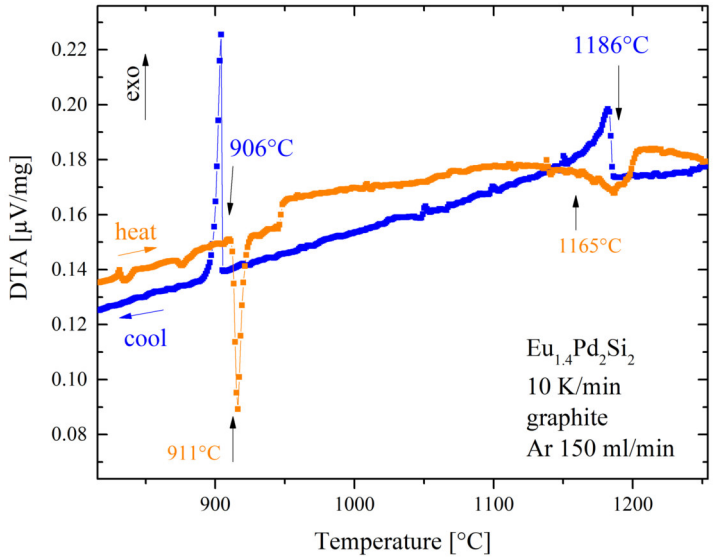

Figure 8.4: DTA signals of the compound $EuPd_2Si_2$ and the Eu-rich self flux [60].

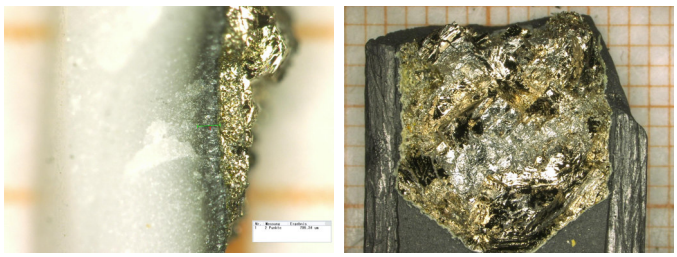

Figure 8.5: Alumina crucible of EC01, severely attacked by the Eu-rich melt; (b) Graphite crucible of EC06, with the recrystallized melt sticking to the crucible wall [61].

An experiment inside a tantalum crucible failed and the crucible ended up to be destructed. It never became clear whether this was an issue of the melt attacking the crucible, or whether there were other issues to the case.
For graphite crucibles, the melt does not seem to dissolve the crucibles to a reasonable amount, but tends to firmly stick to the crucible walls (fig. 8.5b), so that crystals need to be broken out of the crucible in order to investigate or use them. While experiments in graphite thus are clearly operable, they are accompanied by a loss of material of a reasonable scale.
Lastly, the final experiment of Eunhyung Cho's bachelors thesis yielded a sufficiently large crystal of the target phase $EuPd_2Si_2$ to use it as a seed for Czochralski growth experiments from now on (fig. 8.6).

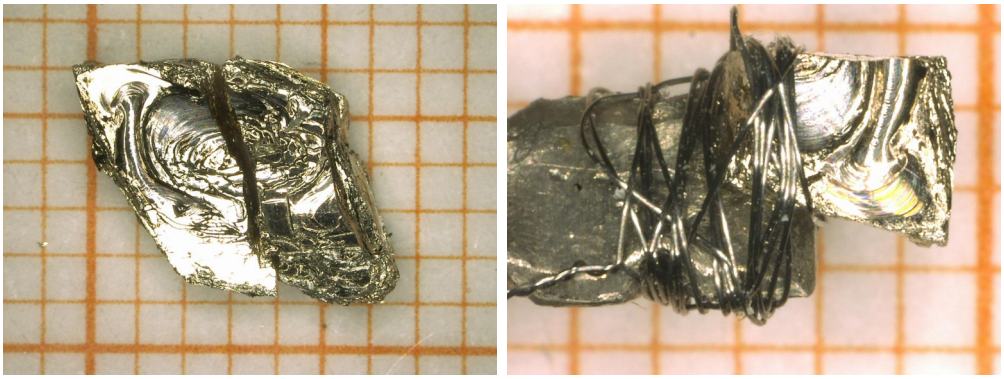

(a) seeding crystal from sample EC06 (b) seeding crystal attached to seedholder

Figure 8.6: Seeding Crystal for Czochralski experiments, gained from Bridgman growth sample EC06 [61]

Self-flux growth experiments with PdSi self flux

In the later course of this work, I tried to employ another self flux with a PdSi surplus instead of europium excess. With this measure, the goal is to reduce the influence of the vapor pressure of europium, and hence potentially loose less europium, since the europium is the most damageable, but also the most expensive ingredient to the growth process. The preparation of the PdSi prereaction is described in section 8.4.2, namely the prereaction subsection.
In different DTA experiments, different fluxes on PdSi basis were employed. The results were investigated structurally, using powder X-ray diffraction and EDX, in order to assess whether $EuPd_2Si_2$ is formed within the growth process. The DTA signals can be used to strengthen this analysis and to differentiate phases and learn about their melting behaviour.

MP418: For the experiment sample MP418, the PdSi molar amount was doubled in order to calculate the stochiometric ratios:

$$Eu + 4\,PdSi \rightarrow EuPd_2Si_2 + 2\,PdSi$$

The total mass of material for this experiment was 0.3 g. The experiment was performed in graphite crucibles, since from the Eu excess flux experiments it is known that the Eu-Pd-Si-melt might attack alumina crucibles. An argon flow was established to protect the setup from potentially emerging vaporous phases. The sample was heated to 1350 °C and cooled down repetitively several times.

Fig. 8.7 shows the signals from the growth experiment in the DTA setup. At

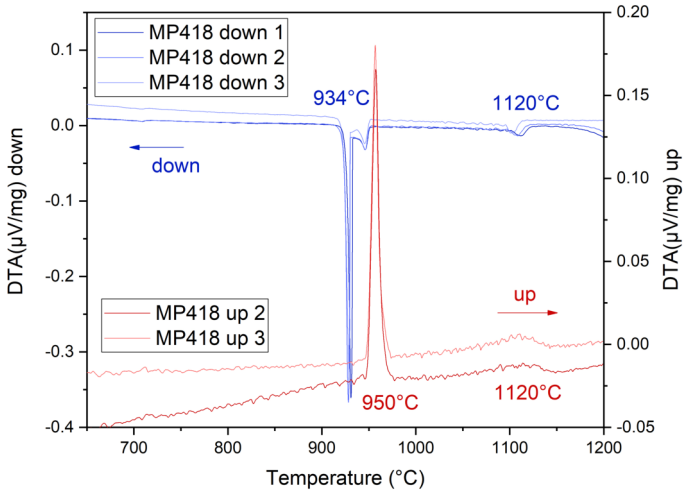

Figure 8.7: MP418 DTA signals, with a peak at 1120 °C, possibly belonging to $EuPd_2Si_2$, and one with a melting temperature at 950 °C and a resolidification temperature at 934 °C, being connected to the flux.

1120 °C, regardless of whether the sample is heated up or cooled down, a small signal occurs, that belongs to the target phase $EuPd_2Si_2$, whose melting temperature seems to be lower in the PdSi environment than in the Eu-excess enviroment (compare fig. 8.4), which further indicates that the phase is probably not congruently melting. Also, the signal is very small, indicating only a small amount of phase being formed. On the other hand, the signal with the melting temperature at 950 °C and a supercooling range of 16 K is in the range of the reported melting temperature of PdSi, wich is discussed to be between 976 °C [62] and 897 °C [63], so I might assume the flux to be actually close to PdSi, the minor change in melting temperature maybe accounting for some europium still contributing to the melt. The signal when cooling down is twinned, and the heating up signal rudimentarily shows a shoulder, so maybe this even indicates some proportion of PdSi without europium contribution. In any case, the flux remnant seems to be divided in two different phases, which are whatsoever sort of similar in melting behaviour.

After the experiment, the carbon crucible was cracked open and the major pieces were investigated with EDX to determine the composition of the results. Most of the sample crystallized as a grey solid, displaying a composition as in table 8.2, phase a, with almost half the amount being silicon, and an europium content of about 7%. Also, not separated from the flux, but integrated into the flux matrix, some patches with another composition (as in table 8.2, phase b) could be identified, which points towards the target phase, but with a strong excess of

Phase	Eu (At-%)	Pd (At-%)	Si (At-%)
a	6.77	44.40	48.83
b	16.56	34.49	48.95

Table 8.2: EDX results for MP418 pieces. (a) flux, (b) possibly target phase.

silicon, to the expense of both palladium and europium. Over the whole sample, a deficit of europium and palladium, or an excess of silicon, is observed. While the deficit of europium might be explained over some evaporation, and also some degradation upon air (green powder, probably europium hydroxide, formed on the samples surface), an explanation for the lack of palladium in the pieces investigated cannot be given so far.
A PXRD analysis of the pieces, that were investigated with EDX previously, confirmed the existence of structures similar to $EuPd_2Si_2$ (which probably corresponds to the patches with the composition from table 8.2, phase b), PdSi, Pd_2Si and Graphite (from the crucible). From these analyses, it remains unclear whether the europium observed in the flux is solved in the structures of PdSi and Pd_2Si, or whether small structures of $EuPd_2Si_2$ are integrated to the bulk and are measured through the flux matrix.

MP419: Since the portion of $EuPd_2Si_2$ in the experiment MP418 seemed to be rather small, a reduction of the PdSi share is the next thing to do. For experiment MP419, the flux was reduced to half the amount of excess PdSi:

$$Eu + 3\,PdSi \rightarrow EuPd_2Si_2 + PdSi$$

The rest of the setup remained the same. The total sample mass was 0.3 g, placed in graphite crucibles, and under an argon flow. The DTA signal data is shown in

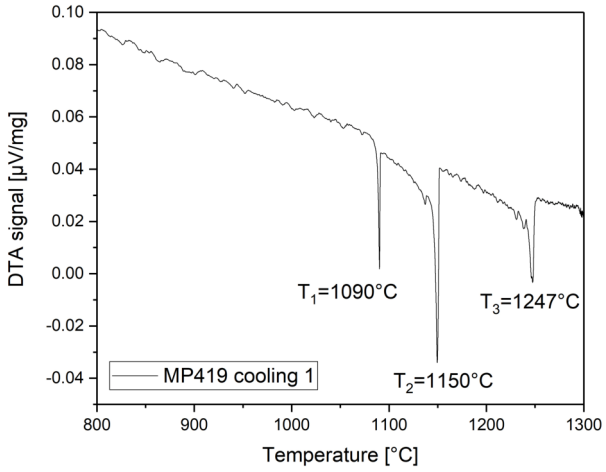

Figure 8.8: MP419 DTA signals.

fig. 8.8. During the experiment, the sample was repetitively heated to 1350 °C

and cooled down again three times. But there is only one set of data available, because the thermocouple desintegrated during the second heating phase. Since the first heating phase mostly yields quite wild and uninstructive data, there only remain the data from the first cooling phase to be analyzed. These show three phases solidifying: one at 1090 °C, one at 1150 °C and one at 1247 °C. The highest of these temperatures might be related to Pd_2Si, which has a melting point of 1331 °C reported by Massalski and Baxi [62], which would be quite a strong supercooling effect, but the PXRD confirmed Pd_2Si structures in the experimental results. The 1150 °C most likely correspond to the target phase, wich would be somewhat in concordance with the findings of the DTA experiments by Eunhyung Cho [5], MP418 and also close to the modal experimental temperature of the Czochralski experiments (see section 8.4.2). The lowest temperature then probably is related to another flux phase, that has also been found in the PXRD, but could not be determined as a binary phase between palladium and silicon. Hence, this flux phase probably will be a ternary phase, featuring some amounts of europium, maybe even quite large amounts.
This last guess is justified by the findings of the EDX measurements. There, three "phases" with quite broad composition ranges (partly probably due to measurement of phase mixtures) could be found: Phase (a) in table 8.3 is the target

Phase	Eu (At-%)	Pd (At-%)	Si (At-%)
a	18.68	35.75	45.57
b	32.51	18.52	48.97
c	10.52	45.49	43.99

Table 8.3: EDX results for MP419 pieces. (a) the target phase, (b) europium rich flux, (c) europium deficient flux.

phase. Phase (c) might be a superposition of the target phase and Pd_2Si. Phase (b) shows an excess of europium, related to what one would expect as a maximum, if all europium was incorporated into the target phase. The ternary phase diagram (see section 8.3) does not provide a suitable phase with the correct composition, or a composition, that allows linearly combining the findings of the EDX measurement from two or more phases, so far. Eu_2PdSi_3 and the Eu-Si binary phases, that might contribute, do not fit the PXRD pattern.
This experiment yielded an additional unknown flux phase in comparison to MP418, which by now stays inaccessible for an investigation that might pin down structure, definite composition or other properties of the phase. But also, the portion of $EuPd_2Si_2$ acquired was significantly higher.

8.4.2 The Czochralski growth experiments

Since the aim of this project (the test of the quantum critical elasticity theory in the long run) requires large and bulky single crystals for sound transport measurements, the growth technique was changed from the self flux method (yielding mostly pieces of doubtful crystallinity, which are also not the easiest to consequently separate from the remnant flux) to a Czochralski method as soon as there

was a crystal available which was suitable as a seed for Czochralski experiments. The self flux employed here is the europium excess self flux; PdSi-flux Czochralski growths were not performed so far.
While the general technique is well known in the lab group of Prof. Krellner, explicitly in person of PostDoc Kristin Kliemt (who also performed the Czochralski growth experiments in this project), every system you want to grow via Czochralski growth requires dealing with new specific problems, and mastering every system anew. With this very system $EuPd_2Si_2$, most of the complications are founded in that europium is part of the melt.
Since europium has quite a steep vapor pressure curve, it is needed to prereact with the other elements in order to prevent it from evaporating too much out of the melt. This is, of course, needed to keep the amount of europium in the melt well above the stochiometric 20%, but also to keep the melting temperature of our melt stable, since another problem we need to deal with is, as it seems, that the melting temperature of our melt is to a large degree dependent on the europium content of the melt, and sensitive even to smaller deviations.

Prereactions

The prereaction process for the Czochralski growth experiments is composed of two experiments: Since europium has a high vapor pressure already at lower temperatures, but palladium and silicon both have high melting temperatures with 1555 °C and 1414 °C respectively [31], the two elements need to be prereacted again to form a compound that has a significantly lower melting temperature, in the range of about europium's melting temperature of 825 °C. In the actual prereaction, Eu, Pd and Si are melted together into a single solid, that does not need to be crystalline or homogeneous, but will on the one hand protect the europium from oxidation before the Czochralski experiment, and on the other hand ease the formation of a homogeneous melt in the Czochralski chamber. With a look into the reported phase diagrams [62, 63], again PdSi qualifies as a candidate, that will later be also used for the PdSi self flux attempts in the DTA, that have been reported above. This compound would have a melting temperature between 976 °C and 897 °C, as stated in section 8.4.1, the PdSi self flux subsection. The compound is reported to form a high temperature stable phase, which is unstable in a thermal equilibrium below 600 °C/800 °C respectively, but quenching the prereaction would stabilize the compound also at lower temperatures. A decomposition would not be expected.
The first prereaction: PdSi is prereacted in a light arc furnace. Palladium and silicon pieces are placed in the furnace in a stochiometrically equal ratio (so that, if the reaction would yield a homogeneous result, this result would be PdSi), which corresponds to a mass ratio of $m_{Pd} : m_{Si} = 79.12 : 20.88$. Usually, I prereacted the PdSi for one Czochralski experiment at the time, which ranged between 8 g and 20 g of Pd and Si. For the self flux experiments later, also several grams of Pd and Si were prereacted to provide for more than only one experiment, since handling of masses lower than 1 g in the light arc furnace is impracticable.
In the furnace, under an argon atmosphere the elements are heated with the light arc, until they collapse to a single droplet. Usually, this droplet should look somewhat homogeneous. If some remnants of the ingredient pieces can still be recognized, the droplet is turned bottom up and melted again in the arc furnace,

until the whole material looks like it reacted to a binary phase. The resulting material is of a light gray (see fig. 8.9). The droplets are usually brittle and can easily be cleaved with a pair of pliers, that is of a suitable size. Despite the fast prereaction, the cleavage sites show to be largely smooth, possibly even indicating larger crystal grain compounds.

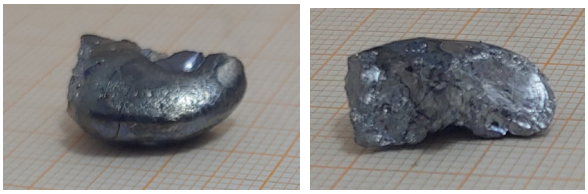

(a) (b)

Figure 8.9: Pd-Si prereaction droplet, (a) surface, (b) cleavage site

The second prereaction: When the PdSi material is obtained, the PdSi is prereacted with the europium. Therefore, the materials are put, with a certain excess of europium, inside a crucible. The total mass of the materials ranged between 30 g for the earlier experiments, and 15 g for the later experiments, which can be explained by both the avoidance of material losses for the later experiments, and the insight that a certain mass maximum exists, that can be handled successfully and without complications during a single Czochralski growth.
The europium excess was a parameter to be optimized. The first experiment was conducted with Eu:Pd:Si = 1.4:2:2 instead of 1:2:2 (so, 0.4 points europium excess, or 40% of the required europium mass as excess mass). As a maximum, 1.5 Euopium was used, as a minimum 1.2 europium. The Czochralski growth experiment results show, that an enhancement of the europium content also enhances the yield of the target phase, but adding too much europium is eventually disruptive to the growth process. The experiments with 1.5 europium content were unstable, and two out of four of them did fail. From experiment MP416 on, I settled for a starting composition of Eu:Pd:Si = 1.45:2:2, which promised a stable reaction during the Czochralski growth with a nearly optimized target phase yield. (The yield of target phase will be discussed more closely later.)
For the earlier prereactions, the crucibles were made from graphite, up until MP412. Later, from MP413a on, I changed the crucible material from graphite to glassy carbon, since in graphite crucibles, the prereacted melt tended to stick to the crucible walls, which lead to noticable material loss rates in the scope of several 10%. In the glassy carbon crucibles, the melt could be removed from the crucible nearly without losses, except of the destruction of the crucible.
The graphite or glassy carbon crucible is then put into a niobium outer crucible, which is sealed in the light arc furnace, to prevent the europium from evaporating. The whole setup is placed inside the Linn box furnace, which is special for the possibility to easily establish an argon protective atmosphere inside the furnace, so that metal crucibles can be handled at higher temperatures without any more protection.
The prereaction materials are heated with a rate of 100 K/h to a target temperature. There, the melt is held for one hour, before the furnace is turned off. The first experiment's prereaction took place at 1000 °C, the prereactions for the

second generation at 950 °C and 900 °C. Here, the melt showed to be less sticky to the graphite wall, the lower the temperature is, and that for a successful prereaction the PdSi melting temperature does not need to be reached. Only the europium needs to melt in order to react with the PdSi wholly. Consequently, from the third generation (as counted for the iterative growth-seeding-processes later in fig. 8.11) on, the prereactions were held at 835 °C.

Parameters of the Czochralski growth experiments

After the prereactions have been successfully conducted and the prereacted material is obtained, the material is brought into the Czochralski setup, where it is placed in a copper cold crucible, and after purging, a static atmosphere of 20 bar is applied, which is the maximal capability of the setup. As a seed for the Czochralski growth experiments (as described in chapter 7.1.3), a crystal of $EuPd_2Si_2$ is used. To where the seeding crystals were taken from, more information is given in the passage on the genealogy of experiments below in this section. The growth experiments were conducted within a day in every case, because the experiment is demanding in terms of supervision, so overnight experiments are impracticable. The Czochralski growth process itself was carried out by Kristin Kliemt.
Apart from contingencies of the experimental setup, there are mainly four parameters, that can actively be controlled:

- **The crystallinity of the seeding crystal**
  This parameter influences not always the conduction of the experiments, but rather the quality of the outcome. A suitable seed should be a piece of crystal of several millimeters in length, with a tip, that should not be larger than $(1 \times 1)\,\mathrm{mm}^2$, but should ideally offer only one crystal grain for the melt to grow on. The grain is oriented in one of the major crystallographic directions. In this case, the seeds were, if possible, selected to induce a growth of the new crystal mainly in a-direction. For seeds cut from previous

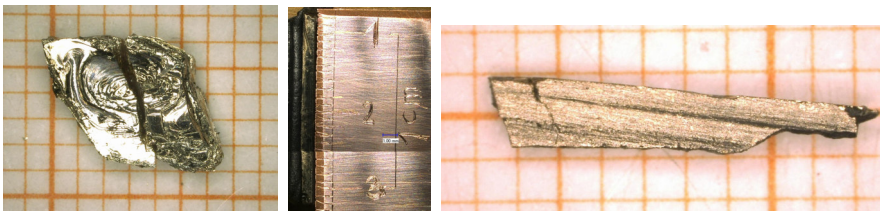

(a) (b) (c)

Figure 8.10: Eu-Pd-Si growth seeds: (a) EC06 [61], seed for MP401; (b) MP401, seed for MP402 and MP409 (scale sections of the copper lineal in 0.5 millimeters); (c) MP412, seed for MP413a and MP413b

  Czochralski experiments, this conditions are easily met by cutting a suitable piece from the sample in a spark eroding machine, when the sample bulge possesses large enough crystal grains (fig. 8.10b/c, a smaller tip is better, since it improves chances to offer only one grain to the melt, and also to start growing only one grain from the melt). For the first Czochralski growth, a

suitable grain (although with a very broad tip, fig. 8.10a) had to be selected from the Bridgman growth results from Eunhyung Cho's bachelor thesis [5].

- **The composition of the melt**
  As described previously, a parameter to be determined in advance to the experiment, that greatly impacts the course of the experiment, is the composition of the melt. $EuPd_2Si_2$ is grown from a self flux with europium excess. Onuki proposed an europium excess of 1.3-1.5:2:2 instead of 1:2:2 starting composition [6]. While enhancing the europium excess rate benefits the amount of phase, that is gained during the growth process, also it destabilizes the growth process due to a stronger evaporation of europium disturbing the melt.
  Beginning the first experiments with a starting composition of 1.4:2:2, after some experiments with 1.2 points europium (which lead to the conclusion, that 1.4 points europium is a good minimum, since the yield was poor in this experiment) and 1.5 points europium (half of which failed due to an unstable growth process, since it forced a faster pulling) I settled with a starting composition of 1.45:2:2, as a tradeoff between a good yield and a stable growth process.

- **The temperature, at which the experiment is performed**
  The temperature of the experiment is, of course, dictated mostly by the melting temperature of the precursor. This temperature is found by, from low temperatures on, enhancing the experimental temperature, until the precursor inside the cold crucible is entirely molten. Then, the temperature is lowered stepwise, until the resolidification of the precursor can be observed. Both observations, the melting and the resolidifying, are to be made by eyesight through a window in the experimental chamber.
  The experiment then takes place at a temperature slightly above the found resolidification temperature, so supercooling is already taken into account. At the seed, the resolidification temperature then is reached by cooling and the crystal starts growing.
  The experimental temperatures of the experiments conducted varied in a range between roughly 1130 °C and 1270 °C. The variety range might be influenced by a possibly changed composition of the precursor due to material losses (which were in the range of several 10% for the first experiments), but the losses were drastically reduced later, and still, there was some variety in the resolidification temperatures (and hence, in the experimental temperatures). Also, there seems to be no evidence on how successful a growth experiment will perform, dependent on the temperature at which it is conducted. The successful growth experiments cover the whole temperature range, while also the failed experiments took place at a broad range of temperatures. Also, no link to crystallinity or sample composition could be found, which both seem to vary more within one sample, than they do between samples (see section 8.6.1, and in this section below).

- **The pulling velocity for pulling the crystal out of the melt**
  For pulling velocities, experience from the experiments is, that they should not drop under a certain treshold, since otherwise, evaporation from the

melt becomes a large issue quite "soon" in terms of the growth progress of the crystal. But also, fast pulling increases the danger of simply tear off the crystal from the seed, resetting the growth progress to zero while altering the melt's composition undeterminably. A pulling velocity of between 1.6 mm/h and 2 mm/h for the main part of the growth experiment has proven to fulfill both needs for a stable but fast growth process quite well. In table 8.5 below, it shows, that the few experiments, that did not stick to this velocity range, did not turn out to bring about the best results. But this is only a weak generalization, the most stable pulling velocity had, in the end, to be found for every growth process on its own, fitting to the other parameters (especially the temperature), and is merely a descriptive evaluation of which pulling velocities were used in the more successful experiments.

Genealogy of experiments

The Czochralski experiments conducted on the growth of $EuPd_2Si_2$ are organized along generations, in that sense, that the seeds for the growth experiments of generation i are extracted from the growth results of generation $i-1$. Over time, or rather, over iterations, it can be expected to enhance the mean crystal quality, the yield and the grain size by such means.

By now, the $EuPd_2Si_2$ experiments count five actual generations, counting the

Sample	Gen	ratio Eu:Pd:Si	Crucible	Max temp/°C	initial mass/g
MP401	1	1.5:2:2	C, Nb	1000	20.4
MP402	2	1.5:2:2	C, Nb	950	29.45
MP409	2	1.2:2:2	C, Nb	900	30
MP411	3	1.5:2:2	C, Nb	835	25
MP413a	4	1.5:2:2	GC, Nb	835	16.4
MP413b	4	1.5:2:2	GC, Nb	835	8
MP412	5	1.4:2:2	C, Nb	835	25
MP416	5	1.45:2:2	GC, Nb	835	15
MP414	6	1.5:2:2	GC, Nb	835	15
MP415	6	1.5:2:2	GC, Nb	835	15
MP417	6	1.45:2:2	GC, Nb	835	15

Table 8.4: Overview over the experimental parameters of the prereactions to the $EuPd_2Si_2$ Czochralski growth experiments. Crucibles: C = Graphite, GC = glassy Carbon.

DTA experiments, that were made in advance, as generation zero. Fig. 8.11 shows the course of experiments over the generations. In the left column, the generation is assigned to the ranks. on the right, the genealogy of experiments is displayed, each white box referring to an independent Czochralski growth exper-

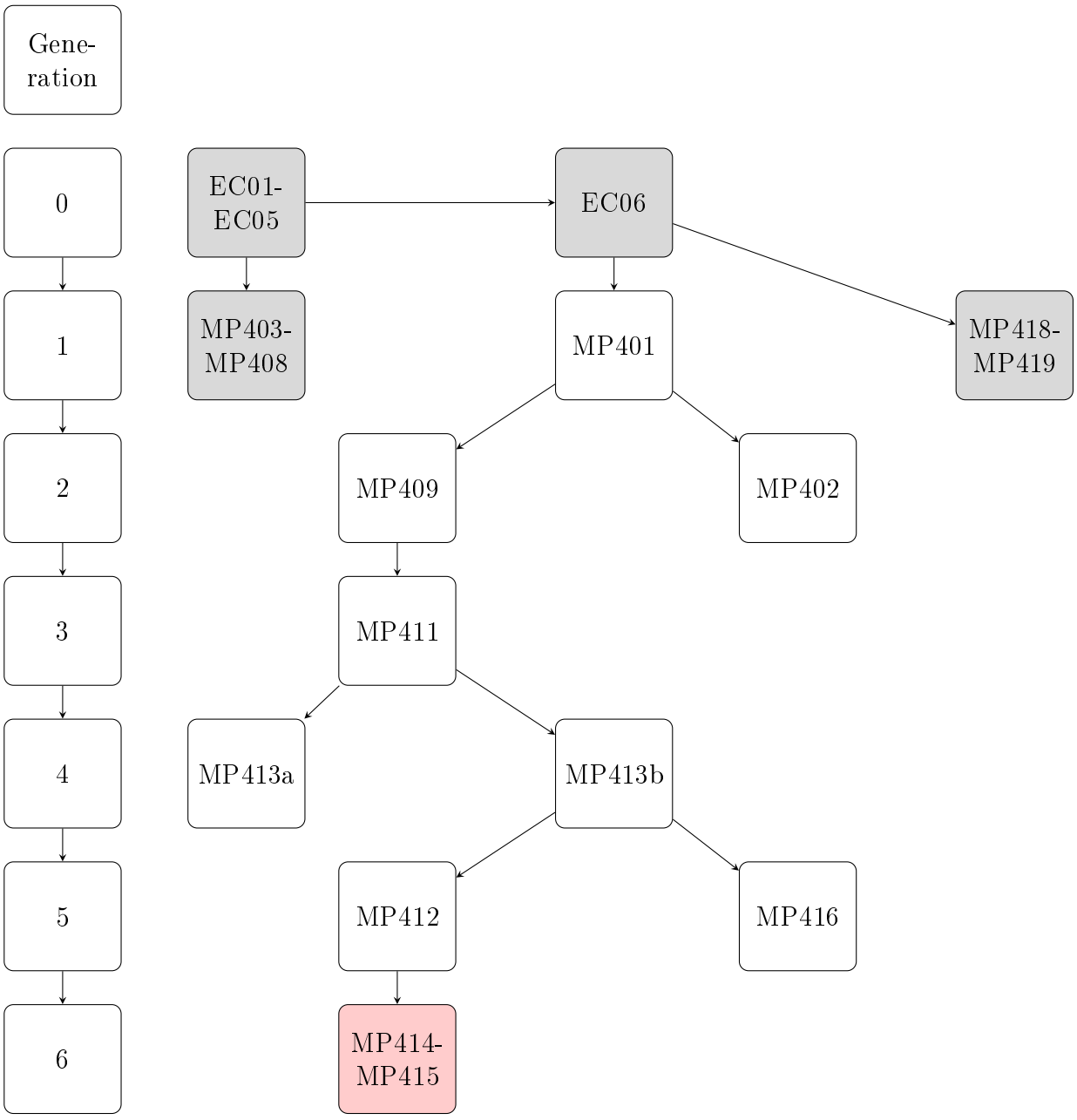

Figure 8.11: Genealogy of experiments. Gray: Bridgman or DTA experiments. White: Czochralski experiments. Red: failed Czochralski experiments.

iment. The names of the experiments follow the order, in which the prereactions were performed, not the order of the Czochralski experiments. The red boxes indicate a Czochralski growth, that did not yield any of the target phase. The grey boxes indicate all the other experiments: The Eu excess flux experiments from the previous work of Eunhyung Cho [5], the external flux growth experiments MP403-MP408 described in section 8.4.1 (the subsection concerning the external fluxes), featuring Indium and tin, and the PdSi excess flux differential thermal analysis experiments MP418-MP419 described in section 8.4.1 (the subsection concerning the PdSi self flux).

	Gen	pulling velocity profile	Seeding temp/°C
MP401	1	4mm/h for 0.3mm, then 1mm/h	1270
MP402	2	0.9mm/h for 2mm, then 0.45mm/h	1130
MP409	2	0.9mm/h for 2.4mm, then 0.45mm/h	1270
MP411	3	begin 3mm/h, soon 2mm/h	1230
MP413a	4	6→13→3.5mm/h, 2mm to 1.6mm/h	1180
MP413b	4	3mm/h (2mm), 1.6 (1.5), 1 (2), 0.5 (3)	1160
MP412	5	10mm/h(1.5mm)→2 (3)→1 (2)	1150
MP416	5	1→1.6→2.4→1.2mm/h	1160
MP414	6	first try aborted, 3mm/h→1.6mm/h	1190
MP415	6	5mm/h (0.5mm)→3 (4)→2.5 (2.5)→1.8	1250
MP417	6	-	-

Table 8.5: Overview over the experimental parameters of the $EuPd_2Si_2$ Czochralski growth experiments [61].

Table 8.4 displays the parameters of the $EuPd_2Si_2$ Czochralski growth experiments, that already had to be set with the prereactions, this is, of course, the maximum temperature of the prereaction and the crucible material with focus on the actual prereaction, but also the chemical composition of the precursor and its initial mass. To the initial mass of the experiments, the only thing to be said is, that a too heavy melt might be problematic in terms of levitation. It might get contact to the cold crucible during the growth experiment, start crystallizing there and disrupt the directed growth process that way. In the beginning, large masses of up to 30 g initial total mass were used, also partly to cope with the large material losses due to the precursor sticking to the Graphite crucibles. When the losses dropped due to the change to Glassy Carbon prereaction crucibles, it showed, that 25 g might be too much for the experimental setup to handle, and 15 g was established as the new mass standard. This happened around experiment MP413: Experiments MP413a and MP413b were prereacted as a 25 g whole precursor, but since 25 g showed to be too heavy to handle in the ADL Czochralski setup, the precursor was divided and used for two experiments.

The coming about of the crucible materials, optimal prereaction temperature and especially composition ratio has been extensively discussed previously.
Table 8.5 on the other hand shows the additional parameters, that only influence the actual Czochralski growth experiment, i.e. the pulling velocity profile and the temperature, at which the growth was performed. As one can see for the experimental temperatures, they somewhat pile up around about 1160 °C, especially for the later generations four and five. This is just ever so slightly above the melting temperature, that has been found for $EuPd_2Si_2$ in various DTA experiments, just as the temperature was set to being just slightly above the melting temperature of the whole precursor, and hence these findings complement each other quite well. Both the failed growth attempts of generation six and the growth generations one to three show higher melting temperatures (except of MP402), and also, they in the end seem to show problems in certain aspects of growth quality, impacting the valence transition (clearly observable with the transition temperature) or the level of magnetic impurities.

8.5 Growth results of the Czochralski experiments

The Czochralski grown crystal bodies usually have a yield mass of somewhat below 10 g (e.g. MP401: 7.4 g, MP402: 9.8 g). This seems to be independent from the initial mass: the crystalline bodies from the later growth experiments with only 15 g of ingredients are of a similar size as the results from the earlier experiments with up to 30 g of ingredient mass, when the growth process starts destabilizing and is brought to its end. The remnant will solidify just in the given composition at the moment as flux remnant again.
The flux itself is not a single phase, but at least two phases, since one phase (or phase mixture), which is gray and shiny, is stable under air, but at least another phase segregates itself and starts degrading under air, leaving behind some yellow powder, that most probably is europium hydroxide. Later, in the structural analysis via powder X-ray diffractometry, some reflexes, that could not be assigned to the target phase, are identified with the stable flux phases, but the phases were not analyzed further. A candidate, that is sort of fitting for at least the reflexes that are showing up regularly, is Eu_3Pd_2 (data after [64]). Examples for the PXRD analysis are given in fig. 8.13. In MP401 and MP413a measurements, additional to the target phase (and a flux phase in the MP413a measurement), copper is observed, since the samples were measured on a copper sample holder. With MP415, one of the two failed attempts is also shown, to show the patterns of the competing phases, EuPdSi (data after [56]) and the flux, which is so far unmatched with other known phases.
The crystalline bodies, where they are consisting of the target phase in the most part, show the golden colour that has been stated for the $EuPd_2Si_2$ phase, but rather dull than shiny due to the crust forming on the crystalline body during the growth process. When the crystals are cleaved, they are shiny at the cleavage site. (Even cleaving one of the crystals under argon atmosphere proves the colour to be genuine, and not itself product of e.g. a thin oxidation film on the surface of the sample).
The crystalline bodies, that resulted from the Czochralski growth experiments, are shown in fig. 8.12. In the cases of MP401 and MP413b, also the flux body is

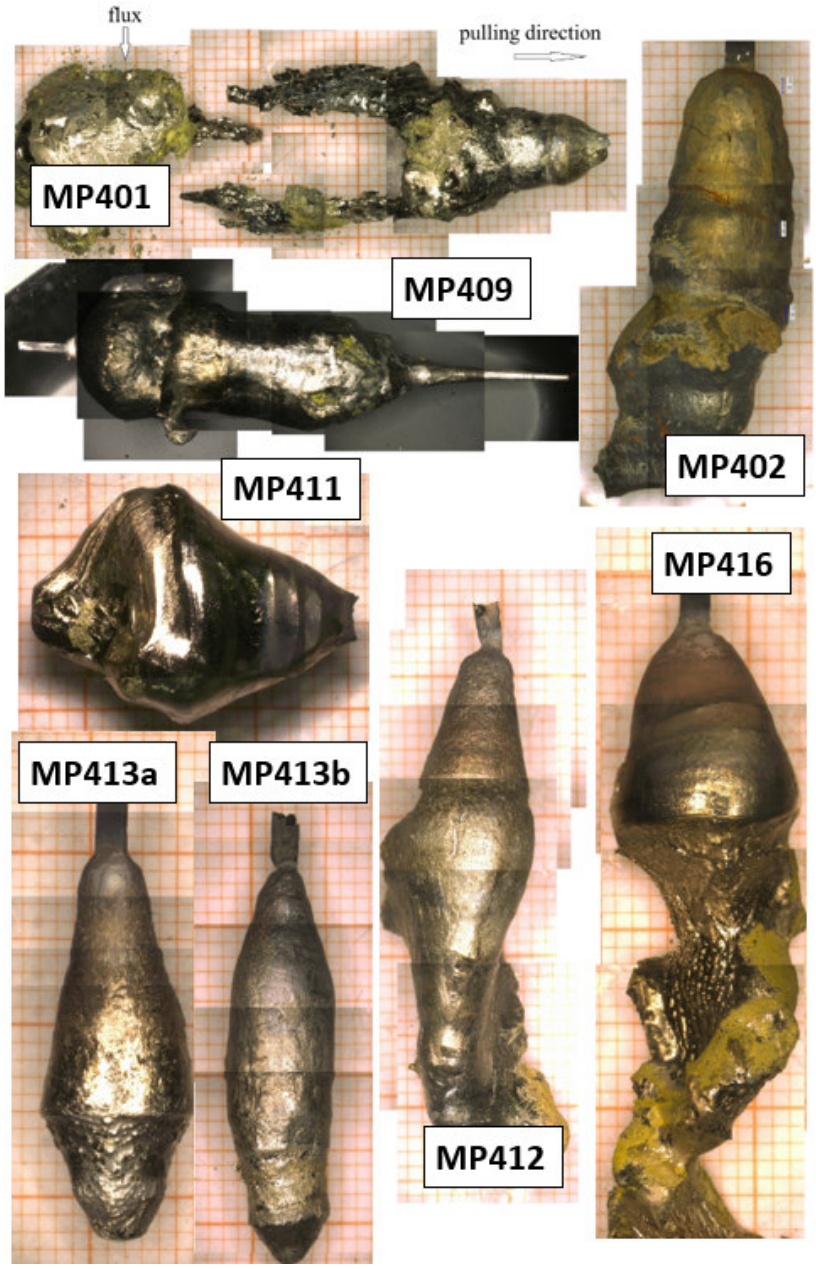

Figure 8.12: Collage of the $EuPd_2Si_2$ growth experiment results, together with [61].

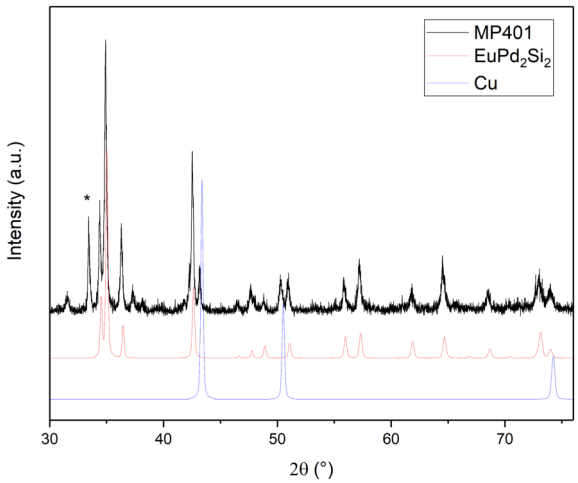

(a) MP401

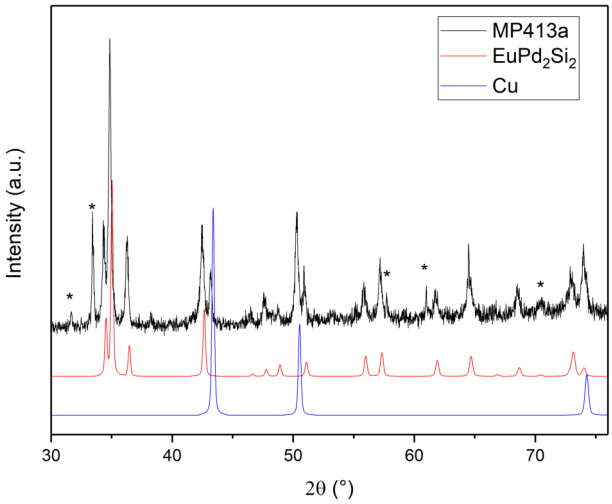

(b) MP413a

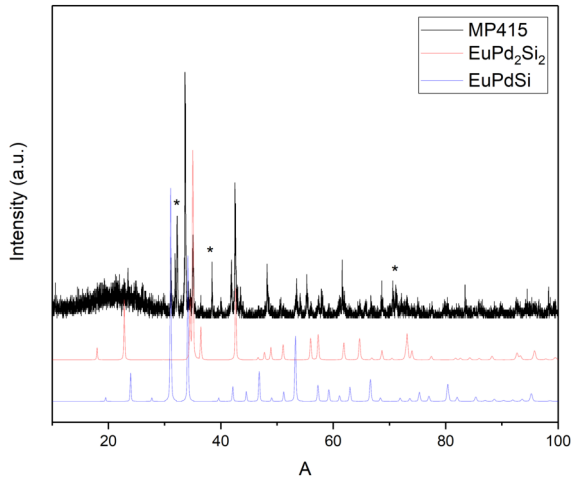

(c) MP415

Figure 8.13: Room temperature PXRD results of the $EuPd_2Si_2$ growth experiments for phase confirmation.

shown beside the main body. But also, analyses, that will be discussed in detail later on in this chapter, suggested, that in the main body, that was pulled out of the melt, only the first seven to ten millimeters of sample (in growth direction) promise to be useable for physical characterization of the system [60]. Over the whole length of the grown crystal, the incorporation of flux and impurities in between the target phase is steadily increasing, and usually, the amount of flux incorporated is so large by that said margin, one cannot assume to actually probe the undisturbed target phase's properties anymore.
From these first seven to ten millimeters, samples can be extracted in a suitable form, e.g. seeding pieces for further growth experiments, that are as long as possible, but with a crossection of ideally smaller than $1 \times 1\,\mathrm{mm}^2$, or, for most other applications, platelets orientated in an arbitrary main crystal direction (surface normal 001 to obtain cleavable platelets for surface probe experiments as ARPES), or even bulky orientated pieces, e.g. for sound transport experiments. Orientated linear cuts to obtain samples in the desired shapes can be made with a spark eroding machine, applying a voltage between a running wire and the sample, eroding the sample with many small, local spark-overs. The correct orientation for the cut is to be obtained by Laue diffractometry in advance.

8.5.1 Crystallinity

Although, if ideal conditions were met, a Czochralski experiment would yield a sole single crystal, a crystalline body consisting of only one crystal grain, that is a direct extension of the grain offered to the melt as a seed, the real growth experiments do not yield single crystals, but a variety of crystal grains attached to each other, that differ in size and orientation. Misorientations between two distinguishable grains can be as small als only few degrees, but in some cases, two grains may even grow in two totally different crystallographic directions.

Laue diffractometry

Crystal grain multiplicity as well as crystal orientation can be determined via Laue diffractometry. Fig. 8.14 shows on the example of an $EuPd_2Si_2$ grain, that is oriented towards the c-direction, how to read a Laue pattern in terms of symmetry. Multiple grains will express in superimposing patterns (from spot doubling to completely distinct patterns).
As an illustration of how different crystal grains are arranged in a crystal body resulting from a relatively successful growth experiment, fig. 8.15 shows a Laue mapping of a crossection of the growth result from the experiment MP413a. The crystal body has been cut in half in a manner, that the surface normal of the resulting surface is the 100 crystalline direction. From the upper part, a larger portion of the sample has been removed in order to prepare other measurements. The missing portion is sketched on the map, as well as the position, where the seed was sitting during the growth process. 23 spots were marked on the cut surface and investigated with Laue diffractometry. A representation of the results is sketched on the map. Each point investigated with Laue diffractometry is represented by a symbol (line, triangle or circle). If the symbol is a line, the line is orientated along the c-axis (001 direction) of the crystal. If the line is blue, this means, that the surface normal is, as preorientated, the 100 direction of the

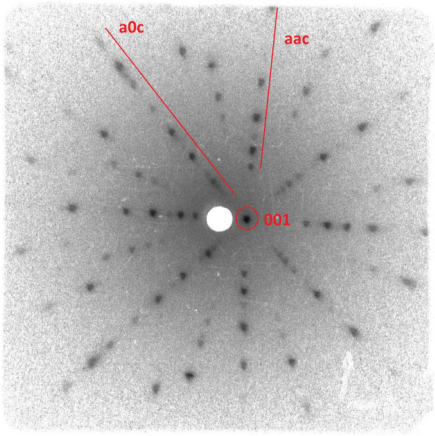

Figure 8.14: Laue example, indicating the most important Laue features: the fourfold rotational symmetric point in the center, belonging to the crystallographic plane set (001), and the eight main garlands of reflexes, belonging to other plane sets - shifting towards (100) or (001) garlands (here called a0c) reaching closer to the center than the garlands shifting towards (110), here called aac.

crystal; for red lines, the surface normal is the 110 direction. The triangles refer to a grain orientation where the 001 direction is tilted out of the plane of observation. The black circles indicate that the Laue pattern recorded was insufficient for analysis. The colour depth refers to the multiplicity of the structure: a very light symbol indicates a single detected grain, while a dark symbol indicates a multiplicity of grains within a slim window of small misorientation of only few degrees (spot doubling, tripling etc).

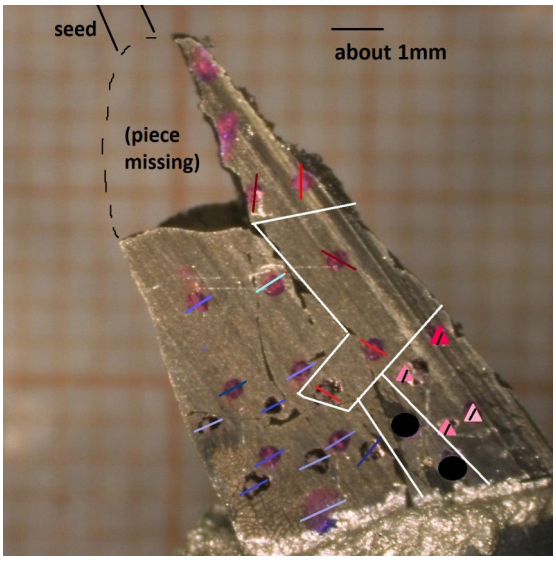

Figure 8.15: Laue mapping of a crossection through the MP413a sample body

Note, that there are four major regions of orientation (on the map schematically divided by white lines): one large area on one side of the sample, where the direction looked upon is the 100 direction, as is the growth direction; on the other

side of the sample two areas, where the direction looked upon is the 110 direction, but with a significantly different orientation regarding the 001 direction, and one area, where the 001 direction is tilted away from the cut surface. Within these main areas of orientation, many smaller grains with slightly different orientations appear and orientation even may shift slightly over the course of the area.
As this instance shows, the samples of $EuPd_2Si_2$ grown in the Czochralski setup are far from being single crystalline. When samples or seeding pieces are being prepared, the orientation for cuts has to be determined locally, and cuts should follow the boundaries of the larger areas of main orientations. Since smaller grain boundaries with a misorientation in the range of less than a degree are found on many Laue patterns recorded, many grains' characteristical length scales probably are in the order of magnitude of the size of the Laue beam spot diameter, which is about 0.5 mm.
Nonetheless, over the generation, the quality of the crystals, i.e. especially the size of the grains, seems to have improved. A short gallery, showing representative examples for Laue patterns from the different samples, all recorded with the 001 spot being the most distinguishable spot of the pattern. It is distinguished by being the center of a fourfold rotational symmetry of the pattern around the point, resembling the tetragonal fourfold rotational symmetry around the c-axis.

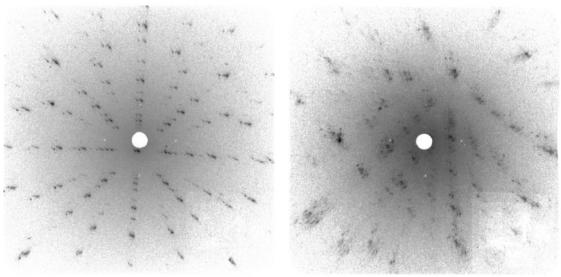

(a) MP401, extracted piece (b) MP402, cut through sample

Figure 8.16: representative Laue patterns for cut surfaces in MP401 and MP402.

Fig. 8.16 shows Laue patterns from the first two generations. The pattern from generation one (MP401, 8.16a) is an extracted piece, that was a candidate to be given away for investigations. Although this was eventually not the case, this vouches for the sample to be one of the best from that sample in terms of crystallinity. The spots are confined, but multiple patterns can be identified.
The pattern representing generation two (MP402, 8.16b) is just from an arbitrary cut through the sample; hence, with a certain time investment, better samples might have been found, but over all, the multiple patterns with broadly smeared spots are representative for this sample, and this generation even.
For a seed, one would ensure, that the crystal quality over at least the first few millimeters is as good as possible, which shows in confined Laue spots, and also, that only one grain is offered at the seeding end, if possible. (Fig. 8.17a, the spot at the seeding end, shows only one confined pattern, while spots in the middle of the seed (8.17b) may also show a lower multiplicity of confined patterns.) Over the length of the seeding piece, the orientation can still shift incrementally (see

the migration of the 001 central spot between the two images in fig. 8.17).

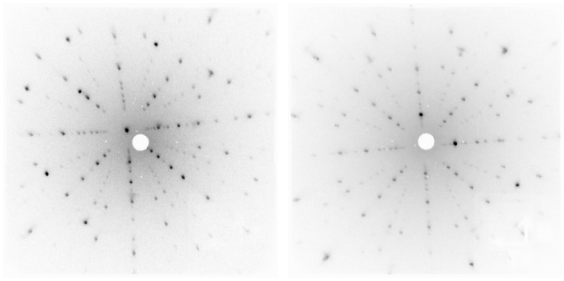

(a) (b)

Figure 8.17: Laue patterns at two locations on the seed extracted from MP401, lengthwise: (a) close to the seeding end of the seed, (b) in the middle of the seed

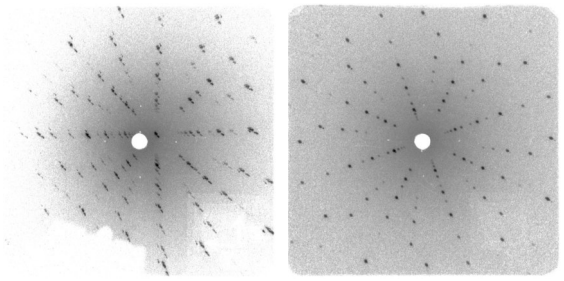

(a) (b)

Figure 8.18: Laue patterns on two pieces of MP411 (a) multiple grains, (b) single crystalline

Later on in the growth iteration process, both the crystallinity (indicated by the confinement of the Laue spots) and the grain size (indicated by how easy and likely it is to actually find an area, which produces only a single reflex pattern) increased especially in the main part, only a few millimeters below the seeding piece. In MP411 (this is: generation 3) already, the Laue spots of pieces extracted from the top of the grown crystal body were quite confined (fig. 8.18). Even though mostly the grains still remained smaller than the Laue beam spot diameter (and hence, mostly superimposing patterns were recorded as in fig. 8.18a), there were some larger areas, and even facets on the surface of the crystal, that showed only a single orientation (fig. 8.18b).
From generation four on, the crystallinity and distribution of grains had improved so far that a standard for about $(2 \times 2)\,\mathrm{mm}^2$-pieces could be established, that they were only commissioned to give them to groups requesting samples for investigations on the $EuPd_2Si_2$ system, if they show a good Laue spot confinement and only a single Laue pattern, as shown in fig. 8.19.

Electron Backscattering Diffraction

Using the Laue method, only a coarse grid of measurement points can be applied to consruct a grain map of a sample. This is (a) costly in terms of time, and

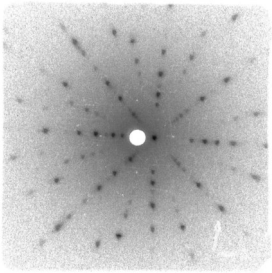

Figure 8.19: Laue pattern on a piece of MP413a, representative for the Laue patterns of pieces commissioned to give them to other groups for deeper investigations

(b) does not yield satisfactory information on the nature of the grain boundaries in the Czochralski grown crystal body; of whether there are distinct mesoscopic grains, or whether the orientation of the grains is structured by defects of the crystal lattice and small-angle grain boundaries.
To gain information on this question, at the Geoscience institute of the Goethe University, an EBSD mapping of one slice of the MP411 sample (that represented the whole length of the sample's usable part, find a photo in fig. 8.24a) was conducted by Jolien Linckens. The EBSD measurement in itself was made within several hours, and the results were highly informative; yet, adding an EBSD detector to the REM of the crystals and materials lab would rather prove impractical, since the sample preparation requires polishing techniques that are out of range of our own technical capacities. For the measurements at the Geoscience institute, the sample preparation was conducted by the Geoscience institute's polishing workshop.
The results of the EBSD measurement are shown in fig. 8.20. With EBSD, both the absolute orientation and the relative orientation of the slice of MP411 could be determined. The mapping of the absolute orientation shows, that in the later samples, even over the course of areas with several millimeters edge length, misorientations don't arise from misalinged mesoscopic grains with genuinely distinguishable orientation, which expresses in an over all monochromatic colour scheme (fig. 8.20a) - on a colour scale between the main crystallographic axes, the whole sample is orientated with a surface normal direction (001).
A mapping of the relative orientation on the other hand revealed, that there still exists misorientation, that does, however, not organize along grain boundaries, separating grains with clearly distinct orientations, but rather expresses in an incremental shift of the orientation. Over the length of 3 mm the crystallographic orientation with respect to a fixed reference point alters up to 3 °, but in a manner, that neighboured spots of investigation show almost no difference, but a continuous trend can be observed (fig. 8.20b).
This incremental misorientation trend hints towards small-angle grain boundaries, emerging from layering defects in the crystal structure, that occur on a very regular base and such shift the orientation of a sample. The maximum misalignment was observed to be about 3 ° in this sample, afterwards bouncing back towards smaller misalignment again. Alas, the EBSD measurement did not yield information about the misorientation coordinates, but only yielded information

about the absolute value of the misorientation.

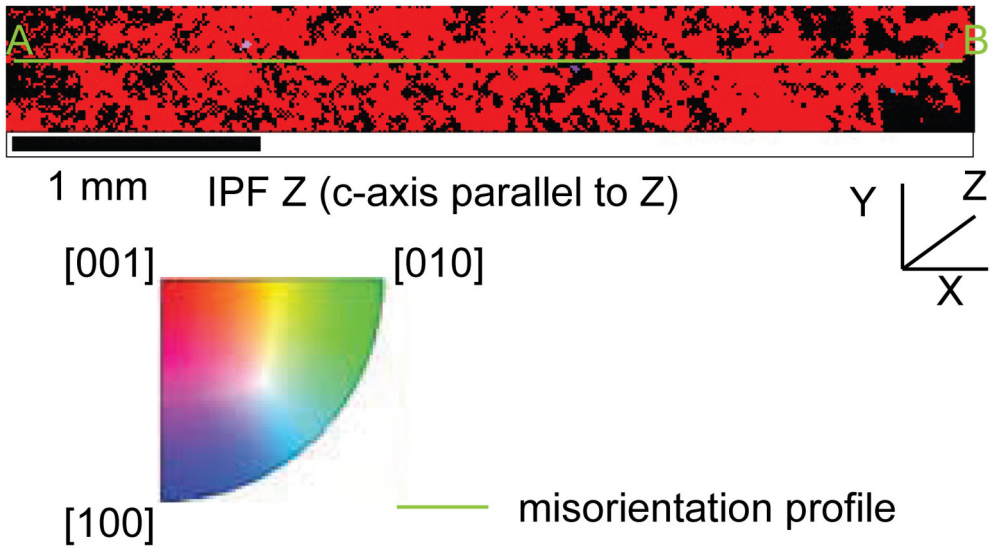

(a) absolute orientation profile

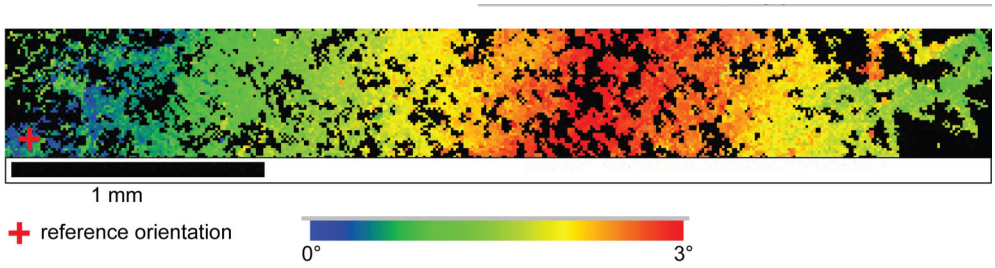

(b) relative orientation profile

Figure 8.20: EBSD patterns for MP411 [65].

With the results from the EBSD method, I can argue, that (although the initial separation of more than one grain growing is still an issue), the crystal quality of e.g. extracted sample pieces, that can be commissioned to other groups' investigations, is rather limited by microscopic defects and small-angle misalignments within the local environment of a grain, than by finding a mesoscopically well orientated grain large enough to prepare samples from. Since the incremental shifting can alter the orientation of the crystal lattice by up to 1 ° over the course of half a millimeter (which is the diameter of the Laue beam), this effect might explain not only the shifting of orientation, as in fig. 8.17, but also the pattern multiplication, as for example in fig. 8.18a.

8.6 Chemical composition

When talking about the 122 structural type, one might assume, that the composition of the associated compounds would show the certain composition of 20 At-% of the rare earth metal and 40 At-% each of the other two ingredients. For most ternary compounds of the 122 structural type, this is actually not the

case. Rather, the composition might deviate from the 122 ideal ratio, and even might spread out into a homogenity region, in which a composition can vary without changing the compound's structure (see section 4.1.4). The composition acquired then depends on the path taken in the phase diagram during the growth process.
The chemical composition of the polished samples was assessed using the EDX detector of a REM in unstandardized measurements. Handwaving gauge of the measurements can be argued by comparing the EDX results of a certain slice of MP411 (the very slice, that also was investigated with EBSD) to a standardized WDX measurement conducted at the Geoscience institute by Heidi Höfer.

8.6.1 Homogenity region

In figure 8.21 (and zoomed in to the region of interest in figure 8.22), representative compositional data for several of the growth experiments conducted are introduced to the ternary phase diagram of the Eu-Pd-Si system (as stated in figure 8.3, also with the used data quoted there).
The larger blue dots (that are found only in fig. 8.21, not in the zoom in) refer to the different starting compositions used for the growth experiments: on the Eu-rich side, the points at 1.2:2:2, 1.4:2:2, 1.45:2:2 and 1.5:2:2 represent the Czochralski experimental starting compositions; and on the PdSi-rich side, the DTA experiments with the starting compositions 1:4:4 and 1:3:3 are found.
The smaller, coloured points then represent the compositional data of a certain experiment, e.g. turquoise the DTA experiment with the sample number MP419. A legend of the colourcode is given in the graphics. What we can see here, is, that each experiment produces two piles of contiguous points (i.e. two areas with clearly distinctive compositions). One of them is in all cases confirmed by powder X-ray diffraction experiments to refer to a phase with the 122 structure, which is the target phase. The yellowish ellipsoid borders all the data points that refer to the target phase. The other pile of data points refers to the remaining flux and are bordered by the gray ellipsoids. (No further analysis will be given to the flux remnants, other than that there exist two regions, in which the flux will end up being found: one, if Eu excess flux is used, and one, if PdSi excess flux is used.)
Between the sets of data points of the target phase, two sorts of distinctions can be observed:

1. Within one "pile" of data points, refering to the target phase of one experiment, there usually is a range, in which the composition can vary - the "pile" has a finite extent. This variation range usually is quite small and allows the composition to vary in the order of magnitude of one At-%. The variations are not reducable to a mere effect of measurement error bars. For the DTA experiments, this range is notably larger; maybe due to the faster growth process, which might enhance both misplacements and microscopic flux inclusions, that might also affect the measurement.

2. Between different "piles" of data points, the center, or the mean composition, around which the data points arrange, also varies. This expresses the effect of the unique experimental conditions for every growth attempt, when for example looking at the difference between the red, blue and purple

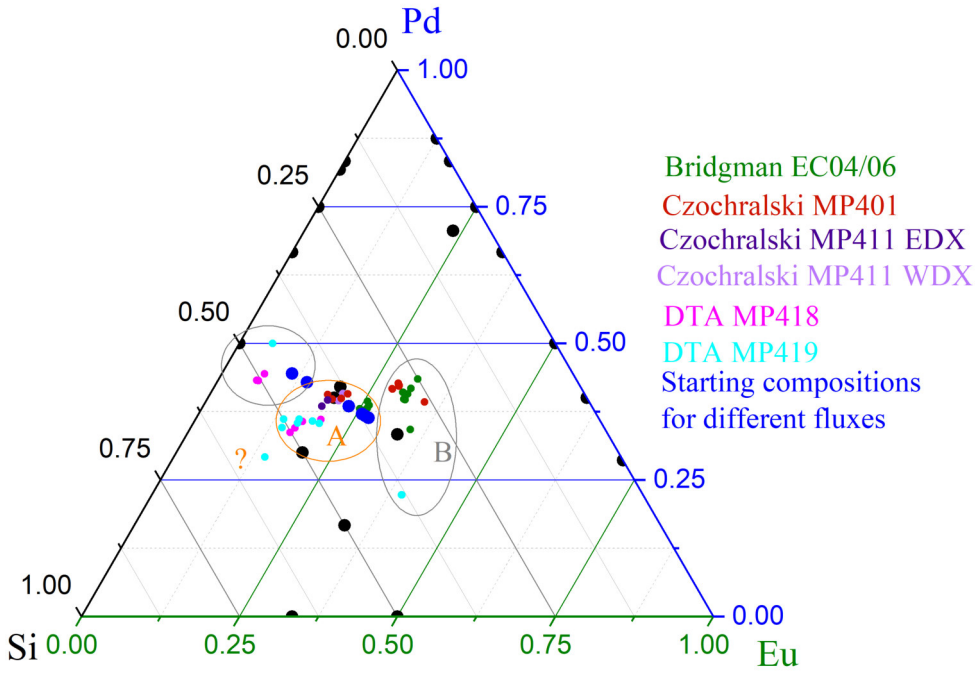

Figure 8.21: Ternary phase diagram of Eu-Pd-Si, as stated in fig. 8.3. Additional blue dots indicate starting compositions for growth attempts (for the Czochralski experiments, the Eu-rich setups are relevant; the PdSi-rich setups only were realized in DTA experiments). Smaller coloured dots indicate compositions of phases found in the analysis of the experiments, colour legend is in the graphics.

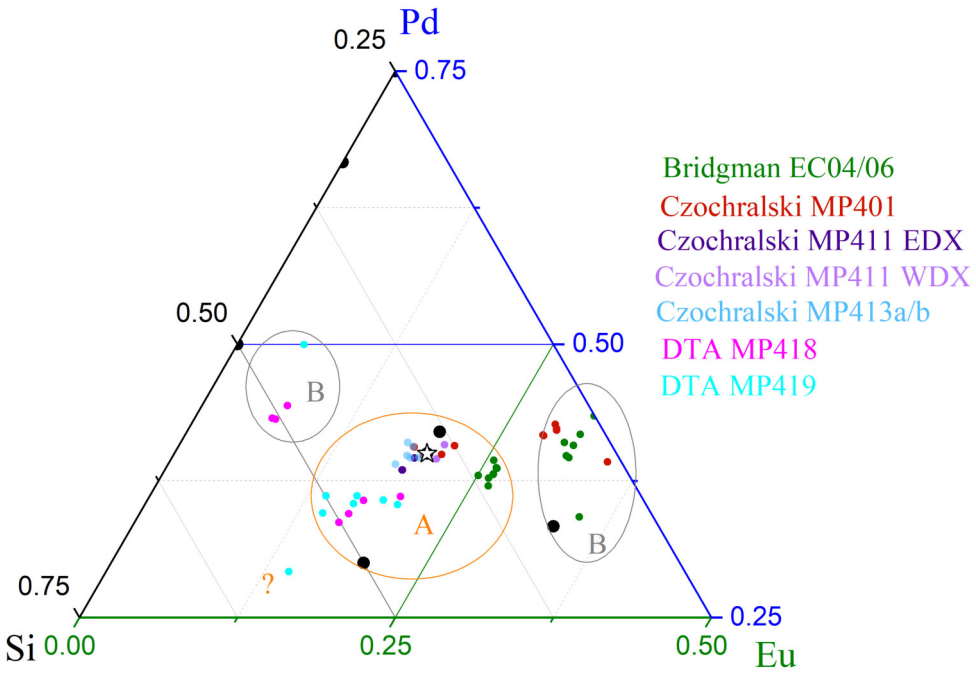

Figure 8.22: Ternary phase diagram of Eu-Pd-Si, as stated in fig. 8.3, zoomed in on the homogenity region. Smaller coloured dots indicate compositions of phases found in the analysis of the experiments, colour legend is in the graphics. White star: target phase.

dots (which are the Czochralski experiments MP401, MP411 and MP413). But also, comparing the different starting compositions brings about, that europium excess experiments (EC04/06, MP401, MP411, MP413) behave significantly different from PdSi excess experiments (MP418, MP419).

While the first distinction already proves the phase to exist in a certain homogenity region, from the second distinction it is suggested, that this homogenity region covers a large portion of the phase diagram. The minimum extent of the homogenity region is defined by the extremal compositions found, that range from (rounded to half percents) 18:41:41 and 22:40.5:37.5 (for the Czochralski europium excess experiments) to 26:37.5:36.5 (for the europium excess flux growths by Eunhyung Cho), and to 16.5:33.5:50 (for the PdSi excess flux growths). The yellowish ellipsoid in figs. 8.21 and 8.22 is placed somewhat arbitrarily - the form of the homogenity region of course does not need to be an ellipsoid, and the exact extent is unknown so far - but it gives an estimation of how large the homogenity region of the phase probably is. Even, besides the target phase $EuPd_2Si_2$ and the once reported $EuPd_{2.1}Si_{1.9}$ [53], that has the same structure and obviously needs to be included into the region, the $Eu_2Pd_3Si_5$, that Silvia Seiro told me about [58] might likely fall into the homogenity region of the phase. Although a realization of $Eu_2Pd_3Si_5$ in the $U_2Co_3Si_5$ structure is known [66], it is still possible, that it actually is a very off-stochiometric realization of the 122 phase. Also, one point is marked with a yellow questionmark, because it is unclear whether this is a third flux composition or even still belonging to the target phase area.
Although it is normal, that phases exist in a certain homogenity range, the homogenity area of $EuPd_2Si_2$ does not only seem to be exceptionally large. Also, as I will discuss in section 8.7 later, the composition has a large impact on the physical properties of the sample. Specifically, the valence transition is very sensitive to changes in the composition. With different compositions, the whole range of reported transition temperatures (from 140 K [10] to 170 K [6]) could be reproduced.

8.6.2 Trends

The composition of the sample pieces seems to not change arbitrarily, but, at least over a certain lengthscale, following a certain pattern, or a trend. These compositional trends were found to be realized in different directions regarding growth - along the growth axis or perpendicular to the growth axis. In all cases of both classes, this is the (100) direction, simply because the samples are usually prepared in a way that they have a (001) surface normal.
Usually, the europium content of the sample remains constant, while an interchange happens between the palladium content and the silicon content of a sample, linearly shifting from a large silicon excess and a slight palladium deficit (as observed in our own EDX setup), towards unbuilding the composition gap between these two elements. This trend can happen over short distances with steep composition gradients as in fig. 8.25a (one percent over 3 mm), or over longer distances, as in fig. 8.23b (half a percent over 8 mm), but in every piece examined, it is to be observed in one way or the other, that exactly this trend - constant europium content, while palladium and silicon content change linearly in spatial scale - is realized. That the europium content is stable, while the

palladium-silicon-ratio changes, might hint towards change of sites between the two elements.
The trends observed are shown in the figures 8.23 (a and b) and 8.25 (a and b). For all plots except 8.23b, every point plotted is averaged over three EDX measurements in close proximity. The WDX data direct data points without averaging.
The piece from MP401 (trend in fig. 8.23a) is taken from some milimeters below

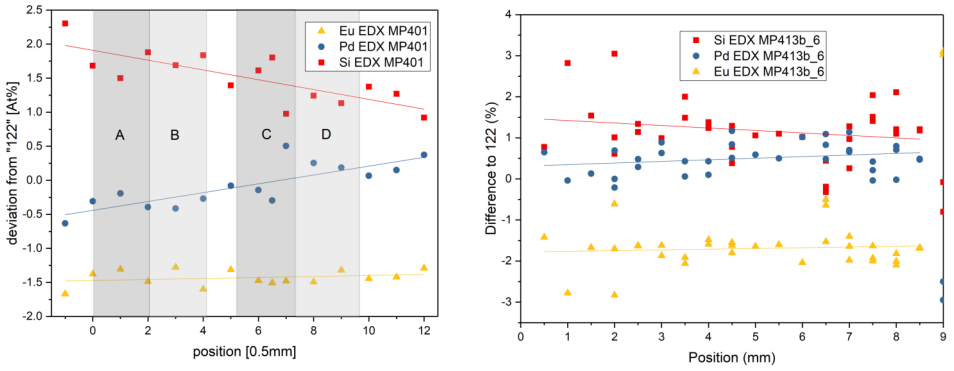

(a) (b)

Figure 8.23: EDX mapping of a composition trend (a) in a piece from MP401, (b) in a piece from MP413b

the seed of MP401 and was investigated along the growth direction. It shows a change of composition of about one percent over 6 mm. This was the right length-scale to investigate the influence of composition differences (even in proximity in terms of the phase diagram) on the valence transition. Hence, in section 8.7, I will show how AC electric resistance and specific heat were observed on different sections of the piece, proving the influence even of small composition changes on the valence transitions temperature. (Therefore, the labels A, B, C and D are added to the plot. They indicate the sections for AC transport measurements.)
A deeper investigation of the nature of this trends in composition has also been conducted on the slice of MP411, which was prepared for thorough structural characterization, and on which the EBSD measurements shown before were performed. The piece is shown in fig. 8.24a, as it is bound in a special resin tablet, the edges covered with a conducting glue on silver base. The narrow end on the right is from directly below the seed, while the cut edge on the left is perpendicular to the growth direction. The whole piece has a length of about 7 mm, thus representing about the whole usable part of the growth.
On this piece, three lines were defined, on which points were investigated both with the unstandardized EDX option of the Krellner group, and a standardized WDX probe in the Geoscience institute, with the help of Heidi Höfer. With this double checking measurement, I planned not only to actually confirm the existence and quantity of the composition trends, but also check on the systematic errors induced by our own missing standardization. One of the lines has been defined along the growth direction (line 1), the other two lines have been defined radial through the crystal body perpendicular to the growth direction, one of them about 2 mm below the seed (line 3) and one of them about 5 mm below the

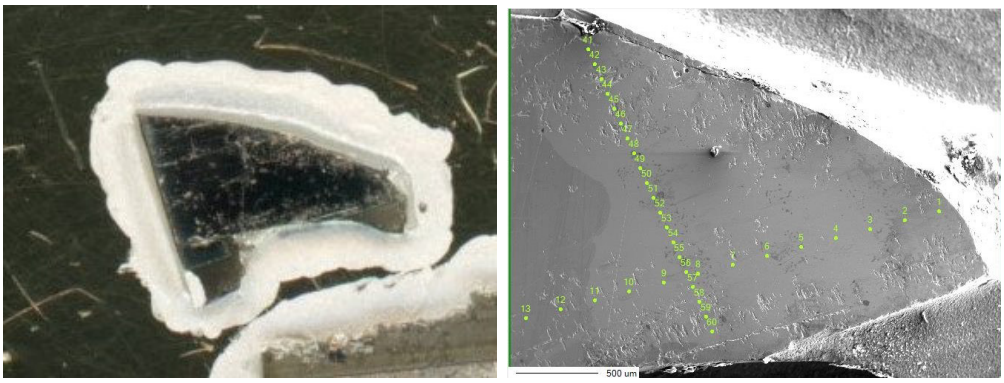

(a) (b)

Figure 8.24: (a) MP411 sample piece prepared for WDX measurements, comparing EDX measurements and EBSD measurements; (b) MP411 WDX measurement lines: line 1 along growth direction (points 1 etc), line 3 perpendicular to growth direction (points 41-60). Comparing EDX measurements done roughly at the same spots. WDX data and photos by Heidi Höfer [67].

seed (line 2). Fig. 8.24b shows the points defined on the upper part of line 1 and on line 3 for the WDX measurements.
The comparative examination of the composition along line 3 with EDX and WDX (as displayed in fig. 8.25a) yields different new information:

1. The trends observed using the Geoscience institute's WDX probe are qualitatively and differentially very similar to the trends observed using our own EDX option. In a sense of rational estimation, they can held to be the same. The difference between the WDX and the EDX results comes down to a constant offset on the measurements of +2 At-% europium, +1 At-% palladium and -3 At-% Silicium. This offset showed also in the comparison along the two other lines and can be expected to represent the systematic errors of the EDX option, dominated by the lacking of standardization of the measurement. Whenever EDX measurements are discussed, this offset is to be added. To not generate too much confusion about the measurement results, the EDX results, especially in section 8.6.1, when discussing the homogenity region, are discussed as they are collected, without gauging them with this offset discovered here.

2. The trend along line 3 looks qualitatively just as the trends discovered in the previous pieces (fig. 8.23), but it is different in an unexpected way: the previous trends were observed along the growth direction. This trend whatsoever evolves radial in the grown piece and thus perpendicular to the growth direction. While a trend in growth direction can be commonly explained via distribution coefficients and material depletion at the growth interface, a trend perpendicular to this direction has other implications, that complicate the explanation of the effect. A possible explanation would be, that the growth boundary is curved, but then, gaining a linear radial composition trend would require a very stable and uniform growth process.

Along line 1 (which is the growth direction, shown in fig. 8.25b), we do not find a monotonous trend anymore (which one would expect, for example, when the composition was mainly dominated by elemental transport in the melt and by elemental depletion at the growth boundary), but the ratio of palladium and Silicium first increasing, then back decreasing closer to equal ratio. Both this trend and the trend along line 3 advocate for that there should be another reason to how the composition trends come about, other than unfitting distribution coefficients. It is noteworthy, that the composition trend along the growth direction evolves with a rate comparable to the rate the misorientation evolves, as it has been measured with EBSD (see fig. 8.20), with a total scope of 2-2.5 mm of monotonous development before inverting the trend direction.

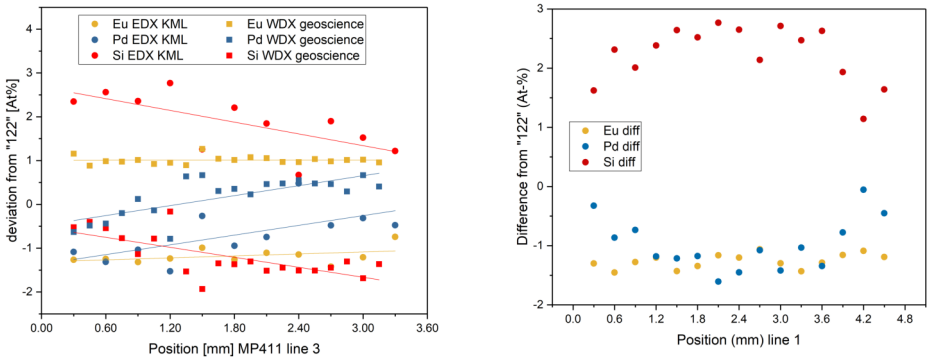

(a) (b)

Figure 8.25: (a) EDX and WDX mapping of a composition trend on line 3 on the MP411 piece, perpendicular to growth direction, about 2 mm below seed; (b) EDX mapping of a composition trend on line 1 on the MP411 piece, along growth direction. WDX data [67].

The existence of trends in composition were also confirmed by Michael Merz from KIT in Karlsruhe, who performed Single Crystal X-Ray Diffraction on different pieces extracted from a piece from MP413b, in which a trend was proposed by our investigations. Progressing along the length of the piece, Michael found a decreasing level of silicon atoms occupying the palladium space (from 3% to 1%) [68], which verifies the existence of a trend, and also gives a concrete idea how the shifts come about - they seem to be, in fact, silicon occupations of the palladium crystallographic places.
Now, since the crystallinity has been enhanced to a level that is hopefully sufficient for most of the investigations that are planned on the $EuPd_2Si_2$ system, and still, the system does not only exist within a certain homogenity region, but also shifts its composition continuously within each sample, this makes it exceptionally hard to tell about the general quality of the samples. The influence of the composition on the valence transition, its location temperaturewise, its positioning in the generalized phase diagram for Eu-compounds (fig. 6.1) and maybe even the order is to be characterized.

8.7 Physical characterization

In this section, the physical characterization of the valence transition in $EuPd_2Si_2$ is described. A basic description of the transition's features can be made with the basic methods of the crystals and materials lab - measuring specific heat, electrical resistance and magnetization in the PPMS and investigating the temperature dependence of the lattice parameters with the cooling option of the D500 X-ray diffractometer
The primary characterization of the valence transition in the $EuPd_2Si_2$ system had to deal with a list of initial questions and problems (that have already been discussed in section 8.2):

- It was known, that the lattice parameter a exhibits an enormous change of its value of $1-2\,\%$ [7, 54], and this posed the problem of finding an appropriate method for a temperaturewise location of the valence transition.
- In the literature, there were initial incoherences on the reported transition temperature of the valence transition. The powder data reported by Wada [10] indicated the inflection point of the valence transition at 140 K and differed from the single crystal data reported by Onuki [6], indicating a transition temperature of almost 170 K. A stage target was to explain this incoherence.
- Also, a characterization on which of this two behaviours is reducable to the desirable, ideally undisturbed properties of the system, so in everyday terms, what a "good sample" is.
- The order of the phase transition was to be characterized: whether the valence transition is of first order (on the white line in the generalized phase diagram in fig. 6.1), or of second order (at the critical endpoint or beyond in the crossover area).

In the following, the measurements taken for physical characterization are described not chronologically, but ordered by the measurement method, since every method has their own problems to deal with and their own conclusions. Each method contributes to the solution of the enumerated problems, and in the end, the insights of the single methods will be combined to give an answer to the posed questions.

ACT measurements

Using the dynamic alloy model, as it is described in section 10.2.2 later in this work after Medvedev [69], one would expect to see the valence transition in the electrical resistivity as a broad hump, which reaches his maximum at the point, at which there is maximum disorder in the sample concerning the evolution of 2+ and 3+ europium states, if described semiclassical, which is at the maximal slope of the curve describing the mean valence, i.e. at the inflection point.
The advantage of an AC resistivity measurement is, that the sample can be probed locally. A larger piece of sample can be divided into different sections, which can be invistigated without actually dissecting the sample into different pieces. This

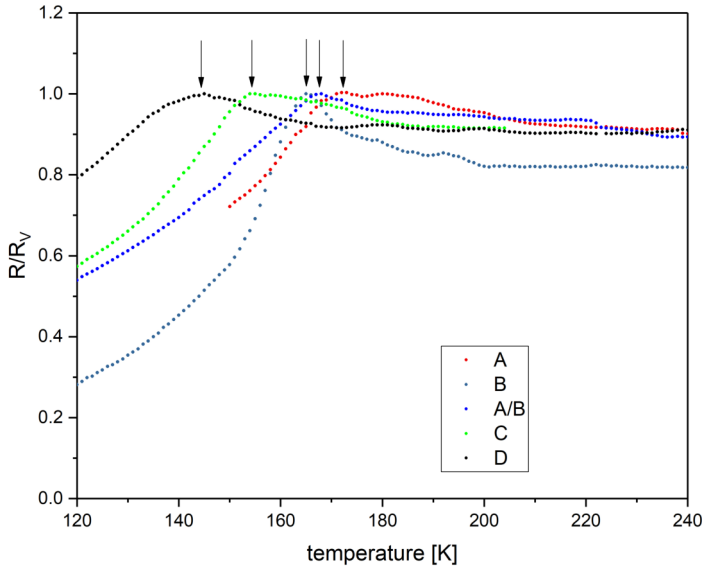

Figure 8.26: $EuPd_2Si_2$ ACT measurements on the MP401 piece, the composition of which is shown in fig. 8.23a. Electrical resistivity measurements were conducted on sections of the sample corresponding to the shaded areas with the names A, B, C and D, as well as an overlapping section between sections A and B. R_V is short for $R(T = T_V)$.

is why this method was the first to be employed for systematic investigation of the influence of composition shifts on the valence transition on the piece of MP401, whose composition was investigated earlier. In the composition of this piece, as shown in fig. 8.23a, a compositional trend was found, shifting the palladium and silicon content by about 2 At-% over a scope of 6 mm. In this figure, four intervals were marked and named with the labels A, B, C and D. This intervals are the length intervals, on which the resistivity measurement was conducted. Also, an interval overlapping with interval A and interval B was measured, and hence the measurement called A/B. The results, normalized to the maximum value of the hump, are shown in fig. 8.26.
The temperature, at which the resistivity curve reaches its maximal value, is identified with the transition temperature, which is also defined by the inflection point of the valence curve. The value of this temperature shifts strongly over the different intervals (and hence, in the range of 2 At-% composition difference). The range of the shifts in the ACT measurements reaches from 140 K (section D) up to 170 K (section A) proportionally to the composition shift and gives a first hint on why the literature values for the valence transition temperature varied so strongly. Still, the effect only appears that strong on the surface of the samples, for which the ACT method is highly sensitive. Later, when probing the bulk properties of the sample via heat capacity measurements, the shift in temperature was found to be about 4 K instead of 40 K, as described later. The surface properties seem to exaggerate the influence of the composition on the sample's properties vastly. Hence, the ACT method was rarely employed later on in the project.
Also, a practical problem when employing the ACT method is the large response of the lattice parameter a to the valence state of the europium atoms. The change

of about 1-2 % in the lattice parameter over quite a small temperature interval strains the contacts, which I simply glued on to the sample with a conducting silver glue, often so strongly, that the contacts are teared apart from the sample during the cooling process. This problem makes the method only applicable in *c* direction, which is much more stable.

Specific heat measurements

Just as in the dynamic alloy model for the resistivity, the slope of the changing intermediate valence can also be expexted to produce an anomaly in the specific heat. The anomaly arises from the statistical entropy of transitioning from one state into another continuously in a two state system. The two states of the system are the two intermediate valence states the europium ions can show, $Eu^{2+\delta}$ and $Eu^{3-\delta'}$. The entropy added is highest, when the valence curve reaches the inflection point. This leads to a peak in the specific heat.
The contrast between the literature values for the valence transition's temperature is very obvious in the specific heat data. The reports of Wada [10] and Onuki [6] (as shown in fig. 8.27) show the difference between the samples to an extreme, with the maxima differing by about 30 K in position, as already described in section 8.2. All findings will later be compared to these two different literature values.

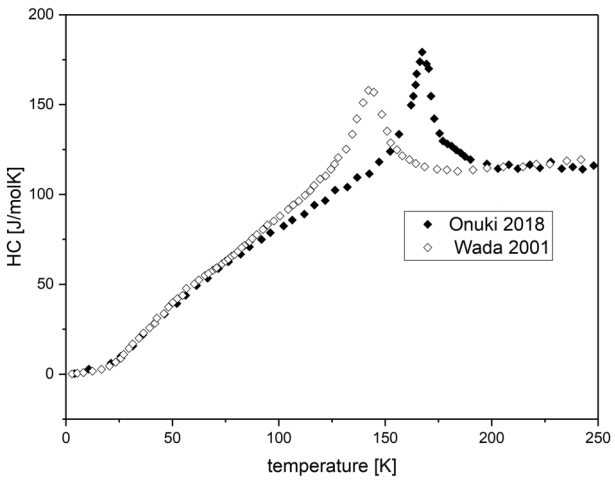

Figure 8.27: $EuPd_2Si_2$ HC literature values by Wada [10] (powder data) and Onuki [6] (single crystalline data), making obvious the disparity between the different samples.

Opposing to the surface sensitive ACT resistivity method described before, the specific heat probes the material's bulk properties. A comparative investigation on the piece of MP401, that has been used for the resistivity measurements previously, proves how much actually is about the large effect of the composition on the valence transition temperature observed in the resistivity. The piece is dissected into three minor pieces named o1, o2 and o3 in fig. 8.28, where o1 corresponds to the top part of the piece (around sections A and B), o3 to the bottom part of the piece (around sections C and D), and o2 being from the middle part.

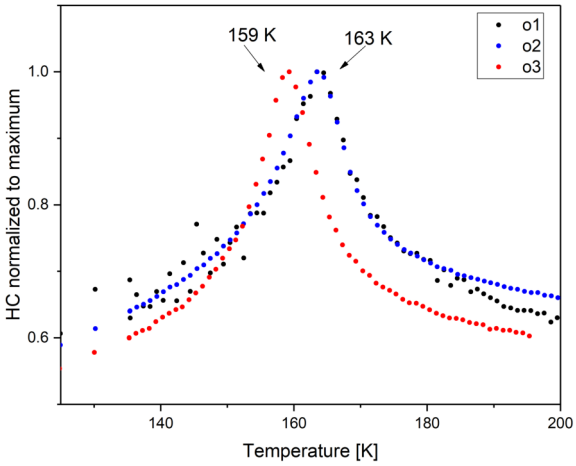

Figure 8.28: $EuPd_2Si_2$ HC measurements on the MP401 piece, the composition of which is shown in fig. 8.23a, and the resistivity of which has been determined in the previous section.

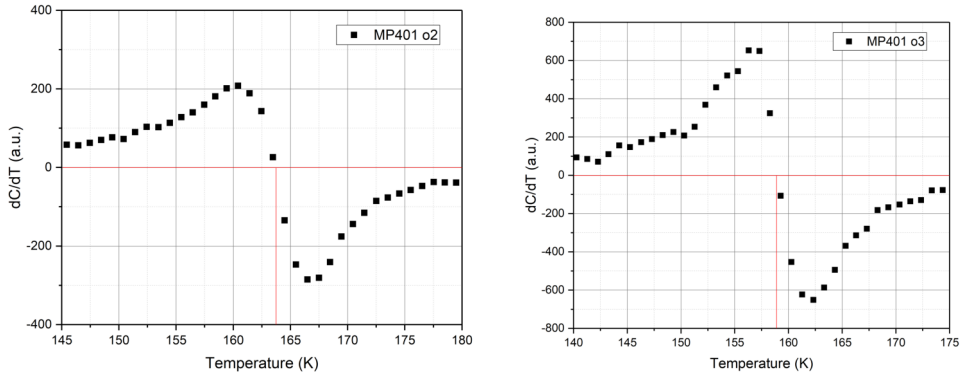

(a) (b)

Figure 8.29: derivatives of the specific heat data were used to determine the transition temperatures given in fig. 8.28 for sample o2 (a) and o3 (b). The red lines determine the maximum of the anomaly.

The measurements on the MP401 pieces (fig. 8.28, determination of the transition temperature by finding of the roots of the specific heat data's pointwise derivative in fig. 8.29) proved the differences in valence transition temperature to be caused by compositional differences between the samples, since the two pieces o1 and o3 showed valence transition temperatures differing by about 4 K, with the composition disparity of some At-% silicon and palladium as the main decisive property between the two samples. But also, it proved the scope of the effect, as it has been suggested by the resitivity measurements, is exaggerated. The scope of 30 K (instead of the 4 K found with the specific heat measurements) seems to be a mere surface effect. In the bulk, the effect is much smaller, yet clearly noticable.
Going from the single piece of MP401 to the bigger picture, the total scope of the compositional effects on the valence transition can be estimated. Comparing between measurements of different samples shows not only differences in the transition temperature, that most likely are dominated by the composition, but also in the shape of the peaks.

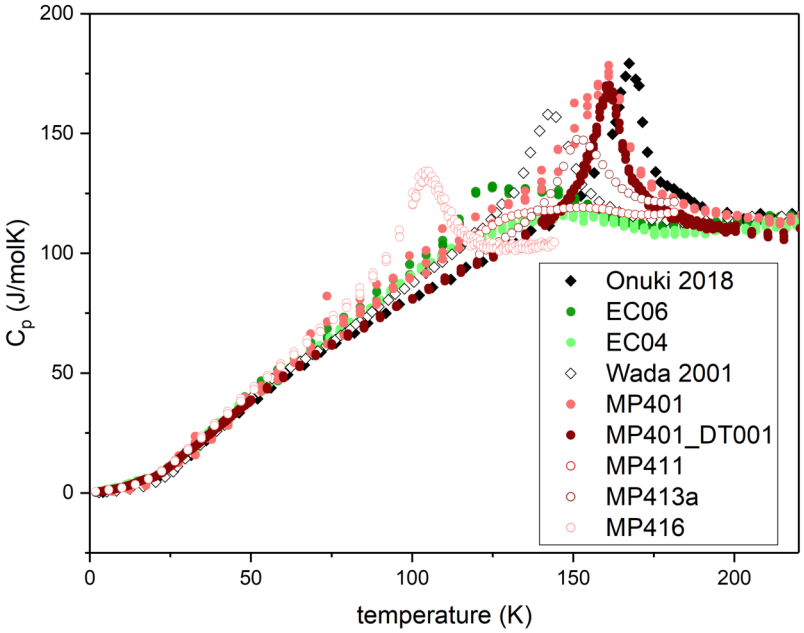

Figure 8.30: $EuPd_2Si_2$ HC measurements on various pieces from different samples, comparative plot. Data EC04 and EC06 [5].

In fig. 8.30, representative specific heat measurements for the investigated samples are put in relation to the literature specific heat data. While in the first Czochralski sample, MP401, the transition temperature is close to the value reported by Onuki [6] with a sharp anomaly, the flux samples EC04 and EC06 as well as the Czochralski sample are temperaturewise resembling the data reported by Wada [10], while not showing a sharp peak (as the literature data did), but only a broad hump. In later samples MP413a and MP413b (which are distinct growth experiments!), a peak shape as the MP413a data in this figure could be stabilized, with transition temperatures slightly above 150 K. While I later concluded, that the transition temperature is not an indicator for sample quality

in itself, samples of the later iterations MP413a and MP413b show this transition temperature consistently. So, this might be the most reproducible condition of the system. An outlier is the later iteration MP416, which yields, without any doping, a much lower phase transition temperature of only about 115 K, not broadened too much, but still with a sharply defined feature. With the amount of investigation put in, so far no reason for the deviations could be pinned down. Although the position of the specific heat anomaly is not taken as a sign of sample quality, the shape of the peak probably is meaningful. In samples with the broad hump instead of the distinct feature, not only the transition temperature is harder to determine (and to argue for to actually coincide with a maximum, that is not substantially higher than the surroundings). Fig. 8.31b shows, that in these samples, the maximum is smeared and in the vincinity, the specific heat shows a constant and near-zero development. (Fig. 8.31a shows a data set of an immaculate sample for comparison.) Not only this, also this broadening of the specific heat feature is found in samples (the flux samples and a certain Czochralski sample I will refer on again later, when discussing the magnetization measurements) with an extraordinarily high amount of foreign phase inclusions. Hence, it seems to be a sign for exceptionally impure samples.

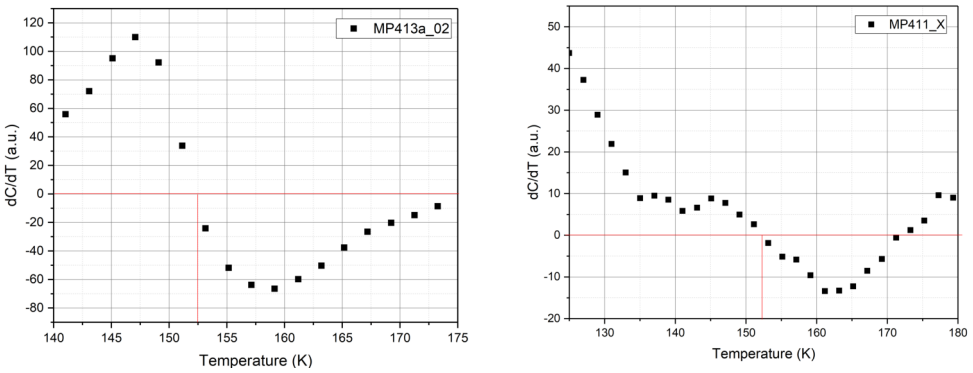

(a) (b)

Figure 8.31: derivatives of the specific heat data of representative measurements on samples MP413a (a) and MP411 (b). The red lines determine the maximum of the anomaly.

To determine the order of the phase transition, on several pieces from several samples (with transitions at several different temperatures), large heating pulse measurements were conducted, where the heating pulse given to the sample was about 15 K instead of 1% of the given temperature. This measurements aimed at whether there is latent heat to be observed. Latent heat would show itself as plateaus of constant sample temperature while heating the sample in the raw data before fitting the heat pulse function. In none of the samples, a latent heat plateau could be measured. Hence, it follows, that all the samples' transitions are located beyond the critical endpoint of the first order phase transition in the crossover region.
Also, with measurements on the first sample, MP401, I attempted to determine the critical exponent α, utilizing equation (2.5). Since a power law is to be found, the fit is carried out on a double logarithmic scale. In order to be able to carry

out a double logarithmic fit, for small values of the reduced temperature t, many data points on a small temperature interval are required. Soon it turned out, that our heat pulse method, which integrates over a certain temperature range und thus needs a certain distance between the data points, is incapable of reaching the required data point density. The fit would converge towards two different values for α as stable solutions, without possibility to decide, which of the solutions is correct. Hence, the analysis of the critical exponents is left to the lab group of professor Lang, who specialized on thermal expansion measurements, which are better endowed to determine the critical exponents.
With the specific heat measurements, I could locate the $EuPd_2Si_2$ system better in the generalized Eu-phase diagram, and found it to be located in the crossover area beyond the critical endpoint of the first order valence transition, since no latent heat connected to a first order phase transition has been visible whatsoever. Also, the puzzle of the inconsistent literature data has been solved with the specific heat measurements linking the bulk valence properties to the chemical composition of the sample. The transition temperature at ambient pressure could be located to be in a range between 140 K and 170 K, depending on the chemical composition. Quantitative investigations of the anomaly's shape via approaching the critical exponent α failed due to lacking data, so here only a qualitative connection between the "sharpness" of the feature and the amount of foreign phase inclusions could be argued for.

Low temperature PXRD measurements

With temperature dependent powder X-ray diffractometry, the lattice anomaly of the $EuPd_2Si_2$ system, that companies the valence transition due to the difference in size between the Eu^{2+} and Eu^{3+} ions, can be investigated. Low temperature PXRD measurements were conducted on samples of three samples: EC06, MP401 and MP413a. The samples were measured in a temperature range between 50 K and 300 K, with a data density of one measurement every 15 K or 10 K, condensing up to one measurement every 5 K in the interval close to the transition temperature. Measurements were conducted with the cooling option of the Siemens D500 diffractometer. As a measurement interval, the range 30° to 76° was chosen. The temperature dependent lattice parameters were extracted from the datasets by refinement using GSAS II [46].
The first thing to state is, that any of the measurements could be refined as a system of the very same I4/mmm symmetry group. No breaking of spatial symmetry occured at any temperature.
With a first glance at the data, simply plotted with the measured intensity against the diffraction angle, qualitatively the lattice parameter anomaly is confirmed already by all three datasets. In fig.s 8.32, 8.33a and 8.33b, it can clearly be seen, that all the reflexes with a non-zero proportion in either of the a-directions undergo a strong shift to larger diffraction angles (i.e. smaller lattice parameters; see the arrows in fig. 8.32), while the reflex (004), with only contributions via the c-direction, remains at its position, indicating no or only minor changes in the c-parameter. Hence, the lattice parameter anomaly is restricted to the a-parameter. This will later be quantified by refinement of the powder diffraction data. Also, the contraction of the lattice shows to take place in an extended in-

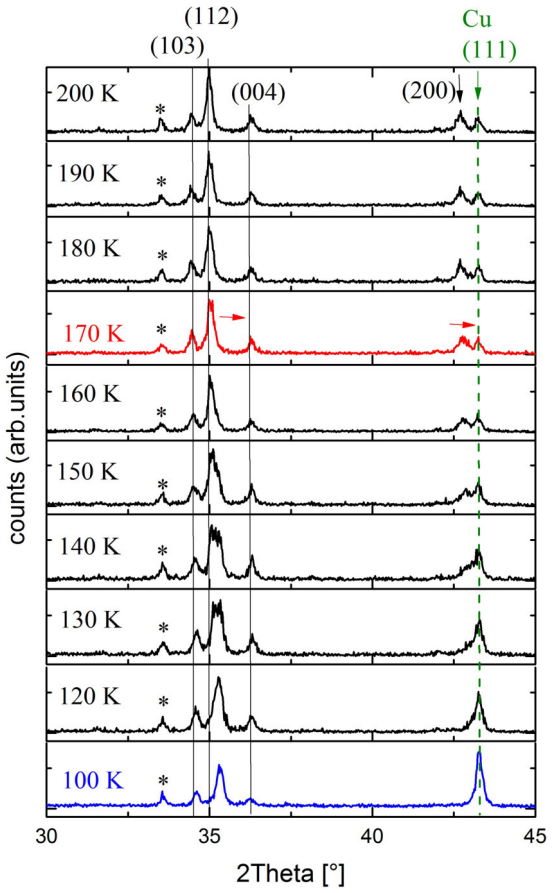

Figure 8.32: EC06 low temperature PXRD, measurements by me, plot by Kristin Kliemt. The black lines mark the positions of the (103), (112) and (004) reflexes at 200 K for comparison with their position at lower temperatures. The green line indicates the copper-(111) reflex. Da reflex assigned with an asterisk does not belong to the target phase or copper.

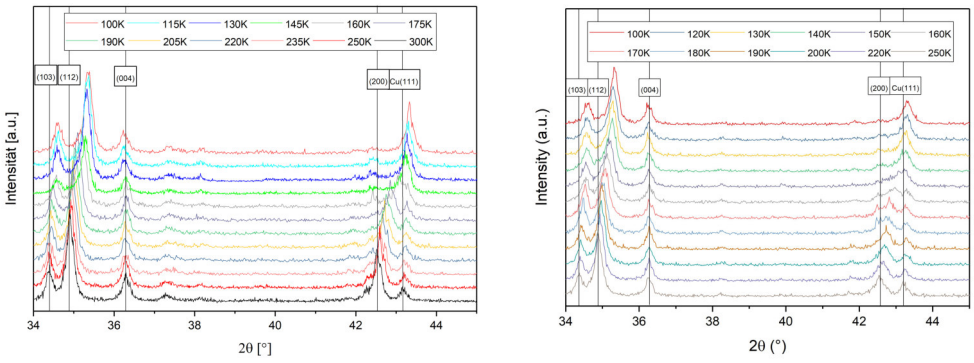

Figure 8.33: low temperature PXRD (a) MP401 (b) MP413a. The black lines mark the positions of the (103), (112), (004) and (200) reflexes at 300 K for comparison with their position at lower temperatures, and the copper-(111) reflex for reference.

terval around the previously determined transition temperatures for each sample respectively.
The comparison between EC06 and the other two samples MP401 and MP413a leaves us with a seeming contradiction, that will later be solved though: While in the Czochralski samples MP401 and MP413a, the reflexes seem to shift gradually to higher angles, thus indicating a smooth contraction of the lattice parameter a, the flux sample EC06 displays a broadening of the reflexes connected to the a-parameter around the transition temperature, which would indicate, that some transitioning effects other than a smooth contraction would be going on.

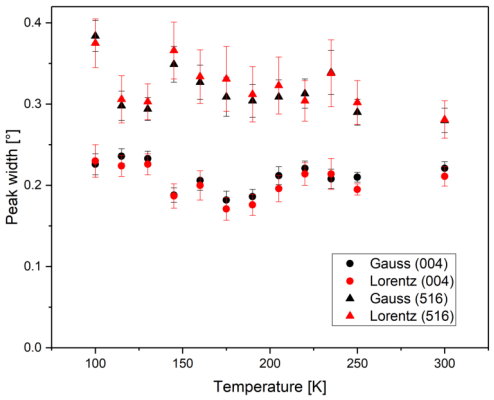

Figure 8.34: Analysis of the temperature dependent peak width of the (004) reflex and the (516) reflex in the diffractograms of MP401, using Gaussian and Lorentzian fit functions.

To shed light on whether the contraction is actually smooth and the flux sample has some other effects going on, or whether the reflex broadening is a real effect, that is not visible to the mere eyesight in the Czochralski samples due to less distinctive manifestation, two reflexes of MP401's diffractograms were fitted with gaussian and lorentzian fit functions to determine the temperature dependent width of the reflexes (full width half maximum). The aim was to see, whether around the transition temperature (which is about 160 K for MP401) a broadening of the reflexes occurs. The fit was conducted between 100 K and 250 K, and is shown in fig. 8.34. No significant broadening of the reflexes connected to the a-parameter could be detected. In fact, the peak width seems do behave alike for reflexes connected to a or not connected to a and remain somewhat constant.
From this I conclude, that the lattice contraction connected to the valence transition is in fact smooth. The broadening of reflexes in the flux growth sample EC06 could be explained by assuming, that the flux grown sample was inhomogeneous to an extent, that lead to noticable alterations in the transition temperature for different parts of the sample. Hence, different parts of the sample undergo the phase transition at slightly different temperatures, which results in a superposition of different e.g. (200) reflexes, that shift at different temperatures. In a temperature interval, in which the main shifting is to be expected, this would lead to slightly offset reflexes adding up. The shape of the envelope would be a broadened reflex.
Now, from the refinement of the powder diffraction data of the different samples,

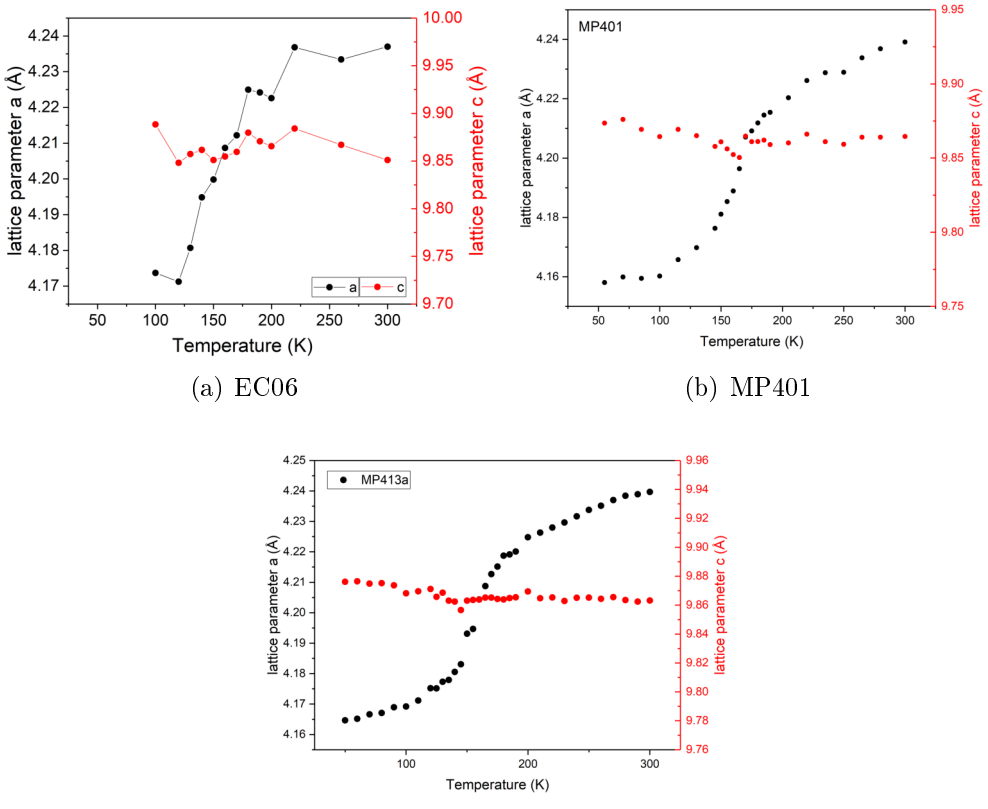

(a) EC06

(b) MP401

(c) MP413a

Figure 8.35: $EuPd_2Si_2$ temperature dependent lattice parameters, refined from the respective data for EC06, MP401 and MP413a. The scales are set in a fashion, that both display a share of about 2% of the respective lattice parameter's value (left scales: a, right scales: c), in order to visualize the proportions of the relative change of the lattice parameters.

quantitative statements on the lattice parameters a and c could be met. In fig. 8.35, the lattice parameter values are displayed temperature dependently, and set to scale in a way, that the scales of the graph resemble approximately the same share of the respective lattice parameter a or c. While the lattice parameter a undergoes a steep, s-shaped transition linked to the valence transition (which expresses the change in valence of the Eu ions, and hence the inflection point of this s-shaped curve coincides with the inflection point of the magnetization and the maxima of heat capacity and resistivity), the c-parameter remains almost constant.
If I define the contraction of the lattice parameters a_i ($a_i = a$,c) as:

$$\delta a_i = \frac{\Delta a_i}{a_i(T = T_{max})} = \frac{a_i(T = T_{max}) - a_i(T = T_{min})}{a_i(T = T_{max})} \tag{8.1}$$

the evaluations for the three samples investigated yield the results as shown in table 8.6. While the contraction of the a-parameter δa is in the order of magnitude of 1.5% to 2% for all three samples, the change in the c-parameter δc is well below 0.5%, and hence almost constant in comparison. The volume anomaly hence ranges between 2.5% and almost 4% for the three samples.

sample	δa	δc	$\delta V = 2\delta a + \delta c$
EC06	0.0149	-0.0038	0.0261
MP401	0.0191	-0.0009	0.0374
MP413a	0.0177	-0.0013	0.0341

Table 8.6: Lattice contraction in $EuPd_2Si_2$

Also, of course, since the lattice contraction is directly linked to the valence of the Eu ions, the shifting of transition temperatures between the different samples can also be seen in the diffractometry data, when the a-parameter evaluations for all three samples are compared directly, as done in fig.8.36 with the a/c ratio. As one sees, the lattice parameter ratio a/c grows apart for the three samples when approaching the transition temperatures and entering the range of the steep changes in the lattice parameter a, which is about 160 K for MP401, about 153 K for MP413a and about 140 K for EC06.
To sum up, with the temperature dependent PXRD, the lattice parameter anomaly could be confirmed to be about 1.5%-2% for the a-parameter, with the main part of the shifting happening between 100 K and 200 K, while the behaviour in the c-parameter is linear in temperature. The volume anomaly was determined as about 3.5%. The analysis of the reflex shape indicates a smooth and consistent shrinking of the lattice parameters, leading to no anomalies in the reflex width. Also, no change in the symmetry of the crystal lattice could be found. Over the whole course of temperature, the same symmetry group I4/mmm was assumed by the system. This is consistent with the classification of the Eu valence transition systems as a candidate for an isostructural elastic quantum phase transition (see sections 5.2.3 and 6.1).

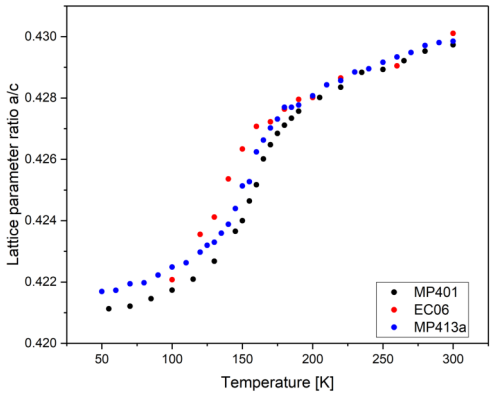

Figure 8.36: $EuPd_2Si_2$ low temperature PXRD a/c ratio comparison for EC06, MP401 and MP413a.

VSM measurements

The measurement of magnetization of $EuPd_2Si_2$ is of specific interest for several reasons:

1. Since the different states of the europium ions display different sorts of paramagnetic behaviour (Eu^{2+} being a Curie paramagnet, while Eu^{3+} being a Van Vleck paramagnet, see section 6.2), that hence respond differently to external magnetic fields (the Curie paramagnetism being much stronger than the Van Vleck contributions), via investigation of the mean magnetic moments in the sample, the valence state is directly represented.

2. Magnetization measurements allow for an estimation of the amount of foreign phases included into the crystal bodies matrix during the Czochralski growth process.

3. Also, with low external fields, magnetic transitions in the foreign phases can be resolved to identify the foreign phases, if needed.

4. A simple fit of a Curie and a Van Vleck function to the magnetization data could even reveal the quantity of the valence in the two different intermediate valent states. Since the Van Vleck contribution is notably smaller than the Curie contribution, even just a Curie fit can yield satisfactory results.

Especially because of bullet point number two, and because of the relative ease of conducting a VSM measurement, in the later phases of the project, when a standard for the crystallinity already was established, the magnetization became the standard method to determine the quality of samples, that were to be given away for investigations by other groups.
The shape of the magnetization curve of the $EuPd_2Si_2$ system is defined by the valence states of the europium ions, which are the carriers of strong, localized 4f magnetic moments in the system. Europium ions in the 2+ state contribute to the Curie paramagnetism of the system. Europium ions in the 3+ state don't, they only add a Van Vleck contribution. If we neglect this Van Vleck contribution, the magnetic behaviour is left to resemble a Curie paramagnet, but not with

the moment of an Eu^{2+} ion μ_{2+}, but with a reduced moment $(1-p)\mu_{2+}$, where p is the probability to find an europium ion in the Eu^{3+} state, dependent on the intermediate valence state. This very coarse method, of course, can only yield an estimate for the order of magnitude of the valence. In the high temperature phase (i.e. the valence state with a valence $2+\delta$), hence a reduced moment $(1-\delta)\mu_{2+}$ should dictate the magnetic behaviour; in the low temperature phase (i.e. the valence state with a valence $3-\delta'$) on the other hand, the reduced moment is expected to amount to $\delta'\mu_{2+}$. In the crossover, the magnetization (as well as the magnetic susceptibility, of course) will show an inflection point, that is identical with the inflection point of the curve directly describing the europium valence.

The magnetization data, measured with the VSM method, behaves just as

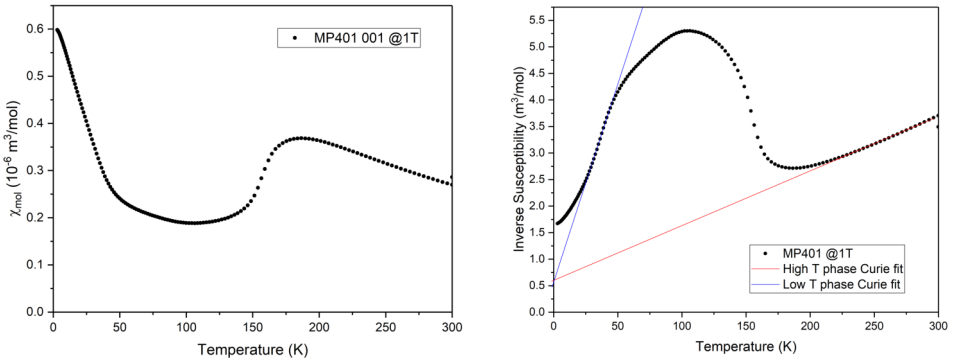

(a) magnetization (b) inverse magnetic susceptibility

Figure 8.37: $EuPd_2Si_2$ magnetization and inverse magnetic susceptibility curves from MP401 at an external field of 1 T. On the inverse magnetic susceptibility data, two Curie fits for the high temperature state (red) and the low temperature state (blue) were performed to find their valence.

predicted, with a notably higher response to external magnetic fields at higher temperatures due to the reduced valence, and then with a dropping response due to an increase in valence (see fig. 8.37a). By neglecting the Eu^{3+} contribution to the magnetic behaviour Curie fitting the parts of the magnetic susceptibility obeying an 1/T-law for both the high temperature and the low temperature phase (fig. 8.37b), an estimation for the effective magnetic moment could be found, and thereby also an estimation for the directly corresponding valence. From the fitting constant C, the effective moment for a single Eu ion could be calculated, choosing $n = 2N_A$, as for to operate with a full mol of the compound, since there are two europium ions in every unit cell, and comparing the effective moment to the theoretical moment of an Eu^{2+} ion, which is $9.74\,\mu_B$ (see section 6.2). The results are shown in table 8.7.

The results calculated from the MP401 magnetization data fit the literature values quite well for the high temperature (low valence) state, and at least qualiatatively yield a rational result for the low temperature (high valence) state. The latter does not contain the literature values by Sampathkumaran [7] in its error interval, deviating by about 0.1 valence. But note, that the errors given in the table of results only arise from the squared errors of the fit. Additional deviations are not only explicable, but even to be expected due to e.g. the magnetic response of the

phase	$1/C = \chi^{-1}/T$	μ_{eff}	valence
high temperature	$(10180 \pm 80)\,\frac{m^3}{mol \cdot K}$	$(5.60 \pm 0.50)\,\mu_B$	2.30 ± 0.06
low temperature	$(74200 \pm 800)\,\frac{m^3}{mol \cdot K}$	$(2.10 \pm 0.20)\,\mu_B$	2.74 ± 0.03

Table 8.7: valence of the low temperature and high temperature state of $EuPd_2Si_2$, gained from MP401 single crystalline magnetization data at 1 T external field. Calculated with the Curie constant as in section 3.2.1 and the Eu moment as in section 6.2.

foreign phase inclusions, that cannot be avoided, and that those error sources become more powerful reaching the low temperature regime, since they contribute at least a full Eu^{2+} magnetic moment to the paramagnetic response, and might even enter an ordered phase at some point. Hence, these results are quite good, especially since the used dataset has not been the dataset with the lowest possible share of foreign phase contributions.
Investigating on the nature of those foreign phases is also possible with the VSM magnetization data. Applying external fields of different strengths between 1 T and 0.01 T to the system shows, that the foreign phase contributions to the susceptibility get suppressed (see fig. 8.38a). This indicates, that the foreign phases to the large part order magnetically, which makes them dominant at low fields, since they reach their saturation; but at higher fields, they become more insignificant compared to the paramagnetic behaviour of the sample. When looking at

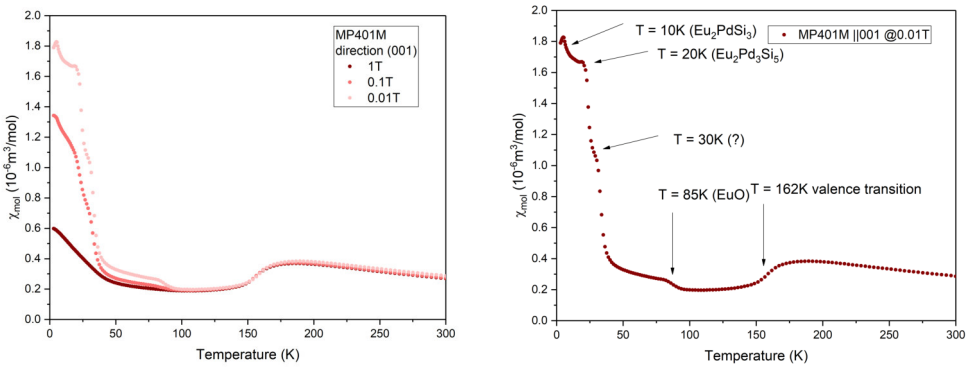

(a) (b)

Figure 8.38: Typology of the magnetic foreign phases included into the $EuPd_2Si_2$ matrix of MP401. (a) Suppression of the foreign phase contributions towards higher fields, (b) identification of magnetic ordering processes in a low field measurement.

the low field data of this series (fig. 8.38b) the foreign phase magnetic ordering transitions become distinguishable. For the MP401M sample piece, five transitions were found: beside the target valence transition at about 160 K, two of the transitions belong to unknown compounds, which I could not identify by knowing the possible constituents and the transition temperature of 30 K, but the other two transitions I could identify as the magnetic transitions in Eu_2PdSi_3 at 10 K

[70], as probably $Eu_2Pd_3Si_5$ at 20 K [66], and as EuO (enriched with a slight europium excess), transitioning at about 80 K [71], that probably formed from incorporated elementary europium upon air contact.
As it is easily seen in fig. 8.39, MP401, for which the foreign phases were analysed, is not representative for all of the samples grown with the Czochralski method. Contrary, each of the samples not only shows the valence transition at different temperatures (as shown in the specific heat section, and as also visible here), but also has a specific profile of foreign phases, differing at least in the amount of inclusions, and, of course, potentially also in the quality of phases (which was not investigated too closely).

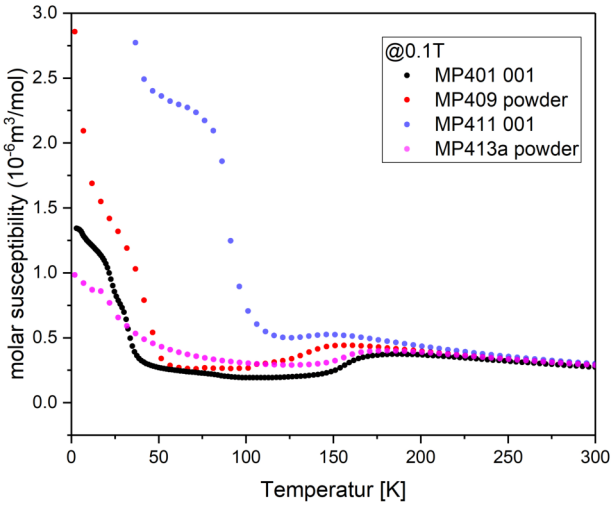

Figure 8.39: $EuPd_2Si_2$ susceptibility comparison between samples at 0.1 T. This is meant to only give an impression of the large varieties between samples, that is better quantified within one set of samples inf fig. 8.40.

While there does not need to be a necessary connection, the instances of the samples grown show, that the amount of inclusions seems to also influence the qualitative form of the valence transition. As foreshadowed in the specific heat section, the transition signal in the specific heat of MP411 was broad, and this coincides with a high amount of foreign phases, that the transition can not even be determined from the magnetization data. Also in the more usable samples MP401, MP413a and MP413b, a lower background in the magnetization data (and hence, lower flux inclusion level) coincides with sharper specific heat features. Hence the conclusion, that a low inclusion level is desirable for samples.
Also, internal comparisons inside a sample show, that the intuition is right, that the inclusion level is not constant for a specific sample, but evolves upon the growth process, starting at a low level, and surely increasing towards the later stages of the growth processes. Hence, the "best" samples (with the least flux inclusions) are to be found at the top of the grown crystalline bodies, while the sample quality decreases towards the lower parts.
Fig. 8.40 shows a comparative study of magnetization data of the samples MP413a and MP413b, just to give an impression, of how wide the flux inclusion

levels can spread inside a single sample (or two quite similar samples, in this case). With 20 measurements, a large variety of flux inclusion levels is covered, while the actual valence transition is apparently not spoiled by the increasing amount of flux inclusions and remains in place. In such a comparative chart, dependent

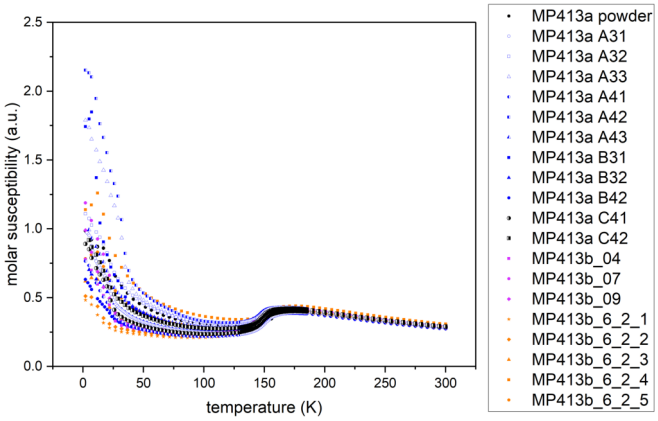

Figure 8.40: $EuPd_2Si_2$ susceptibility comparison in MP413a at 0.1 T. Lower foreign phase inclusions (lower upturns at low temperatures) tend to correspond to an extraction site closer to the seed, but this is not solely determinant.

on the purpose of the sample, an interval can be defined for the low temperature tail indicating the flux inclusions, to define, which samples are acceptable for a certain purpose and which are not[1]. Since there are only few external measurements performed on $EuPd_2Si_2$ samples, that were located in such a comparative chart, the definition of such an interval is, by now, still a little bit from the top of the head, but with the experiences, that will be gathered with the samples given away so far, one will be able to hermeneutically redefine the boundaries of the acceptable interval.

Virgin cooling and aging processes

Not only do the samples of the $EuPd_2Si_2$ system strong crystallographic reaction to external stimuli as temperature. Some share of these reactions is even plastic. As prominently seen, when just cooling a sample down below the transition temperature in the PPMS cryostate, the large contractive response of the lattice parameter a to temperature compromises the structural integrity of the samples, intensifying and reenforcing already existing cracks in the sample, as well as probably producing new cracks. This can incapacitate samples for certain sorts of investigations, that depend on a single structurally intact crystal grain, e.g. sound transport measurements, or depending on an intact surface, as electric transport measurements.
Additional to this virgin cooling effect, that may plastically crack up the samples, also repeated temperature iterations on a sample have proven to exhibit

[1] In the reference paper by Onuki *et al*, magnetization data were cut below 100 K, so no comparison to this very fine reference is possible for this indicator

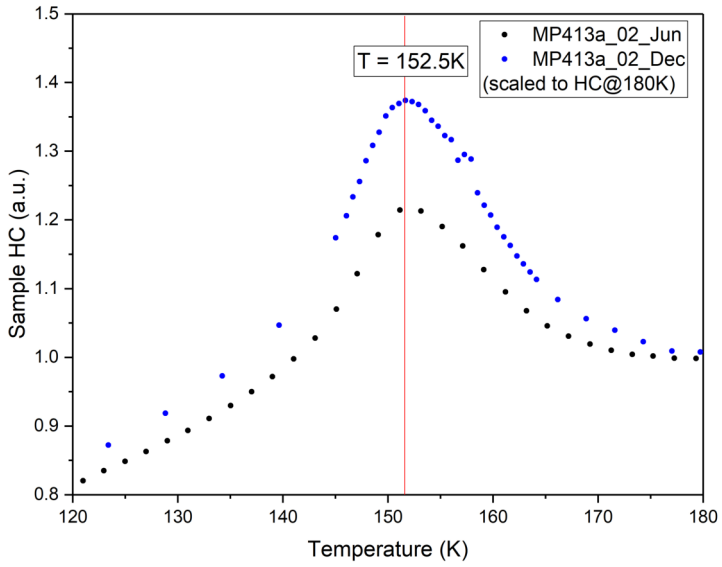

Figure 8.41: $EuPd_2Si_2$ HC measurements on the same sample piece, separated by six months. The data are normalized to the value of the specific heat at 180 K, well above the transition temperature.

some long term effects. As fig. 8.41 shows, six months of constant measurements claimed tribute on the sample, levelling down the prominence of the transition signal in the specific heat in relation to the baseline.
This is to be kept in mind, that not only the virgin cooling process can plastically alter the sample, but also perpetuated stress over a longer time interval can impact the physical properties of the system (negatively in terms of distinguishability).

8.8 Summary

Conclusionary, the primary characterization of the physical behaviour of the $EuPd_2Si_2$ system has been a project with several steps of hermeneutical readjustment. Starting with the puzzle, which of the literature descriptions was the "correct" one, the first idea to grasp was, that different samples of the same system exhibit different behaviour for some reason. Linking electric transport measurements to EDX analysis gave a first impression of that the composition of the samples may be responsible for the different behaviour.
Utilizing specific heat and magnetization measurements, it soon became obvious, that the effect of shifting the transition temperature, presumably with composition and crystallographic site occupation as the main reasons, was a real effect and happens on a notable scale, but is not as exaggerated as it showed to be in the ACT measurements. Within a single sample, the valence transition temperature seemed to exist in a confined interval, while the differences between the samples were much more relevant. Table 8.8 shows the ranges of valence transition temperatures for the different samples to compare.
In parallel to the stepwise discovery of the interdependencies between chemical

Sample No.	range of T_V (K)
MP401	159-163
MP402	not determined
MP409	140, range not determined
MP411	130-152
MP412	155, range not determined
MP413a	152-155
MP413b	152-155
MP416	103-116

Table 8.8: Overview over the $EuPd_2Si_2$ transition temperatures over every sample. For each sample, the minimum and maximum temperature found are shown, if at least two measurements have been conducted; otherwise, one temperature is provided, if available. As a probe, HC and VSM were used, ACT has been ruled out. T_V: valence transition temperature

(compositional), crystallographic and physical properties of the system, also the physical properties were investigated according to the effects of the valence state transition on both the electronic system, i.e. valence states and magnetism, and the lattice, i.e. the enormously large change in the lattice parameters of about 2% connected to the electronic transition.
When approaching the physical properties of the system and connecting it to the chemical and crystallographic properties was a hermeneutical project, so was the growth process a project of iterative reajustment of its own. A Czochralski approach to the system, using an europium excess self flux, could soon be established, but it needed some iterations of experiments to pin down the parameters, that allowed reproducable growth experiments with an optimal ratio between experimental stability (low vapor pressures etc.) and phase yield. By the date, ways were established to also estimate flux inclusions (by VSM measurements) and a maximum flux inclusion bound for "good" samples was freehandedly defined, but it was also established, that a regular level of flux inclusions is something one has to live with in every piece of a sample - of course, distributed dependent on e.g. the relative position to the seed, with increasing level corresponding to an increasing distance to the seed, but never wholly vanishing.
The quest for other fluxes in preparation for a Czochralski growth with fewer (or different/hopefully less magnetic) flux inclusions, i.e. a PdSi rich flux, with a few DTA experiments remained unsuccessful so far. Likewise did all attempts to approach the system with external fluxes, where Indium and tin were used.
But, looking back on the initial targets, all three of them were accomplished in one way or the other:

- A consistent and reproducible growth experimental setup was established, using the levitating Czochralski method with an europium excessing melt. Single crystals of noticable size can be extracted from the Czochralski grown

bodies, also samples with a variety of sizes and shapes, making them fit for different physical characterization methods ranging from ARPES and optical methods over thermal expansion to sound transport.

- The inconsistencies in the literature data regarding the valence transition temperature (where Wada [10] and Onuki [6] represent the extremes of locating the valence transition temperature to 140 K and 170 K respectively) could be resolved with the discovery, that the transition is highly sensitive to chemical and crystallographic alterations. The physical properties were characterized and linked to the chemical and crystallographic properties for a variety of different samples.

- The samples grown are provided to cooperating groups conducting a large variety of tests to pin down the critical behaviour of $EuPd_2Si_2$, and to test the hypotheses formulated in the theory of quantum critical elasticity (see chapter 5).

9 | $EuPd_2(Si_{1-x}Ge_x)_2$

The characterization of $EuPd_2Si_2$ indicates, that in the generalized phase diagram for europium compounds (fig. 6.3) $EuPd_2Si_2$ is located at quite high pressures, already beyond the critical endpoint of the first order valence transition in the second order crossover area. If this estimation is correct, by simply applying physical pressure, the critical endpoint will stay inaccessible for investigations, since the pressure applicable in the laboratory is by nature positive, the critical endpoint on the other hand would theoretically be accessed by applying a "negative pressure".
Something corresponding to a "negative pressure" can be induced to a sample by substituting a share of certain atoms of the unit cell by larger atoms, that ideally do not impact the electronic structure at the Fermi energy. While physical pressure affects the density of states at the Fermi energy by compressing the unit cell and shrinking the lattice parameters of certain directions, the correct substitution does the exact opposite, by expanding the lattice parameters, immitating a "dragging" on the sample instead of "pressing". Therefore, the term "chemical pressure" has been coined for altering the unit cells dimensions by substituting a share of atoms on a certain crystallographic position with larger or smaller atoms isoelectronically.
In the case of $EuPd_2Si_2$, if we want to expand the unit cell for a negative chemical pressure, two substitutions could serve: substituting europium is, of course, off limits, because the electronic behaviour of europium is what is of interest, but palladium could be substituted with platinum or gold, or silicon could be substituted with germanium or tin; both substitutions maintaining the group, but changing to a heavier period.
Hence, in this chapter I will document the efforts on substituting some parts of the silicon with germanium in order to push the valence transition back from the crossover area closer to the critical end point of the first order transition line.
As in the previous chapter, chemicals used for the experiments are more thoroughly described in appendix A.

9.1 The critical endpoint of the $EuPd_2Si_2$ system

On the positioning of the critical endpoint of the valence transition, where it changes from first order to second order and then into the crossover area (see generalized europium valence phase diagram, section 6.3), some rough estimates have been conducted.
Batlogg and others [8] used thermal expansion measurements in 1982 to locate the valence transition in an crossover area beyond a critical endpoint of second order,

which terminates a first order phase transition line at about −8 kbar according to their approximations. They argued for this proposition to be consistent with findings of a first order valence transition in the gold doped system $Eu(Pd_{1-x}Au_x)_2Si_2$ with x>0.1. With the terms "expanded" and "collapsed" in their chart, they do not refer to a Tet-cTet transition, as I will investigate it later with the Phosphides (see chapter 10), but to the contraction of the lattice parameter a, that comes with the valence transition.
As an approximate temperature for the critical endpoint, they give something in the range of 80 K. On the other hand, Wada found the transition to turn to first order in the platinum doped system $Eu(Pd_{1-x}Au_x)_2Si_2$ with $x \approx 0.1$ at about 120 K [10].
Both references induced negative pressure to the system by doping the palladium place (in the case of Wada, isoelectronically with platinum, in the case of Batlogg with gold, even changing the electronic situation). The attempt followed in this work is rather to try and dope the silicon place with germanium and tin. Both substitutions were already performed on polycrystalline material, and are now to be brought to the production of single crystals.
For the germanium substitution, Cho and others conducted a doping series in 2002 [12], in which they found the valence transition disappear between 10% of germanium doping (the last sample displaying valence transitions) and 15% of germanium doping (the first sample to show antiferromagnetism). Since they focussed on the germanium rich side of the series and their magnetism, no comment is given on the order of the valence transition or possible changes within the order. The ordering moment of the antiferromagnetic phase - derived from high temperature Curie fits - is uniformly given as $7.7\,\mu_B/\mathrm{Eu} \leq m \leq 8.1\,\mu_B/\mathrm{Eu}$, identifying the europium as fully 2+ (corresponding moment $7.94\,\mu_B/\mathrm{Eu}$).
For the tin doped system, some previous work by Mishra and Devare from 1983 exists [13]. They report on doped samples, with a doping level of 1-3% and 5% of tin, whose europium valence was probed with the Mössbauer method. For the 3% doped sample, they report the valence transition to be of first order and occur "below 60 K". Within the 5% doped sample, they state long ranged magnetic order at 30 K.
Some peculiarities in this report on the tin doped compounds, that are noteworthy, are, that Mishra and Devare report the lattice parameters of the system to remain completely unaltered upon doping, and that they report a doping of the Eu^{2+} part of the intermediate valent states at 4.2 K.

9.2 Growth of $EuPd_2(Si_{1-x}Ge_x)_2$

Since the goal is to substitute the silicon in $EuPd_2Si_2$ with germanium, the growth experimental design for $EuPd_2(Si_{1-x}Ge_x)_2$ is essentially derived from the Czochralski growth experimental design for the mother compound $EuPd_2Si_2$ (see section 8.4.2), where the amount of germanium 2x is induced at the expense of the silicon share 2(1-x). Since for the growth of $EuPd_2(Si_{1-x}Ge_x)_2$, there are four elements to deal with, an optimization of used fluxes and flux growth methods is not done, but instead, the Czochralski growth is carried out using the europium flux determined for the mother compound, and, at first, just assuming the germanium containing melt will behave just as in the relatively well known case of $EuPd_2Si_2$.

9.2.1 Prereactions

For the prereactions, except of mixing in the right amount of germanium into the first step, where palladium, silicon and germanium are molten together in the light arc furnace. Palladium and germanium also form a 1:1 compound with a low melting temperature of 830 °C [31], which is suitable for the second step of the prereactions. If the elements do not mix homogeneously, the melting point of germanium still is acceptably low for the second step of the prereaction.
The second prereaction takes place just as known from the mother compound: the right amount of europium (1.45:2:2(1-x):2x) is added to the result of the first prereaction in a glass carbon crucible. This crucible is then sealed in a Niobium outer crucible, which is brought to 835 °C with a rate of 100 K/h and held there for an hour in the Linn furnace under a protective argon atmposphere.

9.2.2 Parameters and genealogy of the Czochralski growth experiments

The Czochralski growth experiments, as for the $EuPd_2Si_2$ mother compound, were performed by Kristin Kliemt. The parameters of the growth experiments were, as far as possible, controlled to resemble the experiments for the mother compound. This means for the four parameters described in section 8.4.2:

- crystallinity of the seeding crystal
  The germanium doped experiments are tied to the genealogy of experiments for $EuPd_2Si_2$ insofar, as the first experiment for a germanium doped compound is seeded from one of the experiments for the undoped compound. Later experiments then were tried to be seeded by already doped experiments, minimizing the difference in doping between the seed and the melt, since the doping translates into a difference in the lattice parameters. (When this difference is too large, the grown crystals might get distorted, or growth could be hindered.) The rules for seeding crystals already discussed still apply, such as: if possible, only one crystal grain should be used as a seed; the form of the seed, ideally being a needle of several millimeters in length, but with a base area of less than a square millimeter. The requirements can be met by cutting appropriately from previous experimental results.

- The composition of the melt
  The composition of the melt is something to be carefully controlled, since with the addition of germanium to the whole setup, the melt transitions from a five-dimensional to a six-dimensional phase diagram (from three to four constituent materials). Adjustments are taken in the new, additional dimension of the phase diagram, i.e. the germanium-silicon ratio. In order to control the effect of changing this ratio, the rest of the compositional parameters of the melt needs to remain constant. They are, for best practice, fixed to the amounts that worked best for the undoped compound. Also, from the undoped experiments, it could be learned, that the prereaction and hence the initial material amount should not exceed a mass of 15 g. This was also set as a standard.

The germanium-silicon ratio is adjusted between each pair of experiments, in order to investigate the incorporation of the germanium into the compound, and also to generate a set of samples with different germanium incorporation levels. If the ratio between germanium and silicon is said to be x:(1-x), the stochiometric amount of palladium and europium were fixed following the standardized experiments for the undoped compound, so that the melt constitutes with elemental ratios of Eu:Pd:Si:Ge = 1.45:2:(2-2x):2x.
Table 9.1 and figure 9.1 show the germanium-silicon-ratio parameter x chosen for the different experiments.

- The temperature, at which the experiment is performed
  As for the undoped system, the temperature, at which the experiment is performed, is dictated by the specific properties of the precursor. The solidus and liquidus temperatures are found by subsequently heating the precursors to higher and lower temperatures and monitoring the material through a window in the vessel, in which the experiment is conducted.
  The range of temperatures for the experiments runs from 1150 °C to 1250 °C, with a larger share of the experiments at the lower temperatures. The temperatures for conducting the experiments match very well the temperatures for the undoped compound, and at least up to 20% of germanium doping, no impact of the germanium on the melting point of the total materials can be noticed.

- The pulling velocity for pulling the crystal out of the melt
  Here, the findings of the experiments for the undoped compound reproduced themselves quite nicely. The growth processes were usually stabilized at a pulling velocity of about 1.6 mm/h for the most part (and, except of some short exceptions, within a range of 0.8 mm/h to 2 mm/h).
  Also here, the germanium does not alter the melt's behaviour too noticably from the undoped compound's experiment's melts. The usual parameters for pulling appear way more homogeneous than for the undoped experiments, and also, the experiments turn out to generally be quite successful. Still, this parameter remains being descriptive for what worked best in the work flow of the growth experiment.

9.2.3 Genealogy of experiments

The Czochralski experiments for the doped $EuPd_2(Si_{1-x}Ge_x)_2$ are, just as the undoped Czochralski experiments, organized along generations, but the former for an other reason than the latter. While for the undoped experiments, the genealogic organization in generations tried to achieve an iterative improvement of crystal quality and reliability of the growth process, the doped experiments depend on a generational structure, because the germanium doping induces a change in lattice parameters. The difference between the lattice parameters of the seed and the parameters of the compound, that is to be grown, have to be kept as small as possible. Hence, if possible, seeds are chosen from earlier growth experiments, whose doping level is as close as possible to what is to be grown in the current experiment.

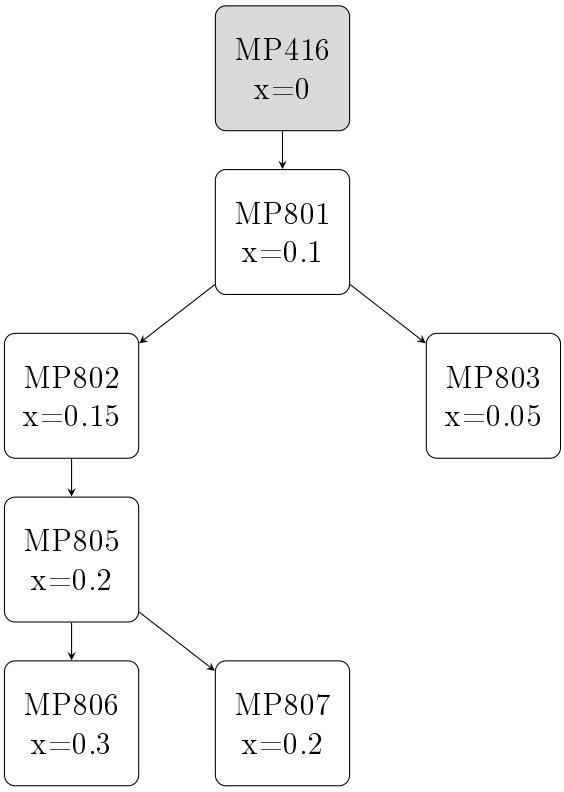

Figure 9.1: Genealogy of Czochralski experiments with Ge doping.

In order to investigate the phase diagram of the $EuPd_2(Si_{1-x}Ge_x)_2$ compound as thoroughly as possible, in the beginning quite a finely meshed doping pattern was chosen, enriching the system with germanium in 5%-doping steps.
A full account of the experiments prepared and conducted is given in table 9.1, where also the experimental parameters (the starting temperature of the experiment and the predominant pulling velocity) are described. Figure 9.1 displays the generational structure of the doped $EuPd_2(Si_{1-x}Ge_x)_2$ systems, also paying respect to the doping level of the experiment and the seeding crystals. In the figure, gray boxes identify undoped experiments, that were used for initial seeding. The names of the experiments follow the order, in which the prereactions were performed, not the order of the Czochralski experiments.

9.3 Characterization of $EuPd_2(Si_{1-x}Ge_x)_2$

In order to find the critical end point of the first order valence transition, that is proposed, not only need the samples to be grown, but also to be investigated in a standardized manner, that ensures both comparability between the samples and completeness of the characterization of the single sample (as far as this can be assured). To achieve this, the standard methods applied to each of the germanium doped Czochralski growth results were chosen to map the crytallinity of the samples, their composition and germanium incorporation level, the valence states, the transition temperature, the effect on the lattice parameters and the latent heat, if any.

Batch	x	seed	Seeding temp/°C	pulling velocity	initial mass/g
MP801	0.1	MP416	1150	1.6mm/h	15
MP802	0.15	MP801	1150	1.6-2mm/h	15
MP803	0.05	MP801	1250	1.6-0.8mm/h	14.9
MP804	1				14.9
MP805	0.2	MP802	1240	3.3-1.6mm/h	15
MP806	0.3	MP805	1120	3.3-1.6mm/h	15
MP807	0.2	MP805	1200	3.3-1.6mm/h	15

Table 9.1: Overview over the experimental parameters of the $EuPd_2Si_{2-2x}Ge_{2x}$ Czochralski growth experiments [61].

The crystallinity of the results is mainly tested with the Laue method, but also with optical investigations. The germanium incorporation level is measured with the EDX method inside a SEM. In order to determine the valence states, magnetization is measured via the VSM method. Together with specific heat measurements, which also capture the latent heat, if some can be found, VSM measurements are also utilized to determine the transition temperature. Finally, the effect on the lattice is determined using low temperature powder X-ray diffraction.
When the germanium incorporation levels are determined, and so are the physical properties, this will be translated into a x-T-phase diagram of the $EuPd_2(Si_{1-x}Ge_x)_2$ system, hopefully resembling the general p-T-phase diagram for europium containing compounds proposed by Onuki [6] as described in section 6.3.

9.3.1 Crystals and crystallinity

The crystalline bodies, that result from the growth experiments (as can be seen in fig. 9.2), usually have a mass of several grams (e.g. MP801: 3.55 g), corresponding to a yield of about 20-25%, already separated from the larger part of the remaining flux, but not free of the flux that was gradually incorporated. Usually, the crystalline bodies already show some natural cracks, which can be easily utilized to cleave the whole body in two halfs, with some other cracks extending during the splitting process and breaking apart some minor pieces. Sometimes, facets already appeared on the outside, but most of the surface of the results was rather dull for all results. Usually, the cleaved parts then do not have a single flat surface, but are somewhat ragged, but within their overall raggedness display some larger areas, which are dominated by facets of the same orientation, or even larger facets, which extend for some several millimeters in growth direction and might take up half the sample radially.
As it is known from the undoped compounds, usually about the first 7-9 mm of crystal in growth direction are elegible for investigational use, while after that mark, usually flux inclusions appear more regularly and hinder the use of samples from the lower regions of the crystal.

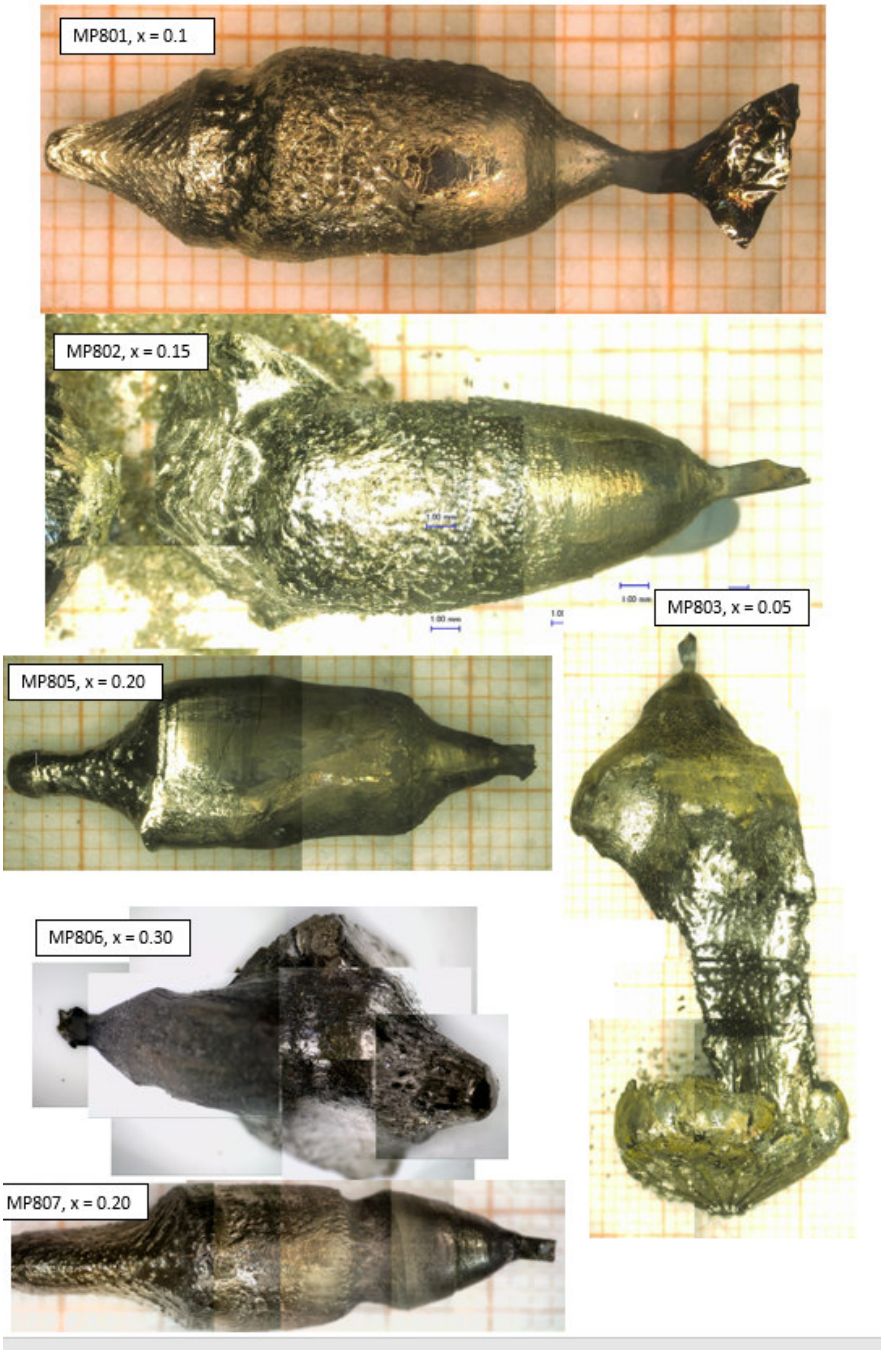

Figure 9.2: $EuPd_2(Si_{1-x}Ge_x)_2$ growth experiment results.

Where a facet in the upper regions can be isolated, that is of at least a millimeter extension of the characteristic length scale, mostly also the Laue reflexes are quite sharp and the pattern usually only one- or, in some cases, twofold, indicating a good crystallinity and (when a facet could already optically be determined) only few grain boundaries. This, however, drastically changes, whenever edges of the cleaved pieces are approached, or it is descended into the lower regions of the crystal. Then, crystallinity can go south remarkably fast and/or multiple grain boundaries can occur on narrow space.
Over all, sample preparation shifted with the doped samples from "mostly cutting" to "mostly cleaving", and crystallinity was comparable to (although on average a bit worse than) the crystallinity of the undoped crystals. MP802 was an exception, where already upon cleaving, the whole sample was shattered into small pieces, the largest just suited to be a seed for a single other growth experiment, and no larger grains could be extracted.
Some of the cleaved parts were already suited to serve as a sample for further investigations, or even as a seeding piece for further growth experiments. Cutting only happened, when no fitting piece could be found, that was cleaved along the natural splitting lines of the crystal.

9.3.2 Incorporation of germanium into the compound

The success of incorporating the germanium into the target compound $EuPd_2(Si_{1-x}Ge_x)_2$ with a fixed share x has regularly been tested using the EDX method in the SEM to determine the sample composition.

Exemplaric examination of MP801 (x=0.1)

As an example for a characterization of the composition of the $EuPd_2(Si_{1-x}Ge_x)_2$ samples, the characterization of the first sample MP801, with $x = 0.1$, will be followed. The findings of the other samples were regularly alike in the most important features that will be discussed, but were not conducted as systematically in all cases, as e.g. sample MP802 desintegrated into small pieces early, that did not allow for a proper reconstruction of the heigth scales along the sample beyond a coarse classification.
The longitudinal evolution of the composition of sample MP801 was probed inside the SEM with a total of 22 different measurement spots for EDX, with at least three measurements at every spot. The spots were arranged along the growth direction of the sample, roughly in distances of 0.5 mm to 0.8 mm, and deviating as little as reasonable from an axis connecting the top and bottom end of the sample. Point 1 is excluded from the analysis, since it investigates the seed. The spatial distribution of the measurement points is shown in fig. 9.3. For later analyses, the points are indicated by their point number, rectifying the spatial distribution of the points to a one-dimensional and equidistant scale. This approximation is justified by minimizing the deviations from such a scale as much as possible.
Fig. 9.4 shows a difference plot of the growth result of MP801 to the aspired $EuPd_2(Si_{0.9}Ge_{0.1})_2$ phase. Differences of the phase measured with the EDX method and the calculated composition of 20-40-36-4 are given in atomic percent. For each element, a trend over the length of the points 2 to 20 is determined,

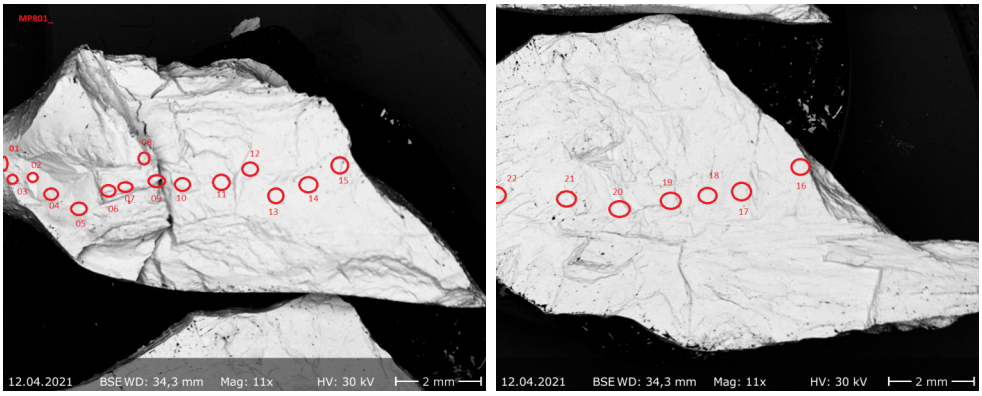

(a) upper half (b) lower half

Figure 9.3: Measurement points for the EDX-Analysis of MP801.

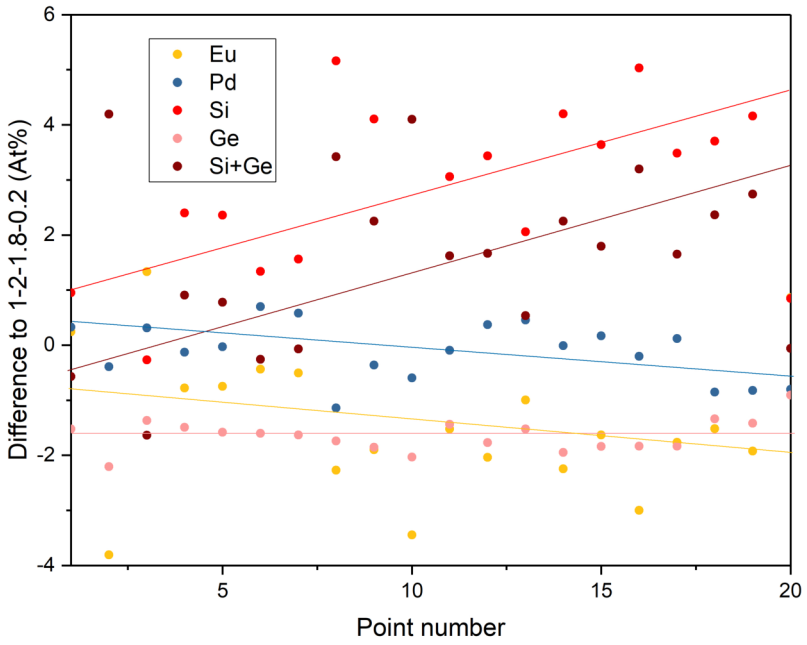

Figure 9.4: EDX analysis along the length of MP801. The point numbers refer to the settings in fig. 9.3. The trend lines are a guide to the eye and not necessarily mathematically accurate representations of the linear fit with the lowest residuals.

since from the undoped compound it is known, that composition of the samples may shift over the respective sample, and that the composition may have major impact on the physical properties.
As can be seen in fig. 9.4, still the composition is driven by a shift of the silicon share over the course of several millimeters; here, this change could be estimated as being 3-4% on 10 mm of sample length. However, unlike in the undoped compound, this large shift is not mirrored by the palladium share, but in this case is distributed over the palladium and europium shares to nearly equal parts. It has to be conceded though, that the trends in this measurements are burdened with really strong deviations and noise (partly due to conduct of measurement on an unpolished sample surface).

The germanium incorporated into the sample appears to be the element, that

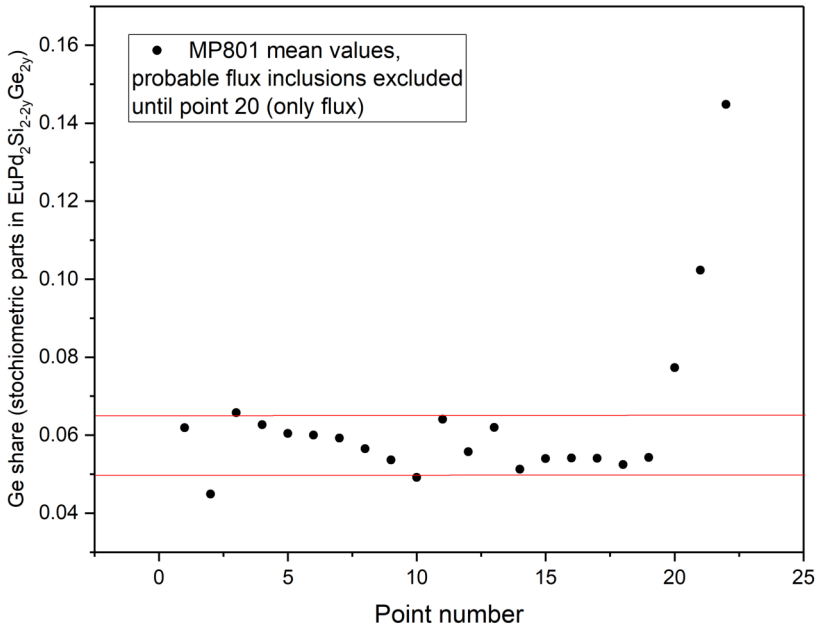

Figure 9.5: EDX analysis along the length of MP801 with focus on only germanium. The point numbers refer to the settings in fig. 9.3.

is incorporated most consistently and on a stable base: It does not seem to show a trend, and also the level of noise is much lower than for the other elements. It is incorporated at a rate, that yields a resulting phase consistently containing an amount of germanium corresponding to $0.05 < x < 0.07$ (see fig. 9.5), i.e. the incorporation rate is $60 \pm 10\%$ consistently for the target phase. Larger incorporation rates were found when examining flux inclusions, which start appearing already after several millimeters, and take over the whole sample after about the 9 mm mark.

Overview over different samples

Following this analysis pattern in general - even if not always the possibility was given to rigorously carry out the measurements along the sample, given the shattered state of sample MP802 for example - an interval of the real germanium

doping for every sample's part, that exhibited the target structure and composition without major flux inclusions, could be determined, as well as the mean value. Those data on germanium incorporation are summarized in table 9.2.
Most samples behaved quite similar in terms of flux inclusions. While the first millimeters in growth direction mostly are virtually inclusion free, flux inclusions then start to be included on a low level first, making up an increasing share of the sample proceeding along the growth direction. Between seven and nine millimeters below the seed, the flux inclusions then reach a level that the sample cannot reasonably be used for any measurements, so the flux has "taken over" the sample then. For worse samples, this take over already happens at about 7 mm (this is mainly MP802), while the better samples usually also have a larger usable part (MP801, MP803). The sample MP805 does not conform to this observations and will especially be dealth with later.

batch	$x_{nominal}$	x_{mean}	x_{min}	x_{max}
MP4xx	0.00	0.000	0.000	0.000
MP803	0.05	0.034	0.024	0.043
MP801	0.10	0.058	0.045	0.067
MP802	0.15	0.089	0.075	0.105
MP805	0.20	0.104	0.089	0.119
	(second phase)	0.186	0.175	0.196
MP807	0.20 (second batch)	0.105/0.122	0.096	0.137
MP806	0.30	0.154	0.142	0.169
	(second phase)	0.255	0.242	0.271

Table 9.2: Germanium incorporation into $EuPd_2(Si_{1-x}Ge_x)_2$ for different dopings. Given are the mean values derived from a larger range of EDX measurements, the minimum and the maximum value obtained.

Steady incorporation rates for lower doping

This incorporation rate of 60%, that was found for MP801, also held true for further samples in the low doping regime. The samples with higher doping concentrations, MP805 and MP806, deviate from this behaviour and will be dealt with in the following section. But in the lower doping regime, a close-to-constant incorporation rate of about 60% of the germanium over the usable parts of the sample can be found in all cases so far. Figure 9.6 compares the real incorporation rates, rather: the mean incorporation of every sample in comparison to its nominal, weighed in doping material (black dots), to the ideal 60% incorporation rate (red line). The data are the same as in table 9.2.

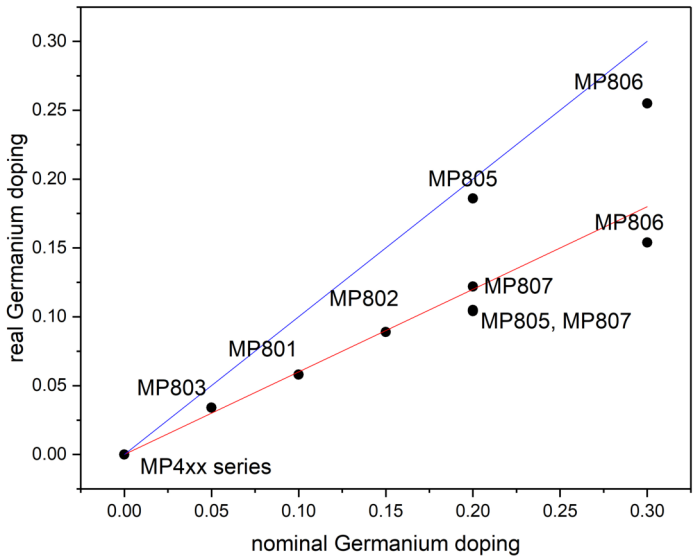

Figure 9.6: germanium incorporation levels by the nominal, weighed in germanium content of the sample. Red line: 60% incorporation rate indicator. Blue line: identity indicator.

Incorporation in the higher doping cases

When aiming at higher germanium doping concentrations of $x = 0.2$ (MP805, MP807) and $x = 0.3$ (MP806), the incorporation behaviour changes in more than one way. As for lower doping rates, the samples usually constituted from one homogeneous main phase (with some flux inclusions possible), now the homogeneity of the samples is strongly affected; in two of the samples (MP805 and MP806), patterns of two phases, each covering large areas and penetrating each other at the fringes, emerge (e.g. fig. 9.7b). In sample MP807, this patterning occurs far less, but instead a drift in the germanium incorporation rate over the length of the sample can be seen.
One of the phases of this pattern (as determined with EDX analysis) corresponds to what is to be expected from the target phase. In those areas, the incorporation rate of the germanium is again reduced (with respect to the constant rate of 60%, that was established before), with incorporation rates of about 55% (MP805) and about 51% (MP806).
The other is also a quarternary phase, but does not only display an enhanced europium content (explaining the split of datapoints in table 9.2 and figure 9.6), but also enhanced europium content on the expense of palladium and germanium share. Figure 9.7a shows the measured composition of the target phase and the main competing phase in the sample MP805.
Sample MP806 was investigated using X-Ray Fluorescence Analysis (XFA) to qualitatively see the whole pattern of the distribution of the two constituing phases at once. In fig. 9.8, the more blueish areas correspond to a phase, that is relatively silicon and palladium rich (compared to the other areas, that is), which is the target phase. The more reddish areas correspond to an enhanced europium and germanium content. In MP806, both phases form relatively stable

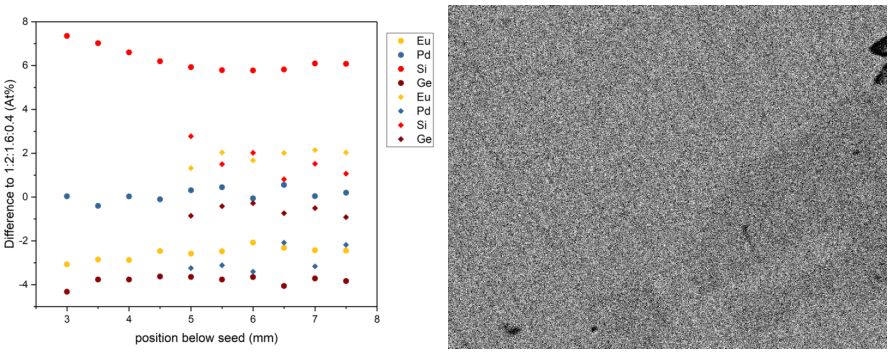

(a) composition (b) SEM backscattering electrons

Figure 9.7: (a) MP805 EDX analysis from 3 mm below the seed onwards along growth direction. Round dots: target phase. Diamonds: Second phase. The silicon and germanium deviations in the target phase are so large, because they are measured against the nominal content, which, with a presumed incorporation rate of 60%, is notably. (b) contrast between two phases at magnification of 1000. Both phases seem to be homogeneous, not allowing resolution on below-μm-scale.

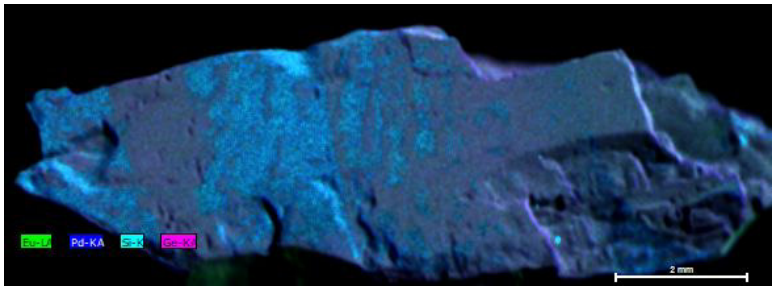

Figure 9.8: MP806 XFA analysis [72]. The density of points of a respective color indicates the elemental concentration. A layering of Eu/Ge-rich phase and Eu/Ge-poor phase along the growth direction is visible.

and extended regimes.
By comparing the individual EDX measured points on the phase with the exalted germanium and europium values on both samples MP805 and MP806 with the respective mean values of the target phase's germanium and europium content, and afterwards generating the mean value of the deviation, one finds the deviations of the elements to appear in a certain range. For MP805, the material that separates the side phase from the target phase contains to (58 ± 6) % europium and the rest is germanium; for MP806, the europium share is (56 ± 6) % with the rest consisting of germanium.
This analysis is of interest, because one explanation for the very odd composition of the additional phase could be, that it actually is the target phase, but in a solid solution (or as separated phases, but on a scale of below 1 µm, so that the phases cannot be separated in SEM pictures with a magnification factor of 1000) with some other binary phase. A second phase being contained to a small share could, if the phase can be identified with the right properties, even help explaining small additional features (hinting a second phase transition) in the physical characterization data. The physical characterization will be discussed later, but the signal, that is to be explained, is in both samples localized at about 17 K (derived from HC and VSM) and could be AFM ordering (hints from VSM signal shape).
Thinking of the additional phase as $a\,EuPd_2(Si_{1-x}Ge_x)_2 + b\,Eu_yGe_z$, one would find from the descriptive data analysis above, that the allowed interval for composition contains Eu_5Ge_3 [73] only. Granting a possible systematic deviance driven by the measurement device, and also the possibility of a homogeneity region for the candidate compounds, also EuGe [74, 75] could be a candidate.
Also, taking into account that in the regions with the deviant composition the palladium share dropped just about 1% less than the silicon share, ternary compounds EuPdGe [76] and $EuPdGe_3$ [77, 78] need to be taken into consideration.
The most promising of these candidates is, of course, Eu_5Ge_3, due to best accordance with the EDX data. It crystalizes in the tetragonal spacegroup 140 (with $a = 7.990$ Å, $c = 15.367$ Å) and the magnetic behaviour is only known insofar as it shows Curie Weiss behaviour down to 50 K [73], below which no literature data seems to exist. This, at least, would not rule out this candidate. In PXRD, this structure could not be found.
For EuGe (orthorombic, $a = 4.715$ Å, $b = 11.26$ Å, $c = 4.101$ Å) and $EuPdGe_3$ (tetragonal, $a = 4.444$ Å, $c = 10.167$ Å) an argument is, that the lattice parameters are at least somewhat close to the lattice parameters of $EuPd_2(Si_{1-x}Ge_x)_2$, which would benefit the coexistence of the two phases if they would form some sort of a heterostructure. But since they also both were not found in PXRD, the composition is sort of off from what was found with the EDX analysis, and both order antiferromagnetically, with two transitions at 37.5 K and 22 K for EuGe, one transition at 12 K for $EuPdGe_3$, these candidates could be ruled out.
The least promising candidate is EuPdGe (monoclinic, $a = 6.181$ Å, $b = 6.136$ Å, $c = 7.439$ Å, $\beta = 109.4°$) which does not fit really well in composition, and neither are the structures compatible. Also, this compound was not found at all in PXRD. With a reported Néel temperature of $T_M = 8.5$ K [79], this compound also does not fit the extra signals and can be ruled out.
So, the candidate that is so far not ruled out just by its physical properties is

Eu_5Ge_3, which is also the favourite in terms of composition. Now, assuming that Eu_5Ge_3 and $EuPd_2(Si_{1-x}Ge_x)_2$ together somehow compose the regions with the unknown phases, would it then be reasonable to not see the compound in PXRD? For the sake of simplicity, assume regions consisting of $EuPd_2(Si_{1-x}Ge_x)_2$ and regions consisting of $a\,EuPd_2(Si_{1-x}Ge_x)_2 + b\,Eu_5Ge_3$ to be distributed equally. From the EDX MP806 data's elemental mean values, one can estimate $a = 17$ and $b = 1$. Equal distribution will about double the content of $EuPd_2(Si_{1-x}Ge_x)_2$, so that Eu_5Ge_3 would only contribute about $1/35 \approxeq 0.03$ to the whole sample. With the signal-to-noise ratio of about 12 (comparing the maximum count rate of the highest reflex with a mean noise value), a 3%-contribution could be argued to maybe be overseen in the noise. Also, the quantity of the signal seen in HC and VSM would support the assumption that there is an additional phase included only with a share of a few percent.
In the end, the nature of the two regions that could be separated composition-wise via EDX measurements could not be reconstructed quite clearly. With the assumption of below-microscale inclusions or a solid solution or sub-microscale inclusions of Eu_5Ge_3 in $EuPd_2(Si_{1-x}Ge_x)_2$, a proposition exists, that can explain the form the two regions present themselves in SEM pictures, and also accounts for the very small additional signals in the physical properties, but cannot be confirmed (nor outhrightly denied) by PXRD (because of low shares and quite large noise levels) or by identifying the phase transition signals (because no literature data was found).
Incorporations of this side phase can also be found in batch MP807, but on a way lower level (as compared by the relative contributions of the 17 K anomalies in VSM measurements). The lower rate of side phase incorporation and the more steady distribution (without patterning over large areas, probed with EDX) in this sample may be connected to the starting condition of the seed. While sample MP805 (and to some extent also MP806) was grown with a seeding crystal with notably different lattice parameters than the target compound (see following subsection) and the growth process may hence have been destabilized, sample MP807 was seeded with a piece of MP805, with the same nominal doping and hence the same lattice parameters. This may have stabilized the growth process and discouraged the incorporation of side phases.
Still, also in MP807, the germanium incorporation rate is deminished relative to the quite steady 60% incorporation rate with the lower dopings, at about 55% to begin with (doping of $x = 0.105$). Other than for the lower doped samples, the incorporation rate does not stay constant though, but approaches 60% (doping of $x = 0.122$) after several millimeters of steady increase. After that point, flux inclusions begin to play a role again.

Lattice parameters at ambient conditions

In the first place, the germanium doping has been performed to apply a chemical pressure to the system in order to shift the compound in the generalized phase diagram (fig. 6.3) towards the first order valence transition. Chemical pressure is called such, because the size of the substituted atoms is suitable to deform the unit cell of a compound, just as the application of an external pressure would do. In the case of chemical pressure, the applied pressure can be positive (if the doping atoms are smaller than the doped atoms, the unit cell shrinks, just as

if it was pressured) or negative (if the doping atoms are larger than the doped atoms, the unit cell inflates, and a pressure "from within" can be stated, or the resulting chemical pressure can be seen as the equivalent of external pressure needed to bring the compound back in shape). The application of chemical pressure by the substitution of germanium on the silicon places should be visible in the deformation of the unit cell, more specifically in an inflation of the lattice parameters of the compound. Since germanium atoms are larger than silicon atoms, the chemical pressure applied is negative.
In fact, such effects are visible when looking at the lattice parameters of the compound with different doping levels at room temperature and ambient pressure. The inflation occurs with about 5 mÅ per 3% of doping in the a parameter and a similar rate in the c parameter. More exact values can be drawn from table 9.3.

batch	x	a(Å)	c(Å)
MP413a	0.000	4.23966	9.86314
MP803	0.034	4.24307	9.86839
MP801	0.058	4.25064	9.87543
MP802	0.089	4.25580	9.87836
MP805	0.105/0.186	4.27275	9.90748
MP806	0.154/0.255	4.3095	9.6992
MP807	0.105/0.122	4.26056	9.88845

Table 9.3: Lattice parameters of $EuPd_2(Si_{1-x}Ge_x)_2$ at ambient temperatures, derived from PXRD measurements.

Estimation for the chemical pressure applied

Using the lattice parameters from table 9.3, an estimation for the chemical pressure applied can be suggested. In order to do so, a relation is needed that connects volume chance and applied pressure for the specific situation of a compound with a certain compressibility. This relation is:

$$\frac{\Delta V}{V} = -\frac{1}{K} \cdot \Delta p \tag{9.1}$$

where K is the bulk modulus of the compound, which is usually given in units of GPa. Since the bulk modulus is unknown for $EuPd_2Si_2$, it can be assumed to be $K = 100\,\mathrm{GPa}$ following the estimation by Onuki for $EuPd_2Ge_2$ [80], which is most probably at least the correct order of magnitude and hence gives a rough estimation for the order of magnitude of pressure applied. The pressures calculated with this estimate are shown in table 9.4. It is of an order of magnitude of $\Delta p = -(10 \pm 2)\,\mathrm{GPa} \cdot x$, where -10 GPa is the estimate for the pressure applicable by 100% of germanium doping.
Also, it is noticable, that this estimation advocates for the Ge-rich/flux phase in MP805 to at least dominate the lattice distortions, possibly via a heterostructure,

batch	x	Δp (GPa)	$\Delta p/x$ (GPa)
MP413a	0.000	0.000	0.000
MP803	0.034	-0.214	-7.136
MP801	0.058	-0.643	-10.710
MP802	0.089	-0.916	-10.174
MP805	0.105/0.186	-2.011	-19.148/-11.170
MP806	0.154/0.255	-1.632	-10.600/-6.402
MP807	0.105/0.122	-1.243	-11.833/-10.185

Table 9.4: $EuPd_2(Si_{1-x}Ge_x)_2$ chemical pressure estimation.

as discussed in the previous sections. The same is not true for MP806. MP807 is coarsely compatible to the rest of the series in terms of pressure equivalent for all possible doping levels.

9.3.3 Effect of doping on physical properties

The effect of the germanium doping on the compound's physical properties (i.e. its lattice and the valence transition) are determined using low temperature PXRD to determine the lattice parameters, VSM to determine the magnetization, and magnetic order, if any emerges, and very coarsely estimate the valence, and specific heat measurements to pinpoint the temperature of the valence transition and scout for signs of first order (in form of latent heat).
Looking at the specific heat data (shown in fig. 9.9), it is obvious, that even small doping, corresponding to relatively small pressures, exert a large impact on the electronic system of the compound, that is, on the valence transition temperature and the magnetic behaviour of the respective samples. The valence transition is suppressed to lower temperatures with a rate of about 10 K per % of germanium doping (with respect to the total occupancy of the Wyckoff position 4e). The general form of the anomaly in the specific heat remains symmetric and "mean-field like" for the lowest dopings up to 15% nominal (about 9% real) doping.
Above that level of doping, the form of the specific heat anomalies changed towards a λ-shape. But this did not herald a change in the nature of the valence transition, but rather the appearance of a long-ranged antiferromagnetic order in the more heavily doped samples, setting in at a nominal doping of 20% (or a real doping of 10.5%). This is consistent with Cho's findings of magnetic order setting in at a doping level of about 10% [12]. The antiferromagnetic order was seen in the magnetization measurements, shown in fig. 9.10, also with prove by anisotropy in fig. 9.10b and metamagnetic behaviour as seen in the inset of fig. 9.10b. The metamagnetic transition of the antiferromagnet occurs in the easy plane (ab0), the hard axis is (001). Fig 9.10c shows, that with magnetic fields in the order of several Tesla, the ordering temperature of the high doping sample is suppressed, as one would expect for long range magnetic order. In the valence fluctuating samples, no anisotropy is visible below the characteristic temperature

(fig. 9.10d), again distinguishing the samples shown in red (AFM) and blue (valence fluctuating) in fig. 9.10a.

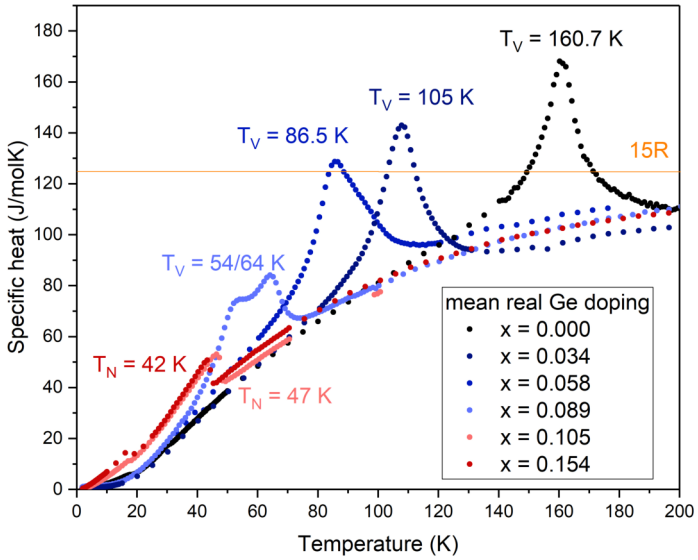

Figure 9.9: Specific heat data comparison of the $EuPd_2(Si_{1-x}Ge_x)_2$ doping series. Black: no doping comparison data; blue: valence fluctuating samples; red: antiferromagnetic samples.

The speculation, that the valence transition would at some point evolve from a phase crossover to a phase transition of first order before entering the magnetically ordered state, seems to be proven wrong for this system though. Thermal relaxation experiments with large heating pulses (of about 15 K per measurement) on the samples did not show any signs of latent heat. The transition anomalies don't even seem to change their temperature range at all. Determining the FWHM of the anomalies in the temperature dependent derivative of the molar susceptibility (in order to determine the broadness of the crossover around the inflection point of the valence transition, fig. 9.10e), for all samples exhibiting a valence transition, a FWHM of 20-21 K was found (except for the 3.4% sample, which had a lower FWHM of about 16 K, but this did not confirm a trend). Hence, a development in broadness of the crossover range in the temperature regime can be rejected.
Additionally, as long as the magnetically ordered phase is not reached, both of the valence states seem to not change significantly. Valence states are shown in table 9.5. The high temperature valence is stable at $Eu^{2.3+}$ for all samples, while the low temperature state evolves somewhat around $Eu^{2.7+}$. Those estimations are quite coarse and have to be taken with care, since they base only on mere Curie fits, which also only take into account the Curie paramagnetism of the Eu^{2+}, ignoring the Van Vleck paramagnetism of the Eu^{3+} as an approximation. For the lower temperature phase, and especially when the transition temperature shifted quite low, finding a fittable data range was not an easy task and is a source for additional estimation errors.
In the magnetically ordered phase on the other hand, the valence seems to not immediately go to pure Eu^{2+} (at least in the high temperature regime, where the

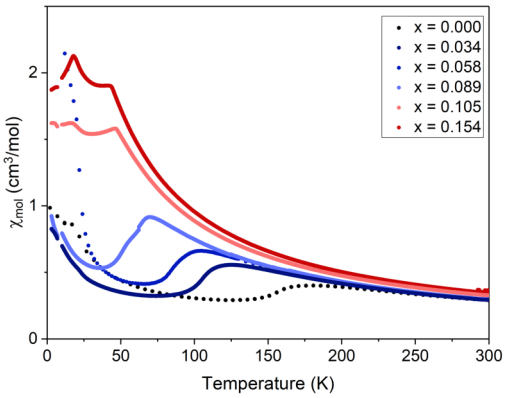

(a) Black: no doping comparison data; blue: valence fluctuating samples; red: antiferromagnetic samples.

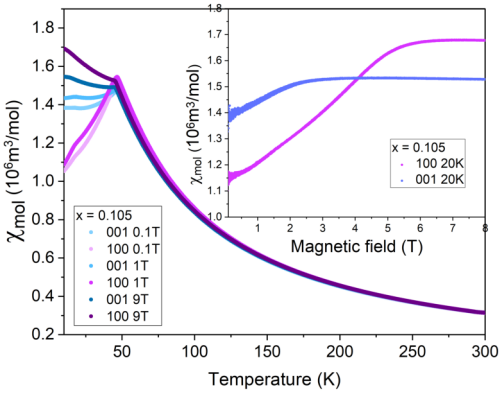

(b) AFM sample anisotropy and metamagnetic transition, blue: strong axis measurements, pink: weak axis measurements.

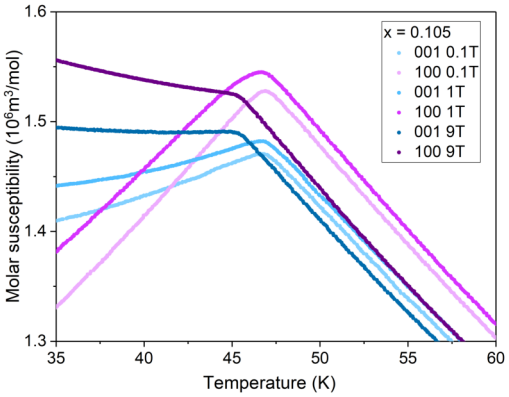

(c) AFM sample transition temperature suppression with field, blue: strong axis measurements, pink: weak axis measurements.

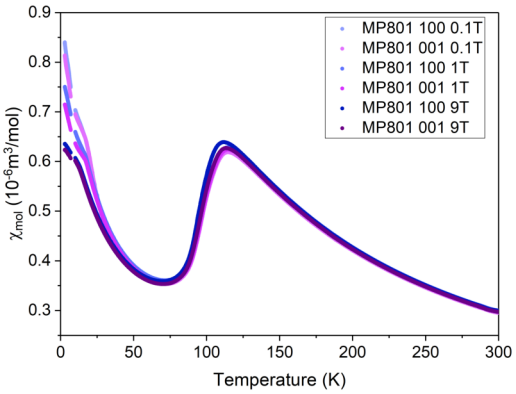

(d) Valence fluctuations behave isotropically in the whole temperature regime.

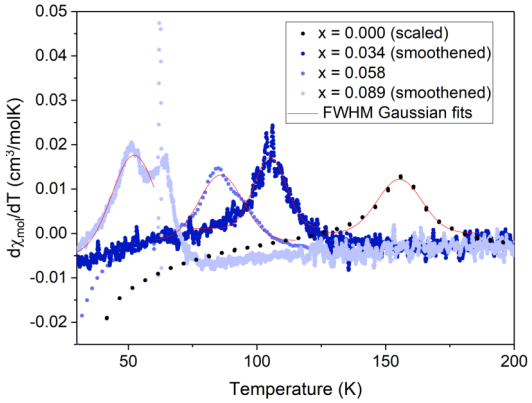

(e) FWHM test for the width of the valence transition.

Figure 9.10: Magnetization data comparison of the $EuPd_2(Si_{1-x}Ge_x)_2$ doping series. (b)/(c) sample from MP807. (d) sample from MP801.

Curie fit was applied), but to degrade from the $Eu^{2.3+}$ intermediate state with a rate, that would even allow a linear evolution towards a pure Eu^{2+} $EuPd_2Ge_2$. How ever this be, a decreasing trend in valence is foreshadowed by the samples MP805 and MP806.

$x_{nominal}$	$x_{measured}$	low T valence	high T valence
0.00	0.000	2.74 ± 0.03	2.30 ± 0.06
0.05	0.034	2.67 ± 0.02	2.30 ± 0.05
0.10	0.058	2.77 ± 0.07	2.30 ± 0.03
0.15	0.089	2.69 ± 0.03	2.31 ± 0.011
0.20	0.105		2.29 ± 0.04
0.30	0.154		2.26 ± 0.03

Table 9.5: Valence of the low temperature and high temperature states of $EuPd_2(Si_{1-x}Ge_x)_2$ for different dopings, gained from single crystalline magnetization data at 0.1 T external field.

Revisiting the heat capacity measurements, the entropy connected to the respective phase transitions can be roughly estimated, if proper account of the phononic and electronic background of the specific heat can be given. Fig. 9.11 shows a comparison between two samples with x = 0.058 (valence fluctuating, 9.11a) and x = 0.105 (antiferromagnetic, 9.11b) in evaluating the entropy of the respective anomalies connected to the two transitions. For the phonon background substraction, a model was built using an analytical formula [81] with two Debye temperatures, and fitted to the high temperature regimes of the respective curve. For the x = 0.058 sample, two Debye temperatures $\Theta_{D1} = 195\,\mathrm{K}$ and $\Theta_{D2} = 341\,\mathrm{K}$ were found. The Debye temperatures for the x = 0.105 sample are $\Theta_{D2} = 162\,\mathrm{K}$ and $\Theta_{D2} = 346\,\mathrm{K}$. The higher Debye temperature, describing excitations of the heavier atoms, remains almost constant, while the lower Debye temperature changes quite strongly, which is plausible, since one would identify it with exciting the lighter atoms - where substitution explains a substantial change between the two samples. In both cases, the fit describes the data well and leaves behind the anomaly belonging to the transition C_A, when the background is substracted (grey dots in the figures). Integration of C_A/T yields the entropy connected to the transition. For the valence fluctuating sample, the entropy of the valence transition is about $S_V = R \cdot \ln(4)$. It is not entirely clear, where this value stems from, but since the saturation value of the anomaly's entropy contribution is exceptionally close to this value, it might help figure out, which configurational system might be responsible for the specific heat anomaly. A magnetic contribution is unlikely, and since it is also not the $R \cdot \ln(2)$ of a two-level system, probably geometrical considerations will have to be mobilized. For the antiferromagnetic sample, one finds about $S_{AFM} = R \cdot \ln(8)$, which is the entropy of an ordering Eu^{2+} moment (with $J = 7/2$ and a total of $n = 2J + 1 = 8$ states condributing). Hence, the magnetism of the antiferromagnetic samples can be accounted to the ordering europium moments as expected.

With PXRD, also the structural concomitants of the electronic transitions in the

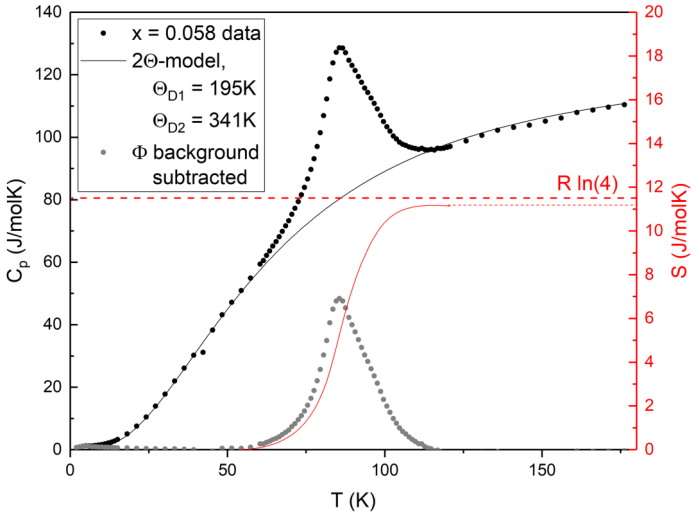

(a) x = 0.058.

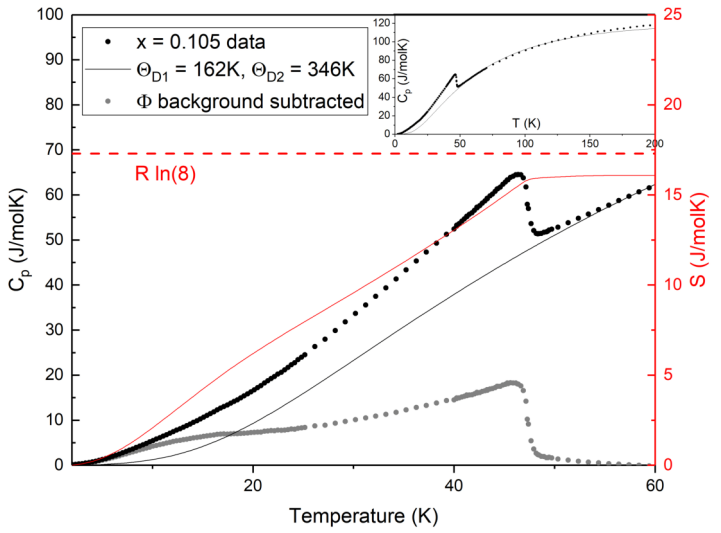

(b) x = 0.105.

Figure 9.11: Entropy analysis for (a) one valence fluctuating sample from MP801 and (b) one antiferromagnetic sample from MP807.

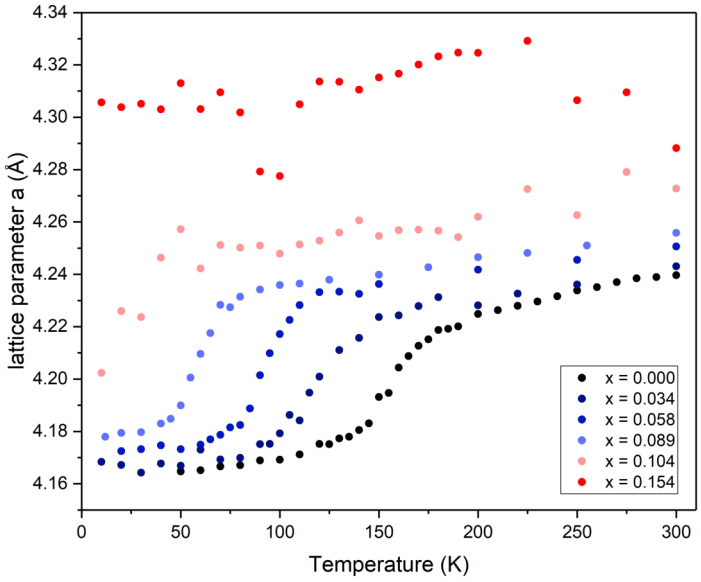

Figure 9.12: Comparison of the lattice parameter a of the $EuPd_2(Si_{1-x}Ge_x)_2$ doping series over temperature. Black: no doping comparison data; blue: valence fluctuating samples; red: antiferromagnetic samples.

$EuPd_2(Si_{1-x}Ge_x)_2$ series were scouted (shown in fig. 9.12). With subsequent addition of germanium, an inflation of the lattice can not only be detected at room temperature, but also consistently at lower temperatures. The inflection point of the nonlinear temperature development of the lattice parameter a again coincides with the valence change in the valence fluctuating samples and connects to the valence transition. In the antiferromagnetic MP806 sample, the collapse feature has then disappeared. However, in the MP805 sample, at the lowest observable temperatures (between 15 K and 20 K as an estimated position for the inflection point), an anomaly in the lattice parameter can be found, that resembles the anomaly connected to the valence transition.

Having a closer look onto the lattice anomaly, one finds in the valence fluctuating samples (fig. 9.13a shows MP801 as an example) a continuous shift of the reflexes connected to the *a* parameter, as it also was found for the undoped compound and as one would expect it. The antiferromagnetic sample with lattice anomaly in question on the other hand (fig. 9.13b) shows a separation of reflexes below about 40 K - one lattice section seems to remain deflating linearly with temperature, while another portion of the lattice undergoes an anomalous contraction. This ties in with the finding, that the crystal MP805 had both areas exhibiting magnetically ordered behaviour and areas exhibiting valence fluctuations. The anomalously contracting portion corresponds to the valence fluctuating part of the sample, while the linearly contracting portion corresponds to the magnetically ordering part of the sample. The kink in the refined lattice parameters for MP805 hence is an artifact stemming from problems with dealing with the separation of reflexes between the two portions of the crystal.

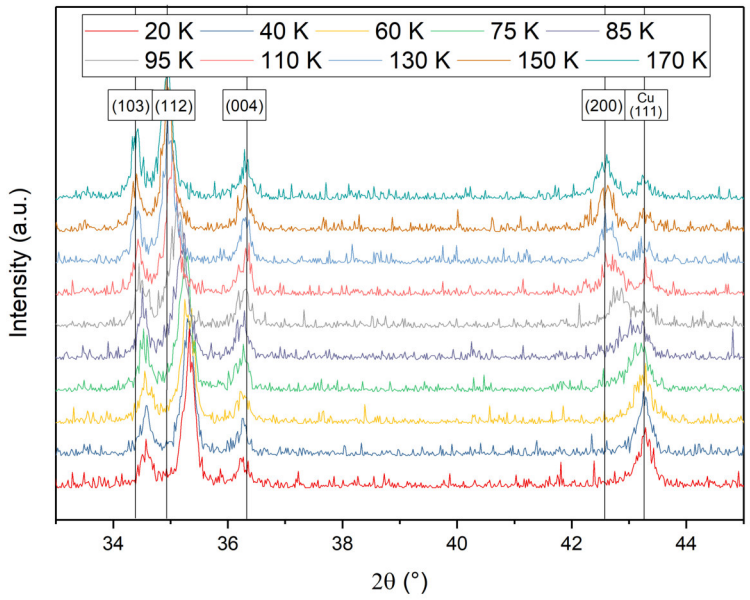

(a) x = 0.058.

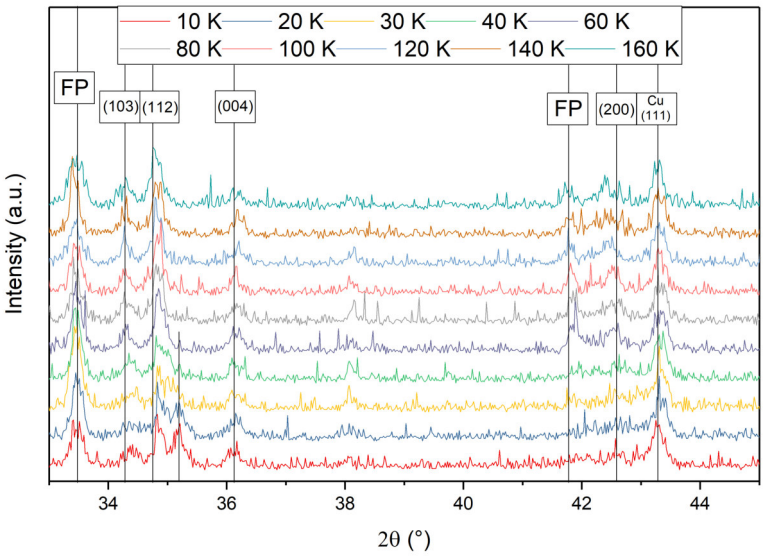

(b) x = 0.105.

Figure 9.13: $EuPd_2(Si_{1-x}Ge_x)_2$ PXRD flux diagrams for (a) one sample from MP801, exhibiting a clear lattice shift connected to valence transitions, and (b) one sample from MP805, exhibiting a remnant anomaly that takes place in the magnetically ordered phase.

9.3.4 Positions in the phase diagram

All those measured features can be summed up in an attempt of a phase diagram in the doping- and temperature-regime. This attempt is shown in fig. 9.14. Positions of the valence transition (i.e. the crossover inflection point) and the long range magnetic order are drawn from the maxima of the anomalies in the specific heat measurements. The lattice contraction positions are determined by the inflection point of the nonlinear part of the lattice parameter development over temperature. The black and blue lines are mere guides for the eye. No fit

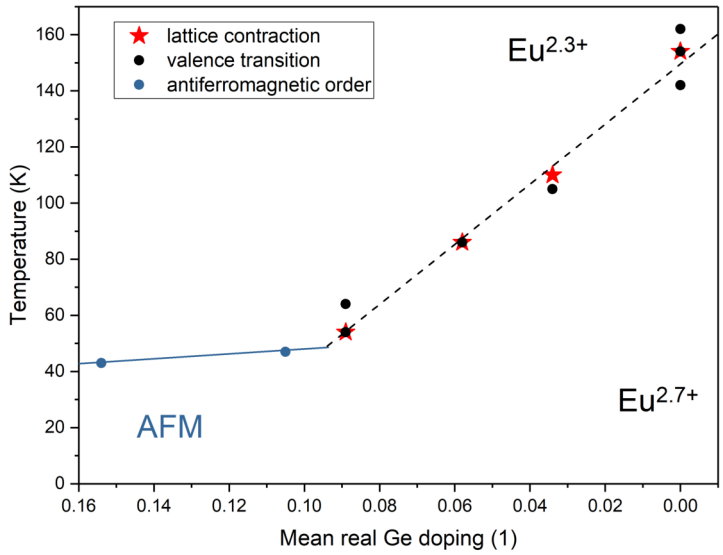

Figure 9.14: Phase diagram of the electronic states in the $EuPd_2(Si_{1-x}Ge_x)_2$ system, tuned by temperature and doping. Valence transition and AFM temperatures from HC measurements, lattice contraction temperatures from low temperature PXRD. Red line star: lattice contraction from PXRD that does not coincide with a valence transition, status not secure.

was applied, and they do not entail any claim about the order of the transition, for it is usual to only represent phase transitions with lines, not crossovers; the black line, however, roughly represents the inflection temperature of the valence state crossover. The valence transition in the germanium system seems to stay a crossover at any doping level and never take the form of a phase transition of first order. A change between long ranged magnetic order and valence fluctuations occurs at a germanium doping level of $0.089 < x < 0.105$.

9.4 Summary

In this chapter, a doping series of $EuPd_2(Si_{1-x}Ge_x)_2$ of six samples with different doping levels between $x = 0.05$ and $x = 0.30$ has been discussed. The transfer of the growth technique from the undoped compound to the germanium doped compound worked out well, leading to mostly homogeneous samples of the target phase with at lower doping levels a constant incorporation rate of 60% of the

offered germanium, which only at higher doping levels ($x = 0.20$ and $x = 0.30$) broke down. Especially in the batches with higher doping levels, a side phase occurred, that may correspond to Eu_5Ge_3, but is not yet clarified to full extent. By using the ambient conditions lattice parameters and assuming a compressibility module of $K = 100\,\mathrm{GPa}$, some estimations were made for the pressure equivalent exerted by the germanium doping. The compounds $EuPd_2Si_2$ and $EuPd_2Ge_2$ are estimated to be in total 10 GPa apart, hence every percent of doping exerting a pressure equivalent of 0.1 GPa.
In the thermodynamic properties, the valence transition of the europium remains for the lower dopings between the same states of valences of about 2.3 and 2.7, but being strongly suppressed in temperature, until the sample's magnetism is changed from valence fluctuating to antiferromagnetic long range order. The character of the valence transition remains crossover-like for all samples. The highest doped sample showing a valence transition is doped with $x = 0.089$, while the lowest doped sample showing long range ordered antiferromagnetic behaviour is doped with $x = 0.105$. Somewhere around $x = 0.1$, hence the valence fluctuations will disappear. Within the magnetically ordered phase, a decrease of the valence heralds itself, extrapolating to pure Eu^{2+} for $EuPd_2Ge_2$.
Until the valence transition vanishes, it never turns to a first order phase transition, but remains in a broad crossover area. This is in conflict to the predictions of Batlogg [8], who predicts the second order critical endpoint at $-0.8\,\mathrm{GPa}$ and about 80 K, if germanium doping and exerting pressure are considered equivalent. Hence, the findings of this series - that the transition never turns into a singularity - advocate for the conclusion, that doping with germanium in fact is not equivalent to exerting physical pressure, but influences the system also in other ways besides contracting the lattice parameters.

10 | EuT_2P_2 (T = Fe, Co, Ni, Ru)

Since the $ThCr_2Si_2$ structure type is a very adaptable structure type, there is a rich variety of compounds in the 122-structure featuring europium as a rare earth element, substituting thorium from the structural family model.
For the matter of investigating the europium valence and the transition from a magnetic divalent europium state to an intermediate valent europium state, the phosphides (compounds, where the silicon is replaced by phosphorus) of this structural family are of special interest. The phosphides of the form EuT_2P_2, where T is a transition metal, occur in two realizations of their structure, which are called the collapsed phase and the non-collapsed phase.
Since the known compounds realized in the non-collapsed phase are magnetic, and the known compounds realized in the collapsed phase are intermediate valent, a relevant question is, whether the transition of the europium's electronic states is in any form accompanied or driven by, or related to the transition between the non-collapsed and the collapsed state of the 122-structure. First, the question is to solve, whether both transitions happen at once. Once this is set, it is to investigate what the actual relation between the two transitions is.
To tackle this problem, first in this chapter the growth of two compounds will be established, one, where the transition metal T is cobalt, in the non-collapsed phase, and one, where the transition metal T is nickel, in the collapsed phase. When the growth of both compounds is established, a series of mixed composition experiments will be conducted to find the composition, where the structure collapses, as well as the composition, where the electronic state of the europium changes, and to find the relation between both transitions that way.
As in the previous chapters, chemicals used for the experiments are more thoroughly described in appendix A.

10.1 Collapsed and non-collapsed phase of the $ThCr_2Si_2$ structure

The basic features of the $ThCr_2Si_2$ structural type, its atomic positions and symmetry elements have been discussed in chapter 8.1 already. For the EuT_2P_2 compounds, the transition metal T takes the Wyckoff position d, which was previously the place of chromium and/or palladium, and the phosphorus covers Wyckoff position e, which is the silicon place in the other compounds.
Phosphorus on Wyckoff position e is now adding another feature to the set of structural features of the 122 structural type family. The additional electron which phosphorus brings compared to silicon has the two options to either estab-

lish an additional covalent bond to the next phosphorus atom in the neighbouring T-P-layer [82], or to not establish this bond and contribute to the metallic bond of the compound.

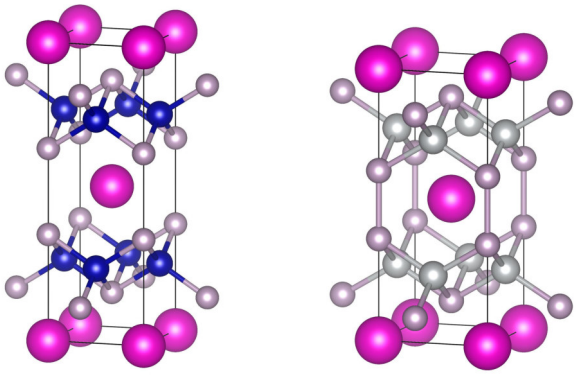

(a) (b)

Figure 10.1: (a) $EuCo_2P_2$, non-collapsed 122 structure, no established P-P-bonds [83] (b) $EuNi_2P_2$, collapsed 122 structure, established P-P-bonds [84], pictures with [85].
Colour code: pink - Eu, blue - Co, light (yellow) grey - Ni, dark (red) grey - P

This possibilities come with consequences on the surrounding of the Th-substituting atom (europium in this cases). The bonding of two phosphorus atoms drastically decreases the P-P-distance between the two bound phosphorus atoms. The usual bond length of a P-P covalent single bond is 2.25-2.45 Å [82], while the P-P distance can be much larger (above 3 Å) when no covalent single bond is established. In the phase, that established no bonds between neighbouring T-P-layers, the c-parameter of the lattice usually is in a range of 11-12 Å (compare table 10.1), which also decreases in the phase with the interlayer bonding to about 9-10 Å (compare table 10.1 and Silicides in chapters 8 and 9). The drastic decrease of both those scales gives rise to the popular imagination of a "collapse" of the structure. Hence, the structure with a P-P-bond is referred to as the collapsed phase, the structure without a P-P-bond is referred to as the non-collapsed phase.
Figure 10.1 shows two of the compounds investigated in this chapter as an example for a non-collapsed compound ($EuCo_2P_2$) and a collapsed compound ($EuNi_2P_2$). Also, table 10.1 displays the lattice parameters and P-P-distances of the phosphides investigated. The decrease of c by about 2 Å from the non-collapsed phases (T = Fe, Co) to the collapsed phase (T = Ni) can be seen, as well as the decrease of the P-P-distance of about 1 Å.
As the compounds discussed later are examples, the state of the structure of the EuT_2P_2 compound, more precisely whether it is collapsed or not, influences the electronic state of the europium atoms in the compound: Whereas for example the iron and cobalt compounds are non-collapsed and europium remains divalent and magnetic, in the collapsed phases, as for example in the nickel compound, the electronic state of europium is intermediate valent. Also, in the nickel compound, a valence fluctuating crossover behaviour can be observed in those compounds.

T	c (Å)	c/a	P-P-distance (Å)	collapsed?
Fe (26)	11.230	2.942	3.268	no
Co (27)	11.348	3.014	3.273	no
Ni (28)	9.469	2.405	2.371	yes
Ru (44)	10.772	2.673	3.302	no

Table 10.1: Lattice parameter c, parameter ratio c/a and P-P-distances of $EuFe_2P_2$ [86], $EuCo_2P_2$ [83], $EuNi_2P_2$ [84] and $EuRu_2P_2$ [87].

10.2 Previous works

In this section, the relevant physical properties will be discussed: the pressure induced collapse in the compounds $EuFe_2P_2$, $EuCo_2P_2$ and $EuRu_2P_2$ and the valence fluctuations in $EuNi_2P_2$.

10.2.1 Structural collapse in $EuFe_2P_2$, $EuCo_2P_2$ and $EuRu_2P_2$

The three compounds $EuFe_2P_2$, $EuCo_2P_2$ and $EuRu_2P_2$ all exist in the non-collapsed phase of the 122 structure and order magnetically under ambient conditions. $EuFe_2P_2$ and $EuRu_2P_2$ order ferromagnetically at $T_C = 29\,\mathrm{K}$ for both the iron [14] and the ruthenium compound [88]. For the iron case, a canting of 17(3)° away from the c direction is reported [89]. The ordering is solely performed by the europium moments with a moment of reportedly $\mu_{eff} = 6.6(3)\,\mu_B$ in the iron case [89] and $\mu_{eff} = 7\,\mu_B$ in the ruthenium case [88]. Also, the iron system was reported to exhibit Kondo type behaviour, for example to be extracted from the magnetoresistance behaviour, indicating a Kondo energy scale of $T^* = 29\,\mathrm{K}$, which is said to be consistent with the ferromagnetic order on the said energy scale [14].
$EuCo_2P_2$ on the other hand is reported to be an incommensurate helimagnet, ordering at $T_N = 67(\pm 1)\,\mathrm{K}$ with moments in the ab plane and a propagation vector of $(0\ 0\ z(T))$, where $z(T)$ evolves between about 5/6 for $T \approx T_N$ and about 6/7 for $T \to 0$ [90]. The *ab* plane is the easy plane of the system, which exhibits a metamagnetic transition at about 7 T [15]. Sangeetha also determined the europium 2+ moment to be the relevant ordering moment and extrapolated a maximum critical field of the magnetic phase of 28 T for $T \to 0$. They characterized the behaviour as AFM spin wave behaviour and gave a Debye temperature of $\Theta_D = 151\,\mathrm{K}$ (with the caveat of underestimation due to magnetic ordering) [15].

All these three compounds can be driven towards the collapsed phase by applying physical pressure. Huhnt and others performed X-ray diffraction on powdered samples of the three compounds. For the iron compound and the ruthenium compound they found a broad collapse of the *c*-parameter by 2 Å and 1.2 Å respectively over a range of 100 kbar for each collapse, while in relation the *a*-parameter only undergoes small changes. The broadness of these collapses might fit a second order transition or a crossover description. Also, over the course of the continuous

structural transition, the valence shifts towards an intermediate valent state [18]. The cobalt compound on the other hand shows a sharp collapse by 1.5 Å at a pressure of about 35 kbar, that hints towards a first order transition. At this critical pressure, the c-parameter shrinks by about 1 Å, while the a-parameter enlarges by about 0.1 Å. Hence, the volume also decreases by about 10 $Å^3$. Huhnt and others account the comparably large decrease in volume (compared to the reference compound $LaCo_2P_2$) to an enhancement of the Eu valence in the high pressure collapsed phase (since the ionic volume of Eu^{3+}-ions is smaller than of Eu^{2+}-ions). They claim the collapse of the structure to be connected to a shift in valence from being divalent and magnetic to being nonmagnetic and intermediate valent or trivalent [91]. When the europium magnetism is suppressed by pressure, cobalt magnetism emerges in the system [92].
In $EuFe_2P_2$ also negative pressure manipulations have been conducted. For a doping series with arsenics in $EuFe_2(P_{1-x}As_x)_2$, it was calculated, that from the volume of the pure $EuFe_2P_2$ of about 164 $Å^3$ onwards to larger cell volumina (i.e. negative pressure e.g. by arsenics doping on the phosphorus place) the europium remains divalent and magnetic [93]. For positive pressures, the electronic behaviour of $EuFe_2P_2$ not reported to be measured or calculated. Hence, it is unclear how the reported structural transition might interplay with the electronic states of the europium ions in the compound. Since the structural transition is reported to take place over a large pressure range of 100 kbar, the question arises whether there might occur a valence shift of the europium to an intermediate valent state in the same pressure range, and whether this can be investigated, eyeing the relation between structural and electonic properties.

10.2.2 Intermediate valence in $EuNi_2P_2$

$EuNi_2P_2$ is a special case among the EuT_2P_2-class of compounds, since it is already collapsed in the ground state at ambient conditions (compare table 10.1), hence also displaying a intermediate valent ground state, that undergoes a valence shift in course of changing temperature. Also, $EuNi_2P_2$ is under investigation on showing heavy fermionic behaviour [17].
In 2013, Hiranaka and others reported on the electronic properties of $EuNi_2P_2$ [17]. They stated for the valence of the europium atoms a development with the course of lowering temperature, that begins with a valence of about 2.25 at room temperature, and leads to an almost maximally mixed valence of about 2.48 at low temperatures. This development is directly coupled to a similar effect in the volume thermal expansion contribution of the 4f electrons. The volume anomaly related to the valence change is about 0.7%.
But what the system was investigated for most recently, was not its intermediate valence properties, but rather the question, whether it is a heavy fermion system or not. In 2009, Danzenbächer and others, after photoemission spectroscopy measurements, stated the effective mass of the system to be 20 to 50 electron masses, and the ground state only weakly affected by hybridization [94], and thus concluded $EuNi_2P_2$ not to be a heavy fermion system.
Later, Hiranaka and others [17] contributed their analysis of electronic properties of $EuNi_2P_2$, which still were favouring a way of understanding them as the

realization of a heavy fermion system dominated by the Kondo effect. They grounded their argument on several separated analyses. First, they found an enhanced Grüneisen parameter $\gamma \approx 100\,\mathrm{mJ/(K^2\,mol)}$ for their low temperature specific heat fit, indicating an enhanced effective mass (but potentially compatible to the estimation from [94]).
At low temperatures they find the magnetic susceptibility to remain approximately constant at an enhanced level of $\chi(0) \approx 0.04\,\mathrm{emu/mol}$ for the in-plane and out-of-plane directions with only a slight anisotropy, which was read as an indicator for a Kondo screening. They also found the thermal expansion coefficient, after being close to constant for a large temperature range at high temperatures, to rise to a maximum at 40 K before it approaches zero for $T \to 0$. This development occurs qualitatively the same way both in-plane and out-of-plane, but quantitatively the effect is anisotropic, being enhanced along the c direction. In the resistivity, Hiranaka found a broad maximum they located at around 80 K, and a Fermi Liquid like behaviour of the resistivity at lower temperatures, with offset $\rho_0 = 19\,\mu\Omega\mathrm{cm}$ and scaling parameter $A = 2.3 \cdot 10^{-2}\mu\Omega\mathrm{cm/K^2}$.
In analogy to findings in $CeRu_2Si_2$ they account all these effects to a supposed Kondo effect in $EuNi_2P_2$ with a characteristic energy scale of $T_K = 80\,\mathrm{K}$, causing the scattering maximum in the resistivity at T_K and a maximum in the thermal expansion coefficient at $T_K/2$. The volume shrinkage with decreasing temperature as well as the valence shift they say to be "reflecting the evolution of the heavy fermion state".
On the other hand, Medvedev and others [69] investigated $EuNi_2P_2$ under pressure and found a different explanation for the broad maximum in resistivity. Upon measuring resistivity up to 31 GPa they found the broad maximum to "shift[.] towards higher temperatures and tend[.] to be smeared out" above 7.5 GPa. Above 24 GPa the maximum even vanishes.
Their attempt to explain the resistivity features is the dynamic alloy model. This model assumes the mixed valence of the sample to root in two pools of integer value ions of europium (i.e. 2+ and 3+) being statistically distributed over the Eu lattice places with occupation probabilities $p_2 + p_3 = 1$. The compound is then described in terms of the majority ions, the minority ions are dealt with as impurities. Hence, from the minority ions an elastic Coulomb scattering potential arises, which istelf fluctuates, since the base of ions is fluctuating. In this setting, the largest scattering will happen und thus the largest resistivity is to be measured at the temperature where the Eu valence undergoes the steepest change (i.e. in the inflection point of the valence development).
Also, just in 2020, Stockert and others investigated on the thermopower of $EuNi_2P_2$ and succeeded quite well in describing the thermopower by a simple two-parameter model $S = A_2T - A_1\dfrac{d\nu}{dT}$, where A_2 fits a linear base-thermopower and A_1 contributes a value resembling the temperature dependence of the non-integer valence of $EuNi_2P_2$ [95]. Thus they succeeded to describe the systems thermo power explicitly not using any hybridisation or heavy fermion models.
For the explanation of the electronic features in $EuNi_2P_2$, it is still unclear, whether they are solely attributable to the valence properties of the europium, or whether they might be influenced by Kondo screening.

10.3 $EuFe_2P_2$

The growth of the iron 122 europium phosphide, $EuFe_2P_2$, was not primarily a target of my work, but rather a means of preparing other experiments, as pursuing the 1144 europium phosphides $EuAFe_4P_4$, as described in chapter 11. For the 1144 compounds, both flux approaches and solid-solid reaction approaches were pursued, and both sorts of approaches had to rely in some way on the growth processes for the ternary mother compound $EuFe_2P_2$. Hence, I report here on flux, direct and solid-solid preparations of the 122 compound $EuFe_2P_2$ very briefly.

Batch number	Method
MP501	Tin flux
MP512	Direct
MP513	Solid-solid
MP524	Solid-solid

Table 10.2: Different growth attempts to $EuFe_2P_2$ and their batch numbers.

In the previous works, investigations on $EuFe_2P_2$ have either been conducted in the low temperature regime, but at ambient pressures (in order to investigate the magnetic structure of the compound [14, 89]), or in the high pressure regime, but at room temperature (to investigate the collapse of the crystal structure [18, 91]). A major interest on this ternary compound hence was to start investigating the combination regime of low temperatures and high pressures. With this, a two-dimensional area of the generalized Eu-valence phase diagram becomes accessible. Therefore, a beam time at ESRF in Grenoble for low temperature, high pressure X-ray diffractometry on $EuFe_2P_2$ and $EuRu_2P_2$ was applied for.
In this subchapter, only the different growth approaches are discussed, since the basic physical characterization (under ambient pressure) of the system was the objective of the master's thesis of Duc Nguyen [96] at the KML Frankfurt.

10.3.1 Flux method growth

The flux growth of $EuFe_2P_2$ only consisted of one growth attempt, where the refinement of the growth process was actually objective of the Master's thesis of Duc Nguyen in the Crystals And Materials Lab [96], to whom the credits for the development of this growth prescription have to go. I include this report to credibly establish the base for the flux approaches to the 1144 compounds in chapter 11.2.2.
The flux growth (experiment with batch number MP501) took place in quite a basic setup. As a solvent, tin flux was chosen and added to the elements (in which, europium was contained with a slight excess) up to about 80 At-% of flux. The total composition of elements was Eu:Fe:P:Sn = 1.2:2:2:20. A total of 15 g of material were piled in elemental layers, separated by flux material, and sealed inside a quartz ampoule with an inner diameter of 14.5 mm, a wall thickness of

1.25 mm and an approximate length of 150 mm. In a box furnace (of the Therm-Concept construction type), the ampoule was heated up to 1100 °C, held there for two days, then cooled down to 880 °C fastly and then down to 680 °C with a slower rate of 4 K/h within approximately two days. The whole temperature profile is shown in fig. 10.2.

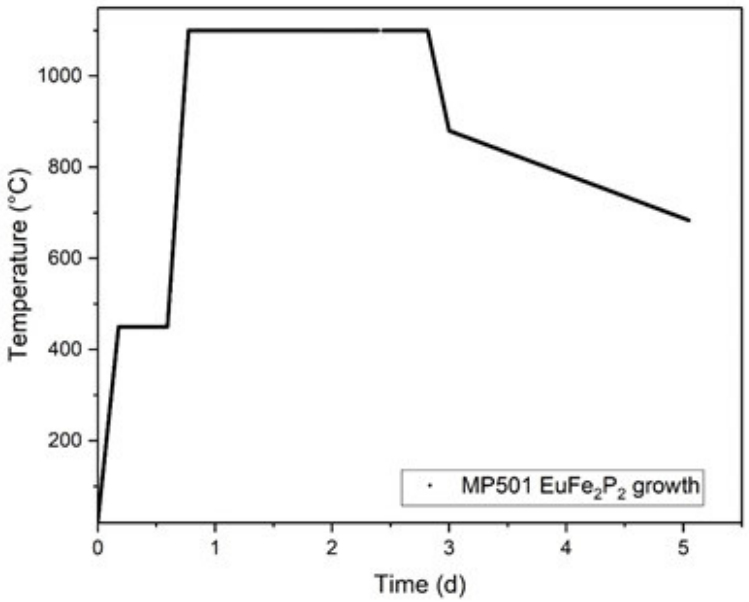

Figure 10.2: Temperature profile for the $EuFe_2P_2$ growth experiments, modified after [96].

After the main growth process, the quartz ampoule is sawed open and heated up to 300 °C again in a smaller box furnace. When the flux has turned liquid again, the ampoule is effused into an Alumina basin, where the melt resolidifies, to enhance the surface of the whole yield (crystals and flux). This is done in order to reduce the time needed for the next step, where the tin flux is removed by etching with hydrochloric acid.
The results of this attempt were satisfactory, yielding platelike crystals of the target phase $EuFe_2P_2$ with characteristic length scales of 3-4 mm, but only in the range of about 50 µm thin, with a mean weight over the ten largest crystals of 7.1 mg. Some crystals of this growth attempt are shown in fig. 10.3.
Alongside with the target phase, also considerable amounts of the binary phase Fe_2P were synthesized. This was detected via PXRD. EDX measurements on the $EuFe_2P_2$ crystals showed a phosphorus surplus of about 4 At-% on the expense of europium (approximately 1-1.5 At-%) and iron (approximately 2.5-3 At-%), measured in April 2020. Later in 2020 and early 2021, a remeasurement showed a phosphorus surplus of about 8-10 At-%. This has also been seen in other phosphides and hints to problems with the EDX detector. In mid 2021, additional WDX measurements were conducted with Dominik Hezel from the Geosciences institute [97], to confirm whether and how much the phosphorus surplus is an actual effect in the crystals. I assumed some of the effect to be due to the crystals (maybe up to the 4 At-% of the first measurement, maybe slightly less, in concordance with findings of a phosphorus surplus in some and none in other

(a) (b) (c)

Figure 10.3: Some $EuFe_2P_2$ crystals from the batch MP501.

crystals of a similar compound, $CeCo_2P_2$, in my master's thesis [32]), and the rest, especially the change in later 2020, to be due to measurement issues.
To conduct this sort of "gauge" measurement for different compounds among those also $EuFe_2P_2$, one crystal each was selected and cut in half. One half was measured by our EDX, the other half with the WDX apparatus of the Geoscience institute. Hence, it can be assumed that the results are comparable.
Indeed, the standartized WDX measurements show an entirely different picture. Since they are much more reliable than our own EDX measurements, it is to assume, that our own EDX heavily underestimates 4f and 3d materials (or overestimates phosphorus, but since the 4d materials appear to be normal, the former is the more probable case). In the specific case of $EuFe_2P_2$, the comparison yields, what can be seen in table 10.3.

	Eu (at-%)	Fe (at-%)	P (at-%)
EDX	17.54	34.11	48.35
WDX	19.76	41.44	38.80
difference	-2.22	-7.33	+9.55

Table 10.3: Comparison of EDX and WDX of $EuFe_2P_2$. The difference means deviation by EDX, hence positive sign is a surplus in EDX over WDX, a negative sign vice versa. WDX data [97].

Phosphorus is overestimated by EDX by about 10 At-%, and iron is more heavily underestimated than europium. This also shows in other crystals investigated. We looked at EuT_2P_2 (with T = Fe, Co, Ni, Ru), $LnCo_2P_2$ (with Ln = La, Ce) and $CeRu_2P_2$. In all crystals investigated, 4f and 3d elements are underestimated to the benefit of the remaining elements; 4d is estimated as it would be expected. The detailed data will be shown later for the compounds discussed in this chapter.

10.3.2 Direct growth

An approach to gain polycrystalline samples of $EuFe_2P_2$ is to simply bring the bare elements to reaction. This approach was conducted in analogy to the prescriptions for AFe_2P_2 by Wenz and Schuster [98], with europium instead of the

alkaline metals. The elements (Eu:Fe:P) are put inside an alumina crucible together with a ratio of 1:2:2, that resembles the compound that shall be targeted. In the MP512 experiment I used a total mass of 1.5 g of elements in that ratio. The arrangement of the elements inside the crucible does not matter too much, since the reactions will take place between a solid (Fe) a liquid (Eu) and a gaseous (P) element, which makes stackings obsolete. To protect the elements from air contamination, and also to shackle the phosphorus, so it reacts with the other elements instead of evaporating, the alumina crucible is sealed inside an outer niobium crucible. The outer niobium crucible is placed inside the Linn box furnace, a box furnace at hand, in which a protective argon atmosphere can be established.
The setup is heated up to 900 °C with a ramp of about 100 K/h, dwelling at 500 °C for 10 hours in order to give opportunity to the slowly evaporating phosphorus to react with the other elements before increasing the heat and therefore the vapor pressure, accelerating the evaporation of phosphorus. At the target temperature, the setup was held for two days.
The analysis of a powder X-ray diffractogram of the resulting grey powder yielded about 54 % of $EuFe_2P_2$, the rest being constituted from different binary compounds (see table 10.4).

Compound	structure	proportion
EuP	Fm-3m [99]	0.22
FeP	Pnma [100]	0.07
Eu_4P_3	I-43d [101]	0.17
$EuFe_2P_2$	I4/mmm [86]	0.54
Total		1.00

Table 10.4: Quantitative PXRD analysis of MP512.

10.3.3 Solid-solid growth

The previous approach of directly reacting the elements together can be enriched with other layers of prereaction to improve the outcome. The method of sintering binary phases of the Eu-P and Fe-P systems in order to achieve $EuFe_2P_2$ has already been conducted before, e.g. by Ren [102], Feng [14] and Ryan [89]. The concrete experiment is designed only in very loose analogy to those reports, since Feng and Ryan refer to Ren, and Ren crafted another compound, a 30% phosphorus doped $EuFe_2As_2$.
Either, the results of a direct approach can be thoroughly ground, pressed into pellets, sealed in another niobium crucible, and sintered for another period of several days. Or, another way to enhance the outcome is to already go into the first round of heating with some prereacted materials in the correct ratio. For $EuFe_2P_2$, this would be for example:

$$1\,\mathrm{EuP} + 1\,\mathrm{Fe_2P} \rightarrow 1\,\mathrm{EuFe_2P_2}$$

Fe_2P can be purchased, the EuP has to be prereacted in advance.

Prereacting EuP

Since for the solid-solid annealing approach, one ideally has to prereact all of the phosphorus involved, besides using iron phosphides, it is necessary for certain mixtures to even prepare some europium phosphides to actually provide the correct amount of phosphorus.
A complete binary phase diagram of the europium-phosphorus system is not reported so far, but a variety of solid phases are known [31]. The most desirable phase would be EuP. Yet, for EuP, an established synthesis process can hardly be found, while for another phase, EuP_3, such a process was recently published [103]. There, europium and phosphorus were sealed in a stochiometric ratio in a carbonized silica ampoule. This setup was heated to 850 °C with a rate of 50 K/h and held there for two days.
Since the described method is very straight forward, and since we don't need a stochiometric compound of EuP, but only an average stochiometry in our result, that is predictable (and predicted by the starting material ratio of the prereaction), the method was simply adapted to the EuP-case with some minor changes: For our purposes, since we can't protect the europium from reducing a silica ampoule by carbonization, we can exchange the silica ampoule in the setup by a closed niobium crucible. Therefore, the experiment was then conducted under an argon atmosphere. Also, the setup was heated up to 900 °C instead of 850 °C.

Compound	structure	proportion	proportion Eu	proportion P
EuP	Fm-3m [99]	0.11	0.055	0.055
EuP_3	C12/m1[104]	0.18	0.045	0.135
Eu_3P_4	Fdd2 [105]	0.11	0.047	0.063
Eu_4P_3	I-43d [101]	0.6	0.343	0.257
Total			0.49	0.51

Table 10.5: europium phosphides gained from the prereaction MP508.

The results of a first Eu-P-prereaction (batch label MP508) are coarse grey solids, mostly of a dull colour, but with occasional shiny surfaces. Upon air, the solid starts slowly degrading from the surface, forming yellow powders, which probably are europium hydroxide (and probably additional phosphane). A powder diffractogram of this result yielded an inhomogeneous mix of different europium phosphides, as listed in table 10.5. In total, the Eu-P-ratio of a portion of the result still is close to the initial ratio of 1:1, even on lower scale. Hence, this inhomogeneous mix of phases is still good enough as a prereaction for europium and phosphorus.

Main reaction

With the batch number MP513, the prereacted Eu-P constituent and the Fe_2P with a ratio of 1:1 and a total mass of 2 g were ground together and put into an alumina crucible together, which was then sealed inside an niobium crucible under argon protective atmosphere. Just as for the direct growth, the setup was

heated up to 900 °C with a ramp of about 100 K/h, dwelling at 500 °C for 10 hours. At the target temperature, the setup was held for two days.
A powder X-ray diffraction analysis of the resulting powder yielded about 50 % of the target phase (which is slightly worse than the direct approach, but the significance of this difference is doubtful), while the other half consists of binary phases, that correspond to the initial ingedients (but the Eu-P complex seemed to be homogenized to EuP). The results are shown in table 10.6.

Compound	structure	proportion
Fe_2P	P-62m [106]	0.10
EuP	Fm-3m [99]	0.40
$EuFe_2P_2$	I4/mmm [86]	0.50
Total		1.00

Table 10.6: PXRD quantitative analysis of MP513.

Subsequent sintering

Both approaches of the direct growth and the solid-solid approach with prereactions of binaries yielded about 50 % of the target phase in the first run. For serious investigations (e.g. the plannings on low temperature X-ray diffractometry under pressure), the gained $EuFe_2P_2$ need to be, of course, as phase pure as possible. In order to purify the samples, the results of the primary growth attempts can be subsequently sintered to induce further solid-solid reactions between the europium phosphides and the iron phosphides and thus to enhance the target phase compound.
The results of the growth attempts MP512 and MP513 hence were pooled together to form a new batch MP524 (with a total mass of about 3 g and constituted of about 50 % $EuFe_2P_2$ and 50 % binary phosphides featuring europium and iron), which was designated to be sintered subsequently. The powders were ground, pressed into pellets and sealed inside niobium crucibles, which were then placed inside the Linn box furnace under an argon protective atmosphere. For the growth process, in order to standardize it to the similar attempts of growing $EuRu_2P_2$ and the Alkaline based KRu_2P_2 and KFe_2P_2, a furnace heating profile was chosen, that was taken from reports of Paul Canfield [107]. The furnace was firstly heated with 50 K/h to 230 °C and held there for an hour (this stage is due to the Potassium in the other attempts), then again held at 500 °C for 10 hours (due to the phosphorus), and lastly brought to 900 °C to be held there for four days. This process can be repeated ad libitum, until the resulting powder is sufficiently pure.
The results of the iterative purification process can be visualized using PXRD as a means of quantitative phase analysis. The results are shown in table 10.7. The growth of $EuFe_2P_2$ with a pureness level of about 85% took three runs of the sintering process depicted above (initial direct growth included).

Compound	Run 1 (512+513)	Run 2 (524)	Run 3 (524)
Fe_2P	0.100	0.340	0.165
EuP	0.400	0.003	0.000
$EuFe_2P_2$	0.500	0.657	0.835

Table 10.7: PXRD quantitative analysis of MP524's subsequent experimental steps.

10.4 $EuRu_2P_2$

When later in the work process on the 1144 compounds Paul Canfield gave some advice to me in a private communication accompanying his paper on the 1144 compounds [107], it became more and more reasonable to also parallely try and grow a ruthenium based 1144 compound, to have another shot. For this, and also in preparation of the planned low temperature X-ray diffractometry under pressure (compare the introductory texts to sections 10.3 and 10.6), it became necessary to also prepare growth attempts for polycrystalline samples of $EuRu_2P_2$. In this work, I will only discuss growth attempts for polycrystalline samples, that are as phase pure as possible. An account of the growth of single crystals of $EuRu_2P_2$ out of an external flux and also a detailled account of the magnetic properties of the compound were the objective of Julian Reusch's master's thesis in the Crystals and Materials Lab [108]. A detailed account of the magnetic properties of $EuRu_2P_2$ was only published recently [16]. This is not included in the above section 10.2, since this compound is here only looked at as a preparation for the experiments towards the existence of a 1144 phase later reported in this work (chapter 11). An account of magnetic characterization of $EuRu_2P_2$ and $EuFe_2P_2$, which was preemted by Proschek, will still be included in a general overview over the EuT_2P_2 systems attached to the high pressure low temperature diffraction experiments' report [109].

10.4.1 Direct growth

Parallel to the direct attempt of the iron compound, the ruthenium based compound $EuRu_2P_2$ is begun to be synthesized by a direct attempt. Experimental batch MP523 has been synthesized like this: In the correct ratio of 1:2:2 (Eu:Ru:P), the elements are placed inside an alumina crucible, that is sealed inside a niobium crucible under an argon protective atmosphere. In the Linn furnace, protecting the niobium crucible from air contact via an argon atmosphere, the temperature profile from the prepreactions in the Canfield 1144 paper [107] was utilized. With a rate of 50 K/h, the setup was heated to 900 °C, dwelling for one hour at 230 °C (for the Potassium in the simultaneously conducted experiments for KFe_2P_2 and KRu_2P_2) and for 10 hours at 500 °C (for the phosphorus to prereact with the other elements), and at last for four days at the target temperature.
Analysing the resulting powder with X-ray diffractometry shows, that the target compound seems to have formed to an extent of below 10% (see table 10.8), but

still, it has formed at least. The ratios between the binary compounds are probably flawed to an extent that is not well quantifiable, since before starting the measurement process, there is some opportunity for the air sensitive europium phosphides to get contaminated.

Compound	structure	proportion
Ru_2P	[110]	0.056
RuP	[100]	0.871
Eu_4P_3	[101]	0.001
$EuRu_2P_2$	[87]	0.072
Total		1.00

Table 10.8: PXRD quantitative analysis of MP523's first run. The Eu_4P_3 compound is underestimated.

A result of about 7% of the target phase is rather poor. This result I tried to enhance later by subsequent sintering of the results, as I will describe in the following subsection.

10.4.2 Solid-solid growth

In order to enhance the yield of the target phase $EuRu_2P_2$, also here a series of subsequent sintering processes can be started. Until the yield is sufficiently large in proportion, the resulting powder will be ground and pressed into pellets, which are sealed in niobium crucibles and then exposed to the same temperature profile as described previously, dwelling four days at 900 °C. Afterwards, a small portion of powder is extracted to perform powder X-ray diffraction and determine the yield. The rest of the sample can be prepared for another round of sintering, if necessary.

Compound	Run 1	Run 2	Run 3
RuP	0.871	0.238	0.015
$EuRu_2P_2$	0.072	0.657	0.940
Others	0.057	0.105	0.045

Table 10.9: PXRD quantitative analysis of MP523's subsequent experimental steps.

Table 10.9 shows the results of a quantitative phase analysis of the growth iterations with powder X-Ray diffractometry. The growth of $EuRu_2P_2$ with a pureness level of 94% took three runs of the sintering process depicted above (initial direct growth included).

10.5 $EuCo_2P_2$

The $EuCo_2P_2$ compound is special among the compounds discussed in this chapter, since the collapse of the tetragonal phase under pressure is of first order (whereas it is seemingly of second order for the iron compound and the ruthenium compound).
This compound was approached with an external tin flux method. Since this work does not focus too much on magnetic order, the physical characterization part was more centered about confirming the reproduction of the previously known physical properties of the system, while the main effort was put into shaping the growth process in a way that the resulting single crystals are fit for further investigations, mainly ARPES.

10.5.1 External flux growth

For the growth of the $EuCo_2P_2$, two previously known experimental prescriptions were tested on whether they also fit for the $EuCo_2P_2$ compound, namely the prescription developed by Duc Nguyen for $EuFe_2P_2$ [96] and the one I myself developed in my master's thesis for $CeCo_2P_2$ [32]. Both were assumed to be a good starting point, since only one of the partaking elements was to be replaced, cerium to europium and iron to cobalt respectively. It is a known word of mouth, that lanthanoids more often than not replace each other quite well due to a chemical "alikeness", and also the transition metals can be expected to behave chemically at least somewhat equal.
Starting from these two setups, five experiments were conducted, which are listed in table 10.10. The transfer of the previously developed prescriptions worked out quite fine, so that not much more effort was necessary. One experiment was conducted to see whether an enhancement of the maximum temperature can lift the already very good results, but apart from this, the transferred prescriptions yielded immediate and reproducable success.

Batch No.	composition	maximum temperature (K)	experimental design
MP601	1.2:2:2:20	1180	A
MP602	1.6:2:2:30	1180	A
MP603	1.6:2:2:30	1300	B
MP604	1.2:2:2:20	1180	A
MP605	1.6:2:2:30	1180	A

Table 10.10: Overview over the $EuCo_2P_2$ growth experiments.

Experimental design A

The elements (in this cases, always about 15 g of total mass) are weighed in according to the designated composition (Eu:Co:P:Sn = 1.2:2:2:20 or 1.6:2:2:30) and then put into a quartz ampoule in an elementwise layered fashion, the elemental

layers separated by flux interlayers. The quartz ampoule is sealed under constant pumping (with a pressure of about 10^{-2} mbar of a threefold purified argon atmosphere inside) and then put inside a box furnace of the ThermConcept type. The applied temperature profile is given in fig. 10.4. With a 10 h hold at 450 °C (in order to let the phosphorus slowly prereact with the other ingredients before the vapor pressure takes over), the setup is heated to 1180 °C with 100 K/h, held for 10 h, then cooled down to 900 °C with 2 K/h and from there to 800 °C with 10 K/h before shutting down the furnace.
After the growth process, the quartz ampoule is sewed open, and in open stance heated up to 300 °C again, in order to pour out the material, especially to have more surface on the tin part for the following step. The tin is then removed by bathing the sample in hydrochloric acid for 1-3 days.

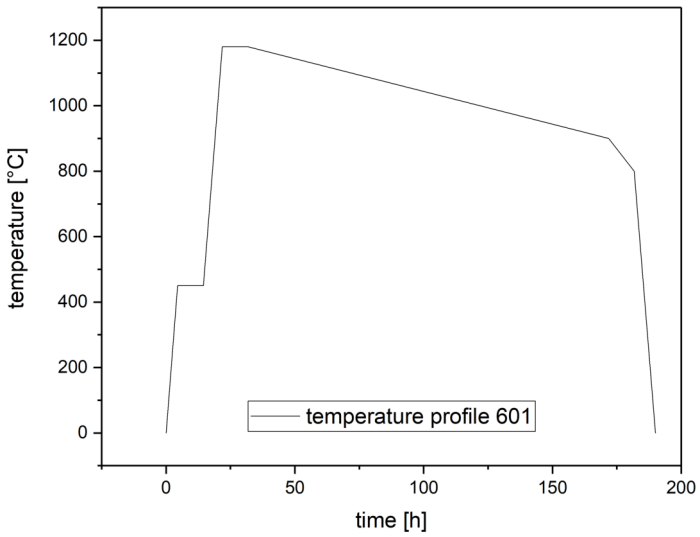

Figure 10.4: Temperature profile for the $EuCo_2P_2$ growth experiments in the ThermConcept furnace, modified from [32].

Following are the descriptions of the growth results and their analyses for the four growth experiments using design A in order to grow $EuCo_2P_2$.

MP601/604: These were the two experiments guided by the $EuFe_2P_2$ approach in [96]. Both experiments were taking place using the same parameters, MP604 simply being a reproduction experiment to solidify the findings (especially in comparison to the other experiments MP602/MP605). The settled composition for these experiments was Eu:Co:P:Sn = 1.2:2:2:20. The temperature profile was guided by [32] instead (fig. 10.4), in order to be able to perform the comparison experiments in the same furnace at the same time.
In MP601, only few crystals of the target phase were to be found, none of them exceeding the characteristic length scale of 1 mm. With PXRD quantitative analysis, about half of the results could be identified as the target phase, the other half as the CoP foreign phase. MP604 on the other hand showed some crystals of up to 2.5 mm edge length and a thickness of estimatedly up to 100 µm, and with an average mass of $\bar{m}_{10} = 6.2$ mg (averaged over the 10 heaviest crystals).

Some of the crystals are shown in fig. 10.5. Also, the amount of the CoP foreign phase was determined to be significantly lower in the MP604 experiment than in the MP601 experiment (5-10%).
These two experiments were set up with the exact same parameters. Hence, the two batches define a range of results which are to be expected if the $EuFe_2P_2$ growth prescription is applied to the $EuCo_2P_2$ system.

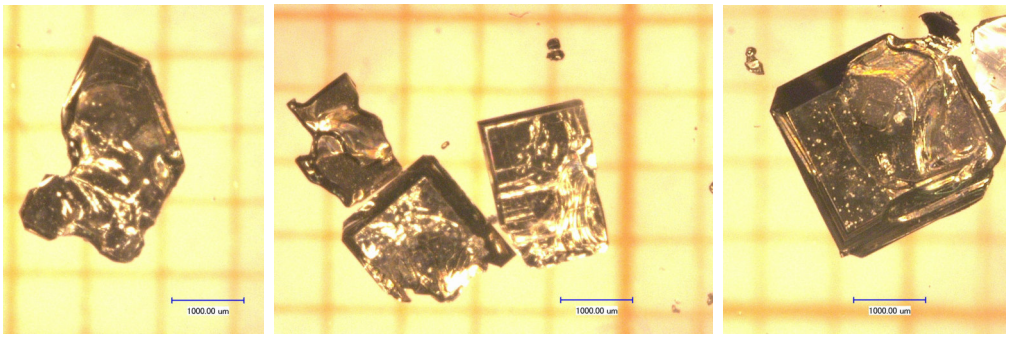

(a) (b) (c)

Figure 10.5: Some $EuCo_2P_2$ crystals from the batch MP604.

MP602/605: These were the two experiments closely related to the growth of $CeCo_2P_2$ in [32]. Also here, experiment MP605 was a reproduction of MP602, to strengthen the verdict on which of the two prescriptions is more appropriate. The composition of both experiments was Eu:Co:P:Sn = 1.6:2:2:30. Other than that, they used the experimental design A. In this case, the temperature profile applied was coherent with the one from the $CeCo_2P_2$ template.
In both experiments, crystals of a size sufficient for further investigations were grown. The characteristic length of the largest crystals was about 3 mm, with a thickness of about 100 µm, in both growth experiments. While in MP601 this was the exception, in MP605 they were to be found much more regularly. Since for both approaches the second try was the more productive one, this is probably due to the specific situation in the furnace. The average mass for the batch yielding the larger and more numerous crystals, MP605, is $\bar{m}_{10} = 12.8\,\mathrm{mg}$. Some of the crystals from batch MP605 are shown in fig. 10.6. With Laue diffractometry, the habitus of the crystal could be confirmed, that the thickness of the plateletts is along the crystalline 001-direction, while the edges of the rectangular surface correspond to the 100-direction in all cases investigated.
Using PXRD, MP602 was found to be quite pure in phase, while during the growth of MP605, a side phase $EuCo_8P_5$ (structure after [111]) formed to an amount of about 15%.
From MP605, also a sample was drawn for a comparative EDX-WDX-characterization. This comparison, as shown in table 10.11, showed quite similar results as in the iron case. While in the EDX analysis made in our own SEM, the sample seemed to relatively lack europium and cobalt, to the benefit of a large share of phosphorus, that was some over 10% above the expected value, the WDX did not confirm this, indicating even a very slight lack of phosphorus, while europium was found to the expected amount and a small excess of cobalt was measured. If anything,

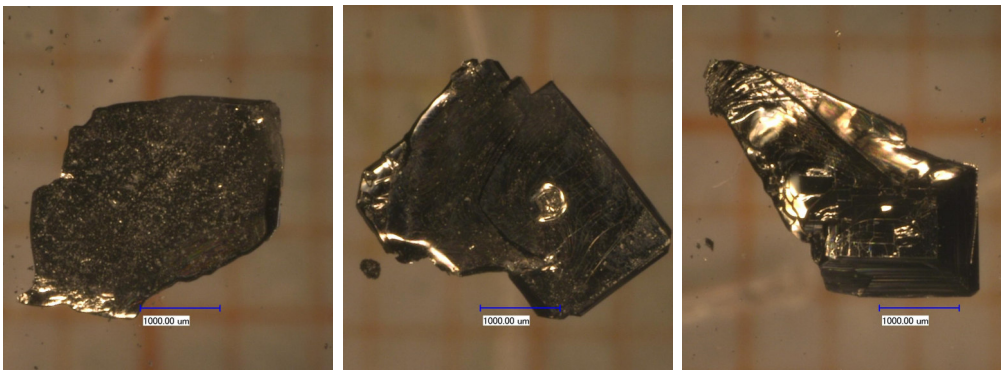

(a) (b) (c)

Figure 10.6: Some $EuCo_2P_2$ crystals from the batch MP605.

the disparity is even more extreme than for the iron compound. Since this also showed for the nickel compound, the problem with the disparity is most probably a problem with either the gauge of our detector (since we do not use standards) or with its sensitivity towards certain ranges of X-ray energies.

	Eu (at-%)	Co (at-%)	P (at-%)
EDX	17.63	32.22	50.15
WDX	20.05	41.85	38.10
difference	-2.42	-9.63	+12.05

Table 10.11: Comparison of EDX and WDX of $EuCo_2P_2$. The difference means deviation by EDX, hence positive sign is a surplus in EDX over WDX, a negative sign vice versa. WDX data [97].

To conclude for the two design approaches in comparison, this second approach, drawn from the $CeCo_2P_2$ system, yielded results, that were consistently better than from the approach drawn from the $EuFe_2P_2$ system, in the sense that the crystals gained were larger, the phase more purely obtained and the experiment more stable against incidental disturbances.

Experimental design B

Experimental design B was applied to lift the experiments to higher temperatures, for which quartz as an ampoule material is not an option anymore because of its softening above 1200 °C. To conduct growth experiments at higher temperatures, it hence is necessary to change the general setup. Instead of a quartz ampoule, a double crucible setup is used, where a graphite inner crucible (that is mostly inert against the melt) is sealed inside a niobium outer crucible (whose function it is to be tight and not let any vaporous parts of the experiments get lost). Since the outer crucible is metallic, it would oxidize at higher temperatures, and hence it is mandatory to use a furnace with an option to establish an argon protective atmosphere. Then, temperatures higher than the said 1200 °C can be applied.

As a furnace with both high enough temperatures and the possibility to establish a protective atmosphere, the Gero high temperature furnace is at hand. It has two additional features, that are something of a downside for the issue of translating the experiment to higher temperatures: It, first, has a temperature gradient on the inside, that is much stronger and more directed than temperature gradients in the box furnaces. It is hence impossible to only change the parameter of temperature - also, the parameter of temperature gradient has to be changed along with it. This is simply to be accepted. Second, the temperature profile is primarily made by driving the furnace around the sample and thus "pulling" the sample out of the furnace. Since the temperature profile of the furnace is nonlinear, it is not possible to recreate the temperature profile previously used. Instead, segments of fast and slow driving of the furnace are combined to another sort of profile. The temperature data can be collected to later display the actual temperature profile.

MP603: In the case of MP603, the adopted starting composition was Eu:Co:P:Sn = 1.6:2:2:30, and the maximum temperature was set to 1300 °C. With the motor of the Gero furnace being programmed to first drive fast for a short time and then with a constant slow velocity over five days, a temperature profile at the sample site as shown in fig. 10.7 was obtained.

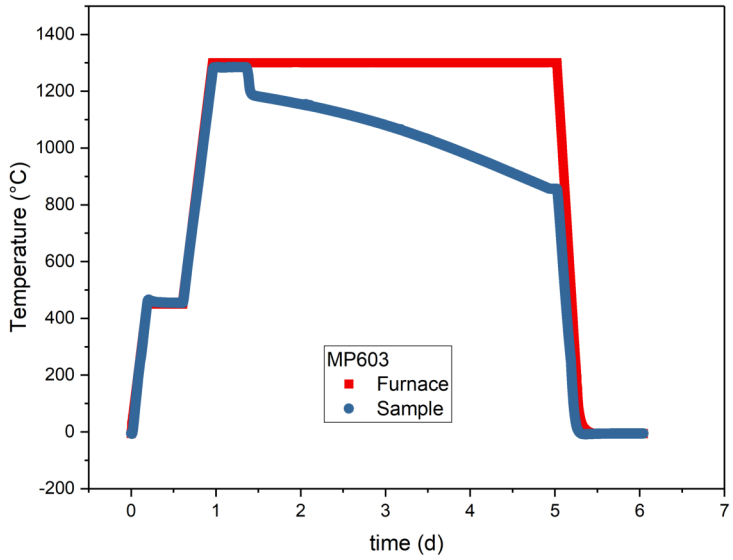

Figure 10.7: Temperature profile for the $EuCo_2P_2$ growth experiment MP603 in the Gero furnace, modified from [32].

The higher temperatures and stronger temperature gradients within the furnace did not benefit the growth of the target system $EuCo_2P_2$, but a competing side phase $Eu_2Co_{12}P_7$, which is a ferromagnet with $T_C = 151\,\mathrm{K}$ [112] and a hexagonal crystal structure [113], that forms crystals with the habitus of needles. Regarding ternary compounds, it was this side phase, that was grown exclusively. This was confirmed structurally by PXRD, and compositionally by EDX measurements. Additionally, binary cobalt phosphide could be found in minor amounts.
Since an enhancement of the experimental temperature seems to handicap the

growth of $EuCo_2P_2$, the way of enhancing temperature was not pursued any further than this one experiment.

10.5.2 Physical characterization

The physical characterization of this system mainly focussed on confirming the established magnetic structure of $EuCo_2P_2$, since the magnetism itself is of minor interest for the main arguments of this work, but information about the basic magnetic properties facilitate further investigation, as for example the ARPES measurements planned by the group of Denis Vyalikh on the europium phosphides as well.
From a specific heat measurement at low temperatures, the coefficients for the linear and T^3 term of the Debye model of the specific heat could be determined and compared to the literature:

Parameter	Value	Literature value
γ (in $\frac{\mathrm{mJ}}{\mathrm{mol\,K^2}}$)	22.4(11)	23.7(5)
β (in $\frac{\mathrm{mJ}}{\mathrm{mol\,K^4}}$)	2.91(8)	2.8(1)

Table 10.12: γ and β of $EuCo_2P_2$'s specific heat, compared to Sangeetha's propositions [15].

In both cases, the values' error intervals overlap to an extent that equality is not to be refused.
Probing the magnetization, first the Néel temperature of the system $T_N = 67\,\mathrm{K}$

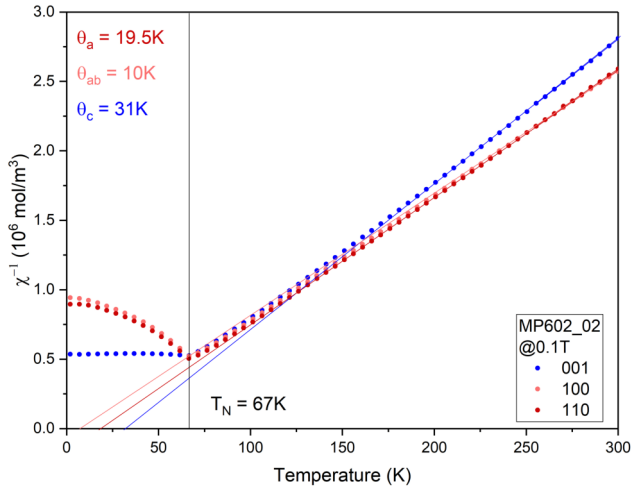

Figure 10.8: Temperature dependent magnetization of $EuCo_2P_2$ with Curie fits for 100, 110 and 001 crystal directions.

can be confirmed (fig. 10.8). Also, the ordering of the moments can be determined to take place in the *ab*-plane already by this simple measurements. The

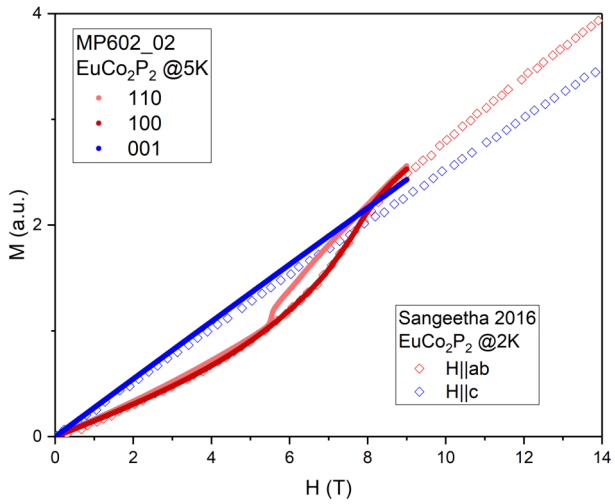

Figure 10.9: Field dependent magnetization of $EuCo_2P_2$ for 100, 110 and 001 crystal directions. In comparison with [15].

susceptibility in c direction remains constant in the ordered phase, and the response to an external field in the ordered phase is linear (fig. 10.9). In plane, on the other hand, susceptibility goes down in the ordered phase, and in the field response at low temperatures, the behaviour is curvy, distantly reminding of a metamagnetic transition.
The in plane behaviour, though, seems to be more complex than Sangeetha described it to be [15]. They simply regarded the 100 and 110 direction to be equivalent. As simple measurements show, both the field response and the temperature response of these directions differ in their quality and quantity, whatsoever. The field response of the two in plane directions was found to be non-equivalent, with only the 100 behaviour resembling what was the *ab*-behaviour for Sangeetha. Larger differences in the Curie-Weiss temperatures (that is: $\theta_{100} \approx 19.5\,\mathrm{K}$, $\theta_{110} \approx 10\,\mathrm{K}$ and $\theta_{001} \approx 31\,\mathrm{K}$) in fig. 10.8 on the other hand should not be overstated, but are probably artifact of the glueing of the samples.

10.6 XRD of $EuFe_2P_2$, $EuCo_2P_2$ and $EuRu_2P_2$ at high pressures and low temperatures

From September 28th until October 5th of 2021, Kristin Kliemt and myself from the Goethe university in Frankfurt, and Michaela Souliou and Amir Haghighirad from KIT in Karlsruhe, with support by Gaston Garbarino as the local contact at the ESRF, investigated on the high pressure regimes - pressure applied using a diamond anvil cell - of EuT_2P_2 at different temperatures, with single crystal X-ray diffraction as a probing technique. Crystals were taken from my works and Duc Nguyen's works [96] for $EuFe_2P_2$ system, from me and Franziska Walther [114] for the $EuCo_2P_2$ system and from Julian Reusch for the $EuRu_2P_2$ system [108]. Data were recorded for $EuFe_2P_2$ and $EuRu_2P_2$ at 15 K, 50 K, 100 K and 300 K in a pressure range from 0.1 GPa to 15 GPa, and for $EuCo_2P_2$ at 15 K and

300 K in a range from 0.1 GPa to about 12 GPa. The idea of this measurements was to track the measurements, that Huhnt performed on powder samples at room temperature [18] down to lower temperatures with single crystals and see, how the collapse of the structure evolves in the low temperature high pressure regime.
During experiments, samples were cooled inside a liquid helium cooled cryostate, and pressure was exerted using a diamond anvil cell. Pressure inside the cell was determined looking at the optical absorption spectra of a ruby crystal.
Data were evaluated in cooperation with Amir Haghighirad from KIT using CrysAlisPro from Rigaku for the integration of the crystallographic data and for testing space groups and lattice parameters, and Jana [115] and WinGX [116] for the refinement of the unit cell.
This part of the chapter in large parts will also be used for publication [109].

10.6.1 $EuRu_2P_2$

From integration of the collected data, the lattice parameters and symmetry group of the compound under the applied conditions can be drawn. For $EuRu_2P_2$, we find that no symmetry-changing transition occurs at any of the temperatures observed (15 K, 50 K, 100 K and 300 K) in the pressure range of 0-15 GPa, and the system can be described entirely in the I4/mmm structure of $ThCr_2Si_2$. At lower temperatures, in the diffraction data the reflex pattern separated some of the reflexes, indicating that maybe a small orthorombic distortion with twinning could play a role. But in general, lattice parameters a and b behaved equivalently (fig. 10.10a). Some sort of lattice anomaly is undergone before the sample is compressed linearly by pressure in ab directions, a small broadening, whose pressure scale is also temperature dependent. Over all temperatures, the pressure dependent behaviour of the compound remains equal (fig. 10.10b). The collapse of the c parameter happens gradually on a broad pressure scale, that finally levels out at about 12 GPa, being clearly not a first order structural transition. For

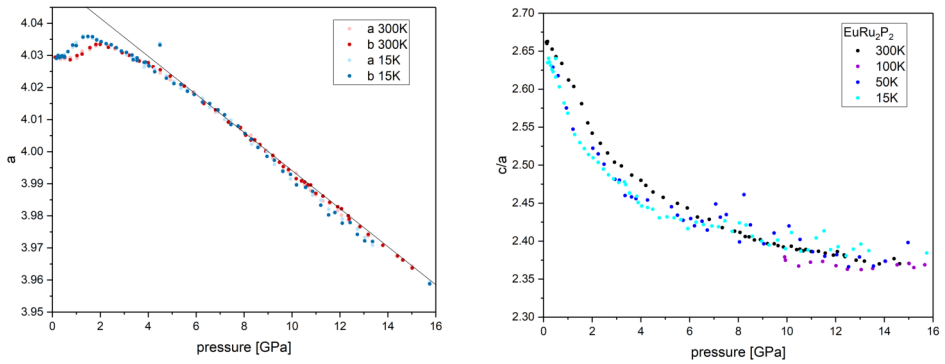

(a) a and b parameter (b) c/a ratio

Figure 10.10: Lattice parameters of $EuRu_2P_2$ from integration at temperatures 15 K, 50 K, 100 K and 300 K with pressures up to 15 GPa. a and b are shown separate, because they come different from integration and are later on symmetrized.

all the pressure sweeps at different temperatures, the collapse of the c direction

happens at a similar rate. In the a parameter, some non-linear feature can be seen, inflating the a parameter when applying low pressures ever so slightly. This effect seems to be temperature dependent.
From the lattice parameter data, a Birch-Murnaghan fit to gain information about the bulk modulus $B_0 = B(P=0) = -V(\partial P/\partial V)|_{P=0}$ of the system can be performed, using the formula developed by Birch [117]:

$$P(V) = \frac{3\,B_0}{2}\left[(V_0/V)^{7/3} - (V_0/V)^{5/3}\right] \cdot \left(1 + \frac{3}{4}\left(\left.\frac{dB}{dp}\right|_{P=0} - 4\right)\left[(V_0/V)^{2/3} - 1\right]\right) \tag{10.1}$$

where $V = a \cdot b \cdot c$ and V_0 is the volume of the unit cell at the lowest pressure. Fitting this empirical equation to the data sets for 300 K and 15 K (fig. 10.11), we find $B_0(300\,\mathrm{K}) = 34 \pm 1$ GPa and $B_0(15\,\mathrm{K}) = 28 \pm 2$ GPa. This is significantly

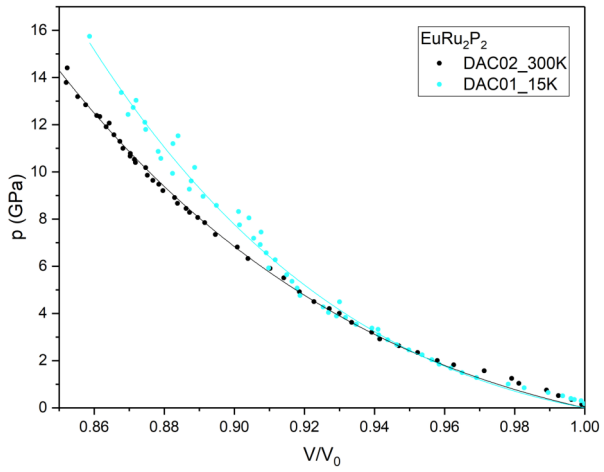

Figure 10.11: Birch-Murnaghan fit on the datasets at 15 K and 300 K for $EuRu_2P_2$.

lower than usually estimated for systems of the $ThCr_2Si_2$ class (e.g. 100 GPa for $EuPd_2Si_2$ [80]).

Refining the data yielded the collapse of the structure, not only in terms of the lattice parameters, but also the phosphorus-phosphorus interlayer distance could be tracked to show that from a large distance of more than 3 Å at ambient pressures, the layers' distance collapses towards 2.3 Å, where the distance levels out, which corresponds to the length of a phosphorus-phosphorus single covalent bond [82], which is established during the collapse. At 15 K, the z atomic position of the phosphorus atoms seems to react quite more intensively to external pressure than at 300 K. The lattice parameter evolves on the same pressure scale (fig. 10.10b), but the establishing of the P-P covalent bond happens significantly faster (fig. 10.12).
Integration of a good dataset identified mostly about 200-300 reflexes, of which at least 70 are marked as not fitting into the identified pattern. Of these 70 unfitting reflexes, about 65 can be accounted to two grains of diamond (the two pressure cell diamonds). From the rest of the unfitting reflexes (between 3 and 20 for some high pressure datasets), 3-7 are usually unidentifiable, and any leftover

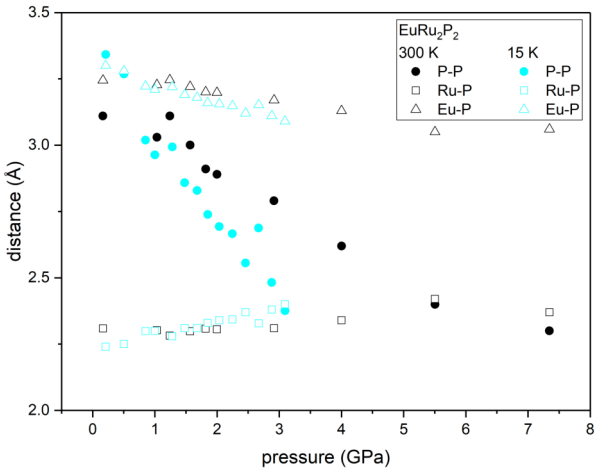

Figure 10.12: Atomic distances in the $EuRu_2P_2$ unit cell. Refinement with Jana did not work out for the 15 K dataset for pressures above 3 GPa.

reflexes in the low temperature (15 K) dataset are resembling the pattern of the target phase and deviating only by a tiny margin. This leaves open for discussion the possibility of small orthorombic distortions in the lower temperature regimes as discussed. In fig. 10.10a, it is shown, that integration yields slightly deviating a and b parameters, which are later symmetrized, but it is not clear that this is entirely correct.

10.6.2 $EuFe_2P_2$

In $EuFe_2P_2$, as in $EuRu_2P_2$, a broad collapse of the lattice parameter c can be seen, that already levels out at about 8 GPa (fig. 10.13a). The pressure scale of the transition in the iron compound appears to be smaller, although its scope is just a little bit larger. Ruthenium is isoelectronically a larger ion

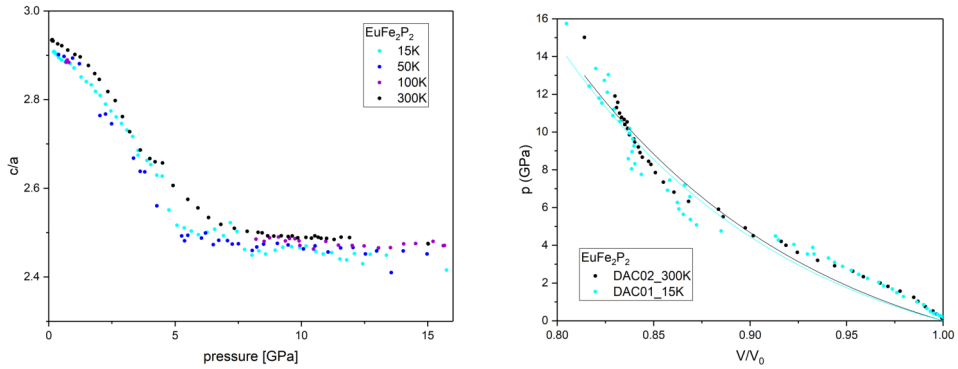

(a) c/a ratio (b) Birch-Murnaghan fit

Figure 10.13: Integrated data for the $EuFe_2P2$ system at 15 K, 50 K, 100 K and 300 K up to 15 GPa.

than iron, but does not in a strict sense correspond to a fixed and isotropic

chemical pressure, since the substitution affects the a and c lattice parameters differently. While the a parameter inflates, the c parameter deflates between $EuFe_2P_2$ and $EuRu_2P_2$. Also, the ruthenium compound is, regarding to the collapse between the two states, already placed somewhere in the process of the collapse, that starts without an onset, while an onset can be seen for the iron compound. Performing a Birch-Murnaghan fit on $EuFe_2P_2$, we can estimate the parameter as $B_0(15\,\mathrm{K}) = 28 \pm 4\,\mathrm{GPa}$ and $B_0(300\,\mathrm{K}) = 31 \pm 4\,\mathrm{GPa}$ to be in the same order of magnitude as for $EuRu_2P_2$. However, the model does not really seem to fit the data (fig. 10.13b), and a more refined model has to be found to make quantitative statements.
The refinement of the $EuFe_2P_2$ diffraction data is at the point of closure of this work still ongoing. Its results will be reported on later [109].

10.6.3 $EuCo_2P_2$

For $EuCo_2P_2$, in the integrated single crystal X-ray data, a sharp first order isostructural transition is clearly visible at 15 K and 2 GPa (fig. 10.14). The cobalt

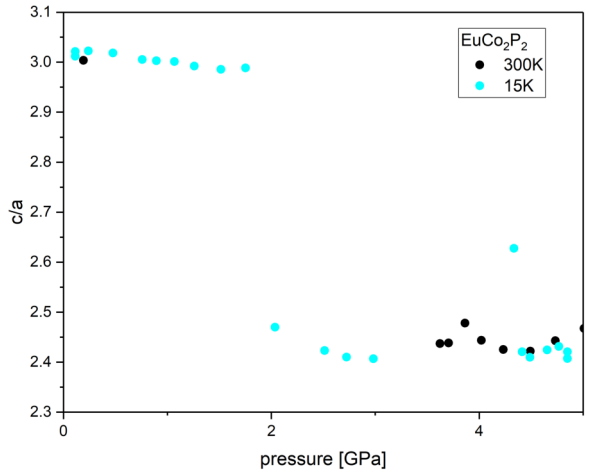

Figure 10.14: cobalt c/a ratio from integrated XRD data.

system could be refined in a I4/mmm structure at high and low temperatures, which both yield a clear model for both a collapsed (high pressure) and a non-collapsed (low pressure) structure. Refinement of the data confirms, that in the low pressure state, the distance between neigbouring phosphorus atoms is $3.1 \pm 0.3\,\text{Å}$ (fig. 10.15a), corresponding to a not established phosphorus-phosphorus covalent bond, and in the high pressure state the distance is $2.30 \pm 0.16\,\text{Å}$ (fig. 10.15b), corresponding to the length of a covalent single bond between two phosphorus atoms [82]. Hence, the first order transition is a true collapse of the I4/mmm structure. At 300 K, not enough data exist to pressurewise locate the transition and hence give a coarse estimation of its temperature dependence.

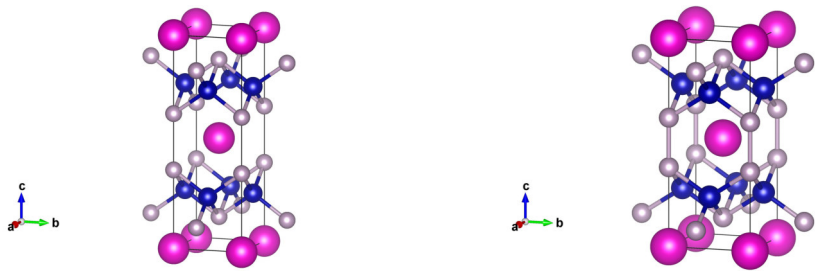

(a) $p = 0.12\,\mathrm{GPa}$ (b) $p = 11.5\,\mathrm{GPa}$

Figure 10.15: $EuCo_2P_2$ unit cells at low and high pressures at 15 K temperature. Pink: europium, blue: cobalt, grey: phosphorus.

10.7 $EuNi_2P_2$

The system of the EuT_2P_2 that is most interesting for our purposes at ambient conditions, is the $EuNi_2P_2$ system, since it has both a non-integer (intermediate) valence at room temperature and undergoes a transition to another intermediate valent state at lower temperatures.
This compound, as the cobalt compound, was approached using a tin external flux method. Samples were prepared for further measurements such as ARPES. Also, measurements were taken to try and get the basic figures of the valence transition described.

10.7.1 External flux growth

Experimental designs for the growth of $EuNi_2P_2$ were chosen just as for the $EuCo_2P_2$ compound: First, a low temperature attempt at up to 1180 °C was tried, that matches the **experimental design A** from section 10.5.1, with two different compositions of materials in a tin flux. One composition was designed after the $EuFe_2P_2$ procedure by Duc Nguyen [96], and one after my own master's thesis' description for the growth of $CeCo_2P_2$ [32]. The composition, that was more successful after two runs, was taken to higher temperatures in a design corresponding to **experimental design B** from section 10.5.1 to test the performance at higher temperatures. An overview over $EuNi_2P_2$ growth experiments conducted is given in table 10.13.

Experimental design A

Four experiments were conducted in the easily accessible quartz setup, as described in section 10.5.1. Experiments MP701 and MP703 were conducted with the composition with lower europium excess and lower flux ratio, while experiments MP702 and MP704 were conducted simultaneously with the experiment with the respective lower batch number in the same furnace, but with a higher europium excess and a higher flux ratio. The used temperature profile was the same as for the cobalt experiments (figure 10.4).

MP701/MP703: This were the experiments, where the composition was guided

Batch No.	composition	maximum temperature (°C)	experimental design
MP701	1.2:2:2:20	1180	A
MP702	1.6:2:2:30	1180	A
MP703	1.2:2:2:20	1180	A
MP704	1.6:2:2:30	1180	A
MP705	1.2:2:2:20	1300	B
MP706	1.2:2:2:20	1250	B

Table 10.13: Overview over the $EuNi_2P_2$ growth experiments. Composition is given as Eu:Ni:P:Sn

by the works on $EuFe_2P_2$ by Duc Nguyen [96], the temperature profile however was again guided by my own works on $CeCo_2P_2$ [32] for the sake of parallelization of experiments.
This approach, in the case of the nickel based compound, was the more successful one. However, characteristic length scales of the crystals (examples shown in fig. 10.16) normally did not exceed 2 mm even in the batch yielding the larger and more numerous crystals, MP703. With an usual thickness of 50-100 µm, the ten largest crystals had an averaged mass of $\bar{m}_{10} = 7.4\,\mathrm{mg}$.
With PXRD, in both batches the large part of the batch could be confirmed to consist of the target phase $EuNi_2P_2$, and only small portions of a binary side phase NiP_2 were found. The crystals are platelets with a surface normal that is the crystallographic c-direction. Since the basal shape of the crystals is rough and does not allow to conclude on the in-plane orientation, Laue diffractometry has to be performed on every crystal that is designated to be investigated on.

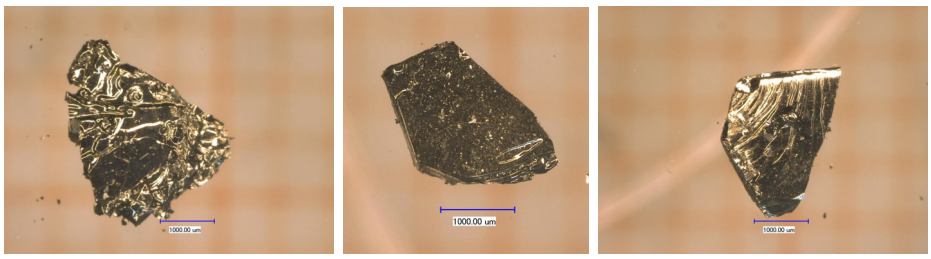

(a) (b) (c)

Figure 10.16: Some $EuNi_2P_2$ crystals from the batch MP703.

MP702/MP704: For these runs, both the composition and the temperature profile were guided by my own previous works on $CeCo_2P_2$. This approach to the system has proven to be less successful than the previously described. Crystals remain smaller, with only few exceeding characteristical length scales of 1 mm. Some crystals are shown in fig. 10.17. In some cases, crystallinity is noticably worse (as in 10.17c, where every part of the surface is coarse and different grains might meet). Using PXRD also a variety of ternary side phases could be identified

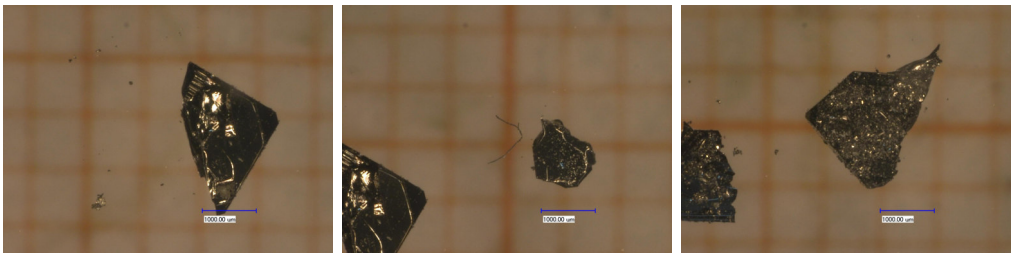

Figure 10.17: Some $EuNi_2P_2$ crystals from the batch MP704.

to be part of the batches, among those Ni_2SnP and small amounts of $EuNi_{10}P_6$ (structures after [118] and [119] respectively), and one not identifiable phase.

From these batches, a crystal for the comparative EDX-WDX-analysis was extracted. WDX shows, again, a deficit in phosphorus; but in this case, other than in the cobalt case, to the benefit of the europium share. This result, which is shown in table 10.14, is due to standardization and lack of suspicions against the performance of the detector more reliable than the EDX result. The result is quite close to an actual 122 ratio. But still, this needs to be treated with care. The large deviations of the EDX measurements render the EDX method quantitatively intricate to interpret. The consistency of lacking 3d and 4f elements indicates a problem only affecting the energy range of these elements, whose peaks in the spectrum regularly overlap.

	Eu (at-%)	Ni (at-%)	P (at-%)
EDX	17.51	32.57	49.92
WDX	21.18	40.22	38.60
difference	-3.67	-7.65	+11.32

Table 10.14: Comparison of EDX and WDX of $EuNi_2P_2$. The difference means deviation by EDX, hence positive sign is a surplus in EDX over WDX, a negative sign vice versa. WDX data [97].

Experimental design B

In experimental setup B (graphite in niobium, see section 10.5.1 for more detail), the more successful composition (which is the 1.2:2:2:20 composition) is now to be brought to slightly higher temperatures, to see whether the growth process of the crystals have to be optimized. Additionally, the experiment has to deal with a strong temperature gradient in the Gero furnace. Two new maximum temperatures were applied, 1250 °C and 1300 °C.
Basically, the effects on the growth in both cases were nearly identical, and probably mostly accountable to the applied temperature gradient. $EuNi_2P_2$ was obtained to a large amount, in large (up to 4-5 mm of characteristic length), but very thin and foil like crystals, proving to be very fragile and consistent of different "patches", each of which being a single crystal. The phase was confirmed via

PXRD and EDX. Only few crystals were a bit thicker (around 50-100 µm again) and robust enough to perform physical handling and preparations for characterization. Some of those are shown in fig. 10.18. Their shape shows both 100- and 110-edges at the 001-platelets (see also in the figures, where some of the edges are marked). Hence, for every single sample, an individual orientation process is necessary.
Additionally, in both experiments the same side phase emerged, showing off the Ni_3Sn_4 structure in PXRD (as reported by [120]), but in the EDX a composition of Ni_2Sn_3. (Maybe, the EDX result is due to the probable detector problem already mentioned.) This side phase emerged in clusters of needles, so that it was easily distinguishable from the target phase, but it was obtained in quite a large amount of about 40%.

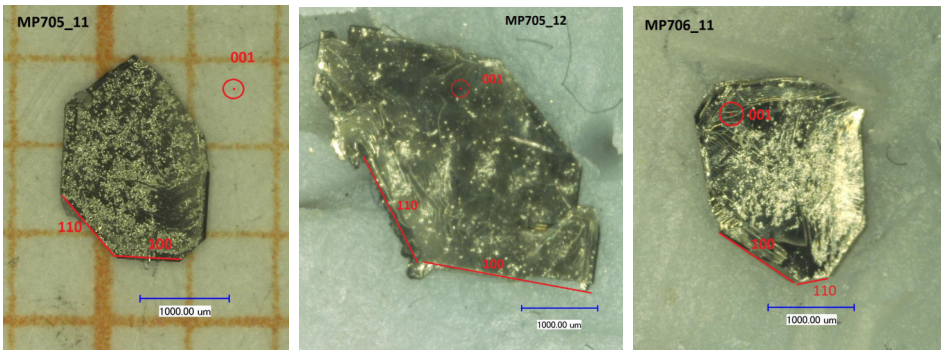

Figure 10.18: Some $EuNi_2P_2$ crystals from the batches MP705 and MP706.

With so large side phase problems, the Gero approaches were abandoned again. Setup A seemed to be sufficient to gain crystals, that are managable for most purposes of thermodynamic characterization. Also, in conclusion for the nickel based compound, the composition derived from the works on $EuFe_2P_2$ seemed to yield more consistent results, although still with potential to generally optimize for crystal size. But with that starting composition, fewer and more managable side phases were obtained, and the crystals gained are, although not superfluently large, both larger than from the other starting composition, and sufficient for interesting further investigation methods such as ARPES.

10.7.2 Physical characterization

In this section, I pin down the basic properties of the valence transition in $EuNi_2P_2$. Therefore, magnetization measurements via VSM were applied to probe the electronic properties of the valence states, low temperature PXRD was used to describe the lattice effects and specific heat measurements were used to look for the entropy of the valence change.
The basic electronic properties of the system, as they were measured with samples from the batches MP701 and MP704, reproduce well the qualitative form of the said properties as reported by Hiranaka [17]. As can be seen in the direct comparison of the resistivity measurements (fig. 10.19c, inset), the $R/R_{2\,K}$-ratio is a factor of two lower than what Hiranaka reported. Also, as the derivative

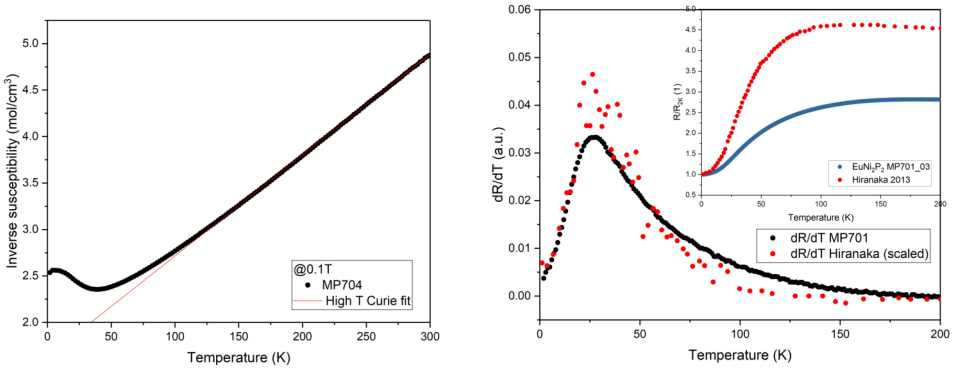

(a) Curie fit on magnetization (b) dR/dT comparison to literature [17]

Figure 10.19: Magnetization and AC transport measurements on $EuNi_2P_2$ crystals from batches MP701 and MP704. For the AC transport measurement, current direction was $j \parallel 100$, for the VSM measurements was the field direction $B \parallel 100$. Noise in the literature data stems from digitalization by hand.

shows (fig. 10.19c), the temperature rise is ever so slightly more pronounced in the literature data. The broadening of the rise in combination with the lower $R/R_{2\,K}$-ratio might indicate some disorder in the crystal structure. This might, again, connect to the WDX results (table 10.14), where a phosphorus deficit could be noticed. The form of the ACT curve is, as reported, inexplicable by a simple model for a metal. Hiranaka described the system as a Kondo system, which would explain the broad hump and the saturation afterwards.
The magnetic susceptibility in the a-direction reproduces also quantitatively correct. On the data, a Curie fit for the high temperature region could be performed to determine the valence of the high temperature valence state. This valence was found to be 2.31 ± 0.06, which agrees with the common estimation of 2.25 [17, 121]. For the low temperature valence state, that literature establishes as $Eu^{2.5+}$ state [17, 121], no set of data could be found to perform a Curie fit on, because the transition between the valence states happens at quite a low temperature (onsetting at about 40 K, which can be identified as the characteristic energy scale) and is also quite broad, so that no linearizable interval could be found before the susceptibility starts turning up at lower temperatures again.

phase	$1/C = \chi^{-1}/T$	μ_{eff}	Valence
high temperature	$(10750 \pm 80)\,\frac{m^3}{mol \cdot K}$	$(5.4 \pm 0.5)\,\mu_B$	2.31 ± 0.06
low temperature	no fit	no fit	no fit

Table 10.15: Valence of the high temperature state of $EuNi_2P_2$, gained from MP704 single crystalline magnetization data at 0.1 T external field. For the low temperature region and valence state, no fit was possible.

On the heat capacity data of $EuNi_2P_2$ (fig. 10.20a: dataset, two Debye model, entropy calculation, b: Sommerfeld fit), first, a Sommerfeld fit was performed in the low temperature regime to determine the electronic Sommerfeld coefficient γ,

as well as the phononic slope β. γ was determined to be $\gamma = (81 \pm 2)\,\frac{\mathrm{mJ}}{\mathrm{mol\,K^2}}$ (the error is the maximum error of the χ^2 of the fit and about 2% of error estimated for mass errors - in the figure, only the χ^2 error is listed). This is somewhat enhanced to what one would expect from normal metals. Still, in order to speak of a heavy fermion system, one would normally demand a value of some hundreds of $\frac{\mathrm{mJ}}{\mathrm{mol\,K^2}}$. But some hybridization, that enhances γ, undoubtedly seems to take place.

With $\beta = (308 \pm 24)\,\frac{\mathrm{mJ}}{\mathrm{mol\,K^4}}$, one finds a Debye temperature of $\Theta_D = (398 \pm 31)\,\mathrm{K}$ (with an error of 23 K accounting to the fit χ^2, and the rest accounting to again the assumption of up to 2% of misdetermination of the sample mass). From a model with two Debye temperatures, fitted to the high temperature data, using an analytical formula [81], two Debye temperatures $\Theta_{D1} = (442 \pm 4)\,\mathrm{K}$ and $\Theta_{D2} = (231 \pm 3)\,\mathrm{K}$ were derived. For comparison, Kakehashi assumed 350 K [122].

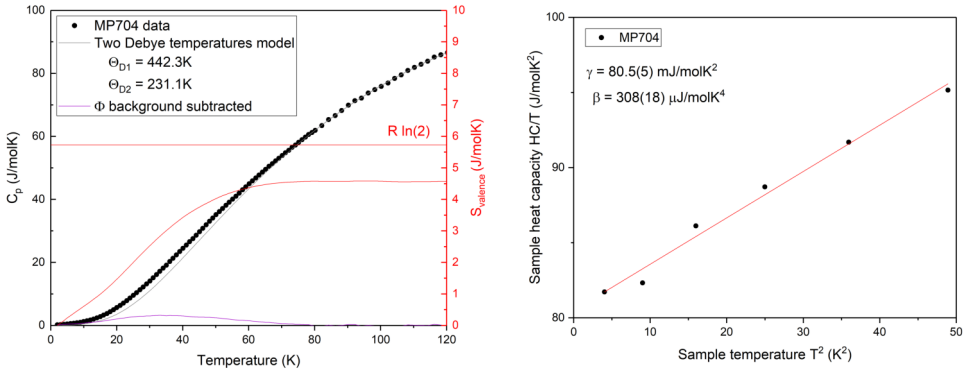

(a) Dataset (b) Low temperature Sommerfeld fit

Figure 10.20: Heat capacity measurements on $EuNi_2P_2$ crystals from batch MP704.

When one tries to identify the valence transition's contribution to the entropy of the system from the specific heat data then, by mere eyesight one is bound to fail. Even when the position of the characteristic energy scale of the transition is known (about 40 K), no feature can be identified by eye. This implies, that the $EuNi_2P_2$ is still far beyond the critical endpoint of the valence transition, deep in the crossover area, and hence the feature broadened to an extent, that an eye can't separate it from the other contributions to the system. The theoretical model with two Debye temperatures gives an estimate of how the feature is broadened and what share of the specific heat is accounted for by the valence change (fig. 10.20a). For the entropy connected to what is left over when subtracting the phonon fit from the model with two Debye temperatures, one finds about $S \approx 4.6\,\frac{\mathrm{J}}{\mathrm{mol\,K}}$, which is about 5/6 of $R \cdot \ln(2)$, which would be the expectation value for a two-level system as the competition between Eu^{2+} and Eu^{3+} states.

In order to gain insight on the lattice dynamics around the valence transition, the $EuNi_2P_2$ system was also probed via low temperature powder X-ray diffractom-

etry. For this, only well grown single crystals from batch MP704 were selected and ground to powder, so that the powder obtained was phase pure. The data were refined with GSAS II [46] in order to obtain temperature dependent lattice parameters. Again, the c-parameter showed some arbitrary noisy development over temperature, but the development of the a-paramenter was directed and consistent (fig. 10.21). Around the valence transition, the a-parameter contracts, and the energy scale coincides with the energy scale identified for the valence transition in the VSM measurement: the inflection point of the lattice parameter development locates somewhere between 35 K and 40 K. However, the change in

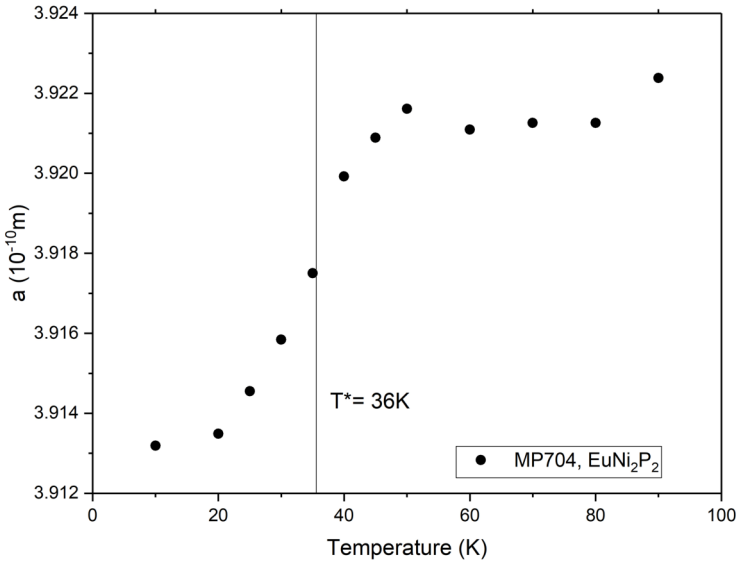

Figure 10.21: Extracted lattice parameter a from low temperature PXRD measurements on $EuNi_2P_2$ crystals from batch MP704.

the a-parameter is only about 0.25%, a whole order of magnitude smaller than in the $EuPd_2Si_2$ system. This is, together with the broadened HC feature and the assumption, that the system is located deeply in the crossover area, why I would rather speak of a characteristic energy scale of about 36 K than calling it a transition temperature.

10.8 Summary

In this subproject, I focussed on the production of ternary europium based phosphides with different transition metals. Four compounds were attempted: $EuFe_2P_2$, $EuCo_2P_2$, $EuNi_2P_2$ and $EuRu_2P_2$. For T = Fe, Co and Ni, single crystals of the compounds in a size of at least 2×2 mm and with several mg up to about 12 mg were obtained. For T = Fe and Ru, powderous samples with a yield of up to 95% could be crafted.
Characterization of the samples showed an anomaly in the phosphorus content, which is until now not clarified to what extent it stems from measurement issues, and to what extent the samples are, in fact, off stochiometric. Magnetic properties of the iron and cobalt based systems were only investigated insofar, as the basic

magnetic properties from the literature were reproduced. In the $EuCo_2P_2$ case, some additional in plane anisotropy was found, that was not previously reported in the literature, but I refrained from a deeper investigation and modelling.
The investigation on the nickel based samples yielded the confirmation of the intermediate valent behaviour of $EuNi_2P_2$ and a characteristic energy scale of the fluctuations of about $T^* = 35\,\mathrm{K}$. For the high temperature site, a valence of 2.31 ± 0.06 was found from VSM, the low temperature valence could not be confirmed. From HC measurements, the system was located quite far in the crossover area.
In order to try and find a valence transition in the iron-, cobalt- or ruthenium-systems, several measures were taken:

- In this chapter, low temperature, high pressure SC XRD experiments were reported. While in the cobalt based compound, a sharp first order lattice collapse, featuring formation of a phoshporus-phosphorus single covalent bond, can be seen, in $EuRu_2P_2$ this collapse is also present, but happens on a broad pressure scale, presenting itself as second order. Orthorombic distortions in this second order transition are not ruled out so far. The $EuFe_2P_2$ data are still undergoing evaluation, but by now appear to behave quite similarly to the $EuRu_2P_2$ case, despite the Birch-Murnaghan plot suggesting some more complex elastic effects in this compound. As a follow up, with the same temperature und pressure dependency, the valence of europium should also be probed directly, to classify how the valence transition is linked to the lattice anomalies.

- During 2021, the bachelor student Franziska Walther tried, continuing from the base of this work onwards, to establish a doping series $Eu(Fe_xNi_{1-x})_2P_2$ [114] in order to shift the system closer to the area in the generalized Eu-valence phase diagram, where a transition would be expected. The hope was to investigate the system at pressures reasonable for the laboratory of e.g. the lab group of Prof. Lang. Alas, a controlled growth of an iron-nickel-based compound could not be established. The phases seemed to seperate on different scales, from macroscopic single crystals down to a scale of below micrometers in an integrated polycrystalline body.

- A similar attempt tried an ordered replacement of 50% of the europium by Alkaline metals in a structure of lower symmetry, the 1144 structure. This attempt is dealt with in chapter 11 of this work.

11 | $EuAT_4P_4$

In the phosphides dealt with in chapter 10, the main target was to investigate how the collapse of the tetragonal phase and the formation of covalent P-P-single bounds relate to a transition of the valence state of europium from a divalent and magnetic state to an intermediate valent and non-magnetic state. Since we have two fixed points for these investigations, with $EuFe_2P_2$ being in the non-collapsed phase and displaying magnetic order, and $EuNi_2P_2$ being in the collapsed phase and displaying intermediate valence, first thought would lead to perform a solid solution series of $Eu(Fe_{1-x}Ni_x)_2P_2$ in order to find an x corresponding to a compound close to the collapse and so investigate the electronics in proximity to the collapse directy. This was conducted by Franziska Walther in a Bachelor's thesis [114], but $EuFe_2P_2$ and $EuNi_2P_2$ tended strongly to separate from each other.
But even conceptually, this approach might be problematic in that sense, that the target of the investigation itself, the nature of electronic and structural phase transitions occurring between the situation of $EuFe_2P_2$ and $EuNi_2P_2$ might be accessible only to a very limited scale due to the disorder of a solid solution system. Hence, in order to be able to investigate the nature and order of the said transitions, electronic and structural, at close-to-ambient conditions, a system must be found leading closer to the transition from one side pressurewise, but in a way, that does not produce a highly disordered system.
One approach to the problem might be not to substitute the transition metal, but europium itself by half the amount of alkali metals, since then there are two options of how the structure of the target compound might come about. Still, there is the possibility of a solid solution crystal in the known $ThCr_2Si_2$-structure, that is $Eu_{0.5}A_{0.5}T_2P_2 = EuT_2P_2 \cdot AT_2P_2(s)$, which is a highly disordered system. On the other hand, under certain circumstances, that will be shortly outlined at the beginning of this chapter, a crystallization of a compound $EuAT_4P_4$ with a new structure, that is similar, but ordered, is possible. This 1144-compounds were investigated for (even europium based) iron arsenides [123] and ruthenium phosphides [107] just in the last years, but it is by now largely unknown, whether this sort of compounds also forms for europium based transition metal phosphides.
In this chapter, attempts to grow $EuAT_4P_4$ as a modification of EuT_2P_2 will be reported, with different alkali metals A = K, Rb, Cs, and different transition metals T = Fe, Ru (starting with Fe-experiments, later adding Ru-experiments, both systems with uncollapsed tetragonal 122 structures).
As in previous chapters, chemicals used for the experiments are described in appendix A.

11.1 122(s) and 1144 structure types

As a starting point for considering the both possible structural realizations of (Eu,A)T_2P_2, we first begin again with the structure of pure EuT_2P_2, which is the well known $ThCr_2Si_2$ structure. The symmetry group is I4/mmm (no. 139). The occupation of the Wyckoff positions is shown in table 11.1 for T = Fe. In the introductory part, I will discuss most things with the iron references, while only bringing in the ruthenium occasionally when referring to considerations made when I already started to not only use iron as a transition metal for these experiments. All points mentioned for iron apply to ruthenium accordingly; if necessary, with quantitative, but not qualitative adjustments.

Wyckoff position	relative position	element	occupation number
a	(0,0,0)	Eu	1
d	$\left(\frac{1}{2},0,\frac{1}{4}\right), \left(0,\frac{1}{2},\frac{1}{4}\right)$	Fe	1
e	(0,0,z), (0,0,$\bar{z}$)	P	1

Table 11.1: Wyckoff positions of the 122 compound $EuFe_2P_2$ [50, 86]. Body centering yields the positions of the second formula unit with the given positions + (0,5; 0,5; 0,5).

A substitution of europium place with an alkaline metal by 50% makes now two

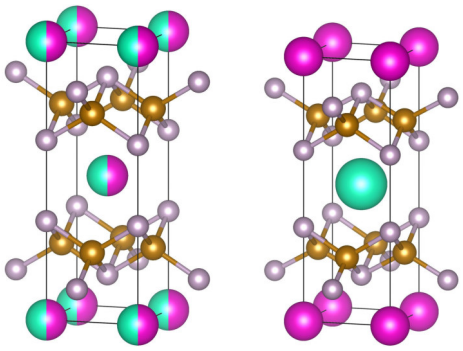

(a) (b)

Figure 11.1: (a) $Eu_{0.5}A_{0.5}Fe_2P_2 = EuFe_2P_2 \cdot AFe_2P_2(s)$ unit cell (b) $EuAFe_4P_4$ unit cell, pictures with VESTA [85]. Colour code: pink: Eu, brown: iron, grey: P, lime: A

different forms of unit cells imaginable: one unit cell, where every Wyckoff position a has equal chance to either carry an europium atom or an alkaline atom (as in fig. 11.1a), and one, where layers of europium and alkaline atoms stack alternally (as in fig. 11.1b). These two possibilities, being conceptually very similar, since both give a possible solution to the problem of substituting $EuFe_2P_2$ with an alkaline metal, are quite different in terms of symmetry and disorder. The solid solution variant preserves the symmetry of the mother compound $EuFe_2P_2$

(space group 139, I4/mmm), while the ordered 1144 variant changes the crystals spatial symmetry to a lower symmetrical class (space group 123, P4/mmm). Comparing the symmetry schemes (fig. 11.2), the latter option, due to the dis-

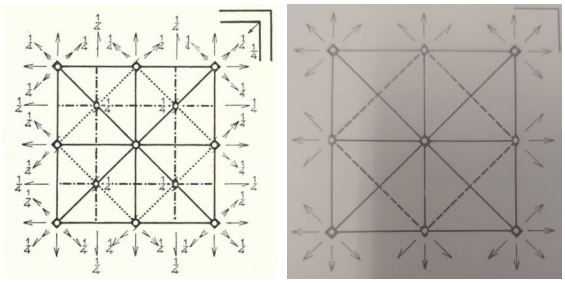

(a) (b)

Figure 11.2: (a) symmetry scheme of space group 139 (I4/mmm) (b) symmetry scheme of space group 123 (P4/mmm) [50].

tinctly alternating stacking of the europium and alkaline layers, loses all symmetry elements, that contain a fractional translation along the c direction (screw rotation, glide reflection, body centering).
In terms of Wyckoff positions, the solid solution variant presents itself as a direct derivate of the mother compound, with occupation numbers on the a place lower than 1 (as in table 11.2). In the lower symmetrical compound 1144 on the other hand, the phosphorus positions close to europium and close to the alkaline would not be crystallographically identical positions anymore, but now would occupy the distinct Wyckoff positions g and h (as in table 11.3), possibly even with different distances to the respective positions a and d. Under suitable circumstances, even only a semi-collapse of the structure between the phosphorus places a or d respectively might be imaginable.
Since the arrangement of the europium and alkaline atoms in the crystal change

Wyckoff position	relative position	element	occupation number
a	(0,0,0)	Eu	0.5
a	(0,0,0)	A	0.5
d	$\left(\frac{1}{2},0,\frac{1}{4}\right), \left(0,\frac{1}{2},\frac{1}{4}\right)$	Fe	1
e	(0,0,z), (0,0,$\bar{z}$)	P	1

Table 11.2: Wyckoff positions of the 122 compound $EuFe_2P_2$ in solid solution with AFe_2P_2 [50, 86]. alkaline added by own considerations. Body centering yields the positions of the second formula unit with the given positions + (0,5;0,5;0,5).

the basic features of symmetry, in case of having reached the target chemical composition, a distinction between the 122 solid solution phase and the 1144 phase can easily be made by any refraction experiment. For example, in X-ray powder diffractometry, with the transition from the 122(s) phase to the 1144 phase

Wyckoff position	relative position	element
a	(0,0,0)	Eu
d	(0.5,0.5,0.5)	A
i	$\left(\frac{1}{2},0,\frac{1}{4}\right), \left(0,\frac{1}{2},\frac{1}{4}\right), \left(\frac{1}{2},0,-\frac{1}{4}\right), \left(0,\frac{1}{2},-\frac{1}{4}\right)$	Fe
g	$(0,0,z_g), (0,0,\bar{z}_g)$	P
h	$(0.5,0.5,z_h), (0.5,0.5,\bar{z}_h)$	P

Table 11.3: Wyckoff positions of the 1144 compound $EuAFe_4P_4$ [50], derived after $CaRbFe_4As_4$ [124].

(lattice parameters held constant), the lower symmetry is connected to less restrictive extinction rules for reflexes, causing new reflexes to emerge. In the given case, that is also simulated in fig. 11.3, the extinction rule corresponding to the ralization of the 122 structure (I4/mmm, group number 139) is, that only reflexes are realized, that have an even sum of Miller indices $h+k+l$ [124]. With the loss of the body centering in the 1144 structure (P4/mmm, group number 123), this rule does not prevail, and reflexes with odd values of $h+k+l$ may emerge. In terms of experimental detail, the 1144 structure can best be distinguished from the 122 phase by the emerging of the (100), (102) and (111) reflexes in a PXRD diagram.

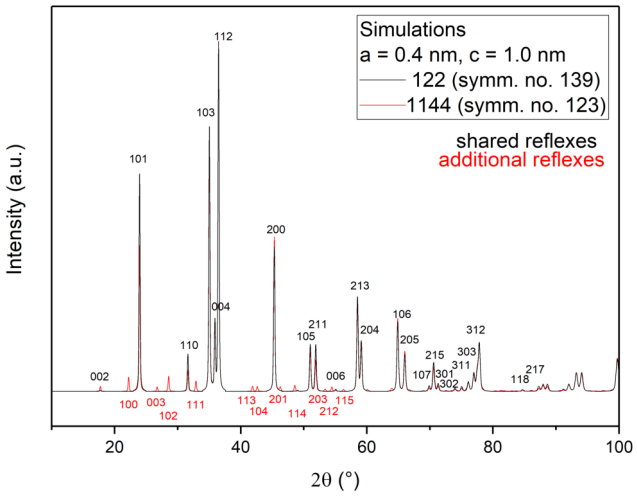

Figure 11.3: PXRD signals of the 122 and 1144 phases with assumed lattice parameters of a = 4 Å and c = 10Å. In black, the 122 pattern is shown, the red reflexes are the reflexes arising additionally for the 1144 phase. Simulated with *powder cell 2.3*.

With these differences in symmetry, there is connected a difference in disorder of the crystal. This can be expressed in terms of a configurational entropy S_{conf} [123]. For the 1144 phase, $S_{conf} = 0$ is obviously true, since the single atoms of a kind are undistinguishable, and besides there is only one possibility to arrange

europium and alkaline atoms relative to each other. For the 122 solid solution phase, the configurational entropy S_{conf} depends on the partition x of europium atoms substituted by alkaline atoms, and is expressed as

$$S_{conf} = 2k_B \left[x \ln(x) + (1-x) \ln(1-x) \right]. \tag{11.1}$$

This expression reaches the maximum right at our case of interest, the fifty percent substitution ($x = 0.5$). A fifty percent substitution of one lattice space leads to the maximal configurational entropy, and hence configurational disorder possible, since expectation of an arrangement is maximally diffuted by even probabilities for every case possible.

11.1.1 Selection of cases

The class of 1144 compounds is a rather new one in terms of experimental accessibility. First results based on actually growing some compounds of this structural type only appeared in the mid 2010's on the field of iron based superconductivity. Iyo and others claim in 2016 to be the first to ever report a realization of this crystal structure [124]. They approached the iron arsenides $CaAFe_4As_4$ and $SrAFe_4As_4$ via solid-solid reactions and sintering, and reported flux approaches to be not successful so far.
Since then, there have been some approaches to these systems, especially on the field of iron based superconductivity. But most reported compounds of this structural type are still only predicted without experimental confirmation. Also, there are no calculations available for the exact compounds we are interested in in this chapter. Since there have been calculations featuring europium and even phosphorus [123], we will still have a look at them, and try to estimate a rough idea for a starting point of our experiments.
Song [123] models the difference of Gibbs free energy between the 122(s) and the 1144 phase to estimate, which of the two phases is the ground state crystal structure for the given composition. They estimate the difference in Gibbs free energy to be

$$\Delta G(T) = G_{122(s)} - G_{1144} = \Delta H - S_{conf} T + \Delta E_0 - \Delta S_{vib} T \tag{11.2}$$

where $H = G - ST$ is the enthalpy, which they determined by DFT calculations, and the entropic contributions are estimated to be divisable into a configurational part (where the configurational entropy is determined after 11.1) and a vibrational (phononic) part, as well as a remaining zero-point energy E_0. To be able to calculate the 122(s) case, the solid solution is estimated to be an ideal solution, where the energy scale of the whole system just is a linear combination of the components' energy scales $E_{122(s)} = xE_{XFe_2P_2} + (1-x)E_{YFe_2P_2}$. Positive ΔG in equation 11.2 corresponds to 1144 being a more stable ground state, negative ΔG to a 122(s) ideal solution being the more stable ground state respectvely.
Two stability conditions for the 1144 phase could be identified:

1. The relaxed lattice parameters for the 122(s) prediction and the 1144 prediction are similar by a measure of $|\Delta a| < 0.07\,\text{Å}$. When the difference is larger, the 122(s) phase is preferred.

2. The 1144 phase is preferred for unequally sized ions. If the ionic radius of the questionable ions differs by more than $|\Delta R| > 0.4\,\text{Å}$, the 1144 phase is stabilized. For equally sized ions, it is much more preferred to have a solid solution. This is intuitively comprehensible, since an exchange of ions would affect the structural integrity of the matrix less, if the ion induced is about the same size as the ion substituted, and with large differences, the 122 matrix would be expected to be distorted. Also, this condition is linearly linked to a difference in the lattice parameter c: $\Delta c \approx 4\Delta R$.

Song calculated compounds featuring europium (Eu(Na,K,Rb,Cs)Fe_4As_4) as well as the phosphides (Ba,Ca,Sr)$CsFe_4P_4$, but no phosphides featuring europium. Still, since the stable phosphides show up next to their associated arsenides in the phase diagram, and since the europium iron arsenides were predicted to be stable 1144 with all 4 alkalines, this was taken as a first hint that a search for a stable 1144 europium phosphide can be started.
The sodium compound $EuNaFe_4P_4$ should be expected to be the least stable or favourable 1144 phase, since sodium and europium ions are almost equal in size, as shown in table 11.4. potassium, rubidium and cesium in order of their weight show a larger difference in ionic radii, and thus would promise a more stable 1144 phase, if it can be found.

Element	ionic charge	coordination number	atomic radius (Å)
Eu	2+	8	1.39
	3+	8	1.206
Na	+	8	1.32
K	+	8	1.65
Rb	+	8	1.75
Cs	+	8	1.88
Ca	2+	8	2.31

Table 11.4: Radii of europium and alkaline ions [125].

Since for Rb and Cs it is most likely to stabilize the 1144 phase, I started off with trying to approach of the europium phosphides $EuRbFe_4P_4$ and $EuCsFe_4P_4$. But later, I completely changed towards $EuKFe_4P_4$ and even $EuKRu_4P_4$, since the lighter alkalines are less likely to stabilize the 1144 phase (similar ion size enhances disordered incorporation), but therefore more likely to form a compound of the target chemical composition at all (similar ion size enhances possibility of incorporation). Song predicted, that those iron based compounds in the 122(s) phase might even be possible to reform into 1144 compounds by tempering [123]. The ruthenium compound was included into the investigation, because in 2021, Paul Canfield and his group reported, that the growth of $CaKRu_4P_4$ was successful [107], and provided detailed information for us to try and resemble their experiments with europium instead of calcium.

11.1.2 Stability calculations

Some calculations over the stability of the 1144 and 122(s) phases for different alkaline metals A were conducted by Young-Joon Song in the group of Roser Valenti at the Goethe university in Frankfurt using Density Functional Theory [126]. They calculated the binding energies of the 122 and 1144 phases, and then calculated the energy difference based on an ideal solution approach. Also, they made a prediction for the relaxed lattice parameters of the 1144 phases. All this calculations were conducted for the assumption of a nonmagnetic, a ferromagnetic and an antiferromagnetic europium ion. In each case for alkaline metals (potassium and heavier), the 1144 phase was predicted to be more stable than the 122(s) phase. With reference to the predicted lattice parameters, the phase can be assumed to be non collapsed under ambient conditions. For the calcium case, the opposite is the case: from the lattice parameters one would assume the 1144 phase to be collapsed, but it would be less stable than the 122(s) phase whatsoever. More detailed results are shown in tables 11.5 and 11.6.

A=	ΔE_{NM}	ΔE_{FM}	ΔE_{AFM}
K	8.399	5.27	5.575
Rb	9.244	5.798	6.104
Cs	10.041	6.069	6.374
Ca	-0.564	-0.836	-1.142

Table 11.5: Stability of 1144 phases as predicted by the Valenti group [126]. The europium is assumed as: NM: nonmagnetic, FM: ferromagnetic, AFM: antiferromagnetic. Units: meV/atom. Positive ΔE favours 1144 phase, negative ΔE favours 122(s) phase

A=	a_{NM}	c_{NM}	a_M	c_M
K	3.81877	11.49822	3.80193	11.94166
Rb	3.82406	11.84371	3.80715	12.29322
Cs	3.82993	12.22799	3.81363	12.67540
Ca	3.82781	10.16925	3.82119	10.52221

Table 11.6: Lattice parameters of 1144 phases as predicted by the Valenti group [126]. The europium is assumed as: NM: nonmagnetic, M: ferro/antiferromagnetic. Units: Å.

For the ruthenium compound, no stability calculations were performed so far, since the stability of at least the in-between results aspired and also a result alike to what I wanted to approach were reported stable [107].

11.2 Growth approaches

Up until now, the research on compounds in the 1144 structural class is quite undeveloped. There are only a few compounds predicted to be stable, of which only some feature either phosphorus or europium, but most of them are alkaline iron arsenides. The arsenides are also the only instances of this structural class realized so far in a polycrystalline form. Single crystals of compounds of this class don't seem to exist up until now, as well as only few non-iron-arsenide compounds in the 1144 structure have been reported at all so far. One example is $CaKRu_4P_4$, grown by Paul Canfield and his group [107]. But those reports are most recent (the Canfield report is just from 2021), and only little knowledge is established for them, and no compounds are reported so far that feature both phosphorus and europium with any given transition metal and alkaline metal to complete the structure.
Hence, first I aspired to try several ways of growing some compound showing the 1144 stochiometry (and, ideally, structure), not with the target of optimizing a crystal growth and gain single crystals in a shape and size suitable for detailled investigation, but rather to find whether the 1144 phase featuring europium and phosphorus can be found and stabilized whatsoever, regardless of a single crystalline or polycrystalline form.
Since this field of activity is such a new one, I employed a variety of different ideas of how to grow $EuAT_4P_4$ compounds, most of which were not successful and in hindsight may even show not to be as promising in the first place. Still, I give a genealogical account of what approaches to the Eu-P-1144 systems I tried, because there is something to learn also from the failures, and the progress in methods derived from the failures; and also, if someone wants to take up work on this field, that not only the current "best practise" I use is reported, but also enough material is at hand not to be bound to use the same unyielding approaches again that shaped my curvy path over this field.
Measurement data to test the results of the growth experiments are mostly restricted to PXRD (and EDX in few cases). PXRD measurement data are evaluated using *powderCell 2.3* and GSAS-II [46]. In this chapter, no raw data are shown, but only the evaluation of phases in the diffractograms, which are referred to qualitatively and quantitatively in text and tabellaric form. Since the growth experiments played on different parameters in 44 experiments, which is not compact enough to present an overview here, in the following on the single experiments will be given, while an overview can be seen in appendix B.

11.2.1 Reference works

When first investigations on growing the Eu-P-1144 systems started, reports to rely on were rather slim. The main experimental reference point of the project was a work of Iyo and others in the beginning [124], where they approached iron arsenides (without europium, instead with calcium on the Wyckoff a position) $AeAFe_4As_4$, with different alkaline metals A and alkaline earth metals Ae.
They reported having successfully grown a large variety of such compounds as polycrystalline material within solid-solid sintering experimental setups, with excess alkalines and arsenic in order to account for evaporation. The characteristic

temperatures were 860 – 920 °C, which later would be used as a first orientation mark for own sintering temperatures.
Also, they reported on experiments with AAs salt fluxes for Ae = Ca and A = K, Rb, in order to grow some single crystals of the said systems. These experiments remained unsuccessful.
A year later, Paul Canfield and his group also reported on the growth of a 1144 arsenide system, $CaKFe_4As_4$, which they approached via the FeAs self flux method [127]. They succeeded in gaining single crystals of the system, and could report, that they seem to be robust against air contamination on the time scale of several months, but are by eyesight indistinguishable from the 122 mothering compounds. Only the X-ray analysis reveals the actual composition of the samples.
It was first in 2021 that a report of the successful growth of a phosphide in the 1144 structure crossed my ways. This was again reported by the Canfield group [107]. They gained $CaKRu_4P_4$ by prereacting the $CaRu_2P_2$ and KRu_2P_2 systems, and afterwards annealing them. This inspired the addition of ruthenium also to our line-up, since this eliminates one "insecure" element - with the search for $EuKRu_4P_4$, now only the substitution of one element - Ca by Eu - separated our experiments from the reports. Hence, a recreation can assumed to be more likely possible. Also, the annealing profile I used was changed to resemble the annealing profile in this report, after I received it. This profile has already been described in section 10.3.2 and 10.4.1, since I applied it to the ternary europium compounds just as well as to the ternary alkaline (at that point in time, solely potassium) compounds and also the quarternary approaches.

11.2.2 Tin flux approaches for $EuAFe_4P_4$, A = Rb, Cs

In the beginning, I chose the naivest possible approach to two $EuAT_4P_4$ systems (with T = Fe in both cases and A = Rb, Cs respectively) within four experiments. One can think of the $EuAFe_4P_4$ systems as $EuFe_2P_2$ systems, that are doped to an amount of 50% with an alkaline metal on the europium place - in a special way, that is, ordered and breaking the spacial symmetry of the system. Hence, for the first experiments, the established experimental prescriptions for the growth of $EuFe_2P_2$ in Tin flux (as described in section 10.3.1) was simply customized in a way, that it features half the amount of the alkaline, of what previously was europium: from 1.2:2:2:20 (Eu:Fe:P:Sn), the starting ratios were changed to 0.6:0.6:2:2:20 (Eu:A:Fe:P:Sn) for between 10 g and 15 g of material, depending on the experiment. Also, to prevent the Quartz ampoules used in the original setup from being reduced by the alkaline metals, a sealed niobium crucible (length of 80 mm, inner diameter of 14 mm) served as inner crucible inside a quartz ampooule to protect the crucible from oxidation in the open furnace. The idea was, that, if growth of the 1144 system in a flux approach should be comparably easy to manage, even single crystals might be extracted.
Samples were heated up to 1100 °C with 100 K/h, with temperature being held at 450 °C in order to already bind the phosphorus to the other elements and reduce vapor pressure, then held at 1100 °C for two days. Afterwards, the samples are cooled down to 900 °C within 4 hours and then to 700 °C with a rate of 4 K/h. For all of this, compare fig. 10.2.
From there, for the first experiments, the furnace was turned off and tin flux was

removed by etching with hydrochloric acid (MP502: A=Rb, MP503: A=Cs). Later, for a more complete analysis of the resulting phases, flux was tried to be removed by centrifugation instead. MP504: A=Rb failed, because the niobium crucible cracked open the quartz ampoule while heating up due to larger thermal expansion and too little leftover space. For MP505: A=Cs, the niobium sieve placed inside the crucible was washed away, so it could only serve its cause partially, and the rest of the remnant flux had to be removed via etching again.
In all three of the experiments (the cracked open one not counted), after washing away the Tin flux if necessary, three phases grown from the melt could be identified using PXRD: in all cases, the iron phosphides FeP and Fe_2P formed to a noticable extent. Only about 40-50% of the results showed to be $EuFe_2P_2$, which also formed nice platelets with a characteristical edge length of about 1.5-2 mm. These platelets could be confirmed via EDX to consist of europium, iron and phosphorus in about what is the 122 ratio (notice the WDX measurements referred to in section 10.3.1 for a discussion of possible deviations; the phosphorus excess in the samples here was only about 4 At-%, which was the usual deviation measured at that time).
So, the alkaline metals added to the melt seemed to just have either formed other compounds, which are not stable against etching with hydrochloric acid, or did stay in the melt and resolidify with the whole remainders. In either case, the alkaline metals were not to be found incorporated into the target compound or other side compounds found after etching. The rubidium completely disappeared, dissolved into the acidic waterous solution most probably. Some of the cesium, on the other hand, could later be found during the EDX measurements of the $EuFe_2P_2$ platelets, where a powder of small salt cubes laid on some of the platelets from the respective two experiments, which was found to be the (already known and reported [128]) alkaline salt Cs_2SnCl_6. This confirms, that the alkaline metals are dissolved in the acid. Together with the existence of the $EuFe_2P_2$ platelets, this also leads to the conclusion, that $EuCsFe_4P_4$ did not form and just happen to be not resistent against hydrochloric acid, since a lot of the material is still bound in acid resistive compounds.
With the alkalines' tendencies to remain in the melt, and inside a Tin matrix to not react with the other ingredients, it did not seem reasonable to further stick to the tin external flux method in order to approach the 1144 systems. This means, that we refrain from trying to grow single crystals of the target compounds directly for now. Rather, from here onwards, methods of direct reaction, annealing and sintering were applied. Those yield their results in form of polycrystalline powders. Also, the Tin flux experiments were the only experiments featuring rubidium and cesium. For the following series of sintering growth processes, usually potassium was chosen for the alkaline metal. This is mostly due to reasons of pricing and availability. Also, in section 11.1.2 I reported, that all three of the compounds ($EuAFe_4P_4$ with A = K, Rb or Cs) are predicted to be stable, hence positive results should be findable also with potassium as alkaline metal, if any.
In order to try and sinter the 1144 systems, many approaches worked with already prereacting the materials for the growth experiments in some ways. Before I describe the attempts to grow $EuKT_4P_4$ in section 11.2.4, I will first describe the prereactions conducted in the following section 11.2.3.

11.2.3 Prereactions

Some of the proposed growth methods require some effort to be put into preparing the reactants for the reaction. Especially, the preparation of alkaline metals is crucial for both the idea of an alkaline phosphide self flux and of a sintering approach. In the following, the prereactions that were considered are shortly explained.

Binary alkaline phosphides

As a prereaction of the alkaline metals, in order to ease conduction of possible experiments, compounding the alkaline with phosphorus is the best consideration. The alkaline is less reactive in the bound state, whereas the vapor pressure of the phosphorus is also lowered.
Unfortunately, no binary phase diagrams for any of the alkaline metals in combination with phosphorus are reported. Still, there are many specific solid phases, that are known. Since the chemistry of the alkaline metals is quite similar among the whole main group, investigation of the existing phases is made for the rubidium-phosphorus system, and prereaction is then conducted with other alkali metals as well. This approach is well justified ex post.
For the rubidium-phosphorus system, there may not be a whole phase diagram available, but a broad variety of solid binary phases is reported [129]. Among those, as the two candidates selected for a thorough investigation of whether they are suitable for this cases, Rb_3P_7 and Rb_4P_6 were selected.
Rb_3P_7 (mistakingly referred to as Rb_2P_5 in the reference [130]) is grown inside an evacuated quartz tube during a destillation process at about 600° [130]. The temperature scale is not specified in terms of whether it is 600 degrees of Celsius, or 600 degrees of Reaumur ($T\,[°C] = 0.8\,T\,[°R]$), but the scale can be expected to be a Celsius scale. Decision was made against this compound, since in the lab we don't have the expertise and the equipment to conduct high temperature destillation experiments. Also, other compounds are reported to attack quartz quite strongly, so the risk of accidentally growing a side phase is actually problematic.
Rb_4P_6 (and also, this can be expanded to other A_4P_6 compounds) on the other hand is grown in a closed niobium crucible under a static argon atmosphere [131], which are conditions we can easily establish in our lab. The elements are weighed stochiometrically and sealed inside a niobium crucible. After the static argon atmosphere is established in the furnace, the sample is slowly heated up to 600 °C, where the temperature is held for two days. Von Schnering describes the result as "coarse" crystals of a dark tone. Both for rubidium and for potassium, the results match this description: the tone of the rough resulting lumps is mainly dark grey or brown, with a tone of purple (for rubidium) or a dark yellowish tone (for potassium) upon direct reflection of one of the rare facets (compare fig. 11.4a).
The samples are reported to be very sensitive against humid air and start degrading to gaseous phosphane and a solid rest very fast. Disposing this remainders, one must be very careful, since phosphane is highly inflammatory and also quite toxic [132].
Since the appearance of the results of a first prereaction run (MP506 and MP507 with K and Rb respectively) fits the description of the target phase, and the

(a) (b)

Figure 11.4: (a) results of the A_4P_6 prereactions with rubidium (left) and potassium (right), (b) degradation product of one of the compounds upon less than a minute after first air contact.

result is homogeneous without any noticable side phases, it is believable, that the targeted phase has actually been grown. Nevertheless, a confirmation of this assumption by characterization would be better. The two main options for this would be an EDX analysis or, as Von Schnering also mentions in his report, powder X-ray diffraction. The previous is not possible, since A_4P_6 are not metallic. The latter is problematic, since we in principle could establish an argon atmosphere inside the Bruker-D8 to protect the sample from degradation while measuring, but bringing the sample to that point turns out problematic. So, both variants are not an option.
When unpacking the remainder of the niobium crucibles in the fume hood, within less than a minute one can observe the described degradation process of the sample remainders on the crucible walls. This can be taken as a second indicator at least, that the correct phase is obtained.

Ternary compounds $EuFe_2P_2$ and ERu_2P_2

The experiments for $EuFe_2P_2$ and $EuRu_2P_2$ are described in sections 10.3.2 and 10.4.1 respectively. For a thorough description of the growth processes, please read there.

Ternary compound $CaFe_2P_2$

The ternary compound $CaFe_2P_2$ was synthesized in order to try and grow $EuCaFe_4P_4$. Following Mewis [133], the growth process was performed in several steps. For the first step, 1.5 g of material with the ratio of 1:2:2 (Ca:Fe:P) were placed inside an alumina crucible, which was sealed inside a niobium crucible. In the Linn furnace, the experiment was brought to 900 °C and held there for a day. In a second step, the resulting powder was pressed to pellets, and the pellets were sealed inside a Quartz ampoule. The quartz ampoule was heated to 1100 °C in one of the ThermConcept box furnaces, held there for 16 hours, then heated again to 1200 °C and held for another 8 hours.
After only one of the Quartz steps (that were repeated up to five times in the reference), the target phase could already be seen in a PXRD probe with over 90%, and only little side phase ratios for Fe_2P and Ca_5P_8.
This experiment has only been performed once, since my subsequent experiments

for growing $EuCaFe_4P_4$ were not successful, and after the subsequent experiment, I received the prediction that this compound is not expected to be stable (compare section 11.1.2) [126].

Ternary compound KFe_2P_2

The first main target of this project, after the flux approach turned out to not lead anywhere, was the $EuKFe_4P_4$ compound. In order to approach the system via sintering of the two ternary compounds $EuFe_2P_2$ and KFe_2P_2, which is one of the possible approaches, first the ternary compound KFe_2P_2 has to be synthesized. This was attempted using mostly a direct growth approach from the elements, but also some experiments using prereacted binary compounds. A series of experiments was performed, altering different parameters:

- the starting materials,
- the temperature profile and
- the crucible materials.

First experiments were set up in alignment with the work of Wenz and Schuster [98] over different AT_2X_2 compounds, with A being restricted to alkaline metals K and Rb, X being a Pnictide P or As, and T featuring a large variety of transition metals from the Fe-, Co- and Ni-families, among those also being KFe_2P_2 and KRu_2P_2. Since the main part of the work describes the determination of lattice parameters, this work also yielded tools to later test for the target compounds.
Wenz and Schuster describe an experimental setup as follows: they bring together a "mix of elements" ("Elementgemenge" [98] - the modus is not specified, whether all of the materials are powderous, some of them are lumped etc) with ratios following the composition of the target compound directly, i.e. 1:2:2 for A:T:X. The elements were placed in alumina crucibles under an argon atmosphere. They were brought to 500 °C, held there for a day, then ramped up to $800-900$ °C and reacted there for another two to three days. The details were that vague, since a large variety of compounds was approached in this work. They also reported the 122-compounds to form a dark greyish powder, which they said to be highly sensitive towards moisture and oxygen contamination.
From this starting point, the setup generated for use in the KML facilities used also the elemental starting materials (between 1 g and 1.5 g for different experiments) with elemental ratios 1:2:2. potassium was used in chunks cut from a large piece. Since the melting point of potassium is about 60 °C, it is not necessary to present it with a large surface. Given the air- and water-sensitivity, presenting too much surface could even be adverse. iron on the other hand is presented as powder to maximize the surface. Phosphorus will evaporate, and hence is simply presented in the given form of small pieces. Three later experiments used other starting ratios, using binary prereactants K_4P_6 and Fe_2P, featuring 1:2:4 of K_4P_6:Fe_2P:Fe.
The starting materials then were put into an inner crucible - alumina in five of seven approaches, carbon in the other two (one featuring the elements, one featuring the binary prereactants). The inner crucible is then encapsuled into an outer crucible. For all relevant experiments, this was a fused niobium tube.

There were also two experiments with alumina in Quartz (one featuring the elements, one featuring the binary prereactants), but both cracked open, probably due to the large vapor pressure caused by both phosphorus and potassium. Metal crucibles were handled in the Linn box furnace, where an argon atmosphere can be employed. The Quartz experiments were conducted in a ThermConcept box furnace under air atmosphere.
For six of the experiments, the temperature profile from [98] was employed with the maximum temperature and timespan of dwelling at 900 °C for three days. For the last attempt a more refined temperature profile reported by Canfield for KRu_2P_2 [107] has been used. There, an additional dwelling step for one hour at 230 °C was introduced. The dwelling time at 500 °C was cut down to 10 hours, the dwelling time at the maximum temperature of 900 °C was extended to four days. This routine was repeated three times for the last experiment.
In all five cases, that survived the heating process, the results could be harvested in form of - sometimes more dense, sometimes more porous - tablets of powder in various shades of gray. At the niobium crucible walls, a foil like, brittle sediment could be found in most of the experiments.
The former was investigated with PXRD (with molybdenum and copper tubes) in every case, and in one case also with EDX. The powders showed to consist of the two iron phosphides Fe_2P and FeP. The potassium was nowhere to be found. The latter could later be identified using EDX, as being a potassium-niobium compound. This is specifically odd, because the binary phase diagrams available [31] do not only not display any binary phases between the two, but explicitly state that there are none. Still, at least this discovery explains where all the potassium vanished to during all the experiments. This was only discovered later, when investigating KRu_2P_2, and there means of adjustment to lower the evaporation rate were employed.
When the growth of KFe_2P_2 remained unsuccessful, the attempts were paused, and more effort was put into KRu_2P_2 to develop a receipe to grow this compound reproducably, since for this compound, the group of Paul Canfield (in person of Paul Canfield himself and Mingyu Xu) did not only report the growth just recently [107], but also obliged to privately communicate advice and help out with the development.

Ternary compound KRu_2P_2

The step to using ruthenium as a transition metal was taken, since the most important concern of this project was, whether or not a 1144-structure featuring europium and phosphorus could be stabilized. The choice of iron as the transition metal followed the idea of having a well known starting point (for the first approaches, which included an external flux). But since these approaches failed whatsoever, sticking to iron was more of a decision to not get too broad and lose the thread of the project in a variety of approaches with different elements. But with the report of the Canfield group, that a ruthenium-based 1144 compound $CaKRu_4P_4$ could be grown and stabilized [107], and their offer of consultation, a good reason was found to shift the focus from the iron-based to the ruthenium-based compounds.
In a series of 10 experiments, a working point for growing KRu_2P_2 was developed, with helpful consultation by Paul Canfield and Mingyu Xu, one of his PhD

students. Nonetheless, a large variety of different adjustments had to be tried, where single parameters were altered in comparison to previous runs. After a first experiment, reproducing the Canfield report [107] was established, different parameters were altered over the course of development:

- the starting materials,
- introduction of a salt flux,
- the crucible materials,
- the starting composition and
- the temperature profile.

As a starting point for the experiments, a setup is used that resembles what Canfield reported recently [107]. The starting materials (with a total mass 1.5 g) are provided in form of elements with a composition of 1:2:2 (K:Ru:P) and placed inside an alumina crucible, that itself is sealed inside a niobium crucible. The niobium crucible then is placed inside the Linn furnace, which is our box furnace with the possibility to establish an argon protective atmosphere, and heated according to the Canfield temperature profile, that has already been described in the KFe_2P_2 section, with dwelling at 230 °C, 500 °C and 900 °C, staying at the maximum temperature for four days. For the first experiment, this was repeated three times, and in between a small specimen of powder was extracted for a phase analysis. Later, the heating profile mostly was applied just a single time. Results in the experiments of this section are usually given in form of powders with different shapes of gray if not mentioned otherwise.
In each of the runs, only RuP could be found in the phase analysis. The potassium seemed to be vanished completely already after the first run. The other two runs were completed whatsoever, for one idea also was, that the potassium may have formed a glassy phase, which would be invisible to PXRD. But this seemed to be not the case, since no potassium was to be found after either run. Two experiments were performed with the same setup, but only one run, and also yielded only RuP.
Only one shot was given to using an external salt flux. Since it was unclear at this point what happens to the potassium, the idea was to use KCl as a flux, which could also serve as a reservoir for potassium and should hopefully solve especially the potassium nicely. In the same setup, to the 1.5 g of materials, an amount of KCl was added with a molar ratio KCl:elements of 6:1. But, not only did the removal of the flux afterwards prove to be problematic - since the targeted material KRu_2P_2 was reported to be sensitive against water and air [98], neither could the salt be simply washed away, nor could the result be excarved outside a protective atmosphere. With quite a large effort, some powder for a phase analysis could be extracted, and only RuP and KCl could be found. It was unclear at this point, whether the potassium, again, had disappeared, or whether it stayed in a solution with the salt and was incorporated upon resolidification.
From here on, the total mass of materials was 2 g for all experiments. The starting materials for one experiment were altered to include the binary K_4P_6 again. The ruthenium was added as an element, so that with a K_4P_6:Ru-ratio of 1:6,

effectively the materials had a 50% potassium excess. In the results, again only RuP could be found, and the potassium had disappeared.
Since the alumina crucibles turned black during the growth experiments, the potassium crawling on the alumina had to be considered, and hence other crucible materials were tried, i.e. one experiment was performed within a graphite crucible. The crucible broke during the experiment, and it seemed rather obvious, that the potassium is probably responsible for attacking the graphite crucible. Another experiment with a glassy carbon crucible, which was hoped to be more robust, was performed, but it also crumbled. Carbon based crucibles seem unfit to deal with potassium melts. So, I returned to alumina crucibles. Also, the experimental results did not improve. Here only RuP was found as well.
In order to compensate for the material losses, from here on (and also, already in the experiment with the glassy carbon crucible) the starting composition was adjusted to a 100% potassium excess, to a K:Ru:P-ratio of 1:1:1. After the growth experiment, the alumina crucible again was turned dark gray. The potassium again had disappeared, leaving only RuP and Ru_2P for the phase analysis via PXRD. But here, the amounts of potassium "disappeared" were so large, that the foil like, brittle sediment peeled itself from the niobium wall and had to be noticed (and hence, could be identified via EDX). So, the secret of where the potassium leaves to has been lifted: it evaporates and then somehow reacts with the niobium (although it is not meant to do that, see previous section). This may be surprising, not only, because improbable compounds are formed, but also, because the potassium remains for about one day in the liquid state, before the boiling temperature (of about 760 °C) is passed, and hence it would have some time to react. But as it seemed, this day has not been enough to capture the potassium. The picture of potassium evaporating and spreading over the crucibles is also supported by a measurement of the masses of the materials and crucibles: the materials extracted from the crucible are the share of potassium lighter than before the run, and the crucibles become heavier accordingly during the growth experiment.
Hence, the next step is to perform an experiment, where the temperature stays below the boiling point of potassium all the time, in order to perserve the potassium pool as far as possible. So, for two experiments, the maximum temperature was set down from 900 °C to 750 °C. Both experiments were performed in alumina crucibles, and one with a ratio of 1:2:2, the other with the ratio of 1:1:1.
And, eventually, with this lowering of temperature, the potassium could actually be contained within the alumina crucible and brought to reaction with the other materials - that is, for a certain part at least. Although the boiling point was not reached, still more than 50% of the potassium evaporated in both experiments due to enhanced vapor pressure, but the remaining rest actually formed the target phase KRu_2P_2. For both experiments, a phase analysis was performed with PXRD. Results are shown in table 11.7. The powder of MP534, containing more than 80% of the target compound, was especially dark and especially loose compared to the results of the other experiments containing mostly or exclusively RuP.
From here one can learn, that even a larger potassium excess would be appropriate, if one wants to optimize the outcome of a single experiment. A temperature of 750 °C is sufficient to grow KRu_2P_2, but I would rather not lower the temper-

Experiment	elemental ratio structure from:	KRu_2P_2 [98]	RuP [100]
MP533	1:2:2	0.101	0.899
MP534	1:1:1	0.841	0.159

Table 11.7: PXRD quantitative analysis of KRu_2P_2 experiments.

ature further to further limit evaporation, but rather offer some more material to partially evaporate. With even lower temperatures, one might soon enter a temperature range, in which the target compound can't be grown anymore.
With the target compound now grown with a purity of over 80%, an attempt for sintering the 1144 compound $EuKRu_4P_4$ from the two ternaries $EuRu_2P_2$ and KRu_2P_2.

11.2.4 Direct and sintering approaches

Using a direct powder synthesis approach, the 1144 compounds can be targeted via three different paths:

- direct synthesis approach from the elements,
- sintering approach from binaries and
- sintering approach from ternaries.

Direct synthesis from the elements

Two experiments tried to synthesize $EuKRu_4P_4$ directly from the elements. 2 g of material (weighed in stochiometrically) were put into quite slim alumina crucibles, so that the material was packed together as a bulky cylinder, ensuring as much contact as possible between the powderous ruthenium and the europium, that was ground to a coarse powder. The potassium was put on top, since it would melt and then penetrate the material bulk from above; as was the phosphorus. The alumina crucible was then sealed inside a niobium outer crucible under an argon protective atmosphere.
Both of the two experiments used a three-step heating profile in the Linn furnace under argon protection: heating up at 100 K/h, the assemblage was held at 230 °C (for the potassium to sink in) for 1 h, at 500 °C (for the phosphorus to slowly be absorbed before rapidly sublimizing all at once) for 5 h and at the target temperature for one day.
For the first experiment, the target temperature was chosen to be 900 °C (after [107]). The experiment resulted (as tested with PXRD) in different ruthenium phosphides RuP and Ru_2P, and in the formation of $EuRu_2P_2$. The potassium had disappeared - vaporized due to the high temperatures, as the boiling point of potassium is reported to be 760 °C at ambient conditions [134].
Hence, the second experiment was conducted at 750 °C. But, the vapor pressure of potassium is then just a little bit below unevitable boiling, and hence, the

potassium again just evaporated, reacted to the niobium crucible and condensed at the alumina crucible's surface. Only, this time the amount of $EuRu_2P_2$ was then noticably smaller, in the range of only few percents, while much of the europium only reacted to binary phosphides. It is from here, that one can easily see, that an approach from the elements will not be easy to make it work, since, going in naively on stochiometry, temperaturewise the potassium is already lost when the europium is still too cold to react at all.
Hence, a potassium enriched atmosphere would be needed, that contains so much potassium, that further evaporation is not a problem even at higher temperatures, or another way, using prereacted materials, has to be found.

Sintering approach from binaries

Since a direct approach from the elements did not form anything promising, and since problems could be identified in a forming of a gaseous phase, trying to present solids and encourage a sintering process might be the next best thing to try. In order to realize the target phase (in this cases with T = Fe) by sintering, the constituent elements need to be induced in a form, that is stable in the temperature range applied; hence, volatile elements such as phosphorus or alkaline metals need to be prereacted. For easy handling, binary prereactants (see section 11.2.3) and temperature-stable elements are used. All compounds used for the sintering reaction need to be thoroughly grinded, the powderous compounds mixed, and then pressed into a pellet altogether. Sintering as a process was described in chapter 7.1.4.
The selection of starting materials is not distinctive. Several combinations of elements and compounds can be found, that both resemble the 1144 stochiometry and fulfill the other requirements, such as that phosphorus and the alkaline metals may not be used as an element, that the amount of elemental europium should be as low as possible and so forth. The selection of a combination is guided by the availabilities of compounds. The following starting materials were chosen (iron phosphide was bought, the rest prereacted in the lab):

$$1\ A_4P_6 + 8\ Fe_2P + 2\ EuP + 2\ Eu \rightarrow 4\ EuAFe_4P_4$$

Pellets of the chosen combination (for the experiments, this is combination no. 4) are sealed in a niobium crucible of 80 mm length and 14 mm diameter. These niobium crucibles are protected from air by quartz ampoules (with an inner diameter of 18 mm and a wall thickness of 2 mm), or using the Linn box furnace, which can establish an argon protective atmosphere.
For the temperature design of the growth experiment, Iyo [124] describes for the iron arsenides to bring the crucible (they use stainless steel) into a furnace, preheated to the target temperature (860 – 920 °C, depending on their alkali and Earth-alkali combination), have the sample at this temperature for 2-6 hours, and then remove the sample from the furnace and immediately cool down and quench the sample (e.g. with ice water, although they did not specify how they cooled down).
Since the sintering happens over time at the target temperature, two of the features seem a little bit suspect. First, the preheating of the furnace is described to prevent stable low temperature 122 phases from forming. But since sintering

takes some time, while heating with a reasonable rate, the threat of accidentally forming stable competitive phases is rather low. Hence, there is no reason to preheat the furnace, only to save some half an hour at an unvafourable temperature, especially when afterwards the target temperature is still to be reached. On the other hand, the quenching *after* the growth experiment seems sensible and should be adapted.
Second, the given time for the sample in the furnace of two to six hours seems oddly short for a solid-solid sintering process, which is usually rather slow. Hence, for the first experiments, a furnace time of 24 hours is chosen, in order to further enable a solid-solid sintering reaction.
First experiments are conducted at three different temperatures with three pellets. With a rate of 200 K/h, the pellets are first heated to 700 °C and held there for a full day. Quenching could not be established as described, since a closed box furnace was used to protect the niobium crucibles from oxidation. After removing the samples from the furnace, one of the pellets is removed for analysis, and the other pellets are again sintered at 800 °C inside a new niobium crucible. After this step, the second pellet is removed for analysis, and the last pellet is sintered a last time at 900 °C. This applies to the MP509-series (A = K) and the MP510-series (A = Rb).
This experiments were conducted very early in the process of trying to obtain the 1144 structure, hence the disappearance of structures containing alkaline metals in the PXRD checks did not immediately lead to the conclusion of the alkaline phosphides being deconstructed and the alkaline metals evaporated, although from a later perspective, this is exactly what needs to be assumed to have happened already at the 700 °C step.
Instead, the first speculation was, that the alkaline phosphides may have formed a glassy state, which can not be easily detected using PXRD. Hence, the higher temperature steps were conducted, although in every X ray powder diffractogram, only the $EuFe_2P_2$ ternary phase, as well as binary iron and europium phosphides could be found. Only later with the findings of the potassium-niobium compounds, this speculation could be ruled out and it could be explained, why no alkalines participated in any reactions - since they were disposed altogether with the first niobium crucible.
Be this as it may, the attempts of producing a 1144 structural type compound by sintering binary prereactants in the described fashion remained unsuccessful.

Sintering approach from ternaries

Another approach for a solid-solid synthesis is to sinter a mixed powder of europium- and alkali-based 122 compounds EuT_2P_2 and AT_2P_2, as e.g. Paul Canfield approached the $CaKRu_4P_4$ system [107].
This way is the most promising, since ternary compounds are more likely to be stable and contain the elements with a high vapor pressure without releasing them. Also, using the 122 compounds already offers them in a related structure, which might benefit the formation of a "heterostructure" of both 122 compounds. This was only tried after trying out binaries, because achieving the 122 starting materials via prereactions requires quite an amount of effort, as reported in section 11.2.3. When the ternary prereactants were achieved, this approach avanced to being the best choice for further experiments. Since only the ternary phosphide

featuring potassium with ruthenium as a transition metal could be obtained, in this section only the branch searching for $EuKRu_4P_4$ was followed.
For all the experiments, the experimental setup from the reactions from binaries was adapted. As starting materials, the prereacted ternaries from section 11.2.3 (with a yield of 85-95%, completed by ruthenium phosphides) are selected, and elemental potassium is added ad libitum - with molar additions as in table 11.8 - to secure the stability of KRu_2P_2. The materials are put inside an alumina crucible that is sealed inside a niobium crucible. This crucible is then brought to 750 °C under a protective argon atmosphere and held there for 5-21 days (the experiments with 0.5 and 0.7 excess potassium were held for three weeks, the rest for five days). The resulting powders were ground and then analyzed with PXRD.
Table 11.8 shows the results of the PXRD analyses of the different attempts towards the 1144 compounds. After the first experiment, which only naively tried to react the two prereactants, most of the ternary compounds were decomposed to binary ruthenium phosphides, while the whole potassium and a good part of the europium had disappeared from the powder. Drawing conclusions from previous experiments, this advocated, that the potassium, albeit bound in a compound relatively stable at ambient conditions, still shows a large vapor pressure and escapes the ternary compound upon heating up. Additionally, the potassium seems to attack the ternary europium based compound.
In order to deal with the vapor pressure of the potassium, different measures were applied: One experiment was set up with a drastically reduced volume of the niobium crucible by placing a Molybdenum full rod inside, but this did not work out. For three other experiments, different amounts of excess potassium were added, hoping, that the elemental potassium would evaporate first and saturate the atmosphere in the crucible, hence containing the bound potassium in the compounds.
There were still problems with the potassium atmosphere attacking the europium based compound, but retaining the potassium based compound worked out quite nicely. Granting the experiment three weeks at exalted temperature and a fitting amount of excess potassium, even the attacks on the europium compound were not severe anymore, so that in the end both ternary compounds were found to an almost equal share without any ruthenium phosphides. But this experiment also stated quite clearly that a 1144 compound with this certain composition can not be reached, at least using solid-solid reactions as applied here.

Starting materials	$EuRu_2P_2$	KRu_2P_2	$EuKRu_4P_4$	Ru_xP
1 $EuRu_2P_2$ + 1 KRu_2P_2	0.134	0	0	0.866
1 $EuRu_2P_2$ + 1 KRu_2P_2 *	0.110	0	0	0.890
1 $EuRu_2P_2$ + 1 KRu_2P_2 + 0.5 K	0.192	0.484	0	0.324
1 $EuRu_2P_2$ + 1 KRu_2P_2 + 0.7 K	0.485	0.515	0	0
1 $EuRu_2P_2$ + 1 KRu_2P_2 + 1 K	0.047	0.589	0	0.364

Table 11.8: 1144 experiments from ternaries. * = lower crucible volume

11.3 Summary

This part was the by far most explorative part of this work, aiming at an elaborate way of trying to shift the possible collapse of the 122 structure in the phosphides towards more ambient conditions without introducing disorder to the system, but paying with a change of spatial symmetry.
In the beginning, theoretical support from Young-Joon Song designated as dopant metals the alkaline metal series, while the alkaline Earth metals were told to be inappropriate. Hence, most of the experiments focussed on alkaline metals, and especially the alkaline metal potassium. Also, different Transition metals (iron and ruthenium) were used in the process.
In order to achieve the 1144 compounds, a wide variety of methods was applied, ranging from external flux method with Tin as a flux over a direct approach from the elements to a series of solid-solid attempts with different prereacted materials. In the end, none of them yielded the searched for compound. Contrarily, one of the last experiments seems to indicate that the 1144 compound $EuKRu_4P_4$ cannot be grown from the methods applied - if it can be grown at all. The direct translation from Paul Canfields approaches to $CaKRu_4P_4$ [107] was probably unsuccessful (despite band structure calculations state, that a structure $EuKRu_4P_4$ can be relaxed), because the ionic radii of europium and calcium are quite distinct. The next resort to turn to, that might be able to grow such compounds, would be to attempt a high pressure growth.

12 Summary

The work leading to this monography comprised several subprojects, all of them evolving around the idea of using the fluctuation of Europium valence states in Europium based intermetallic systems as a probe for the predictions of a theory of quantum critical elasticity. The theory itself, as proposed by Garst et al. [3] has been described in chapter 5. The properties of intermediate valent states and valence fluctuations, as well as how they connect to the general theory has been described in chapter 6. Especially, a generalized phase diagram for Europium based compounds was introduced there (fig. 6.1), proposing a general structure for Europium valence, magnetic order and transitions (first order line, second order endpoint, crossover area) between different intermediate valent states in Europium based systems. As the region of interest, in the frame of SFB TRR 288 the proposed second order critical endpoint of the valence transition was designated, since critical elasticity was expected in its vicinity.
The first and most extensive subproject was the Czochralski growth and extensive characterization of the system $EuPd_2Si_2$, which was discussed in chapter 8. The system shows valence fluctuations between two stable intermediate valent states between which a crossover like transition mediates and a strong lattice anomaly in the a-parameter connected to that. Effects in the electronic system and the lattice convene on the transition temperatures and intervals, and hence the degrees of freedom appear to be coupled in this transition. It could be clarified, that the characteristic temperature for the transition is very sensitive towards the chemical composition of the system and crystal defects (probably change of places between the Palladium and Silicon atoms), yielding a range of 120 K up to 165 K for the transitions and dissolving disagreements between different statements in the literature.
With a stably reproducible growth procedure for $EuPd_2Si_2$, many cooperating groups within the SFB TRR 288 could be provided with crystals of this system to investigate its elastic phenomena.
Still, the $EuPd_2Si_2$ system is located beyond the critical endpoint in the generalized phase diagram 6.1. In order to bring the probe system closer to the proposed critical endpoint to study the properties of the system in close vicinity, a doping series of the system with Germanium $EuPd_2(Si_{1-x}Ge_x)_2$ has been conducted (reported in chapter 9), again via Czochralski growth, with doping levels between $x = 0.05$ and $x = 0.30$ of nominal doping. The incorporation rate of the Germanium was tracked within the single samples and between different samples, showing mostly constant incorporation behaviour with an about 60% incorporation rate.
The doping of the system allowed for the suggestive construction of a specific phase diagram of $EuPd_2(Si_{1-x}Ge_x)_2$, as it is shown in fig. 9.14. The temperature

of the valence transition could be lowered with increased Germanium doping, until it got suppressed and a long range antiferromagnetic order took over. None of the valence fluctuating samples ever showed first order behaviour, although the predicted temperature for the critical endpoint was passed. Conclusive, the doping, although isoelectronic, is not equivalent to applying physical pressure. Hence, approaching the critical endpoint with this series was not successful. Another series, doping the system with gold on the palladium site, where the substitution is not isoelectronic, but a first order transition was reported, has already been taken up by master's student Robert Möller.
Another lattice effect, that is suspected to relate to the valence states of Europium in Europium based 122 compounds, is the collapse of the 122 Phosphides along the *c*-direction alongside with establishment of Phosphorus-Phosphorus covalent bonds. In order to investigate this phenomenon, single crystals of the collapsed tetragonal valence fluctuating $EuNi_2P_2$ and the non-collapsed tetragonal magnetic $EuFe_2P_2$ and $EuCo_2P_2$ were grown in Tin flux, as well as powderous samples of $EuFe_2P_2$ and $EuRu_2P_2$ by direct reaction and sintering.
In $EuNi_2P_2$, a characteristic energy scale for valence fluctuations of $T^* = 36\,\mathrm{K}$ has been found, as well as a lattice anomaly in *a*-direction, being an order of magnitude smaller than in the $EuPd_2Si_2$ system with only about 0.25% lattice parameter contraction. This system still lives clearly in the crossover area beyond the critical endpoint. From magnetic measurements, only the high temperature valence of $Eu^{2.3}$ could be drawn. For the low temperature regime, a Curie fit was not possible anymore. The Sommerfeld parameter was found to be only slightly enhanced with $\gamma = (81 \pm 2)\,\frac{\mathrm{mJ}}{\mathrm{molK}^2}$, indicating a rather small influence of hybridization and the Kondo effect.
Investigating on the compounds that are non-collapsed under ambient conditions, we performed single crystal X-ray diffractometry at low temperatures under pressure of the three respective systems in collaboration with the KIT at the ESRF. The recorded data are still under evaluation. Since this work focusses mostly on crystal growth, I opted to leave this end open and to be reported elsewhere. Riddles to solve include the possibility for twinning between collapsed and non-collapsed unit cells during a crossover transition or the lowering of unit cell symmetry and the appearance of incommensurate reflexes at low temperatures and high pressures.
The collapse of the tetragonal structure was approached in another way, trying to get the system $EuRu_2P_2$ closer to the collapse by substituting half of the Europium in an ordered manner with Potassium, thereby going from the 122 (I4/mmm) structural type to the lower symmetry 1144 (P4/mmm) structural type and the compound $EuKRu_4P_4$. Applying different methods, starting with Tin flux and ending with sintering prereacted ternary 122 compounds $EuRu_2P_2$ and KRu_2P_2, the exploration remained unsuccessful. Due to the extensive trials, we feel quite comfortable to state, that with the methods applied, the requested system remains inaccessible. A next idea is to apply high pressure conditions to the growth.

Conclusively, in this work I provide the SFB TRR 288 with a wide variety of systems relevant for investigations of valence fluctuations in Europium based intermetallics, which is a probe field for testing the theory of quantum critical

elasticity. With the Germanium doping series on $EuPd_2Si_2$, even a first sketch of a Europium valence phase diagram for a specific probe system could be proposed. This showed, that at least not all doping systems show the behaviour proposed by Onuki [6]. It is now to consider, how the different systems displaying both valence fluctuating and lattice effects fit into the picture of the theory of quantum critical elasticity. With establishing the Europium based intermetallics as a possible field of investigation for a large section of the SFB TRR 288 in testing the theory of quantum critical elasticity, I hope to have contributed a part to its self-propellation and scientific productivity.

Bibliography

[1] B. Latour and S. Woolgar, *Laboratory Life: The Construction of Scientific Facts.* Princeton University Press; Reprint Edition, 2008.

[2] S. Schaffer and S. Shapin, *Leviathan and the air-pump: Hobbes, Boyle and the experimental life.* Princeton University Press; Reprint Edition, 2018.

[3] M. Zacharias, I. Paul, and M. Garst *Phys. Rev. Lett.*, vol. 115, pp. 025703: 1 – 5, 2015.

[4] E. Gati, M. Garst, R. S. Manna, U. Tutsch, B. Wolf, L. Bartosch, H. Schubert, T. Sasaki, J. A. Schlueter, and M. Lang *Sci. Adv.*, vol. 2, pp. e1601646: 1 – 7, 2016.

[5] E. Cho, *(Bachelor thesis).* Prüfungsamt Physik, Goethe-Universität Frankfurt am Main, 2019.

[6] Y. Onuki, A. Nakamura, F. Honda, D. Aoki, T. Tekeuchi, M. Nakashima, Y. Amako, H. Harima, K. Matsubayashi, Y. Uwatoko, S. Kayama, T. Kagayama, K. Shimizu, S. Esakki Muthu, D. Braithwaite, B. Salce, H. Shiba, T. Yara, Y. Ashitomi, H. Akamine, K. Tomori, M. Hedo, and T. Nakama *Philos. Mag.*, vol. 97, p. 3399 – 3414, 2017.

[7] E. V. Sampathkumaran, L. C. Gupta, R. Vijayaraghavan, K. V. Gopalakrishnan, R. G. Pillay, and H. G. Devare *J. Phys. C: Solid State Phys.*, vol. 14, pp. L237 – L241, 1981.

[8] B. Batlogg, A. Jayaraman, V. Murgai, L. C. Gupta, R. D. Parks, and M. Croft, *Pressure-temperature studies and the p-T diagram of* $EuPd_2Si_2$. P. Wachter and H. Boppart (eds.), North-Holland publishing company, 1982.

[9] H. Jhans, M. Croft, E. Kemly, B. Grier, and C. U. Segre, *X-ray diffraction and Mossbauer effect measurements near a valence transition. In: Gupta L.C. and Malik S.K. (eds) Theoretical and Experimental Aspects of Valence Fluctuations and Heavy Fermions.* Springer, Boston, MA, 1987.

[10] H. Wada, H. Gomi, A. Mitsuda, and M. Shiga *Solid state commun.*, vol. 117, pp. 703 – 707, 2001.

[11] K. Mimura *et al. Jap. J. Appl. Phys.*, vol. 50, pp. 05FD03: 1 – 2, 2011.

[12] B. K. Cho, J. S. Rhyee, and H. C. Ri *J. Phys. Soc. Jpn.*, vol. 71, pp. 252 – 254, 2002.

[13] S. N. Mishra and H. G. Devare *Hyperfine Interactions*, vol. 15/16, pp. 633–638, 1983.

[14] C. Feng, Z. Ren, S. Xu, S. Jiang, Z. Xu, G. Cao, I. Nowik, I. Felner, K. Matsubayashi, and Y. Uwatoko *Phys. Rev. B*, vol. 82, p. 094426, 2010.

[15] N. S. Sangeetha, E. Cuervo-Reyes, A. Pandey, and D. C. Johnston *Phys. Rev. B*, vol. 94, p. 014422, 2016.

[16] P. Proschek, J. Prchal, M. Divis, J. Proleska, K. Vlaskova, J. Valenta, J. Zubac, J. Kastil, M. Hedo, T. Nakama, Y. Onuki, and F. Honda *J. Alloys and Compounds*, vol. 864, p. 158753, 2021.

[17] Y. Hiranaka, A. Nakamura, M. Hedo, T. Takeuchi, A. Mori, Y. Hirose, K. Mitamura, K. Sugiyama, M. Hagiwara, T. Nakama, and Y. Onuki *J. Phys. Soc. Japan*, vol. 82, p. 083708, 2013.

[18] C. Huhnt, W. Schlabitz, A. Wurth, A. Mewis, and M. Reehuis *Physica B*, vol. 252, pp. 44–54, 1998.

[19] W. Nolting, *Grundkurs Physik 6: Statistische Physik*, vol. 7. Springer, 2014.

[20] L. D. Landau and E. M. Lifschitz, *Lehrbuch der theoretischen Physik V: Statistische Physik*, vol. 1. Akademie-Verlag Berlin, 1966.

[21] J. Wosnitza *J. Low Temp. Phys.*, vol. 147, pp. 249–278, 2007.

[22] C. Krellner, S. Hartmann, A. Pikul, N. Oeschler, J. G. Donath, C. Geibel, F. Steglich, and J. Wosnitza *Phys. Rev. Lett.*, vol. 102, pp. 196402: 1 – 4, 2009.

[23] S. Sachdev *Science*, vol. 288, pp. 475–481, 2000.

[24] S. Sachdev and B. Keimer *Physics today*, vol. 64, pp. 29–36, 2011.

[25] M. Vojta *Rep. Prog. Phys.*, vol. 66, pp. 2069–2110, 2003.

[26] J. M. D. Coey, *Magnetism and magnetic materials.* Cambridge University Press, 2010.

[27] H. Ibach and H. Lueth, *Festkörperphysik - Einführung in die Grundlagen*, vol. 7. Springer, 2009.

[28] H. Ipser, *phase diagrams for crystal growth of intermetallics, in: crystal growth of intermetallics (Eds: P. Gille, Y. Grin).* De Gruyter, 2018.

[29] D. A. Young *Lawrence Livermore Laboratory, University of California*, 1975.

[30] D. R. Lide (Ed.), *CRC Handbook of Chemistry and Physics*, vol. 84. CRC Press, 2003.

[31] T. B. Massalski *et al.*, *Binary alloy phase diagrams.* The Materials Information Society, 1990.

[32] M. Peters, *(Master thesis)*. Prüfungsamt Physik, Goethe-Universität Frankfurt am Main, 2018.

[33] L. D. Landau and E. M. Lifschitz, *Lehrbuch der theoretischen Physik VII: Elastizitätstheorie*, vol. 4. Akademie-Verlag Berlin, 1975.

[34] R. Folk, H. Iro, and F. Schwabl *Z. Physik B*, vol. 25, pp. 69–81, 1976.

[35] R. Folk, H. Iro, and F. Schwabl *Phys. Rev, B*, vol. 20, pp. 1229–1244, 1979.

[36] E. R. Bauminger, D. Froindlich, I. Nowik, S. Ofer, I. Felner, and I. Mayer *Phys. Rev. Lett.*, vol. 30, pp. 1053–1056, 1973.

[37] B. C. Sales and D. K. Wohlleben *Phys. Rev. Lett.*, vol. 35, pp. 1240–1244, 1975.

[38] U. Mueller, *Anorganische Strukturchemie*, vol. 6. Vieweg+Teubner, 2008.

[39] R. M. J. Konings *et al. J. Phys. Chem. Ref. Data*, vol. 43, p. 013101, 2014.

[40] M. Kanatzidis, R. Poettgen, and J. W. *Angew. Chem. Int. Ed.*, vol. 44, p. 6996, 2005.

[41] K. Kliemt, *Crystal growth and characterization of Cerium- and Ytterbium-based Quantum Critical Materials (PhD thesis)*. Goethe-Universität Frankfurt am Main, 2018.

[42] G. S. Upadhyaya, *Powder Metallurgy Technology*. Cambridge International Science Publishing, 2002.

[43] J. Bauch and R. Rosenkranz, *Physikalische Werkstoffdiagnostik*. Springer, 2017.

[44] W. Massa, *Kristallstrukturbestimmung*. Teubner, 2007.

[45] *powderCell 2.3*. Bundesagentur für Materialforschung und Prüfung, 1999.

[46] B. H. Toby and R. B. Von Dreele *J. Appl. Cryst.*, vol. 46, pp. 544–549, 2013.

[47] *PPMS hardware and options manuals*. Quantum Design, 1999.

[48] R. W. Newsome and E. Y. Andrei *Rev. Sci. Inst.*, vol. 75, pp. 104–110, 2004.

[49] Z. Ban and M. Sikirica *Acta cryst.*, vol. 18, pp. 594–599, 1965.

[50] M. J. Buerger, C. H. MacGillarvy, N. F. M. Henry, J. S. Kasper, and K. e. c. Lonsdale, *International Tables For X-Ray Crystallography*. The Kynoch Press, 1952.

[51] A. Palenzona, S. Cirafici, and F. Canepa *J. Less Common Metals*, vol. 135, pp. 185 – 194, 1987.

[52] D. M. Adams, A. E. Heath, H. Jhans, A. Norman, and S. Leonard *J. Phys.: Cond. mat.*, vol. 3, pp. 5465 –5468, 1991.

[53] I. Felner and I. Nowik *Physica B, cond. mat.*, vol. 182, pp. 145 – 148, 1992.

[54] D. Rossi, R. Marazza, and R. Ferro *Jour. Less Common Metals*, vol. 66, pp. P17–P25, 1979.

[55] U. C. Rodewald, R. D. Hoffmann, R. Poettgen, and E. V. Sampathkumaran *Z. Naturforsch. B*, vol. 58, pp. 971–974, 2003.

[56] D. T. Adroja, B. D. Padalia, S. K. Malik, R. Nagarajan, and R. Vijayaraghavan *J. Magn. Magn. Mater.*, vol. 89, pp. 375–378, 1990.

[57] S. K. Dhar, R. Nagarajan, S. K. Malik, D. Rambabu, and R. Vijayaraghavan *J. Magn. Magn. Mater.*, vol. 31, pp. 393–394, 1983.

[58] S. Seiro, *Private communication.* 2018.

[59] H. Okamoto *Bull. Alloy Phase Diagr.*, vol. 11, pp. 140 – 143, 1990.

[60] M. Peters, I. Reiser, M. Ocker, D.-M. Tran, E. Cho, F. Ritter, C. Krellner, and K. Kliemt *in preparation*, 2022.

[61] K. Kliemt, *Private Communication.* Universität Frankfurt, 2018-2022.

[62] H. C. Baxi and T. B. Massalski *J. Phase Equilib.*, vol. 12, pp. 349–356, 1991.

[63] Z. Du, C. Guo, X. Yang, and T. Liu *Intermetallics*, vol. 14, pp. 560–569, 2006.

[64] A. Iandelli and A. Palenzona *J. Less Common Metals*, vol. 38, pp. 1–7, 1974.

[65] J. Linckens, *Private Communication.* Universität Frankfurt, 2021.

[66] R. N. Patil, L. C. Gupta, C. Godart, R. Vijayaraghavan, and B. D. Padalia *Hyperfine Interactions*, vol. 42, pp. 1063–1066, 1988.

[67] H. Hoefer, *Private Communication.* Universität Frankfurt, 2020.

[68] M. Merz, *Private communication.* Karlsruhe Institute for Technology, 2021.

[69] S. A. Medvedev, P. Naumov, O. Barkalov, C. Shekhar, T. Palasyuk, V. Ksenofontov, G. Wortmann, and C. Felser *J. Phys. Condens. Matter*, vol. 26, p. 335701, 2014.

[70] R. Mallik, E. V. Sampathkumaran, M. Strecker, G. Wortmann, P. L. Paulose, and Y. Ueda *J. magn. magn. mater.*, vol. 185, pp. L135–L143, 1998.

[71] M. W. Shafer *J. Appl. phys.*, vol. 36, p. 1145, 1965.

[72] C. Guguschev, *Private Communication.* IKZ Berlin, 2021.

[73] R. Poettgen and A. Simon *Z. anorg. allg. Chem.*, vol. 622, pp. 779–784, 1995.

[74] F. Merlo and M. L. Fornasini *J. Less Common metals*, vol. 13, pp. 603–610, 1967.

[75] S. Matsuda, W. Iha, F. Honda, J. Gouchi, Y. Uwatoko, M. Nakashima, Y. Amako, T. Takeuchi, T. Kida, M. Hagiwara, M. Hedo, T. Nakama, and Y. Onuki *JPS Conf. Proc.*, vol. 29, p. 012003, 2020.

[76] R. Poettgen *Z. Naturforsch. B*, vol. 50, pp. 1181–1184, 1995.

[77] D. Kaczorowski, B. Belan, and R. Gladyshevskii *Solid State Commun.*, vol. 152, pp. 839–841, 2012.

[78] M. A. Albedah, K. Al-Qadi, Z. M. Stadnik, and Przewoznik *J. Alloys and Compounds*, vol. 613, pp. 344–350, 2014.

[79] X. Rocquefelte, R. Gautier, J.-F. Halet, R. Muellmann, C. Rosenhahn, B. D. Mosel, G. Kotzyba, and R. Poettgen *J. Solid State Chem.*, vol. 180, pp. 533–540, 2007.

[80] Y. Onuki, M. Hedo, and F. Honda *J. Phys. Soc. Jpn.*, vol. 89, p. 102001, 2020.

[81] W. W. Anderson *AIP Advances*, vol. 9, p. 075108, 2019.

[82] R. Hoffmann and C. Zheng *J. Phys. Chem.*, vol. 89, pp. 4175–4181, 1985.

[83] R. Marchand and J. W. *J. Solid State Chem.*, vol. 24, pp. 351–357, 1978.

[84] B. Jaberg and J. W. *J. Solid State Chem.*, vol. 35, pp. 312–317, 1980.

[85] K. Momma and F. Izumi *J. Appl. Crystallogr.*, vol. 44, pp. 1272–1276, 2011.

[86] M. Reehuis and J. W. *J. Phys. Chem. Solids*, vol. 51, pp. 961–968, 1990.

[87] G. Wenski and A. Mewis *Z. Naturforsch. B*, vol. 41, pp. 38–43, 1986.

[88] M. Hedo, Y. Miura, A. Mori, H. Tsutsumi, Y. Hirose, F. Honda, T. Takeuchi, A. Nakamura, Y. Hiranaka, T. Nakama, H. Harima, and Y. Onuki *JPS Conf. Proc.*, vol. 3, p. 011010, 2013.

[89] D. H. Ryan, J. M. Cadogan, S. Xu, Z. Xu, and G. Cao *Phys. Rev. B*, vol. 83, p. 132403, 2011.

[90] M. Reehuis, W. Jeitschko, M. H. Meoller, and P. J. Brown *J. Phys. Chem. Solids*, vol. 53, pp. 687–690, 1992.

[91] C. Huhnt, W. Schlabith, A. Wurth, A. Mewis, and M. Reehuis *Phys. Rev. B*, vol. 56, pp. 13796–13804, 1997.

[92] M. Chefki, M. M. Abd-Elmeguid, H. Micklitz, C. Huhnt, W. Schlabitz, M. Reehuis, and W. Jeitschko *Phys Rev L*, vol. 80, pp. 802–805, 1998.

[93] H. S. Jeevan, D. Kasinathan, H. Rosner, and P. Gegenwart *Phys. Rev. B*, vol. 83, p. 054511, 2011.

[94] S. Danzenbaecher, D. V. Vyalikh, Y. Kucherenko, A. Kade, C. Laubschat, N. Caroca-Canales, C. Krellner, C. Geibel, A. V. Fedorov, D. S. Dessau, R. Follath, W. Eberhardt, and S. L. Molodtsov *Phys. Rev. Lett.*, vol. 102, p. 026403, 2009.

[95] U. Stockert, S. Seiro, N. Caroca-Canales, E. Hassinger, and C. Geibel *Phys. Rev. B*, vol. 101, p. 235106, 2020.

[96] T. D. Nguyen, *(Master thesis).* Prüfungsamt Physik, Goethe-Universität Frankfurt am Main, 2020.

[97] D. Hezel, *Private Communication.* Universität Frankfurt, 2021.

[98] P. Wenz and H. U. Schuster *Z. Naturforsch.*, vol. 39b, pp. 1816–1818, 1984.

[99] K. E. Mironov and G. P. Brygalina *Izvestiya Akademii Nauk SSSR, Neorganicheskie Materialy*, vol. 10, p. 787, 1974.

[100] S. Rundqvist *Acta Chem. Scand.*, vol. 16, pp. 287–292, 1962.

[101] F. Hulliger and O. Vogt *Solid State Communications*, vol. 8, pp. 771–772, 1970.

[102] Z. Ren, Q. Tao, S. Jiang, C. Feng, C. Wang, J. Dai, G. Cao, and Z. Xu *Phys. Rev. Lett.*, vol. 102, p. 137002, 2009.

[103] J.-A. Dolyniuk, J. Mark, S. Lee, N. Tran, and K. Kovnir *Materials*, vol. 12, p. 251, 2019.

[104] T. Chattopadhyay, P. J. Brown, P. Thalmeier, W. Bauhofer, and H. G. von Schnering *Physical Review B: Condensed Matter and Materials Physics*, vol. 37, p. 269, 1988.

[105] H. G. von Schnering, M. Wittmann, and D. Sommer *Zeitschrift fuer Anorganische und Allgemeine Chemie*, vol. 510, pp. 61–71, 1984.

[106] B. Carlsson, M. Goelin, and S. Rundqvist *J. Solid State Chem.*, vol. 8, pp. 57–67, 1973.

[107] M. Xu, O. Palasyuk, S. Budko, B. Song, K.-M. Ho, and P. C. Canfield *APS March Meeting*, 2021.

[108] J. D. Reusch, *(Master thesis).* Prüfungsamt Physik, Goethe-Universität Frankfurt am Main, 2021.

[109] M. Peters, K. Kliemt, J. D. Reusch, T. D. Nguyen, F. Walther, A. Haghighirad, S. M. Souliou, M. Merz, and C. Krellner *in preparation*, 2022.

[110] S. Rundqvist *Acta Chem. Scand.*, vol. 14, pp. 1961–1979, 1960.

[111] M. Reehuis, W. Jeitschko, E. Moersen, and W. Mueller-Warmuth *J. Less Common Metals*, vol. 139, pp. 359–369, 1988.

[112] M. Reehuis and W. Jeitschko *J. Phys. Chem.*, vol. 563, 1989.

[113] E. Moersen, B. D. Mosel, W. Mueller-Warmuth, M. Reehuis, and W. Jeitschko *J. Phys. C: Solid State Phys.*, vol. 21, p. 3133, 1988.

[114] F. Walther, *(Bachelor thesis).* Prüfungsamt Physik, Goethe-Universität Frankfurt am Main, 2021.

[115] V. Petricek, M. Dusek, and L. Palatinus *Z. Kristallogr.*, vol. 229, pp. 345–352, 2014.

[116] L. J. Farrugia *J. Appl. Cryst.*, vol. 45, pp. 849–854, 2012.

[117] F. Birch *Phys. Rev.*, vol. 71, pp. 809–825, 1947.

[118] S. Furuseth and H. Fjellvag *Acta Chem. Scand. A*, vol. 39, pp. 537–544, 1985.

[119] V. Keimes, A. Hellmann, A. Mewis, C. Huhnt, and N. Schuette *Z. Anorg. Allg. Chem.*, vol. 626, pp. 1653–1659, 2000.

[120] H. Nowotny and K. Schubert *Naturwissenschaften*, vol. 32, p. 76, 1944.

[121] R. Nagarajan, G. K. Shenoy, L. C. Gupta, and V. Sampathkumaran, E *Phys. Rev. B*, vol. 32, pp. 2846–2850, 1985.

[122] Y. Kakehashi and S. Chandra *Physica B*, vol. 447, pp. 19–22, 2014.

[123] B. Q. Song, M. C. Nguyen, C. Z. Wang, and K. M. Ho *Phys. Rev. B*, vol. 97, p. 094105, 2017.

[124] A. Iyo, K. Kawashima, T. Kinjo, T. Nishio, S. Ishida, H. Fujihisa, Y. Gotoh, K. Kihou, H. Eisaki, and Y. Yoshida *J. Am. Chem. Soc.*, vol. 138, pp. 3410–3415, 2016.

[125] A. F. Holleman, E. Wiberg, and N. Wiberg, *Lehrbuch der anorganischen Chemie, 101. Auflage.* de Gruyter, 1995.

[126] Y.-J. Song, *Private Communication.* AG Valenti, Universität Frankfurt, 2020.

[127] W. R. Meier, T. Kong, S. Budko, and P. C. Canfield *Phys. Rev. Mat.*, vol. 1, p. 013401, 2017.

[128] T. B. Brill, R. C. Gerhart, and W. A. Welsh *Journal of Magnetic Resonance*, vol. 13, pp. 27–37, 1974.

[129] J. M. Sangster *JPEDAV*, vol. 31, pp. 73–76, 2010.

[130] L. Hackspill and R. Bossuet *Compt. Rend. Hebd. Seances Acad. Sci.*, vol. 154, pp. 209–211, 1912.

[131] H. G. von Schnering, T. Meyer, W. Honle, W. Schmettow, U. Hinze, W. Bauhofer, and G. Kliche *Z. Anorg. Allg. Chem.*, vol. 553, pp. 261–279, 1987.

[132] IFA, "Sicherheitsdatenblaetter," *GESTIS Stoffdatenbank*, abgerufen 2020/2021.

[133] A. Mewis *Z. Naturforsch.*, vol. 35b, pp. 141–145, 1979.

[134] A. N. Nesmeyanov, *Vapor Pressure of the Chemical Elements.* Elsevier Publishing Company, 1963.

A | Chemicals

Overview over the chemicals used to conduct the growth experiments.

Material	Purity	Vendor	Hazard warnings
Silicon (Si)	6N	Cerac	
Phosphorus (P)	6N	Chempur	H228, H412
Potassium (K)	2N5	Aldrich	H260, H314, EUH014
Potassium Chloride (KCl)	2N5	Carl Roth	
Iron (Fe)	3N5	Cerac	H228, H251
Iron Phosphide (Fe_2P)	2N5	Aldrich	H315, H319, H335
Cobalt (Co)	5N	Johnson Matthey	H228, H302, H317, H319, H330, H334, H341, H350i, H360F, H400, H410
Nickel (Ni)	4N	Chempur	H228, H317, H351, H372, H412
Nickel (Ni)	4N5	EvoChem	H228, H317, H351, H372, H412
Germanium (Ge)	4N		
Rubidium (Rb)			H260, H314, EUH014
Palladium (Pd)	4N	Heraeus	
Indium (In)	6N	EvoChem	H228, H315, H319, H332, H335
Tin (Sn)	4N	EvoChem	
Cesium (Cs)			H260, H314, EUH014
Europium (Eu)	4N	EvoChem	H250, H261

Table A.1: Elements and compounds as starting materials for the growth experiments (hazard warnings by GESTIS [132])

Material	Size
Quartz	$18 \times 17 \times 1200\,\mathrm{mm}$
Quartz	$22 \times 20 \times 1200\,\mathrm{mm}$
Niobium	$27 \times 26 \times 80\,\mathrm{mm}$
Niobium	$14 \times 13 \times 80\,\mathrm{mm}$
Graphite	$25 \times 22 \times 40\,\mathrm{mm}$
Glass Carbon	$25 \times 22 \times 40\,\mathrm{mm}$
Alumina	diverse

Table A.2: Crucible materials

Material	Vendor	Use
Hydrochloric Acid 37% (HCl)	VWR Chemicals	Removal of Tin and Indium fluxes
4922N	Dupont	Single component silver based conductive glue, ACT contacts
E-Solder 3025	EPOXY	Two components silver based conductive glue, Cutting in the spark erosion
Low temperature varnish	Cryoandmore	"GE", VSM sample mounting
Apiezon N	Apiezon	Low temperature fat, PXRD and HC sample preparation
Acetone (2N8)	Fisher Chemicals	Removal of two component silver glue and GE varnish
Toluene (2N7)	Sigma-Aldrich	Removal of Apiezon N
(2-Butoxyethyl)Acetate	Merck	Solving 4922N

Table A.3: Acids, glues and solvents

B | 1144 project experiments table

Exp. No.	Target phase	Mass (g)	Weigh in	T steps (° C)	flux removal
MP501	$EuFe_2P_2$	15	1.2:2:2:20	450-1100	HCl
MP502	$EuRbFe_4P_4$	13.32	0.6:0.6:2:2:20	450-1100	HCl
MP503	$EuCsFe_4P_4$	10.81	0.6:0.6:2:2:20	450-1100	HCl
MP504	$EuRbFe_4P_4$	14.38	0.6:0.6:2:2:20	450-1100	Centrifuge
MP505	$EuCsFe_4P_4$	12.43	0.6:0.6:2:2:20	450-1100	Centrifuge, HCl

Table B.1: Experiments in tin flux in the 1144 project. Weigh in as element 1:element 2:...:flux. Experiments in niobium crucibles, except MP501 in a quartz ampoule. Green: phase obtained. Red: phase not obtained.

Exp. No.	Target phase	Mass (g)	Weigh in	T steps (° C)
MP506	Rb_4P_6	2	4:6	650
MP507	K_4P_6	5	4:6	650
MP508	EuP	4	1:1	850

Table B.2: Prereactions of binaries in the 1144 project. Experiments in niobium crucibles. Green: phase obtained with yield close to 100%. Blue: other phases prereacted.

Exp. No.	Target phase	Mass (g)	Weigh in	T steps (° C)	Dwelling time (d)
MP512	$EuFe_2P_2$	1.5	1:2:2 elements	500-900	2
MP513	$EuFe_2P_2$	2	1:1 EuP: Fe_2P	500-900	2
MP523	$EuRu_2P_2$	2	1:2:2 elements	230-500-900	3×4
MP524	$EuFe_2P_2$	3	MP512+MP513	230-500-900	3×4
MP539	$EuRu_2P_2$	5	1:2:2 elements	500-900	5
MP540	$EuRu_2P_2$	2	1:2:2 elements	500-900	4

Table B.3: Prereactions of Eu based ternaries in the 1144 project. Crucible setup alumina in niobium. Blue: phase obtained with yield <80%. Green: phase obtained with yield >80%.

Exp. No.	Target phase	Mass (g)	Weigh in	T steps (°C)	Dwelling time (d)
MP511	KFe_2P_2	1	1:2:2 elements	500-900-950	3
MP515	KFe_2P_2	1	1:2:2 elements	500-900	3
MP516	KFe_2P_2	1	1:2:4 K_4P_6:Fe_2P:Fe	500-900	3
MP518	KFe_2P_2	1	1:2:4 K_4P_6:Fe_2P:Fe	500-900	3
MP519	KFe_2P_2	1	1:2:4 K_4P_6:Fe_2P:Fe	500-900	3
MP520	KFe_2P_2	1	1:2:2 elements	500-900	3
MP521	KFe_2P_2	1.5	1:2:2 elements	230-500-900	3×4
MP522	KRu_2P_2	1.5	1:2:2 elements	230-500-900	3×4
MP525	KRu_2P_2	1.5	1:2:2 elements	230-500-900	4
MP526	KRu_2P_2	2	1:2:2 elements	230-500-900	4
MP528	KRu_2P_2	2	1:6 K_4P_6:Ru	230-500-900	4
MP529	KRu_2P_2	2	1:2:2 elements	230-500-900	4
MP530	KRu_2P_2	2	1:2:2 elements	230-500-900	4
MP531	KRu_2P_2	2	1:1:1 elements	230-500-900	4
MP532	KRu_2P_2	2	1:1:1 elements	230-500-900	4
MP533	KRu_2P_2	2	1:2:2 elements	230-500-750	4
MP534	KRu_2P_2	2	1:1:1 elements	230-500-750	4
MP537	KRu_2P_2	2	1.5:1:1 elements	230-500-750	4
MP538	KFe_2P_2	2	1.5:1:1 elements	230-500-750	4

Table B.4: Prereactions of K based ternaries in the 1144 project. Crucible setup: graphite in niobium for 519, 520 and 531, glassy carbon in niobium for 532, alumina in quartz for 515 and 516, alumina in niobium else. Red: phase not obtained. Blue: phase obtained with yield <80%. Green: with yield >80%.

Exp. No.	Target phase	Mass (g)	Weigh in	T steps (°C)	Dwelling time (d)
MP514	$CaFe_2P_2$	1.5	1:2:2 elements	500-900-1200	1

Table B.5: Prereactions of Ca based ternaries in the 1144 project. Crucible setup: alumina in niobium. Green: phase obtained with yield >80%.

Exp. No.	Target phase	Mass (g)	Weigh in	T steps (° C)	Dw.time (d)
MP509	$EuKFe_4P_4$	1	1:8:2:2 K_4P_6:Fe_2P:EuP:Eu	500-700/800	1
MP510	$EuRbFe_4P_4$	1	1:8:2:2 Rb_4P_6:Fe_2P:EuP:Eu	500-700/800	1
MP517	$EuCaFe_4P_4$	1	1:1 Eu122:Ca122	900	5
MP527	$EuKRu_4P_4$	2	1:1:4:4 elements	230-500-900	1
MP535	$EuKRu_4P_4$	2	1:1:4:4 elements	230-500-750	1
MP536	$EuKRu_4P_4$	0.87	1:1 Eu122:K122	230-500-750	5
MP541	$EuKRu_4P_4$	1.5	1:1:1 Eu122:K122:K	230-500-750	5
MP542	$EuKRu_4P_4$	1.5	1:1 Eu122:K122 + Mo rod	230-500-750	5
MP543	$EuKRu_4P_4$	1	1:1:0.5 Eu122:K122:K	230-500-750	21
MP544	$EuKRu_4P_4$	1	1:1:0.7 Eu122:K122:K	230-500-750	21

Table B.6: Quarternary reactions in the 1144 project. Crucible setup: alumina in niobium. Red: phase not obtained.

Danksagung

Eine Forschungsarbeit ist niemals die Leistung einer Einzelperson, obgleich am Ende der Name einer Einzelperson das Deckblatt zu schmücken hat. Wie in der Einleitung bereits besprochen, ist eine Forschungsarbeit immer eine Gemeinschaftsleistung eines kleinen wissenschaftlichen Gruppe sowie assoziierter Gruppen, die gemeinsam ein wissenschaftliches Netzwerk bilden. Insbesondere die Rolle derjenigen Gruppe, der die zu prüfende Person direkt angegliedert ist, ist in jedem Punkt der Arbeit von allergrößter Bedeutung.

Zuerst bin ich Prof. Dr. Cornelius Krellner sehr dankbar, dass er mich in seine Arbeitsgruppe aufgenommen hat, die mein wissenschaftliches Arbeiten in den letzten Jahren strukturiert hat. Du sorgst in Deiner Gruppe nicht nur für eine vielfältig ausgestattete Arbeitsumgebung, sondern auch für eine angenehme und (soweit ich das feststellen kann) inklusive Gruppenatmosphäre. Ich danke dir auch dafür, dass dein Interesse darin liegt, Begeisterung für Forschung zu teilen, und dass deine Tür immer offen für Diskussionen und Rücksprachen war. Eine bessere Betreuung hätte ich mir in dieser Zeit nicht wünschen können!
Außerdem muss ich Cornelius sehr dafür danken, dass er mir eine sehr freie Entfaltung auch neben den Projekten ermöglicht hat. Es ist seiner Unterstützung und seinem Wohlwollen zu verdanken, dass ich neben meiner Arbeit an diesem Projekt noch beinahe ein ganzes Zweitstudium absolvieren konnte, das mich auch über die schwere Zeit der Kontaktbeschränkungen mit gerettet hat.

Vielen Dank auch an Prof. Dr. Michael Lang, der das zweite Gutachten für diese Arbeit anfertigte!

An besonderer Stelle möchte ich gerne Dr. Kristin Kliemt danken, die gemeinsam mit Cornelius Krellner das Projekt innerhalb des SFB TRR 288 als PI leitet, in dessen Rahmen diese Arbeit stattfand. Kristin Kliemt operierte überdies die ADL und somit den Czochralski-Züchtungs-Schritt des $EuPd_2Si_2$-Unterprojekts. In Sachen der physikalischen Charakterisierung insbesondere dieses System-Komplexes kam es ebenfalls zu vielen fruchtbaren Diskussionen.

Klaus-Dieter Luther und Tim Förster danke ich für technische Unterstützung allerlei Art, und Franz Ritter für technische Expertise und Gerätebetreuung insbesondere im Bezug auf die unterschiedlichen Röntgenanlagen. Ebenso danke ich Herrn Pfeiffer und Herrn Hohmann stellvertretend für die Gerätewerkstatt, die kleine Anfertigungen und Verarbeitungen immer schnell besorgt hat.

Diese Arbeit baute auch auf andere im Rahmen des Kristall- und Materiallabors angefertigte Abschlussarbeiten auf oder war mit solchen verwandt oder verzahnt. Ich danke Eunhyung Cho, deren Bachelorarbeit Ausgangspunkt des $EuPd_2Si_2$-Projekts war; Tanh Duc Nguyen und Julian Dominik Reusch, die an der EuT_2P_2-Familie parallel an anderen Verbindungen im Rahmen ihrer Masterarbeiten gearbeitet haben, und mit denen wichtiger Austausch bestand; und Doan-My Tran und Franziska Walther, die ihre Master- bzw. Bachelorarbeit sehr eng angebunden an diese Arbeit durchgeführt haben, und die entsprechend zu

betreuen mir eine große Freude war; außerdem Robert Möller, der mit der Gold-Dotierung des $EuPd_2Si_2$-Systems in seiner Masterarbeit den nächsten Schritt des Projekts zu gehen beginnt.

Michelle Ocker, Isabel Reiser und Janina Schröder danke ich für ihre Unterstützung beim zeitaufwändigen Überblick- und Probenpräparationsprozess im $EuPd_2Si_2$-Projekt, in dem alle drei zu einem Zeitpunkt als HiWi beteiligt waren.

Auch dem Rest des Kristall- und Materiallabors danke ich für eine unvergessliche Zeit, gute Laboratmosphäre und die diversen kleinen Diskussionen, die einen Arbeitsprozess formen, ohne dass man ohne weiteres mit dem Finger daraufzeigen könnte.

Außerhalb des Kristall- und Materiallabors sind die Projekte dieser Arbeit zunächst eingebettet in den SFB TRR 288 der Goethe-Universität Frankfurt, des Karlsruhe Institute of Technology, der Johannes-Gutenberg-Universität Mainz, der Ruhr-Universität Bochum und des MPI für Chemikalische Physik fester Stoffe in Dresden. In einer derart ausdifferenzierten Arbeitsumgebung muss aber natürlich die hervorgehobene Rolle besonders eng kooperierender Gruppen gewürdigt werden. Die Ausrichtung des $EuPd_2Si_2$-Projekts (mit Substitutionsreihen) wurde gemeinsam mit der Arbeitsgruppe von Prof. Dr. Michael Lang vorgenommen und evaluiert, die in diesem Teilprojekt am nächsten zur Arbeit des KML verknüpft war. Als Personen sind hier zu nennen: Michael Lang, Bernd Wolf, Steffi Hartmann und Jan Zimmermann.

Im Rahmen des $EuPd_2Si_2$-Projekts hatte ich einige Unterstützung bei der chemischen und kristallographischen Analyse. Mit Einkristalldiffraktometrie beteiligten sich Michael Merz und Amir Abbas Haghighirad vom KIT. Am Institut für Geowissenschaften der Goethe-Universität konnte ich auf die Hilfe von Heidi Höfer und Dominik Hezel durch WDX-Analysen und von Jolien Linckens bei der großflächigen Bestimmung von Kristallorientierung durch EBSD zählen. Am IKZ Berlin untersuchte Christo Guguschev Proben qualitativ chemisch und simultan auf ihre Orientierung hin durch Anwendung von Röntgenfluoreszenzanalyse.

Bei der Planung des 1144-Projekts habe ich zu verschiedenen Zeiten, insbesondere bezüglich des des Umgangs mit Alkalimetallen, Ratschläge eingeholt. Für die Beratung zu diesem Projekt danke ich Martin Schmidt vom Fachbereich Chemie der Goethe-Universität, Anton Jesche von der Universität Augsburg, sowie Paul Canfield und Mingyu Xu von der Iowa State University.

Außerdem gilt mein sehr großer Dank denjenigen Gruppen und Wissenschaftler*innen, die mit mir auf Messzeiten an Großeinrichtungen gearbeitet haben, sowie den Einrichtungen für die Genehmigung der Messzeiten. Das bezieht sich auf ARPES-Messungen mit der Gruppe von Denis Vyalikh im Jahr 2018 am Beschleuniger Bessy II in Berlin und im Jahr 2019 am SLS des Paul-Scherrer-Instituts, namentlich Denis Vyalikh, Alexander Generalov, Max Mende und Susanne Schulz. Ebenso sind natürlich eingeschlossen Kristin Kliemt, Sofia Michaela Souliou (KIT) und Amir Abbas Haghighirad (KIT), sowie als local contact Gaston Garbarino,

die im Jahr 2021 an einer Einkristall-Röntgendiffraktometrie-Messzeit bei hohem Druck und tiefen Temperaturen am ESRF in Grenoble beteiligt waren.

Julian Dominik Reusch möchte ich zudem für den gemeinsamen Lesekreis danken, der die Anregungen aus dem Vorwort und einige weitere Reflexionsprozesse geformt hat.

Vielen Dank auch an alle Menschen, die sich bei der Finalisierung der Druckversion dieser Arbeit am Kampf gegen den Fehlerteufel beteiligt haben. Das sind: Kristin Kliemt, Sarah Krebber, Alexej Kraiker und Katharina Zoch.

Zuletzt entsteht eine solche Arbeit niemals unabhängig von ihren äußeren Bedingungen. Seit März 2020 fand diese Arbeit - fast zwei Jahre also - unter den Vorzeichen der CoVid-19-Pandemie statt. Mit den jeweils angemessenen Sicherheitsmaßnahmen wurde es mir jedoch immer ermöglicht, vor Ort zu arbeiten. Gemeinsam mit dem zweiten Studium hat mich das so weit beschäftigt gehalten, dass mir in den zwei Jahren nicht die Decke auf den Kopf gefallen ist. Auch meine Eltern und ein paar wenige Freunde, mit denen ich unterschiedliche Wege der regelmäßigen Beschäftigung gefunden habe, haben mir über diese Zeit geholfen. Danke an alle, die mir geholfen haben, diese Zeit durchzustehen, und ich hoffe, dass ich andersherum auch das meine dazutun konnte.